Dissertation

submitted to the
Combined Faculties of the Natural Sciences and Mathematics
of the Ruperto-Carola-University of Heidelberg, Germany
for the degree of
Doctor of Natural Sciences

Put forward by

Diplom-Physiker Thomas Gerner

Born in: Friedrichshafen, Germany

Oral examination: 16.10.2014

Chemical characterization of the early evolutionary phases of high-mass star-forming regions

Referees: apl. Prof. Dr. Henrik Beuther
Prof. Dr. Ralf Klessen

Abstract

The formation of high-mass stars is a very complex process and up to date no comprehensive theory about it exists. This thesis studies the early stages of high-mass star-forming regions and employs astrochemistry as a tool to probe their different physical conditions. We split the evolutionary sequence into four observationally motivated stages that are based on a classification proposed in the literature. The sequence is characterized by an increase of the temperatures and densities that strongly influences the chemistry in the different stages.

We observed a sample of 59 high-mass star-forming regions that cover the whole sequence and statistically characterized the chemical compositions of the different stages. We determined average column densities of 18 different molecular species and found generally increasing abundances with stage. We fitted them for each stage with a 1D model, such that the result of the best fit to the previous stage was used as new input for the following. This is a unique approach and allowed us to infer physical properties like the temperature and density structure and yielded a typical chemical lifetime for the high-mass star-formation process of 10^5 years.

The 18 analyzed molecular species also included four deuterated molecules whose chemistry is particularly sensitive to thermal history and thus is a promising tool to infer chemical ages. We found decreasing trends of the D/H ratios with evolutionary stage for 3 of the 4 molecular species and that the D/H ratio depends more on the fraction of warm and cold gas than on the total amount of gas. That indicates different chemical pathways for the different molecules and confirms the potential use of deuterated species as chemical age indicators.

In addition, we mapped a low-mass star forming region in order to study the cosmic ray ionization rate, which is an important parameter in chemical models. While in chemical models it is commonly fixed, we found that it strongly varies with environment.

Zusammenfassung

Die Entstehung massereicher Sterne ist ein sehr komplexer Prozess und bis heute existiert darüber keine umfassende Theorie. Diese Doktorarbeit untersucht die frühen Stadien von Regionen mit massereicher Sternentstehung und benutzt Astrochemie als Werkzeug, um die verschiedenen physikalischen Bedingungen zu erforschen. Wir teilen die evolutionäre Abfolge in vier durch Beobachtungen motivierte Stadien, welche auf einer vorgeschlagenen Klassifizierung aus der Literatur basieren. Die Sequenz ist dabei durch einen Anstieg der Temperaturen und Dichten charakterisiert, was einen starken Einfluss auf die Chemie in den unterschiedlichen Stadien hat.

Wir beobachteten eine Auswahl von 59 Regionen mit massereicher Sternentstehung, die die gesamte Sequenz abdecken und charakterisierten statistisch die verschiedenen Stadien bezüglich ihrer chemischen Zusammensetzung. Wir bestimmten die Säulendichten von 18 verschiedene Molekülsorten und fanden im Allgemeinen einen Anstieg der Häufigkeiten mit dem Stadium. Wir modellierten diese für jedes Stadium mit einem 1D-Modell, wobei das Ergebnis des besten Modells des vorhergehenden Stadiums als Startbedingungen für das folgende Stadium benutzt wurde. Dies ist ein einzigartiger Ansatz und erlaubte es uns auf die physikalischen Eigenschaften, wie die Temperatur- und die Dichtestruktur zurückzuschließen und ergab eine typische chemische Lebenszeit des Entstehungsprozesses massereicher Sterne von 10^5 Jahren.

Unter den 18 analysierten Molekülarten waren auch vier deuterierte Moleküle, deren Chemie besonders sensibel gegenüber der thermischen Geschichte ist und damit ein aussichtsreiches Werkzeug um auf das chemische Alter rückschließen zu können. Wir fanden eine abnehmende Tendenz des D/H-Verhältnisses mit evolutionärem Stadium für 3 der 4 Molekülsorten und dass das D/H-Verhältnis stärker vom Anteil von warmem zu kaltem Gas als von der Gesamtmenge des Gases abhängt. Dies weist auf verschiedene chemische Reaktionswege für die unterschiedlichen Moleküle hin und bestätigt den potentiellen Nutzen von deuterierten Molekülen als Kennzeichen für das chemische Alter.

Zudem fertigten wir eine Karte einer Region mit massearmer Sternentstehung um die Ionisationsrate der kosmische Strahlung, die ein wichtiger Parameter in chemischen Modellen ist, zu erforschen. Während sie in chemischen Modellen üblicherweise fix ist, fanden wir heraus, dass sie sich stark mit der Umgebung ändert.

Contents

List of Figures

List of Tables

Chapter 1

Introduction

The formation of stars is an important process that effects galaxies on all possible size scales. Although the total number of stars is dominated by low-mass stars, feedback processes of massive stars energetically dominate due to their enormous luminosities. During their whole lifetime, massive stars eject a huge amount of material and energy into their environment in the form of winds and outflows, but also strong radiation across all wavelengths and finally through their end in a supernova explosion. These processes not only influence the physical structure of the interstellar medium surrounding them, but also considerably its chemical structure through the synthesis of heavy elements in their interiors. Hence, understanding the high-mass star formation process is an important goal in astrophysics.

1.1 High-mass star formation

Over the past years there has been huge progress in the understanding of the formation of these stars. However, in contrast to low-mass star formation, high-mass star formation is still a relatively poorly known and understood process (Beuther et al. 2007a; Zinnecker & Yorke 2007; Tan et al. 2014). The term high-mass star is generally used for stars with masses $> 8 M_{\odot}$. This is approximately the mass at that the core of the forming star starts to burn hydrogen. In a simplistic 1D approach, the basic concepts of low-mass star formation only allow to form stars up to $8 M_{\odot}$, at which point the radiation pressure becomes strong enough to stop the accretion flow onto the star and halts further growth to higher masses. High-mass star formation sides are extreme environments involving many physical processes, e.g. turbulence, self gravity and magnetic fields (McKee & Ostriker 2007), that have an effect on many different scales and make it difficult and computational expensive to model those. Improvements in the theoretical understanding have been made over past years through the capability to increase the spatial resolution of models, to be able to perform 3D simulations and to include more physical effects (e.g., Kuiper et al. 2011). In order to test these simulations it is important to compare them with actual observations. However, on the observational side also exist a number of reasons that complicate studies of high-mass star formation. High-mass stars are believed to form in embedded environments within clusters. Due to their high masses, their lifetimes are short and they are less frequent compared to low-mass stars. They are on average more distant, especially concentrated within the galactic plane, where the gas and dust densities are highest.

1.2 An evolutionary sequence of high-mass star-forming regions

An evolutionary classification of low-mass stars is well established and the general scenario widely accepted, although many details are not fully understood yet (e.g., André 1995; André et al. 2000; McKee & Ostriker 2007). The described sequence is based on the spectral energy distribution (SED) of the objects and groups them into four classes: Class 0, I, II, III. Figure 1.1 shows a sketch of this sequence. Class 0 objects consist of a deeply embedded small core surrounded by an envelope that dominates the total mass and have very cold spectra that peak in the far-infrared or even submillimeter regime. In Class 1 objects, the mass of the envelope decreases while the mass of the core is increasingly growing. The envelope starts to flatten and the energy spectrum shifts to higher temperatures up to the mid-infrared regime. In Class 2 objects, the envelope material is mainly concentrated in a circumstellar disk. The SED is composed by the radiation from the protostar and from the circumstellar disk and peaks in the near-infrared. The SED of Class 3 objects finally is dominated by the star and the emission of the disk becomes negligible.

In contrast to that, an evolutionary sequence for high-mass star formation is still under debate. However, in the literature exist attempts to classify different stages of high-mass protostars. Similarly to the low-mass star formation case, Beuther et al. (2007a); Zinnecker & Yorke (2007) proposed a scenario for high-mass stars based on their physical properties. The sequence starts with the high-mass starless cores. These are regions of dense, cold gas in that no embedded protostellar heating source has formed yet. Infrared dark clouds (IRDCs), first identified by the mid-infrared space observatories ISO (Infrared space observatory) (Perault et al. 1996) and MSX (Mid-course Space Experiment) (Egan et al. 1998) were potential candidates for harboring high-mass starless cores. They detected the IRDCs as dark patches against the bright Galactic mid-infrared background. Later, continuum observations in the millimeter and sub-millimeter regime allowed to detect them also in emission and study their physical properties (e.g., Ragan et al. 2012). IRDCs are massive dense clumps with masses between several $100 - 1000\ \mathrm{M}_{\odot}$, sizes of few $0.25 - 0.5$ pc, column densities between $10^{23} - 10^{24}\ \mathrm{cm}^{-2}$ and temperatures between $10 - 20\,\mathrm{K}$. IRDCs are now widely believed to be the birthplaces of massive stars and good candidates to cover the earliest stages of the high-mass star formation sequence. Initially starless, dense cores in the IRDCs can harbor low-mass and intermediate-mass protostars leading to observations of IRDC with embedded sources below $100\,\mu$m.

The next stage of the high-mass protostar is considered then the forming protostars reach a mass of $> 8\,\mathrm{M}_{\odot}$ enter the hydrogen burning phase. These so called high-mass protostellar objects (HMPOs) are accreting the surrounding gas and heat

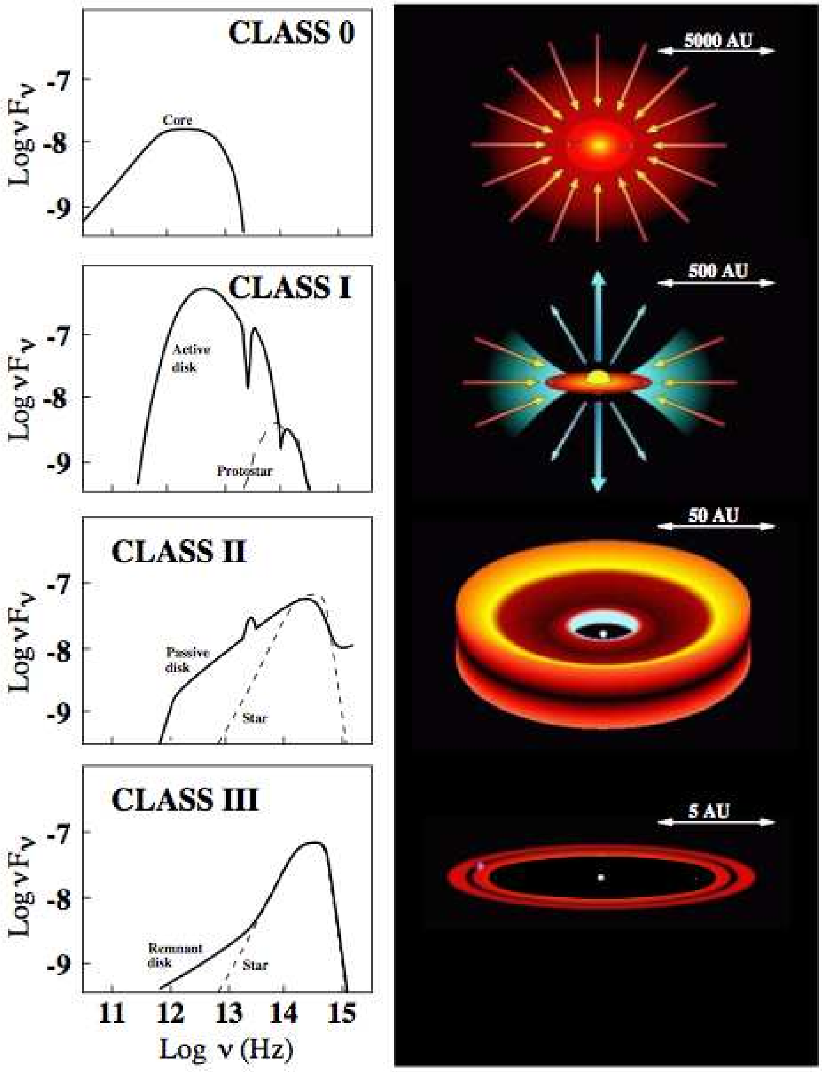

Figure 1.1 Schematic illustration of the evolutionary sequence of low-mass star formation with typical spectral energy distributions on the left and system geometries on the right. The figure is taken from the PhD thesis of Andrea Isella (`http://www.astro.caltech.edu/~isella/home_files/Thesis.pdf`).

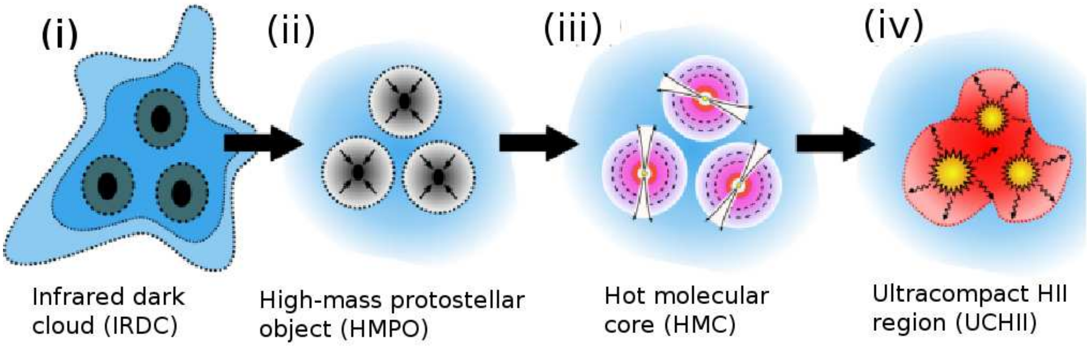

Figure 1.2 Schematic illustration of the evolutionary sequence of high-mass star-forming regions. The sequence used in this thesis divides the early phases of the high-mass star formation process into four stages illustrated by the four pictures, (i) infrared dark cloud, (ii) high-mass protostellar object, (iii) hot molecular core, and (iv) ultra-compact HII region. The figure is adopted from the PhD thesis of Cormac Purcell (`http://www.ast.leeds.ac.uk/~phycrp/publications.html`).

up their immediate environment. The typical physical conditions, like masses and sizes, are similar to the masses and sizes found in IRDCs, but the temperature and the mean densities increase. This accretion phase continues until the final star is formed. The star can still be embedded and can continue its accretion phase when it starts to burn hydrogen and reaches the main-sequence. But many of them will have lost their envelope and stopped accreting and finally ionize their surroundings due to their UV-radiation and create ultra-compact HII (UCHII) regions around them. The last stages can have overlaps in the same object.

The evolutionary picture we use in this thesis is based on the sequence outlined in Beuther et al. (2007a) and an illustration of the stages is given in Figure 1.2. The basic sequence IRDC-HMPO-UCHII outlined above is kept, but based on their chemical appearance, the stage of an HMPO is split into typically colder, chemically poorer, less evolved sources and hotter, chemically richer, more evolved sources. These chemically rich sources are commonly referred to as hot molecular cores Kurtz et al. (e.g., 2000); Cesaroni et al. (e.g., 2005). Hence, our evolutionary picture is dividing the sequence into four different stages based on their physical and chemical properties leading to the nomenclature starting from an infrared dark cloud (IRDC) to a high-mass protostellar object (HMPO) to a hot molecular core (HMC) and finally an ultra-compact HII (UCHII) region, which is the last considered stage in our sequence.

1.3 Astrochemistry

An important phase of the interstellar matter cycle is dominated by cold and dense gas and dust that ultimately form new stars. Observations of continuum emission of the dust and molecular line transitions at infrared and (sub-)millimeter wavelengths are a unique tool to probe these environments. Studying the chemistry in these objects serves to understand the chemistry itself. Moreover, the responsible chemical processes are very sensitive to physical parameters, such as the density, temperature, ionization rate. Hence, the understanding of the chemistry allows also to deduce physical parameters and particular lines of molecules can be used to probe different physical conditions and components (see, e.g., Evans 1999). Molecules have been identified that trace various processes, physical parameters and environments. SiO, for example, has been theoretically predicted to be enhanced in shocked regions (Hartquist et al. 1980) and is used as a tracer of outflows and jets (Ziurys et al. 1989; Martin-Pintado et al. 1992; Schilke et al. 1997b). Also a number of other molecules, such as HCN, SO, CS and CH_3OH are seen to trace outflows (Jørgensen et al. 2004a). Species like NH_3 and H_2CO can be employed to measure gas kinetic temperatures (Walmsley & Ungerechts 1983; Ho & Townes 1983; Mangum & Wootten 1993). Species with unpaired electrons, like OH or CN, are potential tracers of magnetic fields due to the Zeeman effect (Bel & Leroy 1989; Crutcher et al. 1996, 1999). Time dependent chemical models are thought as a key to derive the chemical age of an observed region, since the chemical composition is also a function of time. The understanding of the chemistry goes with the combination of observations, a detailed modeling of chemical networks and laboratory work studying specific chemical reactions.

The places where star formation occurs are dense clouds of gas and dust consisting mainly of molecular hydrogen and helium. At the high densities and low temperatures mainly simple molecules form. The chemistry in the gas-phase is dominated by exothermic reactions between ions and neutrals that do not require additional energy to overcome an activation barrier (van Dishoeck & Blake 1998). Another important reaction type is dissociative recombination reactions that take place between ions and free electrons. The rate of these reactions is mainly limited by the electron abundance in the cloud. In contrast, neutral-neutral reactions have substantial activation barriers. This decreases the rate coefficients of neutral-neutral reactions compared to ion-neutral reactions, but their importance increases with increasing temperatures (e.g., Herbst & Klemperer 1973; van der Tak 2005).

Parallel to the gas-phase reactions, chemistry also takes place on dust grains. At low temperatures atoms and molecules can accrete (adsorption) onto dust particles via physical or chemical forces to form ice mantles (e.g., Ruffle & Herbst 2001). The surfaces of the grains then can act as catalysts by receiving the excess energy. The best-studied mechanism so far is the Langmuir-Hinshelwood mechanism, that is illustrated in Figure 1.3 (described, e.g., in Herbst & van Dishoeck 2009).

Atoms or molecules can stick onto minima in the potential of the surface with a sticking efficiency S and the binding energy E_{D}. The reactants move via tunneling and thermal hopping over the irregular potential of the surface with energy barriers E_{D} and eventually can react then they meet a reaction partner. The heavier the moving atom or molecule is, the more energy it needs to move over the surface. At low densities atomic hydrogen is more abundant on grain surfaces and hydrogenation is dominating (Gibb et al. 2000). This process leads to the transformation of, e.g., atomic oxygen (O) into water (H_2O), nitrogen (N) into ammonia (NH_3) or carbon monoxide (CO) into formaldehyde (H_2CO) and methanol (CH_3OH) (van der Tak 2005). At higher densities oxygen becomes more abundant and oxygenation presumably starts to be important, leading to solid carbon dioxide (CO_2) that is observed in solid form

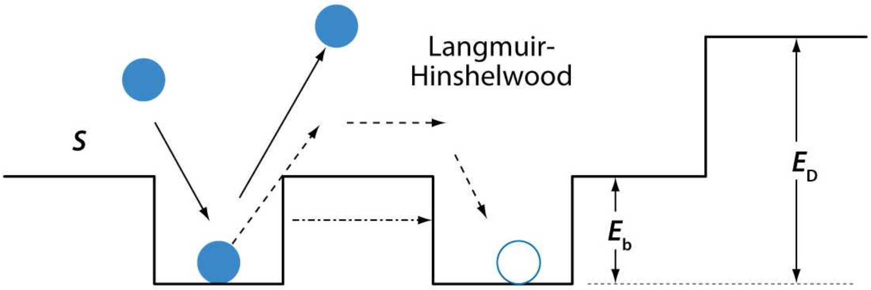

Figure 1.3 Schematic illustration of the Langmuir-Hinshelwood mechanism. S is the sticking efficiency of a gas-phase species, E_D is the binding, or desorption, energy of the adsorbate to the surface, and E_b is the barrier from one site to an adjacent one. The figure and the caption are adopted from Herbst & van Dishoeck (2009).

along lines of sight towards massive protostars (Gerakines et al. 1999). Similarly to the adsorption process, atoms and molecules can also desorb from the grain surface by thermal and non-thermal processes. This leads to the enrichment of molecules in the gas-phase that have been formed in grain-surface reactions. Many details of grain-surface chemistry, like the formation of complex organic molecules, still need to be studied and understood (Taquet et al. 2012b).

1.4 Chemistry in high-mass star-forming regions

From a chemical point of view, high-mass star formation proceeds with a wealth of chemical diversity, since it offers extreme conditions with high densities ($> 10^5$ cm^{-3}), high column densities ($> 10^{22}$ cm^{-2}), and a range of temperatures, from low temperatures on the order of $10 - 20$ K at the beginning to high temperatures of > 100 K and strong UV-emission in the later phases. While observations of interstellar molecules were already successfully used to study and clarify the evolutionary stages in low-mass star formation (van Dishoeck & Blake 1998), the chemistry of high-mass star formation is not as well understood. From the beginning of chemical studies of high-mass star formation regions, strong sources such as Orion-KL and Sgr B2 have been prime targets to observe (e.g., Johansson et al. 1984; Sutton et al. 1985; Cummins et al. 1986; Blake et al. 1987). Line surveys of these sources revealed their chemical richness and were used to analyze their chemical and physical properties on large spatial scales.

Improvements in the spectral and spatial resolution of single-dish observations and eventually interferometric observations made it possible to resolve different components in various high-mass star forming sites that show different chemical features (e.g., Beuther et al. 2009; Qin et al. 2010; Wang et al. 2012). The chemically rich HMCs, revealed huge numbers of lines of simple molecules as well as various complex organic molecules present in these environments. An example for the chemical richness of a HMC is shown in Figure 1.4. It shows a spectral scan taken with Herschel/HIFI of Orion-KL (Bergin et al. 2010), the closest high-mass star forming region. In this spec-

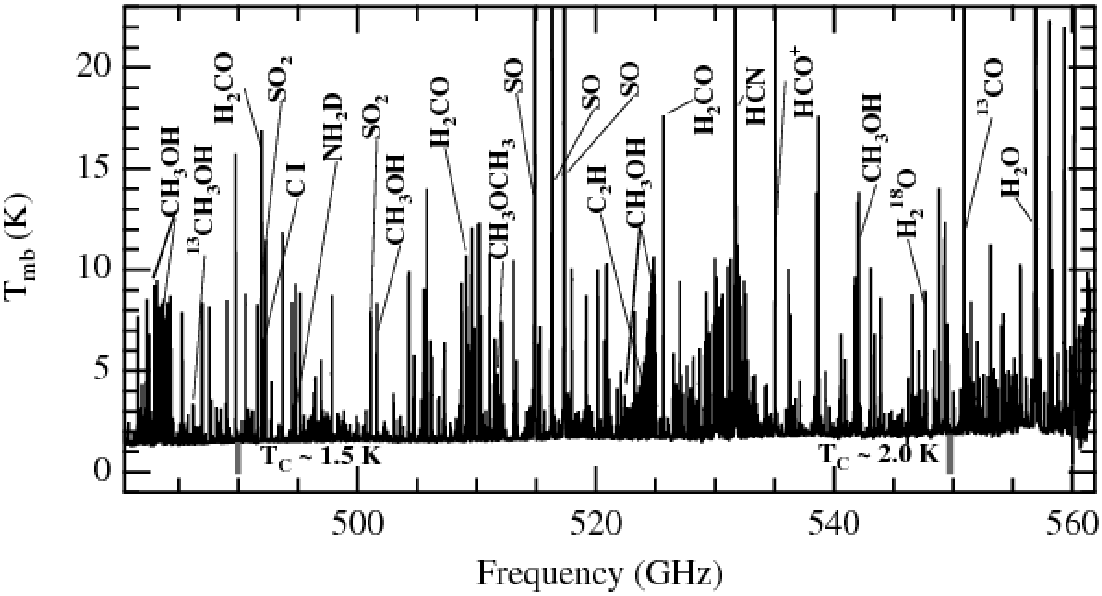

Figure 1.4 Herschel/Hifi spectral scan covering 480 − 560 GHz as an example for the complexity and chemical richness of a hot molecular core. The spectrum is taken from Bergin et al. (2010).

trum, a variety of molecular transitions are visible revealing the existence of, e.g., the complex organic molecule methyl ether (CH_3OCH_3) as well as deuterated ammonia (NH_2D) and many others. Hot core chemistry is seen in protostellar regions that are heated up to temperatures $>$ 100 K. Ice grains evaporate and release molecules that are trapped in the ices and on their surface into the gas-phase. At these temperatures, with the sublimation of the grain mantles, only gas-phase chemistry can occur and the chemical reactions can also take place more efficiently (e.g., Herbst & van Dishoeck 2009; Rolffs et al. 2011).

Improvements in the sensitivity of the detectors also allowed to observe weaker and chemically poorer sources. Observations by Vasyunina et al. (2013) revealed the presence of complex organic molecules in IRDCs. Since then, studies of a variety of high-mass star forming regions mainly concentrated on detailed line-surveys of single targets (e.g., Thompson & MacDonald 1999; Kim et al. 2006; Remijan et al. 2008) or observations of larger samples of a specific subsample (e.g., IRDCs or HMCs Hatchell et al. 1998; Fontani et al. 2005; Vasyunina et al. 2011) with small spectral setups. In the recent past, more detailed studies of a large number of sources covering different evolutionary stages aiming at the chemical characterization, e.g. the MALT90 survey (see Foster et al. 2011), have been initiated and are part of ongoing research.

1.5 Aims and structure of this thesis

[1] This thesis is aiming for a better understanding of the chemistry in the early phases of high-mass star-forming regions in an evolutionary sense. In order to study the differences in the chemical compositions of the different stages shown in Figure 1.2 in a systematic approach it is important to observe a large number of sources of various evolutionary stages and in various molecular transitions in a consistent way. This approach is combined with the comparison of the observations with the fit of a chemical model with a simple physical structure. Therefor we determine for each stage its average chemical composition. The model fits each stage individually, starting with the IRDC until the UCHII stage. The results of the best-fit model of each stage are used as initial parameters for the next stage. While the physical parameters are fixed in one stage, they are varied between the different stages in order to achieve the best-fit solutions. The model helps to constrain physical parameters, e.g., the temperature and density structure and yields typical chemical ages for the different stages. This is the first study of a larger sample of sources that cover the early phases of high-mass star formation and chemically characterizes the evolutionary sequence in a coherent way. The approach to fit the observations of each stage with a model step by step, using the results of the previous stage as initial conditions for the next stage, is a new way applied here for the first time. Such an inventory of the chemical characteristics can serve as templates for future observations and help to characterize the evolutionary state of single objects.

The thesis is separated into three chapters. In Chapter 2 we present IRAM 30m single-dish spectra of a sample of 59 sources that cover different evolutionary stages along the high-mass star formation sequence and characterize the chemical characteristics in the different stages. The observational analysis of 14 different species is then combined with a modeling approach that aims to fit the chemistry in the observed evolutionary sequence and allows us to conclude basic physical parameters and yields characteristic chemical timescales for the star-formation process.

In Chapter 3 the previous work is complemented with the analysis of additional observations of four deuterated molecules with the SMT telescope on Mount Graham, Arizona. The chapter describes the basic properties of deuterium chemistry that makes it a promising tool to study current and past temperature conditions and discusses the chemical differences observed in the deuterated molecules in an evolutionary sense. The observational results are again compared to a state-of-the-art chemical model and the implications of the findings based on the peculiar properties of deuterium chemistry are presented.

In Chapter 4 observations performed with the IRAM 30m of the low-mass star-forming region NGC 1333 are used to study the cosmic ray ionization rate, a parameter that still is a source of uncertainties in chemical models. The actively star-forming region was mapped in different molecular species and maps of the ionization fraction and cosmic ray ionization rate were determined in order to study variations of these parameters with the environment.

---

[1] The chemical model used in this thesis was provided by Dmitry Semenov who also did the fits to the data under close collaboration. All other parts were done by me.

Chapter 5 summarizes the results of my work shown in this thesis and gives an outlook for the future.

Chapter 2

Chemical evolution in the early phases of massive star formation

This Chapter has been published in A&A. (Gerner, Beuther, Semenov, Linz, Vasyunina, Bihr, Shirley and Henning, A&A 563 A97)[1]

2.1 Introduction

The chemical evolution of star-forming regions is an important topic from various perspectives. From an astrochemist's point of view, one wishes to understand the chemical properties of the gas to be able to characterize the chemical composition and evolution of the interstellar medium (ISM) in general. This starts with the chemistry associated with diffuse clouds and the formation of relatively simple molecules like H_2 or CO, and continues to the formation of complex molecules (even pre-biotic ones) in hot molecular cores or protostellar accretion disks. Complementing this approach, astrophysicists need to have a good understanding of the chemical constituents of the ISM to use different molecules as tools to probe physical conditions such as densities, temperatures, or kinematical properties. These two approaches are interdependent.

Chemical inventories of (high-mass) star-forming regions have so far largely concentrated either on complete line-surveys toward selected regions (e.g., Orion-KL or NGC6334I &I(N), Sutton et al. 1985; Schilke et al. 1997a, 2001; Walsh et al. 2010) or have targeted small spectroscopic setups toward specific subsamples (e.g., hot molecular cores, HMCs, or infrared dark clouds, IRDCs, Hatchell et al. 1998; Bisschop et al. 2007; Vasyunina et al. 2011). In addition to these line surveys, a few interferometric high-spatial resolution studies of limited samples of high-mass star-forming regions exist (e.g., Blake et al. 1996; Beuther et al. 2009).

Many studies suffer either from too limited sample sizes or spectral coverages to be able to characterize the chemistry of high-mass star-forming regions at various evolutionary stages in a statistical sense. A number of more recent studies aimed at a

---

[1] The model used in this publication and its description in Section 2.5.1 as well as Figures 2.4, 2.5, 2.6, 2.7, 2.8, 2.9, 2.10, 2.11 were provided by Dmitry Semenov. All other parts were done and written by me.

deeper understanding of a broader chemistry in the various evolutionary stages of high-mass star formation. Vasyunina et al. (2011) compared abundances in the IRDCs with the data for more evolved sources taken from the literature, and the main problem was systematic, where different spectral setups, beam sizes, and integration times were used in different samples. Fontani et al. (2005) studied a larger sample of protostellar candidates from the IRAS Point Source Catalog on the basis of their IR color and observed them in CS and $C^{17}O$ and the 1.2 mm continuum. Based on these observations and results from the literature, they were able to classify the evolutionary stages as very early and probably previous to the formation of an UCHII region. Zinchenko et al. (2009) observed five high-mass star-forming regions in a handful of simple molecular species to estimate their physical and molecular parameters. They found systematic differences in the distributions and the abundances of various molecules and discussed the importance of HCO^+, HNC and, especially, N_2H^+ as potentially valuable indicators of massive protostars. Pirogov et al. (2007) mapped twelve high-mass star-forming regions in CS, N_2H^+ and 1.2 mm dust continuum and derived the physical parameters, the density and chemical structure of the associated dense cores within. Reiter et al. (2011) also studied 27 high-mass clumps in a larger set of molecules and amongst others discussed the dependence of various physical clump properties on chemical properties. They found that molecular column densities are only weakly correlated with any of the derived physical properties of the clumps. Another still ongoing study is the MALT90 survey, which aims to chemically characterize dense molecular clumps (Foster et al. 2011; Sanhueza et al. 2012; Hoq et al. 2013; Jackson et al. 2013).

To continue the chemical characterization of high-mass star-forming regions, it is important to study all evolutionary stages in a systematic and consistent way for all sources. Furthermore, it is desirable to include more molecular species as well as be able to understand the complete chemistry along the evolutionary sequence with models.

In this work we divide the early evolution of the high-mass star-forming regions into four different stages that are observationally motivated and guided by the evolutionary sequence shown in Beuther et al. (2007a) and also in Zinnecker & Yorke (2007) who divided the different stages based on their physical conditions. In the first, earliest considered phase, quiescent infrared dark clouds (IRDCs) are formed. They consist of cold and dense gas and dust and emit mainly at (sub-)millimeter wavelengths. Their physical conditions are close to isothermal. In our sample this group consists of starless IRDCs as well as IRDCs already starting to harbor point sources at μm-wavelengths.

Previous theoretical works, for instance by Krumholz & Thompson (2007); Narayanan et al. (2008); Heitsch et al. (2008), suggested that there might be a long-lived pre-IRDC massive clump stage. This stage was also seen in the observations by Barnes et al. (2011) and supported by extragalactic works, for example, by Koda et al. (2011) who suggested a long-lived pre-MSF stage in M51. The existence of a long-lived pre-IRDC phase as a precursor is not doubted in our approach. But from a modeling point of view, in our opinion $\sim 20\,000$ years are enough to convert almost all initially atomic gas in regions with densities $\geq 10^5$ cm^{-3} into molecular-rich gas and thus reach the molecular IRDC stage. Thus, based on chemistry, we define the year zero in our evolutionary sequence when the objects reach densities of $\gtrsim 10^4$ cm^{-3} and become detectable as cold dense molecular clouds. The evolution prior to this stage is not considered in this work and took already an unknown amount of time.

In the second phase, the so-called high-mass protostellar objects (HMPOs) form, hosting an actively accreting protostar(s) with > 8 M$_\odot$, which already shows an internal emission source(s) at mid-infrared wavelengths. The central temperature rises and the temperature profile starts to deviate from the isothermal case. In this work we split the physically homogeneous HMPO phase into two subsequent phases with the HMPO being followed by the much warmer hot molecular core phase (HMC). This phase is distinguished from the earlier HMPO phase from a chemical point of view. In the HMC stage the central source(s) heats the surrounding environment, evaporating molecular-rich ices and giving rise to molecular complexity in the gas. Finally, the UV-radiation from the embedded protostar(s) ionizes the surrounding gas and an ultra-compact HII (UCHII) region is formed (fourth stage). In these objects many of the previously formed complex molecules are no longer detected because they are most likely destroyed by the ionizing radiation. Physically, many UCHII regions have probably stopped accretion at this point, but this class is not entirely homogeneous either and accretion may still continue in some UCHII regions.

Because the evolution in high-mass star formation takes place on rather short timescales and in clustered environments, the transitions from one into the next stage are smooth and not always clearly distinct. There might be overlaps among the HMPO, HMC and even UCHII region stage. Some regions are already surrounded by an ionized medium but still show the rich hot core chemistry. Due to the large beam, regions with different evolutionary stages in their proximity can also be observed as one object showing the characteristics of the different stages. In this work we wish to disentangle this from an observational point of view to be able to characterize the evolution in every considered stage statistically and also to model the evolution on a consistent timeline. On the one hand, we follow the evolution based on physical quantities, especially the temperature, which is rising from IRDCs to HMPOs to UCHII regions and on the other hand, based on the chemistry which splits the HMPOs into early, chemical poorer HMPOs, and HMCs with a molecular richer chemistry.

To set the observational results into context, an extensive multidimensional modeling and fitting of the observationally derived column densities is performed. The modeling of each individual evolutionary stage is based on the iterative fitting of the data with a set of 1D power-law physical models coupled to a pseudo-time-dependent gas-grain chemical model, calculated over 1 Myr. The cloud density and temperature structures of the environment, as well as its chemical age, are the variable parameters. The chemical characterization of the presumed evolutionary sequence in a statistical sense, together with the unique approach to fit the observed chemical evolution in high-mass star formation directly with a model, enables us to set the results into a broader context.

We describe the source sample in Section 2.2 followed by the observations in Section 2.3. The derivation of the chemical abundances and a chemical characterization of the four different subsamples based on the observational data are given in Section 2.4. In Section 2.5 we describe our model and the fitting process and interpret the observed values in combination with the fitting results in more detail and compare the results with other studies. We conclude with a summary in Section 2.6.

2.2 Source sample

The source sample contains 59 high-mass star-forming regions, consisting of 19 IRDCs and 20 HMPOs as well as 11 HMCs and 9 UCHIIs. The complete sample is listed in Table 2.1 with coordinates and distances. The telescope pointings were centered on the column density peaks derived from the dust continuum observations obtained either with Mambo (at 1.2 mm) or from the ATLASGAL and SCUBA surveys at 870 μm and 850 μm, respectively (Schuller et al. 2009; Di Francesco et al. 2008). From these maps we determined the corresponding H_2 column densities (see Section 2.4.3). The sources are mostly located within the galactic plane, with an average heliocentric distance of ~ 4 kpc.

The sources were selected from different source lists. The lists of the IRDCs were first presented in Carey et al. (2000) and Sridharan et al. (2005) and are part of the *Herschel* guaranteed time key project EPOS (Early Phase of Star Formation, Ragan et al. 2012). This sample consists of 6 IRDCs showing no internal point sources shortward of 70 μm and 13 IRDCs that have internal point sources at 24 μm and 70 μm (see source list in Table 2.1 for individual internal point source detections). The HMPOs were taken from the well-studied sample by Sridharan et al. (2002), and Beuther et al. (2002b,c). HMC sources are selected from the line-rich sample of Hatchell et al. (1998) including a few additional well-known HMCs, W3IRS5 and W3(H_2O) and Orion-KL. For the UCHIIs, we selected line-poor high-mass star-forming regions from Hatchell et al. (1998), and additional sources from Wood & Churchwell (1989b).

2.3 Observations with the IRAM 30 m

2.3.1 Data collection

The 59 sources were partly observed in the winter semester (20.1.2011-17.3.2011) and mainly in the summer semester (28.10.2011-30.10.2011, 23.11.2011) with the IRAM 30 m telescope at Pico Veleta (Spain). We performed a spectral line survey in two setups at 3 mm and 1 mm using the EMIR receiver with the FFTS backends. The system temperatures of the observations taken in the two different semesters are comparable with $T_{\mathrm{sys}} \sim 100$ K in the 3 mm band and $T_{\mathrm{sys}} \sim 250$ K in the 1 mm band. The large 16 GHz bandwidth allowed us to efficiently study the chemical properties of this relatively large sample of high-mass star-forming regions over a broad range of simultaneously observed molecular transitions. Due to changes in the instruments and thus the coverage in frequency during distinct observation runs we only analyzed the fre-

Table 2.1 Source list showing the position, the distance, and the evolutionary stage of all observed high-mass star-forming regions.

source	α (J2000.0)	δ (J2000.0)	galactic l [°]	galactic b [°]	distance[a] [kpc]	type	24 μm	70 μm	continuum data
IRDC011.1	18:10:28.4	-19:22:34	11.108	-0.115	3.6	IRDC	y	y	ATLASGAL
IRDC028.1	18:42:50.3	-04:03:20	28.343	0.060	4.8	IRDC	y	y	ATLASGAL
IRDC028.2	18:42:52.1	-03:59:54	28.397	0.080	4.8	IRDC	y	y	ATLASGAL
IRDC048.6	19:21:44.4	+13:49:24	48.657	-0.285	2.5	IRDC	n	n	ATLASGAL
IRDC079.1	20:32:22.0	+40:20:10	79.338	0.341	1.0	IRDC	-	y	SCUBA
IRDC079.3	20:31:57.7	+40:18:26	79.269	0.386	1.0	IRDC	-	y	SCUBA
IRDC18151	18:17:50.3	-12:07:54	18.319	1.792	3.0	IRDC	-	y	Mambo
IRDC18182	18:21:15.0	-14:33:03	16.578	-0.081	3.6	IRDC	y	y	Mambo
IRDC18223	18:25:08.3	-12:45:27	18.605	-0.075	3.7	IRDC	y	y	Mambo
IRDC18306	18:33:32.1	-08:32:28	23.297	0.0550	3.8	IRDC	n	n	Mambo
IRDC18308	18:33:34.3	-08:38:42	23.209	-0.001	4.9	IRDC	y	y	Mambo
IRDC18310	18:33:39.5	-08:21:10	23.478	0.115	5.2	IRDC	n	n	Mambo
IRDC18337	18:36:18.2	-07:41:00	24.374	-0.158	4.0	IRDC	y	y	Mambo
IRDC18385	18:41:17.4	-05:09:56	27.179	-0.104	3.3	IRDC	y	y[b]	Mambo
IRDC18437	18:46:21.8	-02:12:21	30.390	0.123	(6.2) 7.3[c]	IRDC	y	y	Mambo
IRDC18454.1	18:48:02.1	-01:53:56	30.854	-0.109	(3.5) 6.4[d]	IRDC	n	n	Mambo
IRDC18454.3	18:47:55.8	-01:53:34	30.848	-0.083	6.0 (6.4)[e]	IRDC	n	n	Mambo
IRDC19175	19:19:50.7	+14:01:23	48.617	0.214	1.1	IRDC	n	n	Mambo
IRDC20081	20:10:13.0	+27:28:18	66.145	-3.197	0.7	IRDC	-	n[f]	Mambo
HMPO18089	18:11:51.6	-17:31:29	12.889	0.489	3.6	HMPO			Mambo
HMPO18102	18:13:11.3	-18:00:03	12.623	-0.017	2.7	HMPO			Mambo
HMPO18151	18:17:58.1	-12:07:26	18.341	1.768	3.0	HMPO			Mambo
HMPO18182	18:21:09.2	-14:31:50	16.585	-0.051	4.5 (11.8)[g]	HMPO			Mambo
HMPO18247	18:27:31.7	-11:45:56	19.755	-0.129	6.7	HMPO			Mambo
HMPO18264	18:29:14.6	-11:50:22	19.884	-0.535	3.5 (12.5)[g]	HMPO			Mambo
HMPO18310	18:33:48.1	-08:23:50	23.455	0.063	5.2 (10.4)[g]	HMPO			Mambo
HMPO18488	18:51:25.6	+00:04:07	32.991	0.034	5.4 (8.9)[g]	HMPO			Mambo
HMPO18517	18:54:14.4	+04:41:40	37.430	1.517	2.9	HMPO			Mambo
HMPO18566	18:59:10.1	+04:12:14	37.554	0.200	6.7	HMPO			Mambo
HMPO19217	19:23:58.8	+16:57:44	51.679	0.720	10.5	HMPO			Mambo
HMPO19410	19:43:11.0	+23:44:10	59.784	0.066	2.1	HMPO			Mambo
HMPO20126	20:14:26.0	+41:13:32	78.122	3.633	1.7	HMPO			Mambo
HMPO20216	20:23:23.8	+41:17:40	79.127	2.279	1.7	HMPO			Mambo
HMPO20293	20:31:12.9	+40:03:20	78.982	0.352	1.3 (2.0)[g]	HMPO			Mambo
HMPO22134	22:15:09.1	+58:49:09	103.876	1.856	2.6	HMPO			Mambo
HMPO23033	23:05:25.7	+60:08:08	110.093	-0.067	3.5	HMPO			Mambo
HMPO23139	23:16:10.5	+59:55:28	111.256	-0.770	4.8	HMPO			Mambo
HMPO23151	23:17:21.0	+59:28:49	111.236	-1.238	5.7	HMPO			Mambo
HMPO23545	23:57:06.1	+65:24:48	117.315	3.136	0.8	HMPO			Mambo
HMC009.62	18:06:15.2	-20:31:37	9.621	0.193	5.7	HMC			ATLASGAL
HMC010.47	18:08:38.2	-19:51:50	10.472	0.027	5.8	HMC			ATLASGAL
HMC029.96	18:46:04.0	-02:39:21	29.956	-0.017	7.4	HMC			ATLASGAL
HMC031.41	18:47:34.2	-01:12:45	31.412	0.308	7.9	HMC			ATLASGAL
HMC034.26	18:53:18.5	+01:14:58	34.257	0.154	4.0	HMC			ATLASGAL
HMC045.47	19:14:25.7	+11:09:26	45.466	0.045	6.0	HMC			ATLASGAL
HMC075.78	20:21:44.1	+37:26:40	75.783	0.343	4.1	HMC			SCUBA
NGC7538B	23:13:45.4	+61:28:11	111.542	0.777	2.65 (5.61)[h]	HMC			SCUBA
Orion-KL	05:35:14.4	-05:22:31	208.993	-19.385	0.44	HMC			SCUBA
W3IRS5	02:25:40.7	+62:05:52	133.715	1.215	1.8	HMC			SCUBA
W3H_2O	02:27:04.6	+61:52:25	133.949	1.065	2.0	HMC			SCUBA
UCH005.89	18:00:30.4	-24:04:00	5.886	-0.392	2.5	UCHII			ATLASGAL
UCH010.10	18:05:13.1	-19:50:35	10.099	0.739	4.4	UCHII			ATLASGAL
UCH010.30	18:08:55.8	-20:05:55	10.300	-0.147	6.0	UCHII			ATLASGAL
UCH012.21	18:12:39.7	-18:24:20	12.208	-0.102	13.5	UCHII			ATLASGAL
UCH013.87	18:14:35.8	-16:45:43	13.872	0.280	4.4	UCHII			ATLASGAL
UCH030.54	18:46:59.3	-02:07:24	30.535	0.021	6.1	UCHII			ATLASGAL
UCH035.20	19:01:46.4	+01:13:25	35.200	-1.741	3.2	UCHII			SCUBA
UCH045.12	19:13:27.8	+10:53:37	45.122	0.132	6.9	UCHII			ATLASGAL
UCH045.45	19:14:21.3	+11:09:14	45.454	0.060	6.0	UCHII			ATLASGAL

Notes. For the IRDCs we indicate whether or not they show embedded 24 or 70μ m point sources with y(es) or n(o) (or "-" if there are no data available). In the last column the sources of the dust continuum data are presented.

[a] unbracketed values are preferred, bracketed values are alternative values

[b] very weak emission compared with the background located at the same position as 24μm emission source

[c] for $v_{\rm lsr} = (97.6)111.3\ \mathrm{km\,s^{-1}}$

[d] for $v_{\rm lsr} = (52.8)100.2\ \mathrm{km\,s^{-1}}$

[e] for $v_{\rm lsr} = 94.3(98.4)\ \mathrm{km\,s^{-1}}$

[f] no embedded central point source found, a nearby extended source with emission inside the beam is detected

[g] for the near (far) kinematic solution

[h] parallactic (kinematic) distance

quency ranges at which all sources were observed, namely 86-94 GHz, 217-221 GHz, and 241-245 GHz.

The frequency ranges were chosen to cover transitions of important molecules containing nitrogen, oxygen, sulfur, carbon, and silicon. The observations were carried out in wobbler-switching mode with 1.25 min on-source integration time with a spectral resolution of $\sim 0.3\,\mathrm{km\,s^{-1}}$ at 1 mm and $\sim 0.6\,\mathrm{km\,s^{-1}}$ at 3 mm. The beam sizes of the IRAM 30 m telescope are $11''$ at 1 mm and $29''$ at 3 mm. Typical 1- sigma rms values are on the order of ~ 0.1 K at 1 mm and ~ 0.03 K at 3 mm, respectively. To reduce all spectroscopic data, the standard GILDAS[2] software package CLASS was used.

2.3.2 Data analysis strategies

For the analysis we focused on a specific sample of 15 different molecular species for which we calculated the column densities (see Table 2.2 for a list of the molecules). To directly compare the derived values with the modeled values (see Section 2.5.1) we relied on the most common molecules among the different sources at a distinct evolutionary stage (e.g., N_2H^+, HCN, C_2H, HNC, HCO^+). These molecules we complemented with more complex molecules that are typical of more evolved stages of high-mass star-forming regions, for instance, the HMC phase (e.g., CH_3CN, OCS). The homogeneous list of molecules from various chemical "families" made our search for the best-fit model parameters (T, n_H, age) more reliable. The spectra of these molecules were fitted with a Gaussian profile and the corresponding column densities were obtained (see below). For that we excluded all lines that deviate extremely from Gaussian profiles, because this makes the derivation of column densities, based on the assumptions described in Section 2.4.3, unreliable. The reasons for such complex line shapes might be optical depth effects, self-absorption, flux accidentally measured at an $240''$ off-position due to the limited distance in the wobbler-switching mode, or peculiar gas kinematics. Furthermore, the spectra of very abundant molecules might be affected by foreground and background emission. Infall or outflow motions also lead to a departure of a line profile from Gaussian shape toward double-peaked profiles.

In the source W3(H_2O) a masering methanol line caused a high intensity in one channel around the line peak of that line. Other problems in fitting the line profiles were broad line-wings that we were unable to fit with a single Gaussian, but only with a combination of a narrow main component and a broader underlying component. In these cases we fitted the narrow component, which most likely traces the bulk component of the molecular gas. Some of the lines with slightly asymmetric shapes still allowed Gaussian fitting, which we also included in the analysis, with the caution that the derived values are probably underestimated.

The hyperfine line of HCN (1-0) shows anomalies in the line ratios compared with the predicted theoretical values in a substantial number of sources, which was found by other groups as well (see Cernicharo et al. 1984; Loughnane et al. 2012). In the optical thin LTE case the relative intensities of the three HCN(1-0) hyperfine components are F(0-1):F(2-1):F(1-1) = 1:5:3 (e.g., Wannier et al. 1974). In our spectra we see various

---

[2] http://www.iram.fr/IRAMFR/GILDAS

deviations from these ratios with either F(0-1)/F(1-1) $\geqq 1$, which cannot be solely explained by the optical thickness of the line. The probable reason for this behavior is scattering of radiation from the core in a moderate-density envelope (Cernicharo et al. 1984). This is possibly enhanced by an inherently complex spatial distribution of HCN through the cloud or clumpiness of the cloud itself, which causes tricky absorption and re-emission of the radiation. In such a case we refrained from using this line in the data analysis. In summary, the main problems in the analysis of the spectral lines were optical depth effects, a poor off-position, foreground and background emission, a complex velocity structure of the source, and anomalies in the HCN hyperfine structure.

The assumptions used to derive molecular abundances and column densities are presented in Section 2.4.3, and we discuss the uncertainties in Section 2.4.4.

2.4 Results

2.4.1 Chemical characteristics of the four evolutionary stages of high-mass star-forming regions

In Figure 2.1 we show sample spectra for each of the four evolutionary stages. We now describe the general characteristics of each stage on the basis of these four examples. In the object IRDC048.6 we only detected simple and common molecules such as isotopologues of CO or HCO^+ and tracers of cold and dense matter such as N_2H^+.

The spectra of HMPO18151 already shows a higher number of detected molecules and higher intensities of the observed lines. In this phase the temperature starts to increase, which allows radicals to become mobile on the dust grain surfaces, synthesizing complex (organic) ices and simpler species that may be able to evaporate to the gas phase. This also leads to an overall increase in the intensities of the detected lines (e.g., C_2H, H_2CO, HCN, HCO^+ and isotopologues), such that more species appear on the spectrum. We detected an organic species, methanol (CH_3OH), SiO – a molecule that is a tracer of outflows and shocks, and we began to see sulfur-bearing molecules (e.g., CS, SO, H_2CS and isotopologues).

In the HMC stage the spectrum shows the largest number of lines, including transitions of long and complex molecules such as methyl formate CH_3OCHO. Some of the HMC spectra already show recombination lines (e.g. HMC029.96), which is typically only visible in the spectra of UCHII regions. In this case they are generated by a nearby UCHII region (see Beuther et al. 2007b) that is also covered by the single-dish beam.

During this late evolutionary phase many complex, photofragile molecules might be destroyed by the intense ionizing radiation of the central star(s). This enhances the amount of ionized medium and thus reduces the amount of the neutral medium compared with HMCs, leading to lower line fluxes and column densities. Correspondingly, the UCHII spectrum shows fewer molecular lines. Apart from additional recombination lines of hydrogen, the UCHII spectra looks qualitatively very similar to the

HMPO spectrum.

We selected 15 different molecular species that trace the physical conditions and chemical evolution to analyze and compare them with a chemical model. A list of all the selected lines is given in Table 2.2. To exclude optically thick lines we used the rarer isotopologues, when available. Specifically, we did not analyze ^{13}CO, HNC, HCO$^+$, or CS. The assumed isotopic ratios are given in Section 2.4.3. The detected lines in each source were fitted with a Gaussian profile to obtain the total line intensities. For sources in which we did not detect a specific transition we used the 3- sigma rms value to estimate an upper limit of the corresponding column density.

2.4.2 Calculation of the H_2 column densities

To derive abundances we first calculated the H_2 column densities for all observed regions. Many of our sources are covered by the galactic plane survey ATLASGAL (Schuller et al. 2009), which observed dust emission at 870μm. Most of the HMPOs were observed at 1.2 mm with the bolometer MAMBO at the IRAM 30m. The data for the remaining sources were taken from the SCUBA Legacy Catalog published by Di Francesco et al. (2008) which are bolometer maps observed at 850μm with the JCMT. In Table 2.1 we list which continuum data were taken for each of the sources.

The coordinates for the spectral observations were centered on the highest intensity peak in the bolometer map. With the observed value of the peak intensity we derived H_2 column densities following Equation 2.1 taken from Schuller et al. (2009). The typical temperatures for the observed sources were assumed. Average IRDC temperatures are around 15 K based on several NH_3 IRDC surveys (e.g., Sridharan et al. 2005; Pillai et al. 2006; Chira et al. 2013). Typical HMPO temperatures were estimated from SED fits and are $\sim$ 50 K. HMCs are usually warmer and we chose $T = 100$ K as the average temperature. The same temperature of $T = 100$ K is assumed for the UCHII stage. Finally, the dust opacities were interpolated from Ossenkopf & Henning (1994), assuming grains with thin ice mantles, gas densities of $n = 10^5$ cm^{-3}, and a gas-to-dust mass ratio $R = 100$. The actually used dust opacities are $\kappa_{850\mu\mathrm{m}} = 1.48$, $\kappa_{870\mu\mathrm{m}} = 1.42$, $\kappa_{1.2\mathrm{mm}} = 0.97$. Using these assumptions and assuming that the emission is optically thin and at LTE, the H_2 column density is calculated as

$$N_{H_2} = \frac{F_\nu \cdot R}{B_\nu \cdot \Omega \cdot \kappa_\nu \cdot \mu \cdot m_H}. \tag{2.1}$$

In this calculations we also assumed that the dust and the gas are collisionally coupled and thus have the same temperature. The observations with the IRAM 30m at 1 mm have a HPBW of 11″ and at 3 mm a HPBW of 29″. The data obtained with MAMBO have a resolution of 11″, the ATLASGAL maps 19.2″ and the SCUBA data 22.9″. For the molecules observed at 3 mm we smoothed the maps with a Gaussian kernel to obtain the same resolution and derived the corresponding H_2 column density. For the molecules observed at 1 mm we used the original dust continuum maps to calculate the H_2 column density. Thus we have two different H_2 column densities measured for each source on two different spatial scales. While the H_2 column densi-

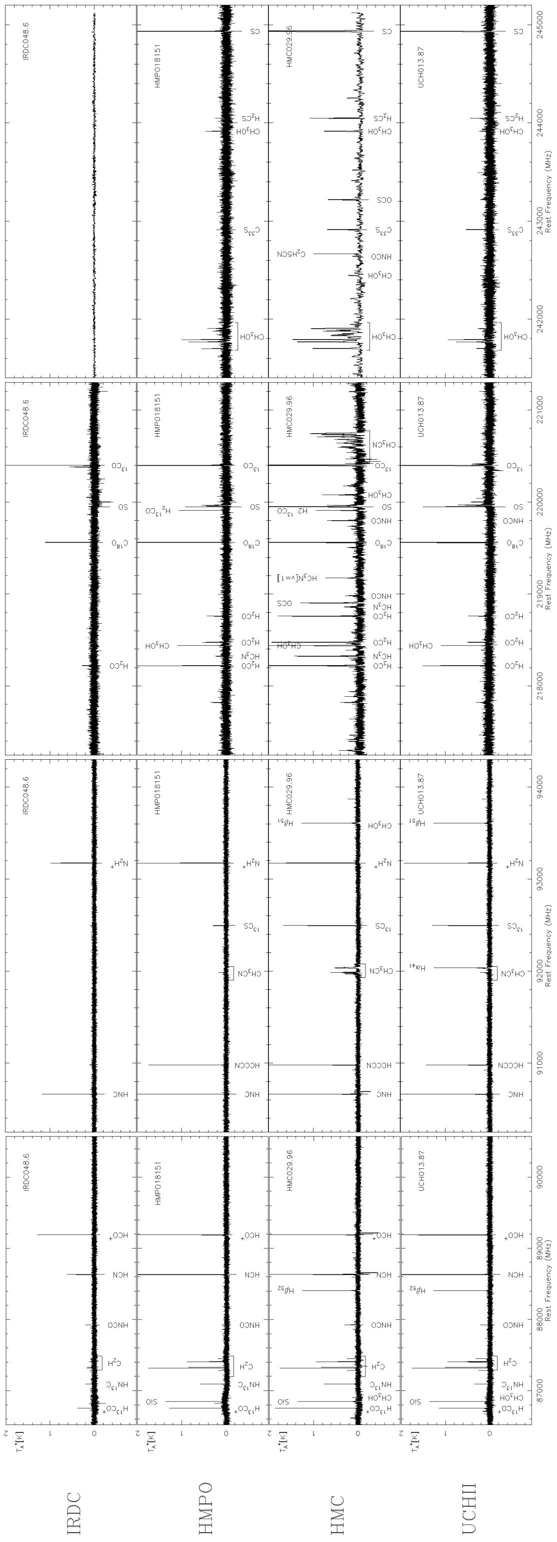

Figure 2.1 From left to right, we show sample 16 GHz spectra of the sources IRDC048.6, HMPO18151, HMC029.96, and UCH013.87, representing the four selected evolutionary stages of high-mass star formation. The frequency resolution is ~ 0.2 MHz and typical rms values are ~ 0.1 K at 1 mm and ~ 0.03 K at 3mm.

ties for the molecules at 3 mm are beam matching, this is not the case for all sources for the molecules at 1 mm. We slightly underpredict the H_2 column densities in the cases of the 1 mm molecular line data, where we only have ATLASGAL or SCUBA data because of the larger beam. To facilitate the modeling, we calculated for each angular resolution the corresponding physical radius, using estimates of the distances to the sources. Thus, we avoided effects from the heterogeneous nature in angular resolution of the continuum and spectroscopic data. For sources with a distance ambiguity we used the lowest value. Three of the sources show different velocity components in some transitions, resulting in different estimates of the kinematic distances. In these cases we chose the kinematic distance corresponding to the main velocity component that was detected in all transitions.

Another uncertainty in the comparison of the continuum data and the molecular line data comes from the different techniques of measuring. The continuum data are observed with bolometer arrays and suffer for some degree from spatial filtering of the large-scale structures (see Motte & André 2001; Schuller et al. 2009). In contrast, the spectroscopic data are observed with heterodyne receivers and have no filtering problems. This is a general uncertainty in all comparisons between bolometer- and heterodyne-receiver-based measurements and leads to an underestimation of the true flux of the bolometer-based measurements. Hence, in our case the derived abundances are slightly overestimated. This effect is hard to quantify, but is not expected to play an important role in our case. It is reasonable to assume that the large-scale structure, which is filtered out, consists of diffuse gas with low density. A possible way to quantify this effect of missing large-scale structures in a first approximation is to take the canonical CO abundance of 10^{-4} and compare it with our derived values, which are about a factor 2-4 lower. Thus, the estimated H_2 column densities are even higher than the canonical values and the spatial filtering seems to have only a minor impact.

2.4.3 Calculation of the molecular column densities

To calculate column densities for the different molecules in Table 2.2 we made several simplifying assumptions. The uncertainties introduced by these assumptions are discussed in Section 2.4.4.

1) Local thermodynamic equilibrium (LTE), since the densities in the observed high-mass star-forming regions are on the order of $10^5\,\mathrm{cm}^{-3}$ and higher, which exceeds the critical densities for many of the observed transitions. 2) A uniform gas kinetic temperature for all molecules observed in the same evolutionary stage. In the first iteration of the comparison with the model we assumed $T = 15$ K for IRDCs, $T = 50$ K for HMPOs, $T = 100$ K for HMCs and $T = 100$ K for UCHIIs, respectively (iteration 0). In a second step we changed the assumed temperatures based on the outcome of the model (iteration 1). Due to the large beam sizes used to observe the high-mass star-forming regions, we took lower average temperature values for the later stages than the values observed with high-density tracers such as methyl cyanide. 3) The dust and gas temperatures are equal. 4) Line emission was assumed to be optically thin. For the species for which a rarer isotopologue line is also detected,

Table 2.2 List of analyzed molecules with transitions, frequencies, energies of the upper level, critical densities, and effective densities calculated for 10 K and 100 K.

Molecule	Transition	Frequency [GHz]	E_u/k [K]	n_{crit} for $T = 10$ K [10^5cm^{-3}]	n_{crit} for $T = 100$ K [10^5cm^{-3}]	n_{eff} for $T = 10$ K [10^3cm^{-3}]	n_{eff} for $T = 100$ K [10^3cm^{-3}]
$H^{13}CO^+$	1-0	86.7543	4.2	1.5	2.1	3	0.9
SiO	2-1	86.8470	6.3	2.7	3.0	20	4
$HN^{13}C$	1-0	87.0909	4.2		10^b	-	-
C_2H	$1_{3/2,2}$-$0_{1/2,1}$	87.3169	4.2		1^c	-	-
HNCO	4(0,4)-3(0,3)	87.9252	10.6	9.8^d	5.3^e	30	3
HCN	1-0	88.6316	4.3	10.1	26.6	29	5.1
CH_3OCHO	7(2,5)-6(2,4) E	90.1456	19.7		-	-	-
CH_3CN	5-4 (K=2)	91.9800	41.8	4.2^d	2.7	-	20
^{13}CS	2-1	92.4943	6.7	3.3^f	3.8^f	-	-
N_2H^+	1-0	93.1737	4.5	1.4	2.0	4	2
H_2CO(para)^g	3(0,3)-2(0,2)	218.2221	21.0	23.5	50.3	100	15
CH_3OH^h	4(2,2)-3(1,2)	218.4401	45.5	133.9	781.1	-	-
H_2CO(para)^i	3(2,2)-2(2,1)	218.4756	68.1	30.2	56.1	-	50
OCS^j	18-17	218.9034	99.8	4.2	4.0	-	-
$C^{18}O$	2-1	219.5604	15.8	0.08	0.10	-	-
SO	6-5	219.9488	35.0	22.6^k	37.4	-	50
$C^{33}S$	5-4	242.9136	35.0	51.4^f	54.0^f	-	-
OCS^l	20-19	243.2180	122.6	5.9	5.6	-	-
CH_3OH^m	5(1,4)-4(1,3)	243.9158	49.7	8.0	15.5	-	-

Notes. Values are taken from the LAMDA database (Schöier et al. 2005), unless otherwise noted. Other species, visible in Figure 2.1, were not analyzed due to presumed high optical depth, as explained in the text. The effective densities were calculated with RADEX (van der Tak et al. 2007) assuming $\log \frac{N}{\Delta v} = 13.5\mathrm{cm}^{-2}(\mathrm{kms}^{-1})^{-1}$ (Evans 1999). For some molecules only the value for $T = 100$ K is given, because at $T = 10$ K the transition is too weak.

[b] Sakai et al. (2012), [c] Sakai et al. (2010), [d] for $T = 20$ K, [e] for $T = 80$ K, [f] value for the main isotopologue $C^{34}S$, [g] hereafter referred to as H_2CO-K0, [h] hereafter referred to as CH_3OH-4, [i] hereafter referred to as H_2CO-K2, [j] hereafter referred to as OCS-18, [k] for $T = 60$ K, [l] hereafter referred to as OCS-20, [m] hereafter referred to as CH_3OH-5

we used this line to derive the column density (in particular, $HN^{13}C$, $H^{13}CO^+$, ^{13}CS, $C^{33}S$, and $C^{18}O$). For N_2H^+ and HCN we fitted the hyperfine line structure and constrained the optical depth. 5) Derived column densities were beam averaged. 6) The medium is spatially homogeneous. 7) The Rayleigh-Jeans approximation of the Planck function was used. 8) No isotopic fractionation. Because we only provide single-dish measurements with limited spatial resolution at single pointings, only mean values smoothed over the beam were derived.

We calculated the molecular column densities following the equations in Tielens (2005):

$$N_u = \frac{1.94 \cdot 10^3}{A_{ul}} \cdot \nu_{ul}^2 \cdot \int T_{mb} \delta v, \tag{2.2}$$

where the line frequency ν_{ul} is in GHz, the integrated intensity is in K km s^{-1}, and the Einstein coefficient A_{ul} is in s^{-1}. Then the total column density can be calculated,

$$N_{tot} = N_u \cdot \frac{Q}{g_u exp[-E_u/kT_{ex}]}, \tag{2.3}$$

where Q is the partition function, g_u the statistical weight of the upper level, E_u the upper state energy, and k the Boltzmann constant. T_{ex} is the excitation temperature and assumed to be equal to T_{kin}. Finally, we converted the derived column densities for the rarer isotopologues given in Table 2.2 into the column densities of their main isotopologues. We hereby assumed for all sources the same relative isotopic ratios representative of the Sun and local ISM: $^{12}C/^{13}C$=89, $^{16}O/^{18}O$=499, and $^{32}S/^{33}S$=127 (Lodders 2003).

The molecular column densities were then divided by the H_2 column densities and the abundances were derived. The derived abundances for the molecules with transitions at 1 mm are upper limits because of the differences in resolution between ATLASGAL/SCUBA and the 1 mm molecular data. This does not affect the modeling, because we directly converted the beam sizes into physical sizes. The resulting median abundances including all detections and upper limits for each subsequent evolutionary phase are given in Tables 2.3 – 2.6. In addition to the molecules listed in Table 2.2, in some regions we detected also HC_3N, H_2CS, CH_3CHO, and other species. However, analyzing these is not a main focus of the current paper. The more detailed investigation of these species will be presented in future publications.

2.4.4 Uncertainties in the observed values

Our estimates of the column densities are based on simplifying basic assumptions, such as optically thin line limit, uniform excitation temperature for all observed molecules, and all sources being at a particular evolutionary stage, uncertainties in the derived H_2 column densities, which all need to be taken into account in the data analysis and further modeling.

We assumed a fixed dust opacity for all sources. In addition, we assumed a single excitation temperature for all sources and molecules in one evolutionary sample that is equal to the assumed kinetic temperature in this evolutionary stage. In this way, we did not account for source peculiarities or a possible misclassification of the stage or an overlap of several stages in a single source. Furthermore, the kinetic temperature of single molecules might deviate from the real excitation temperature in case of subthermally excited lines. This might especially be the case for the HMCs and UCHs, which have the highest kinetic temperatures. Comparing the calculated abundances derived with the high excitation temperature $T_{\rm ex}$ = 100 K with those derived with the lower excitation temperature of $T_{\rm ex}$ = 50 K, we found that the abundances decrease by factors of $3 - 10$ in the case with the low $T_{\rm ex}$. HNCO, CH_3CN, CH_3OH, and CH_3OCHO are the most affected molecules.

We made the same exercise for the IRDCs and compared the abundances calculated with $T_{\rm ex}$ = 15 K with those calculated with 10 K. The difference in the abundances reaches at most a factor of 3, with the exception of OCS, which shows a large difference of a factor of 15. We attributed this deviation to a non-LTE effect because a high J rotational line of OCS was employed, which might be subthermally excited even at typical densities of the high-mass star-forming regions. A more detailed discussion of the effect of uncertainties on the excitation temperature is given in Section 2.5.3. Furthermore, assuming optically thin lines implies that the calculated column densities may also be just lower limits.

Moreover, uncertainties in the conversion of the dust into gas densities constitute a factor of about 1.5 compared with Draine (2011). The isotopic ratios vary between different environments and the uncertainties in the adopted isotopic ratios are a factor of $2-4$ (e.g., Wilson & Rood 1994). Glassgold et al. (1985) found that the $^{12}C/^{13}C$ ratio in PDRs might deviate even by more than a factor of 10 from the solar value. More recently, Röllig & Ossenkopf (2013) suggested strong fractionation effects in C-chemistry.

In combination, these systematic errors result in an overall uncertainty of about one order of magnitude in the derived molecular abundances. This level of uncertainty is typical for astrochemical studies. It is present in the assumptions made to analyze observational data as well as in the intrinsic uncertainties of chemical models (e.g., Wakelam et al. 2010; Vasyunina et al. 2011, 2012; Albertsson et al. 2013). Improvements of this situation are an area of active study.

In this work, these uncertainties were taken into account during the data fitting, as explained in Section 2.5.1. To avoid suffering strongly from possible misclassifications and peculiarities of single sources, we treated the sample in a statistical way and were mainly interested in the median characteristics of a subsample. That might lead to larger spreads within one subsample, but makes the analysis and comparison with the model more robust and reliable.

2.4.5 Chemical evolution

In Sections 2.4.2 and 2.4.3 we calculated the column densities of H_2 and other molecular species. From these values we derived averaged abundances for each source. In the next step we combined all these abundances from all sources at a specific evolutionary stage and derived a characteristic chemical "portrait" for each phase. The results are given in Tables 2.3 – 2.6 together with the detection fractions. The detection fractions are plotted in Figure 2.2 and the abundances are plotted in Figure 2.3 for the IRDCs, HMPOs, HMCs and UCHII regions. The individual column densities for each stage are presented in the appendix of this chapter in Figures 2.8 – 2.11.

All abundances in all four evolutionary stages have values ranging between 10^{-11} and 10^{-6}. The spread of column densities within a particular stage is about one order of magnitude or lower, except for H_2CO in the IRDCs and N_2H^+ in the HMCs with spreads of almost three orders of magnitude. Within the two subsamples of IRDCs (with and without associated point sources at wavelengths below 70 μm) the difference in median abundances does not exceed a factor of 2. But in terms of detected molecules we found a stronger difference. The molecules ^{13}CS, CH_3CN, and OCS are only detected in the more evolved IRDCs. The detection fractions of SiO, SO, and

Table 2.3 Observed median abundances and standard deviation in $a(x) = a \cdot 10^x$ for the IRDCs for $T = 15$ K and $T = 20.9$ K. x(e) is the ionization fraction.

Molecule	Abundance $T = 15$ K	Standard deviation	Abundance $T = 20.9$ K^a	Standard deviation	det	lim	none
HCN	1.6(-09)	1.1(-09)	3.2(-09)	2.1(-09)	7	0	12
HNCO	8.3(-11)	7.3(-11)	1.8(-10)	1.5(-10)	17	2	0
$HN^{13}C$	5.8(-11)	4.3(-11)	1.2(-10)	8.6(-11)	19	0	0
C_2H	1.2(-08)	6.3(-09)	2.3(-08)	1.2(-08)	19	0	0
SiO	8.4(-11)	1.3(-10)	1.6(-10)	2.5(-10)	12	7	0
$H^{13}CO^+$	4.5(-11)	2.6(-11)	9.1(-11)	5.2(-11)	19	0	0
N_2H^+	6.0(-10)	3.3(-10)	9.6(-10)	5.4(-10)	19	0	0
^{13}CS	≤6.1(-11)	4.5(-11)	≤1.3(-10)	8.7(-11)	8	11	0
SO	≤1.9(-10)	1.8(-10)	≤2.4(-10)	2.3(-10)	8	11	0
$C^{18}O$	5.6(-08)	2.1(-08)	9.0(-08)	3.4(-08)	19	0	0
H_2CO	6.6(-10)	1.4(-09)	5.3(-10)	9.9(-10)	24	13	1
$C^{33}S$	≤1.0(-10)	1.4(-10)	≤1.1(-10)	1.7(-10)	0	19	0
OCS	≤3.7(-08)	7.3(-08)	≤1.1(-08)	1.6(-08)	2	36	0
CH_3OH	≤9.9(-10)	1.3(-09)	≤1.2(-09)	≤1.7(-09)	16	22	0
CH_3OCHO	≤2.1(-10)	5.3(-10)	≤3.9(-10)	3.1(-10)	0	19	0
CH_3CN	≤1.5(-10)	9.9(-11)	≤1.8(-10)	1.1(-10)	2	17	0
x(e)	4.6(-09)	2.6(-09)	9.0(-09)	5.0(-09)	19	0	0

Notes. The last three columns show the number of sources with a detection (det), non-detection (lim), and detection but no derived column density (none) due to reasons described in Section 2.3.2.

[a] mean value of T for the best-fit model

Table 2.4 Observed median abundances and standard deviation in $a(x) = a \cdot 10^x$ for the HMPOs for $T = 50$ K and $T = 29.5$ K. x(e) is the ionization fraction.

Molecule	Abundance $T = 50$ K	Standard deviation	Abundance $T = 29.5$ K^a	Standard deviation	det	lim	none
HCN	1.1(-08)	7.1(-09)	3.8(-09)	2.4(-09)	14	0	6
HNCO	1.8(-10)	3.4(-10)	7.7(-11)	1.5(-10)	17	3	0
$HN^{13}C$	3.7(-10)	1.9(-10)	1.3(-10)	6.6(-11)	18	2	0
C_2H	1.4(-07)	3.8(-08)	5.0(-08)	1.4(-08)	20	0	0
SiO	4.0(-10)	4.0(-10)	1.4(-10)	1.4(-10)	16	4	0
$H^{13}CO^+$	4.5(-10)	1.4(-10)	1.5(-10)	4.8(-11)	20	0	0
N_2H^+	2.4(-09)	1.4(-09)	1.1(-09)	5.7(-10)	20	0	0
^{13}CS	9.0(-10)	7.5(-10)	3.2(-10)	2.6(-10)	17	3	0
SO	1.3(-09)	9.4(-10)	6.4(-10)	4.6(-10)	20	0	0
$C^{18}O$	2.7(-07)	1.2(-07)	1.1(-07)	4.9(-08)	20	0	0
H_2CO	7.1(-10)	5.6(-10)	4.7(-10)	6.0(-10)	38	1	1
$C^{33}S$	≤1.3(-10)	1.2(-10)	≤6.8(-11)	6.5(-11)	8	12	0
OCS	≤1.3(-09)	1.6(-09)	≤2.0(-09)	2.7(-09)	17	23	0
CH_3OH	9.1(-10)	1.6(-09)	1.0(-09)	1.5(-09)	32	8	0
CH_3OCHO	≤2.5(-10)	2.7(-10)	≤2.1(-10)	2.3(-10)	0	20	0
CH_3CN	1.3(-10)	1.6(-10)	1.0(-10)	1.2(-10)	13	7	0
x(e)	4.3(-08)	1.3(-08)	1.5(-08)	4.6(-09)	20	0	0

Notes. The last three columns show the number of sources with a detection (det), non-detection (lim), and detection but no derived column density (none) due to reasons described in Section 2.3.2.

[a] mean value of T for the best-fit model

Table 2.5 Observed median abundances and standard deviation in $a(x) = a \cdot 10^x$ for the HMCs for $T = 100$ K and $T = 40.2$ K. x(e) is the ionization fraction.

Molecule	Abundance $T = 100$ K	Standard deviation	Abundance $T = 40.2$ K[a]	Standard deviation	det	lim	none
HCN	4.9(-08)	0	7.4(-09)	0	1	0	10
HNCO	1.6(-09)	1.3(-09)	1.5(-10)	1.3(-10)	10	1	0
$HN^{13}C$	4.9(-10)	4.9(-10)	7.5(-11)	7.4(-11)	11	0	0
C_2H	3.1(-07)	1.6(-07)	4.6(-08)	2.4(-08)	11	0	0
SiO	1.3(-09)	2.5(-09)	2.1(-10)	3.9(-10)	11	0	0
$H^{13}CO^+$	8.2(-10)	6.7(-10)	1.3(-10)	1.0(-10)	11	0	0
N_2H^+	7.8(-10)	2.5(-09)	2.7(-10)	4.9(-10)	11	0	0
^{13}CS	5.6(-09)	3.0(-09)	8.8(-10)	4.7(-10)	11	0	0
SO	1.3(-08)	2.4(-08)	2.8(-09)	5.0(-09)	11	0	0
$C^{18}O$	1.7(-06)	6.1(-07)	3.0(-07)	1.1(-07)	11	0	0
H_2CO	9.3(-09)	4.9(-09)	1.9(-09)	1.4(-09)	20	0	2
$C^{33}S$	1.8(-09)	1.9(-09)	4.3(-10)	4.5(-10)	11	0	0
OCS	1.3(-08)	1.1(-08)	9.6(-09)	9.1(-09)	22	0	0
CH_3OH	2.6(-08)	3.7(-08)	3.6(-09)	4.3(-09)	22	0	0
CH_3OCHO	≤2.5(-09)	2.7(-09)	≤2.4(-10)	2.5(-10)	5	6	0
CH_3CN	2.9(-09)	1.9(-09)	4.4(-10)	2.9(-10)	10	1	0
x(e)	7.7(-08)	6.1(-08)	1.2(-08)	9.5(-09)	11	0	0

Notes. The last three columns show the number of sources with a detection (det), non-detection (lim), and detection but no derived column density (none) due to reasons described in Section 2.3.2.

[a] mean value of T for the best-fit model

Table 2.6 Observed median abundances and standard deviation in $a(x) = a \cdot 10^x$ for the UCHIIs for $T = 100$ K and $T = 36.0$ K. x(e) is the ionization fraction.

Molecule	Abundance $T = 100$ K	Standard deviation	Abundance $T = 36.0$ K[a]	Standard deviation	det	lim	none
HCN	4.6(-08)	1.4(-08)	5.6(-09)	1.6(-09)	5	0	4
HNCO	1.1(-09)	1.3(-09)	8.6(-11)	9.9(-11)	6	3	0
$HN^{13}C$	7.6(-10)	1.0(-09)	9.2(-11)	1.3(-10)	9	0	0
C_2H	3.9(-07)	2.3(-07)	4.6(-08)	2.7(-08)	8	1	0
SiO	3.7(-10)	1.2(-09)	4.6(-11)	1.6(-10)	5	4	0
$H^{13}CO^+$	1.0(-09)	4.5(-10)	1.3(-10)	5.4(-11)	9	0	0
N_2H^+	4.1(-09)	4.1(-09)	7.4(-10)	9.2(-10)	9	0	0
^{13}CS	6.3(-09)	5.3(-09)	7.9(-10)	6.7(-10)	9	0	0
SO	5.5(-09)	2.2(-09)	1.0(-09)	4.0(-10)	5	1	3
$C^{18}O$	1.3(-06)	9.9(-07)	2.0(-07)	1.5(-07)	8	1	0
H_2CO	4.9(-09)	3.7(-09)	7.2(-10)	8.8(-10)	16	2	0
$C^{33}S$	1.2(-09)	6.3(-10)	2.5(-10)	1.3(-10)	7	2	0
OCS	≤1.6(-09)	3.5(-09)	≤1.3(-09)	3.2(-09)	6	12	0
CH_3OH	8.7(-09)	2.4(-08)	9.7(-10)	2.5(-09)	10	8	0
CH_3OCHO	≤1.3(-09)	3.0(-09)	≤9.7(-11)	2.3(-10)	0	9	0
CH_3CN	1.3(-09)	1.2(-09)	1.6(-10)	1.6(-10)	7	2	0
x(e)	9.4(-08)	4.3(-08)	1.2(-08)	5.6(-09)	9	0	0

Notes. The last three columns show the number of sources with a detection (det), non-detection (lim), and detection but no derived column density (none) due to reasons described in Section 2.3.2.

[a] mean value of T for the best-fit model

CH_3OH are at least 20% lower toward IRDCs without a point source than in sources with an embedded point source. This is a sign that the latter group is already at a slightly more advanced chemical evolutionary stage.

In general, the detected abundances over all evolutionary stages tend to increase with rising temperature during the evolution. To identify the chemical traces of the evolution we compared the abundances within the 25%-75% range of the median value between the different evolutionary phases. The abundances in the IRDC stage are around 10^{-10} and 10^{-9}, with the OCS, C_2H, and the CO isotopologue having abundances higher by one to two orders of magnitudes. Compared with the HMPOs, all abundances in the IRDCs are lower by about a half to one order of magnitude. Exceptions are the organic species CH_3OH, CH_3CN, and H_2CO, which have abundances similar to those in the HMPOs. Moreover, OCS is remarkably much more abundant, but only detected in IRDC028.2. The overall detection rate in the IRDCs is lower than that of the HMPOs.

Next, in the HMPOs the abundances have values mainly in the range of 10^{-10} to 10^{-8}. They are even higher in the HMCs. Only N_2H^+ has similar abundances across these stages. The abundances of $H^{13}CO^+$ and $HN^{13}C$, while still higher in the HMC phase, are closer to the respective HMPO values than the values of other molecules.

The abundances of most of the molecules in the HMCs have values between 10^{-9} and 10^{-7}. This is the only phase where we detected the most complex molecule analyzed in our sample, methyl formate CH_3OCHO. However, methyl formate was detected in IRDC028.2 by Vasyunina et al. (2013), which means that this non-detection might be a combination of lower sensitivity and a weaker transition.

From the HMCs to the UCHII stage, abundances of CH_3OH, CH_3CN, OCS, $C^{33}S$, H_2CO, SO, and SiO become lower. The remaining molecules have similar or slightly higher abundances in the UCHII stage. However, the overall detection rate of the different molecules for the HMCs is much higher than for the UCHIIs. Complex or heavy molecules such as CH_3OCHO, CH_3OH, SiO, HNCO, and OCS are not detected in $> 30\%$ of the UCHIIs and are almost always found in the HMCs.

2.4.6 Ionization degree

In our spectral setup we observed two molecular ions, $H^{13}CO^+$ and N_2H^+. Together with the observed H_2 densities this enables us to calculate lower limits of the electron fraction following Caselli et al. (2002c). This method is based on calculations from Caselli et al. (1998) using a simple chemical model and is only valid for homogeneous clouds. Since the deuterated counterparts are not covered by our setup we were only able to derive the electron fraction based on these two molecular species. The median electron fractions are given in Tables 2.3 – 2.6. The median value increases with evolutionary phase from $5 \cdot 10^{-9}$ in the IRDCs to $\sim 10^{-8} - 10^{-7}$ in the UCHII regions (depending on the assumed excitation temperature). This behavior agrees with the scenario of an increasing ionization radiation during the evolution of the central source that finally reaches its maximum in the UCHII phase. The derived values are also consistent with a lower limit from Caselli et al. of 10^{-9} and the work by Miettinen et al.

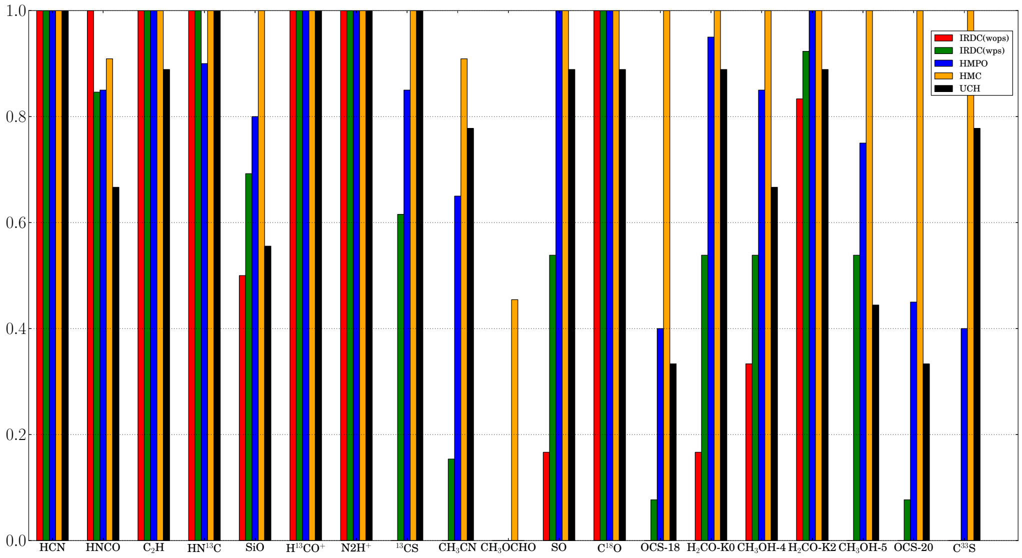

Figure 2.2 Relative detection fractions for each analyzed molecular transition ordered from left to right: IRDCs without associated point sources at wavelengths below 70 μm, IRDCs with associated point sources, HMPOs, HMCs, and UCHIIs. The color notation for the different source types is explained in the upper right corner.

(2011), who found lower limits of $\sim 10^{-8} - 10^{-7}$ in massive clumps associated with IRDCs.

2.5 Discussion

In the previous section we described the observational results about the chemical composition of the different evolutionary phases. In the next step we model the chemistry over the full evolutionary range. A detailed background of the presumed evolutionary sequence is outlined in the introduction in Section 2.1. Furthermore, combining the information from observations and model, we give a comprehensive description of this evolutionary sequence in Section 2.5.5.

2.5.1 Model

In this section we describe our iterative chemical fitting model 'MUSCLE' ('MUlti Stage CLoud codE'), which we used to constrain mean physical properties and chemical ages during the evolution from the earliest IRDC phase till the late UCHII phase of the high-mass star formation.

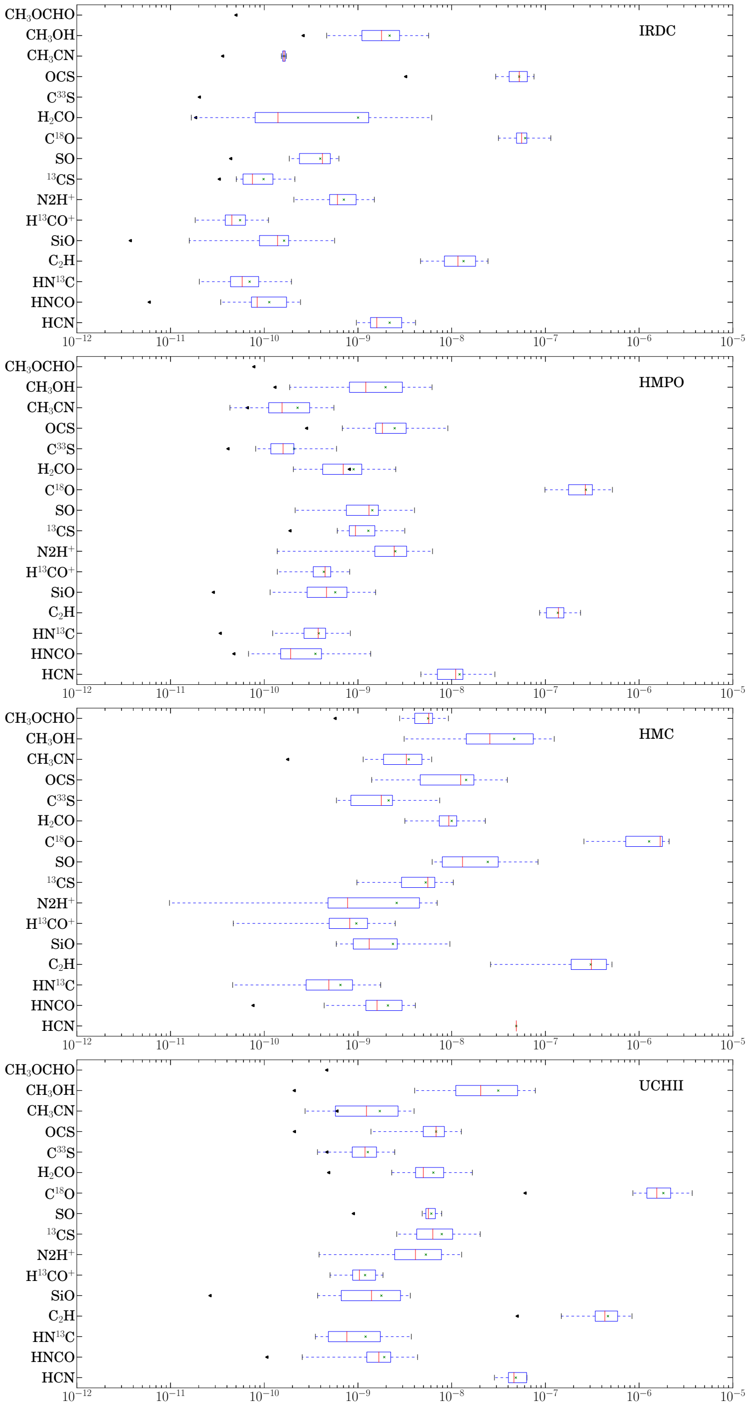

Figure 2.3 From top to bottom abundances (with respect to H_2) of the analyzed molecules in the IRDC, HMPO, HMC and UCHII sample. The red line shows the median, the green cross is the mean, the bar indicates the inner 25%-75% range around the median and the whiskers mark the total range of all detections. The black arrows indicate the lowest upper limit of all calculated upper limits for this particular molecule and stage.

Physical model

We modeled each evolutionary stage in a 1D approximation. Each environment is spherically symmetric, homogeneous, and has a fixed outer radius of $r_{\rm out} = 0.5$ pc. This radius is close to a typical value for dense parts of high-mass star-forming regions and also represents the largest 29″ IRAM beam size used in our single-dish observations as derived for the mean distance of the sample. The radial density and temperature profiles are modeled by modified power laws,

$$\begin{array}{ll} \rho(r) = \rho_{\rm in}(r/r_{\rm in})^{-p}, & r \geq r_{\rm in}; \\ \rho(r) = \rho_{\rm in}, & r < r_{\rm in} \end{array} \tag{2.4}$$

and

$$\begin{array}{ll} T(r) = T_{\rm in}(r/r_{\rm in})^{-q}, & r \geq r_{\rm in}; \\ T(r) = T_{\rm in}, & r < r_{\rm in}, \end{array} \tag{2.5}$$

respectively. Here, $r_{\rm in}$ is the inner radius below which temperature and density are assumed to be constants and p and q are the corresponding radial profiles of density and temperature. The parameters $r_{\rm in}$, p, $\rho_{\rm in}$ and $T_{\rm in}$ are the fitted physical quantities. $r_{\rm in}$ was varied between $10^{-4} - 10^{-2}$ of $r_{\rm out}$. The gas and dust were assumed to be in thermal equilibrium, therefore we did not calculate dust and gas temperatures separately. Eq. 2.4 was numerically integrated from $r = 0$ till $r = r_{\rm out}$ to derive the total modeled H_2 column density of a cloud. For that, a grid of $30 - 40$ radial cells was found to provide sufficient accuracy, and hence was adopted in large-scale chemical modeling.

We assumed that at each stage a cloud is furthermore embedded in large-scale, low-density matter that shields it from the interstellar FUV radiation by visual extinction of 10 mag. For UCHII regions we assumed that the size of a forming Strömgren zone is still small, < 0.1 pc, such that it can be neglected for calculations of bulk beam-averaged quantities such as molecular column densities.

Chemical model

The adopted time-dependent gas-grain chemical model based on the 'ALCHEMIC' code is fully described in Semenov et al. (2010). A brief summary of the updates is provided below. The chemical rate file is based on the 2007 realization of the OSU network[3]. The network is supplied with a set of $\sim$ 1000 reactions with high-temperature barriers from Harada et al. (2010) and Harada et al. (2012). The recent updates as of September 2012 to the reaction rates are implemented (e.g., from KIDA database[4]), see Albertsson et al. (2013). We considered cosmic-ray particles (CRP) and CRP-induced FUV radiation as the only external ionizing sources. The CRP ionization rate $\zeta_{\rm CR} = 5 \cdot 10^{-17}$ s^{-1} was used. The UV dissociation and ionization photorates

---

[3] See: `http://www.physics.ohio-state.edu/~eric/research.html`

[4] `http://kida.obs.u-bordeaux1.fr`

from van Dishoeck et al. (2006)[5] were adopted, assuming the case corresponding to the spectral shape of the interstellar FUV radiation field.

In addition to pure gas-phase chemical processes, the chemical network includes gas-grain interactions. We assumed that molecules stick to grain surfaces at low temperatures with 100% probability. We did not allow H_2 to stick to grains because the binding energy of H_2 to pure H_2 mantle is low, $\sim$ 100 K (Lee 1972). The ices are released back to the gas phase by thermal, CRP-, and CRP-induced UV-photodesorption. The grain re-charging was modeled by dissociative recombination and radiative neutralization of ions on grains, electron sticking to grains. Chemisorption of surface molecules was not considered. We used the UV photodesorption yield for ices of 10^{-3} (e.g., Öberg et al. 2009a,b).

The synthesis of complex molecules was included using a set of surface reactions (together with desorption energies) and photodissociation reactions of ices from Garrod & Herbst (2006) (see also Semenov & Wiebe 2011). We assumed that each 0.1 μm spherical olivine grain provides $\approx 1.88 \cdot 10^6$ surface sites for accreting gaseous species. The surface recombination solely through the Langmuir-Hinshelwood formation mechanism is considered. Upon a surface recombination, the reaction products are assumed to remain on the grain as the grain lattice would absorb all energy released during the recombination. Following interpretations of experimental results on the formation of molecular hydrogen on dust grains (Katz et al. 1999), we employed the standard rate equation approach to the surface chemistry without H and H_2 tunneling through the potential walls of the surface sites. Overall, our chemical network consists of 656 species made of 13 elements, and 7907 reactions. No chemical parameter was varied during the iterative fitting of the observational data.

Our ALCHEMIC Fortran code (Semenov et al. 2010) is based on the double-precision variable-coefficient ordinary differential equation solver with the preconditioned Krylov (DVODPK) method GMRES for the solution of linear systems[6]. The approximate Jacobi matrix is generated automatically from the supplied chemical network. For astrochemical models dominated by hydrogen reactions the Jacobi matrix is sparse, with $< 1\%$ of non-zero elements. The corresponding linearized system of algebraic equations is solved using a high-performance sparse unsymmetric MA48 solver from the Harwell Mathematical Software Library[7].

Initial abundances

The initial abundances very close to the low-metals set of Lee et al. (1998) were used to model the chemistry at the IRDC evolutionary stage (see Table 2.7). The only difference was the initially atomic abundance of Si ($3 \cdot 10^{-9}$ with respect to H) and S ($8 \cdot 10^{-7}$ with respect to H), which we had to use to achieve a better fit to the observational data. Other initial abundance sets with different amounts of oxygen and sulfur, which have been proposed in studies of chemistry in molecular clouds and protoplanetary disks,

---

[5] `http://www.strw.leidenuniv.nl/~ewine/photo/`

[6] `http://www.netlib.org/ode/vodpk.f`

[7] `http://www.hsl.rl.ac.uk/`

Table 2.7 Initial atomic and molecular abundances.

Species	Relative abundance
H_2	0.499
H	2.00(−3)
He	9.75(−2)
C	7.86(−5)
N	2.47(−5)
O	1.80(−4)
S	8.00(−7)
Si	3.00(−9)
Na	2.25(−9)
Mg	1.09(−8)
Fe	2.74(−9)
P	2.16(−10)
Cl	1.00(−9)

did not produce as good a fit to our IRDC data (see e.g., Wakelam & Herbst 2008; Graedel et al. 1982; Jenkins 2009; Hincelin et al. 2011; Dutrey et al. 2011). For modeling the chemistry of the evolutionary stages after the IRDC stage, the final chemical abundances from the best-fit model of the previous evolutionary stage were used as initial abundances (i.e., to model HMPOs we used the molecular abundances of the best-fit IRDC model at the best-fit chemical age). This allowed us to reproduce an approximately steady warming of the matter during the evolution of the high-mass star-forming clouds.

Iterative fitting of the data

Using the physical and chemical models described above, we iteratively fitted the mean observed molecular column densities for each individual evolutionary stage by varying the inner radius $r_{\rm in}$, the density at the inner radius $\rho_{\rm in}$, the temperature at the inner radius $T_{\rm in}$ and the density slope p. First, for each 1D cloud model with a grid of 30 cells we derived appropriate ranges of $r_{\rm in}$, the $\rho_{\rm in}$, and the density profile ρ by calculating beam-averaged H_2 column densities such that they are within a factor of 3 to the observationally derived values. To limit the computational time and storage space required for our large-scale modeling, we restricted the density profile parameter p to lie between the values of 1.5 and 2.0, as seen in a variety of observations by Beuther et al. (2002b); Mueller et al. (2002) and Hatchell & van der Tak (2003). The inner radius was varied between $5 \cdot 10^{-5} - 5 \cdot 10^{-2}$ pc. Another parameter whose value was iteratively varied was the temperature at the inner radius, $T_{\rm in}$ (between $15 - 27$ K for IRDCs, $50 - 250$ K for HMPOs, $150 - 500$ K for HMCs and UCHII regions). All other physical parameters were fixed during iterations, including the temperature profile q, which we set prior to the modeling. In the first stage we assumed an isothermal sphere with $q = 0$ and in the later stages a temperature profile with fixed $q = 0.4$ as a standard value. Simulations of massive star formation by van der Tak et al. (2000) found that the temperature profiles have steeper indices in the inner regions, but flatten outside

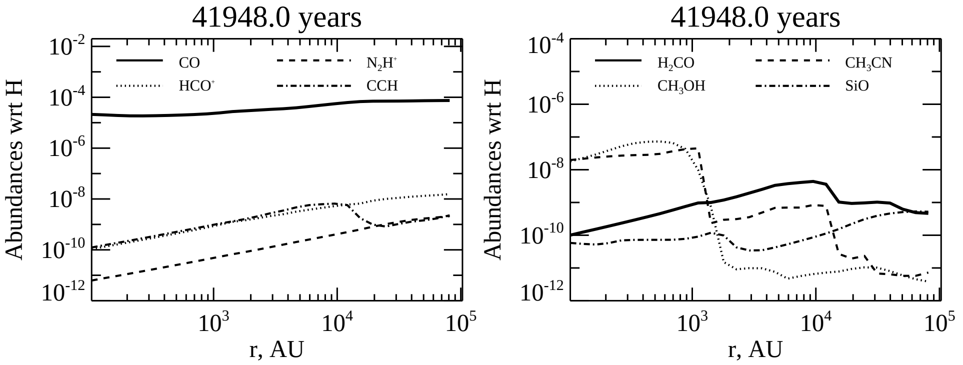

Figure 2.4 Snapshot of the radial distributions of CO, HCO^+, N_2H^+, C_2H, H_2CO, CH_3OH, CH_3CN, and SiO at the time of the best-fit model of the HMC phase. The time is given relative to the beginning of the HMC phase.

the inner 2000 AU and run asymptotically into a distribution with $q = 0.4$. Typically, by varying the parameters $r_{\rm in}$, $\rho_{\rm in}$, $T_{\rm in}$ and p for each stage, one model realization consists of 500-3 000 cloud models.

Using this large set of cloud models and our chemical model described above, we calculated corresponding time-dependent chemical structures over 1 Myr (with 99 logarithmically taken time steps between 10^4 and 10^6 years). After that, we calculated the corresponding beam-averaged column densities and the goodness of the fit for each cloud model, observed molecule, and each time step by using a confidence criterion from Equation 3 in Garrod et al. (2007). As the standard deviation σ for all observed molecules we assumed an order of magnitude variation between the modeled and the observed column densities. For molecules for which only the upper limits of the observed column densities were available in more than 50% of the sources (due to non-detections), we set the goodness-of-fit to be 0 when the modeled column density was lower than the upper limit multiplied by 10. Then, the confidence criteria for all molecules at a given time step and for a given cloud model were summed and divided by the number of observed molecules, and a total goodness-of-fit was obtained. Finally, a code searched for the lowest value that represented the best-fit physical model and the best-fit chemical age. Because we modeled averaged data, the chemical age is also an average for each of the evolutionary stages. These ages can be considered as a typical mean time for an object with a certain chemical composition to evolve to the stage with the subsequent characteristic chemical composition. A typical execution time of the MUSCLE model for one evolutionary stage is between 2 and 10 hours on a server with 24 Intel Xeon 3.2 GHz CPUs.

2.5.2 Radial distributions of molecules in the model

In Figure 2.4 we show the radial distribution of several molecules for the best-fit model of the HMC stage. Simpler molecules like N_2H^+ and HCO^+ , which are produced in the gas-phase, have a flatter distribution or even increase with radius, whereas more complex molecules like CH_3OH and CH_3CN are predominantly abundant in

Table 2.8 Parameters of the best-fit IRDC model.

Parameter	Symbol	Value
Inner radius	$r_{\rm in}$	102 AU
Outer radius	$r_{\rm out}$	0.5 pc[a]
Density at the inner radius	$\rho_{\rm in}$	$1.2 \cdot 10^9$ cm^{-3}
Average density with a beam of 26 000 AU	$\bar{\rho}$	$1.0 \cdot 10^6$ cm^{-3}
Average density with a beam of 54 000 AU	$\bar{\rho}$	$3.0 \cdot 10^5$ cm^{-3}
Density profile	p	1.8
Temperature at the inner radius	$T_{\rm in}$	20.9 K
Average temperature	$\bar{T}$	20.9 K
Temperature profile	q	0

Notes. [a] This value is limited by the largest 29″ IRAM beam size used in our observations.

the warm inner region, where ices are able to thermally desorb from dust grain surfaces. This leads to the conclusion that to properly account for these effects it is also necessary to assume different beam-filling factors for different molecules. Interferometric observations with high spatial resolutions are needed to address this problem in detail.

2.5.3 Comparison of observations and the best-fit models

The comparison of the data with the best-fit model described in Section 2.5.1 for our samples of IRDCs, HMPOs, HMCs, and UCHIIs, shows good overall agreement between the observed and modeled column densities. The best-fit parameters are shown in Tables 2.8 – 2.11 and their corresponding column densities in Tables 2.12 – 2.15. Furthermore, we list the corresponding radial temperature and density profiles as well as the chemical age of the individual stages derived with the time-dependent chemical code. Figure 2.5 shows the observed and modeled abundances as a function of evolved time. In this plot, the modeled abundances between the different stages seem to have discontinuities. This is because the best-fit models of various stages do not have similar physical structures. The chemistry reacts quickly to these changes in the physical structure at the beginning of a new stage. The abundance at each subsequent stage is plotted 100 years after the starting time of the new stage and thus the abundance occurs as a discontinuity.

In the IRDC stage the best-fit model was able to successfully explain 14 out of 14 different species. The best-fit age is $\sim$ 11 000 years (with an uncertainty of a factor of 2-3). The chemical age of a given stage is the time the model needed to evolve from the starting conditions to the best-fit model of this stage. For the later stages, the chemical composition of the best-fit model of the previous stage was set as the starting conditions for the next one.

In the second stage of an HMPO the best-fit model was able to successfully explain 12 out of 14 different species. The two species that are not explained are H_2CO and CH_3OH. The model strongly overproduces H_2CO by a factor of more than 100.

Table 2.9 Parameters of the best-fit HMPO model.

Parameter	Symbol	Value
Inner radius	$r_{\rm in}$	1 130 AU
Outer radius	$r_{\rm out}$	0.5 pc[a]
Density at the inner radius	$\rho_{\rm in}$	$5.0 \cdot 10^6$ cm^{-3}
Average density with a beam of 21 725 AU	$\bar{\rho}$	$4.1 \cdot 10^5$ cm^{-3}
Average density with a beam of 57 275 AU	$\bar{\rho}$	$9.8 \cdot 10^4$ cm^{-3}
Density profile	p	1.5
Temperature at the inner radius	$T_{\rm in}$	77.3 K
Average temperature	$\bar{T}$	29.5 K
Temperature profile	q	0.4

Notes. [a] This value is limited by the largest 29″ IRAM beam size used in our observations.

Table 2.10 Parameters of the best-fit HMC model.

Parameter	Symbol	Value
Inner radius	$r_{\rm in}$	102 AU
Outer radius	$r_{\rm out}$	0.5 pc[a]
Density at the inner radius	$\rho_{\rm in}$	$2.7 \cdot 10^9$ cm^{-3}
Average density with a beam of 45 400 AU	$\bar{\rho}$	$7.6 \cdot 10^5$ cm^{-3}
Average density with a beam of 63 100 AU	$\bar{\rho}$	$5.0 \cdot 10^5$ cm^{-3}
Density profile	p	1.9
Temperature at the inner radius	$T_{\rm in}$	268.3 K
Average temperature	$\bar{T}$	40.2 K
Temperature profile	q	0.4

Notes. [a] This value is limited by the largest 29″ IRAM beam size used in our observations.

Table 2.11 Parameters of the best-fit UCHII model.

Parameter	Symbol	Value
Inner radius	$r_{\rm in}$	102 AU
Outer radius	$r_{\rm out}$	0.5 pc[a]
Density at the inner radius	$\rho_{\rm in}$	$2.4 \cdot 10^8$ cm^{-3}
Average density with a beam of 57 800 AU	$\bar{\rho}$	$1.8 \cdot 10^5$ cm^{-3}
Average density with a beam of 85 400 AU	$\bar{\rho}$	$8.7 \cdot 10^4$ cm^{-3}
Density profile	p	1.5
Temperature at the inner radius	$T_{\rm in}$	293.1 K
Average temperature	$\bar{T}$	36.0 K
Temperature profile	q	0.4

Notes. [a] This value is limited by the largest 29″ IRAM beam size used in our observations.

Table 2.12 Median column densities in $a(x) = a \cdot 10^x$ for observations and best-fit IRDC model. When the molecule was detected in fewer than 50% of the sources, we marked it as an upper limit.

Molecule	Observed col. den. [cm^{-2}]	Modeled col. den. [cm^{-2}]
CO	1.9(18)	2.1(18)
HNC	1.5(14)	2.0(14)
HCN	9.1(13)	2.1(14)
HCO$^+$	1.2(14)	5.4(13)
HNCO	1.9(12)	5.3(11)
H_2CO	3.5(13)	7.2(13)
N_2H^+	2.2(13)	3.0(12)
CS	$\leq$6.0(14)	1.4(15)
SO	$\leq$8.4(12)	7.6(13)
OCS	$\leq$2.7(15)	2.8(12)
C_2H	3.8(14)	1.9(14)
SiO	1.9(12)	6.0(12)
CH_3CN	$\leq$5.2(12)	3.3(12)
CH_3OH	$\leq$4.8(13)	2.0(12)
Agreement		14/14 = 100%

Table 2.13 Median column densities in $a(x) = a \cdot 10^x$ for observations and best-fit HMPO model. Modeled best-fit values in italics disagree with the observed values within one order of magnitude. When the molecule was detected in fewer than 50% of the sources, we marked it as an upper limit.

Molecule	Observed col. den. [cm^{-2}]	Modeled col. den. [cm^{-2}]
CO	6.7(18)	4.1(18)
HNC	7.0(14)	7.5(14)
HCN	2.2(14)	1.3(15)
HCO$^+$	9.6(14)	4.3(14)
HNCO	4.7(12)	3.5(12)
H_2CO	4.4(13)	*7.2(15)*
N_2H^+	4.8(13)	4.1(13)
CS	1.3(15)	1.2(15)
SO	9.1(13)	7.9(14)
OCS	$\leq$6.9(13)	2.2(14)
C_2H	2.8(15)	6.8(14)
SiO	9.1(12)	9.4(12)
CH_3CN	2.4(12)	2.2(13)
CH_3OH	7.3(13)	*5.7(12)*
Agreement		12/14 = 86%

Table 2.14 Median column densities in $a(x) = a \cdot 10^x$ for observations and best-fit HMC model. Modeled best-fit values in italics disagree with the observed values within one order of magnitude. When the molecule was detected in fewer than 50% of the sources, we marked it as an upper limit.

Molecule	Observed col. den. [cm^{-2}]	Modeled col. den. [cm^{-2}]
CO	4.2(19)	1.1(19)
HNC	2.4(15)	*1.1(14)*
HCN	1.3(15)	1.4(15)
HCO^+	2.6(15)	6.9(14)
HNCO	6.3(13)	5.9(13)
H_2CO	4.4(14)	5.6(14)
N_2H^+	7.3(13)	7.4(13)
CS	2.4(16)	*1.5(15)*
SO	8.6(14)	7.8(15)
OCS	8.8(14)	1.2(15)
C_2H	1.0(16)	*1.8(14)*
SiO	5.0(13)	2.2(13)
CH_3CN	1.2(14)	7.6(13)
CH_3OH	2.2(15)	5.1(14)
Agreement		11/14 = 79%

Table 2.15 Median column densities in $a(x) = a \cdot 10^x$ for observations and best-fit UCHII model. Modeled best-fit values in italics disagree with the observed values within one order of magnitude. When the molecule was detected in fewer than 50% of the sources, we marked it as an upper limit.

Molecule	Observed col. den. [cm^{-2}]	Modeled col. den. [cm^{-2}]
CO	2.8(19)	6.4(18)
HNC	1.1(15)	*9.0(13)*
HCN	3.7(14)	4.0(14)
HCO^+	1.8(15)	4.8(14)
HNCO	1.1(13)	1.8(13)
H_2CO	1.2(14)	2.4(14)
N_2H^+	7.3(13)	5.4(13)
CS	5.0(15)	5.3(14)
SO	1.3(14)	*6.7(15)*
OCS	$\leq$1.9(13)	1.6(14)
C_2H	7.8(15)	*8.0(13)*
SiO	8.5(12)	1.7(13)
CH_3CN	2.0(13)	8.7(12)
CH_3OH	1.9(14)	1.2(14)
Agreement		11/14 = 79%

Methanol is underproduced, but only slightly lower than the assumed criteria of one order of magnitude. In general, problems with fitting the data are due to environmental effects that are not taken into account in the model, such as shocks and UV-penetration. CH_3OH and SiO are known shock tracers and thus more likely to be not explained by the model. A not yet fully understood surface chemistry is another source of uncertainty in the model. H_2CO is partly produced in the gas phase and on the grains. The two different formation routes are strongly time dependent, and so far there is no consensus in the community about how to implement this dependency or the implementation of different desorption mechanisms that allow molecules to return to the gas phase (see e.g., Garrod et al. 2007; Vasyunin & Herbst 2013b). In this case the timescale seems to be too short to transform H_2CO into CH_3OH, which can partly explain the overproduction and underproduction, respectively. The best-fit age of the HMPO phase is $\sim$ 60 000 years (with an uncertainty of a factor of 2-3).

In the third stage of an HMC the best-fit model was able to successfully explain 11 out of 14 different species. The three species that differ are HNC, CS, and C_2H. While HNC and CS are only slightly underproduced compared with the agreement criteria, C_2H is underproduced by almost more than a factor of 50. In the model the HMC is still surrounded by an external shell with a visual extinction of 10 mag with no external UV-field, which leads to lower C_2H abundances. In reality, the cloud might be highly fractal and fragmented such that UV-photons can penetrate deeper and produce more C_2H. The best-fit age of the HMC phase is $\sim$ 42 000 years (with an uncertainty of a factor of 2-3).

In the fourth stage of an UCHII the best-fit model was able to successfully explain 11 out of 14 different species. The three species that are not reproduced are HNC, SO and C_2H. A caveat for our models of UCHII regions is that it has an internal UV-source that is not properly taken into account in the model. Furthermore, since this stage depends on all best-fit models of the previous stages, it is the most doubtful one. The successful fitting of 80% of the molecules is very remarkable already. The best-fit age of the UCHII regions is $\sim$ 11 500 years (with an uncertainty of a factor of 2-3).

This is the first time that the chemical evolution was modeled and reasonably well fitted over the entire span of the early evolution of high-mass star formation regions. The mean temperatures of the best-fit model temperature profile for the last three stages (see Tables 2.8 – 2.11) are considerably lower, by a factor of 2-3, than the excitation temperatures used to calculate the observed column densities. This difference is much smaller in the IRDC stage.

In a second step we took the mean temperatures from each best-fit model as excitation temperatures to recalculate the observed column densities. The difference in abundances for the two different excitation temperatures for the IRDCs is at most a factor of 2 for all molecules, except for OCS, which differs by a factor of 3. The abundances in the HMPOs change at most by a factor of 3. The discrepancy between the temperatures originally used and the mean temperatures derived in the best-fit for the HMCs and UCHII regions is larger than for the IRDCs and HMPOs. Thus, the change in the abundances is higher by about a factor of 6 for the HMCs (only CH_3OH and CH_3OCHO differ by factors of 7 and 10, respectively) and 6-9 for the UCHIIs (only HNCO and CH_3OCHO differ by a factor of 13). These values are shown in Tables 2.3

– 2.6 as well.

In this iterative step we sought again to find best-fit solutions for the newly derived values with more consistent temperatures. To keep the model physically meaningful, the temperature profile of the last three stages was set as a power-law with a constant temperature of the IRDC best-fit value in the outer parts. This resulted in a stable solution for the IRDCs. But for the later stages the model tends to produce a small and dense inner hot part and a large isothermal outer part. A decrease in the modeled best-fit temperature leads to higher observationally derived H_2 and lower observationally derived molecular column densities. Fitting the new higher H_2 and lower molecular column densities lowers the mean temperatures even more and leads to a non-converging feedback. However, temperature measurements of tracers of the inner dense part such as CH_3CN show a hot inner component with $T > 50$ K.

The discrepancy in temperatures between model and observations is caused by uncertainties and simplifications in both. On the observational side we have single-pointing single-dish spectra for which we assumed a single excitation temperature. However, the observed sources are most likely inhomogeneous and have structures of differing environments. We partly took this into account in the model by assuming a 1D physical structure with a temperature and density profile. Another reason for this mismatch could be subthermal excitation. To avoid the effect of non-converging feedback and to account for all the caveats, we stopped the modeling process and report the results of the first iteration of the best-fit model.

Based on the probable explanations for the mismatch between the temperatures used for the observations and derived with the model, improvements on both sides might help to solve the discrepancy. Detailed gas and dust temperature maps and dust continuum radiative transfer calculations might solve the degeneracy in constraining the temperature. Interferometric observations with higher resolutions would help to decrease uncertainties in the beam filling fraction. Moreover, extending the observed species toward deuterated molecules might help to better constrain temperatures since deuterium chemistry is sensitive to the previous thermal history of the environment (see Caselli & Ceccarelli 2012). In addition, the model might be improved by including radiative transfer, a gradual warm-up phase (see Garrod et al. 2008; Vasyunin & Herbst 2013a), and in general more physics like the proper treatment of shocks, outflows and UV radiation transport. Furthermore, at least 2D models would be necessary to be able to explain observations with higher resolutions.

2.5.4 Comparison of observed and best-fit molecular ratios

In addition to the information from column densities of single molecules, the ratios between different molecules provide another interesting tool for investigating the chemical evolution. In Figure 2.6 the observed and best-fit ratios of several molecular pairs are shown. Due to the limited sensitivity in the observations the overall dynamic range of observed ratios is smaller than in the model. In general, the ratios of the observed median column densities show no obvious trends with evolution that cannot be explained within the uncertainties. Because of the poorly explained molecular column densities in the best-fit model for a few species, such as H_2CO or C_2H, and

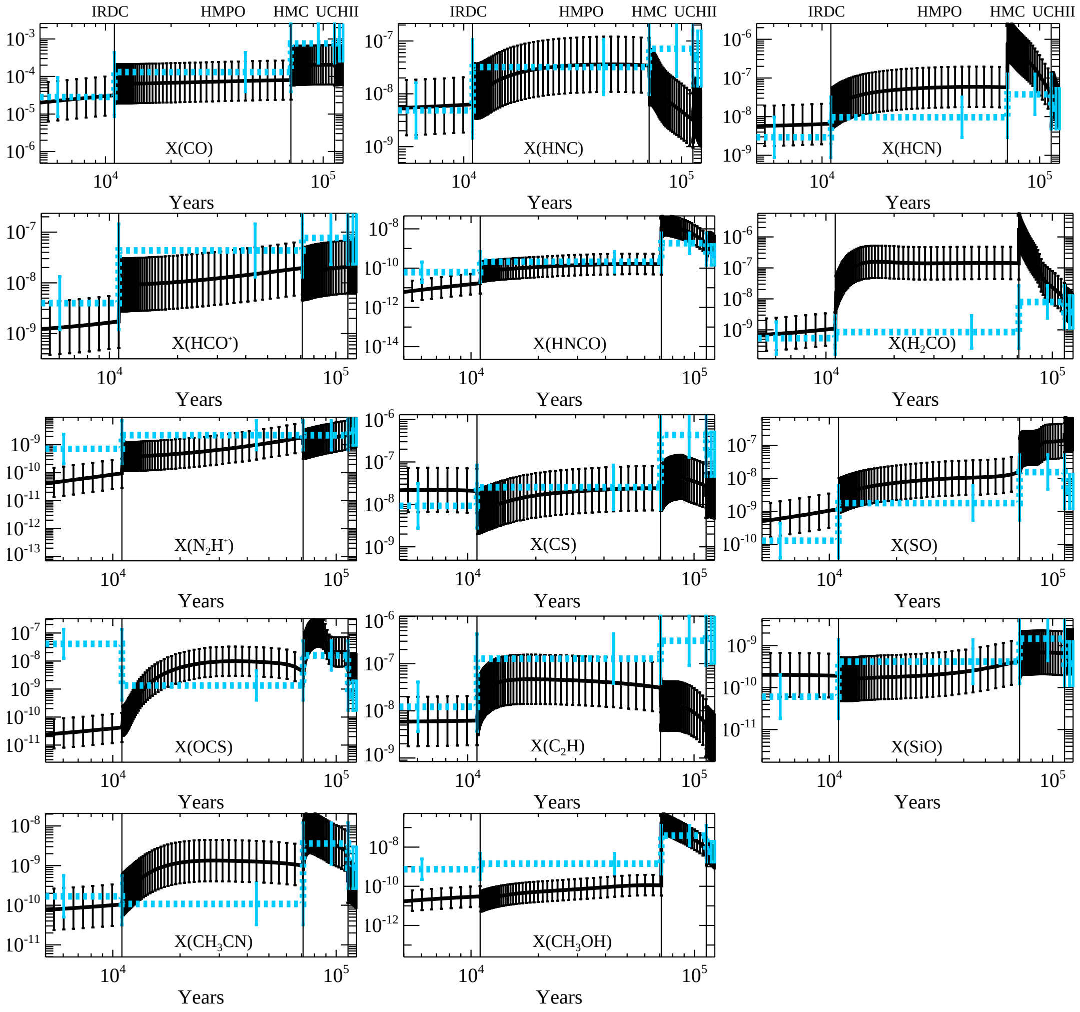

Figure 2.5 Relative abundances to H_2 plotted for all four stages. The modeled values are shown as a black solid line, the observed values are depicted by a blue dashed line. The error bars are indicated by the vertical marks.

the agreement criteria between model and observations, some of the ratios deviate strongly, depending on the specific molecule and evolutionary phase.

HCN/HNC

Previous observations showed that the ratio of HCN/HNC depends on the temperature of the medium, for example, observations of Orion-KL show a decreasing ratio from the warm inner core toward the cold outer edge from 80 to 5 (Goldsmith et al. 1986; Schilke et al. 1992). The best-fit model follows this trend and increases until it reaches the highest value of ~ 50 in the beginning of the HMC phase, whereas our observations do not show significant differences between the four stages with a ratio between $0.3 - 0.6$. The total value of the observed ratio < 1 might be underpredicted due to the assumptions of the isotopic ratio in the conversion from $HN^{13}C$ to HNC. Furthermore, due to self absorption, high optical depth, and other effects discussed in Section 2.3.2, we refrained from using the observed HCN lines in the analysis in many cases. In these cases, the sources more likely have higher column densities. That might bias the derived column densities toward lower optical depths and therefore lower column densities.

HCO^+/N_2H^+

The ratio of the two molecules N_2H^+ and HCO^+ is a candidate for a chemical clock. There is evidence that their abundances are anticorrelated in chemical models of low-mass star-forming regions (e.g., Jørgensen et al. 2004b) and massive star formation (Barnes et al. 2013), since both molecules are sensitive to the amount of CO. According to the models, N_2H^+ is more abundant during the early phases when CO is frozen out and is destroyed after CO returns into the gas phase. This behavior of the anticorrelation between CO and N_2H^+ is seen by Bergin et al. (2002) toward the low-mass star-forming region B68 and in the ratio of N_2H^+ and CO of this work. The abundance of HCO^+ is directly dependent on the CO abundance and the ionization degree and thus is anticorrelated with N_2H^+. Our observations reproduce this trend of an increasing ratio with evolutionary stage. However, in the model the ratio is almost constant within the given errors. A possible explanation are the uncertainties in the observed values, which are larger than the total change of that particular ratio. Nevertheless, observations and model agree within the uncertainties and show a total spread of the ratio between 10 and 100.

CH_3OH

In our model, the ratios of the more complex molecule methanol with simple molecules such as CO is almost constant at 10^{-6} during the IRDC and HMPO phase and jumps at the beginning of the hot core phase to 10^{-3}. During the IRDC and HMPO phases CH_3OH is steadily produced on and in ice mantles of dust grains. One of our model restrictions is that the methanol ice can only be desorbed to the gas by cosmic-ray particles (CRP) and CRP-UV heating. In the HMC phase the entire solid reservoir of dust mantles is released into the gas phase, leading to a sudden increase of the gas-phase concentration of many complex molecules. Their abundance may decrease with time after that event if they are actively destroyed or converted to other species in the gas, because surface chemistry becomes insignificant at $> 100 - 150$ K. Afterwards it steadily declines until it reaches 10^{-5} at the end of the evolution. This behavior is imprinted by the abundance variability of CH_3OH and is thus seen in most of its ratios. It agrees with the observational ratio for the last three stages, but underestimates the IRDC stage.

S-bearing molecules

The ratio of the S-bearing molecules CS and SO is poorly described by the model and represents a well-known problem with sulfur chemistry in modern astrochemical databases (Druard & Wakelam 2012; Herpin et al. 2009; Loison et al. 2012; Dutrey et al. 2011). While in the observations for the IRDC stage both molecules have only an upper limit, the later stages show an increasing trend of the ratio between 10 and 100. In contrast, the model predicts a strongly decreasing CS/SO ratio over about three orders of magnitude. The ratio of SO with the early type molecule N_2H^+ is also poorly described by the model. Only the HMPO and HMC phase agree slightly, with a decreasing ratio with time. Since the model for CS and SO alone does not agree very well for both, it is natural that the ratio does not agree either.

For completeness and to outline the strengths and caveats of our modeling approach, Figure 2.6 presents a few more ratios that we do not discuss in detail here.

2.5.5 Chemical evolutionary sequence – synthesis of observations and models

With observational and modeled data at hand we can derive a general picture of the chemical evolution in high-mass star-forming regions. The starting condition at the year 0 in our model is a cold dense molecular cloud, which is still close to isothermal with the initial chemical composition given in Table 2.7. Any evolution prior to the IRDC stage to these initial conditions is not considered in this work. In our IRDC model the temperature remains constant, and the chemical evolution proceeds under these conditions for about 11 000 years. At this time the best overall agreement between the observed and the calculated molecular column densities is reached. The modeled abundance of the best-fit model at the best-fit age are used as input abundances for the next HMPO stage of the evolution.

From that time the HMPO phase begins in our model. An internal source heats the surrounding medium, such that the temperature increases toward the inner region. This is implemented in the modeling by a temperature profile $q = 0.4$. Increased temperature results in a higher mobility of the surface molecules and a more efficient desorption of ices into the gas phase. Consequently, the molecular abundances increase. Our best-fit model matches the observed values for the HMPOs after 60 000 years (with a total age of 71 000 years from time zero). As temperatures and densities con-

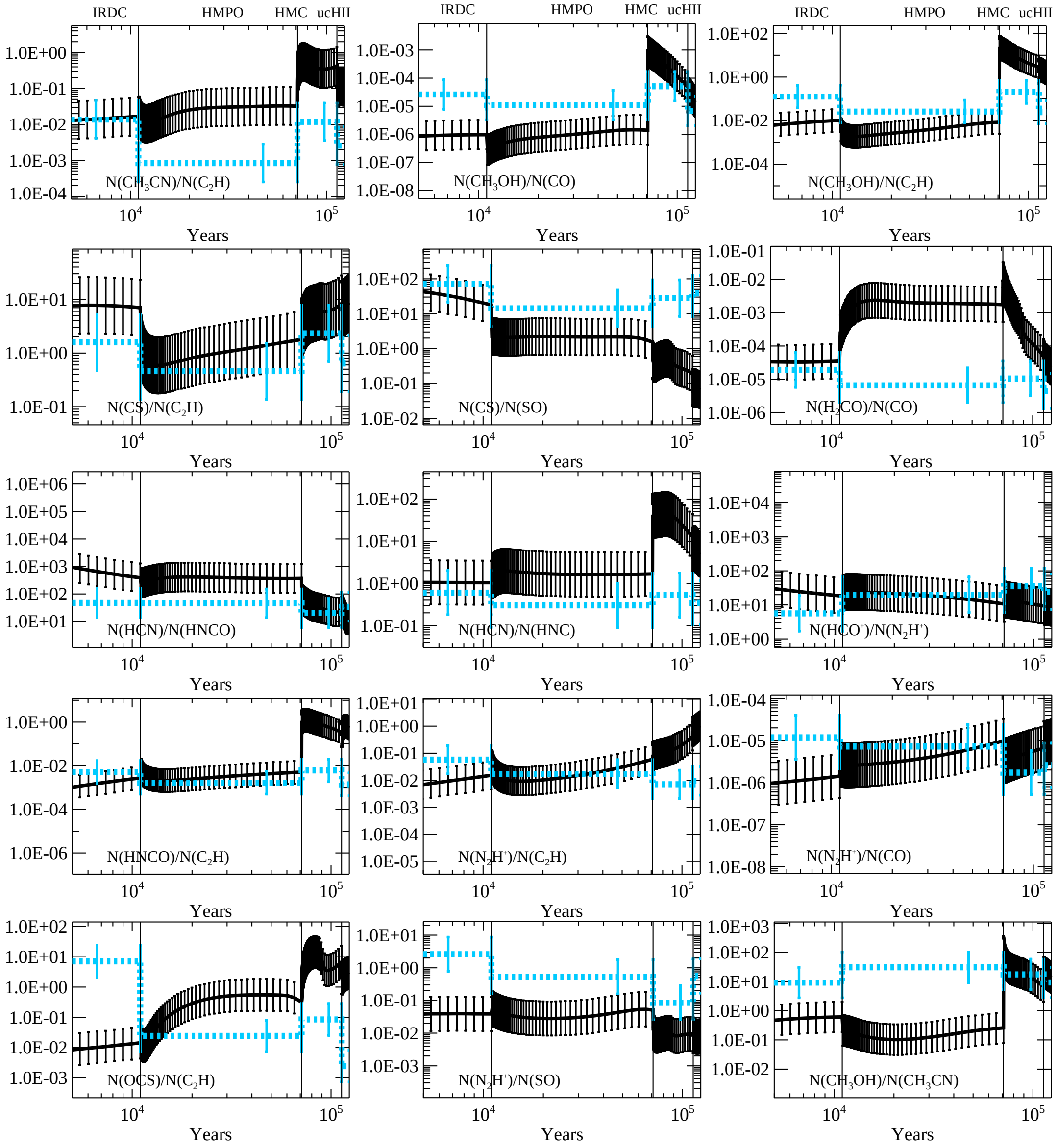

Figure 2.6 Column density ratios for 15 different combinations of molecules plotted for all four stages. The modeled values are shown by the black solid line, the observed values are depicted by the blue dashed line. The error bars are indicated by the vertical marks.

tinue to rise due to formation of a central protostar(s), the object enters the HMC phase. The subsequent increase in temperature releases most of the molecules locked along with water ice in the grain mantles into the gas phase. This increases gas-phase abundances of already abundant molecules even further and observed transitions become stronger. The detection rate of molecular lines increases as well, including those from complex and heavy molecules. According to our best-fit model, the HMC phase lasts for about 42 000 years, leading to a total age of 113 000 years.

Finally, the last considered stage of high-mass star-forming regions begins. For the UCHII phase the temperature and density structures are re-adjusted again. The best-fit age derived for this last stage is 11 500 years. Thus, we predict that the total evolution from the formation of an IRDC until the formation of an UCHII region takes about 124 500 years (with an uncertainty of a factor of 2-3). It appears to be consistent with the estimates obtained from modeling of the formation of high-mass stars (e.g., McKee & Tan 2003).

2.5.6 Observed ionization degree compared with model data

In Section 2.4.6 we calculated lower limits for the ionization degree in the four evolutionary stages of high-mass star formation. In addition, the best-fit model provides all necessary information to derive the exact modeled ionization degrees to compare. The modeled abundances of the main constituents, namely, electrons, N_2H^+, and HCO^+ and the observed abundances for N_2H^+ and HCO^+ , are shown in Figure 2.7. While the observed lower limit increases with evolutionary phase, the ionization degree in the best-fit model remains almost constant at $\sim 10^{-7}$ throughout the whole evolution. In comparison with the observed data it is off by about one order of magnitude in the first two stages and agrees for the last two stages. This leads to the conclusion that a lower limit for the ionization degree derived from HCO^+ and N_2H^+ is a good first approximation. However, it also indicates that in particular in the early evolutionary phases, other ions contribute more strongly to the total ionization degree. These are deuterated ions in the dense cores, which we will observe in a follow-up study, but the singly ionized carbon is also important during these stages. For example, Miettinen et al. (2011) took deuterated ions into account as well and found slightly higher lower limits for $x(e) \sim 10^{-8} - 10^{-7}$, which are comparable with the results of our model. In addition to this, more sophisticated methods are needed to estimate the ionization degree with an uncertainty better than one order of magnitude. Here, any deviation from the assumption of a homogeneous medium used in our model (e.g., clumpiness on various scales) will tend to increase the modeled ionization fraction for the later evolutionary stages when some high- energy photons might already be produced by forming protostar(s).

2.5.7 Comparison with literature

Our comprehensive study of the chemical evolution in the early phases of massive star formation can be set in context to previous studies focusing on distinct evolutionary phases.

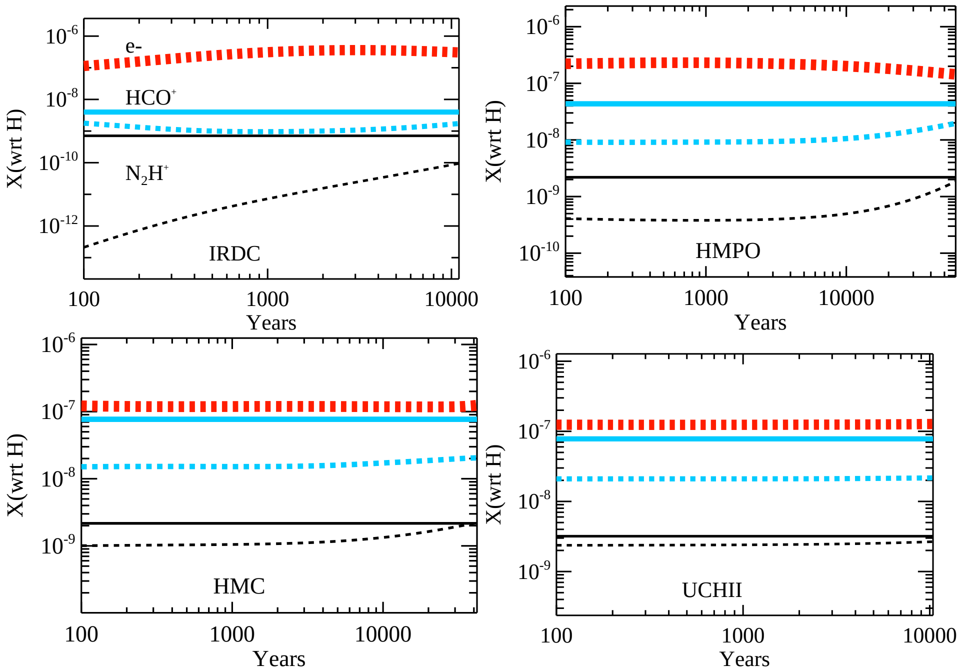

Figure 2.7 Averaged relative abundances to H_2 for electrons, HCO^+, and N_2H^+ plotted for the all four stages. The observed values are shown as solid lines, the modeled values are depicted as dashed lines. The electron abundances are plotted in red, N_2H^+ abundances in black, and HCO^+ abundances in blue. The error bars for both the model and the observational data are a factor of about 3 (not shown).

The comparison of our work with the study of IRDCs from Vasyunina et al. (2011) qualitatively agrees. Assuming uncertainties of about one order of magnitude for each of the derived abundances, only 2 of 9 molecules show a stronger deviation, namely, HNCO and SiO with lower abundances of slightly more than one order of magnitude in our sample. We detected CH_3CN only in two sources in our IRDC sample, which was not detected by Vasyunina et al. either. In a more recent study, Vasyunina et al. (2013) additionally derived abundances of H_2CO and CH_3OH for a sample of IRDCs. The range of abundances they found are overlapping with, but slightly higher than, our findings.

The observed sample of clumps in IRDCs from Sanhueza et al. (2012) shows in general higher abundances for all observed molecules, but 5 out of 6 of them agree with our values. Sakai et al. (2008) derived for a sample of IRDCs column densities of N_2H^+ with values that are similar to our results. For CH_3OH our findings fall into the lower end of their observed range of column densities, but are still consistent. Sakai et al. (2010) calculated the column densities for HMPO-like sources. Comparing their sample of MSX sources with our HMPO sample we find good agreement with their observed range of column densities and our median values. Only CH_3OH and CS isotopologues show a bigger deviation on the order of 10, which still agrees with the uncertainties of the observed values in our study.

Our derived median abundances of the detections for the HMCs and UCHIIs are similar to each other within the uncertainties. However, we derived higher median column densities for the HMCs due to a smaller mean distance and higher H_2 column densities. Hatchell et al. (1998) inferred the H_2 column densities from virial mass estimates of the observed gas, assuming a specific source size and extension. Therefore, their H_2 column densities are different for different molecules. Comparing our median column densities for the HMCs and UCHIIs with their results, we find an overall good agreement. The only molecule that deviates by a factor of more than 10 is CH_3OH (for both phases) and CH_3OCHO (for the UCHII stage). Reiter et al. (2011) derived molecular column densities of high-mass clumps coincident with water maser emission and mainly associated with HII regions for a larger set of molecules. These values we can compare with our more evolved sources. The range of values they found for HCO^+, C_2H, HNC and CS are slightly lower, by a factor up to 5, than the median values in our sample. The column densities of N_2H^+ and SO are similar to our findings.

The most prominent source in our sample is the well-studied Orion-KL hot core. A summary of abundances in this source is given in van Dishoeck & Blake (1998). Our results also agree well with these values. The SiO abundances differ by a factor of 6, while all other eight molecules in comparison show differences by factors of 1-4.

2.6 Conclusion

We observed the chemistry in 59 sources covering the early stages in massive star formation to study and characterize the physical and chemical evolution. This was the first consistent attempt to follow the evolution of physics and chemistry over several evolutionary steps in high-mass star formation. The underlying part of the evolutionary sequence assumed in this work started with an IRDC that evolved over the HMPO and HMC phase and ended with the formation of an UCHII region. Using this approach, we obtained a consistent sample of spectra for all of the sources. The spectra show an increasing number and intensity of the molecular transitions for more evolved stages. More complex and heavy molecules are formed with evolving age until the richness of molecular composition reaches its maximum in the HMC phase and declines for the UCHII stage, because these molecules are probably destroyed by the UV-radiation from the forming stars.

We calculated column densities for different molecular species that are in general increasing with evolutionary phase. Their ratios are less dependent on the temperature than the abundances. Thus we see a more obvious evolution in the abundances than in the ratios of these data. Furthermore, the derived lower limits of the ionization degree in the different stages increase along the evolutionary picture, as well.

In a second step we compared the characteristic median column densities of each evolutionary stage with a model. We calculated the best-fit parameters and ages, using a 1D physical model coupled to a gas-grain chemical model, in which the evolutionary sequence was approximately taken into account. The observed column densities and abundances agree reasonably well with the overall fit of our model. Furthermore, our results agree with previous observational studies. Based on the fit of the chemical model to 14 different molecular species of unresolved data, we were able to derive constrains on the underlying physical structure. The best-fit duration for the full evolution from an IRDC with atomic gas composition to the stage of an UCHII region is about 125 000 years. This is consistent with estimates from theoretical models of the formation of high-mass stars. The results from this study can be considered as chemical templates for the different evolutionary stages during high-mass star formation.

2.7 Appendix material

Table 2.16 Integrated intensity $\int T_{\mathrm{mb}}$ in K km s^{-1}. For N_2H^+ we give T_{mb} in K derived from the standard hyperfine fitting CLASS routine. Non-detections are indicated by $\leq$ and the 1σ rms value is given. A blank entry means that the molecule is detected, but rejected from the analysis due to reasons discussed in Section 2.3.2.

Source	HCN	HNCO	C_2H	$HN^{13}C$	SiO	$H^{13}CO^+$	N_2H^+	^{13}CS	CH_3CN	CH_3OCHO	SO
IRDC011.1		1.25	1.53	1.76	2.47	2.08	3.53	0.37	0.29	≤0.03	≤0.08
IRDC028.1		2.70	2.03	1.94	4.52	1.96	5.87	0.74	≤0.05	≤0.05	1.59
IRDC028.2		4.20	3.32	1.93	7.94	2.59	2.32	1.45	0.95	≤0.05	9.89
IRDC048.6	3.47	0.34	0.24	0.38	≤0.03	0.79	1.99	≤0.03	≤0.03	≤0.03	0.26
IRDC079.1		≤0.04	1.52	0.83	≤0.04	2.00	2.98	0.38	≤0.06	≤0.06	3.20
IRDC079.3	5.73	0.44	1.96	1.25	≤0.04	1.87	2.26	≤0.06	≤0.06	≤0.06	≤0.19
IRDC18151	47.03	0.85	5.28	1.38	1.97	2.88	7.62	0.40	≤0.03	≤0.03	3.34
IRDC18182		0.49	1.37	0.82	≤0.03	0.91	2.09	≤0.03	≤0.03	≤0.03	≤0.07
IRDC18223	17.08	0.86	2.33	3.05	2.56	2.82	5.27	0.37	≤0.03	≤0.03	1.15
IRDC18306		0.38	0.76	0.76	≤0.03	0.68	1.00	≤0.03	≤0.03	≤0.03	≤0.07
IRDC18308	13.70	1.85	1.42	0.83	2.09	0.91	2.25	0.25	≤0.03	≤0.03	≤0.07
IRDC18310		1.69	0.82	1.52	2.52	1.14	5.40	≤0.03	≤0.03	≤0.03	≤0.07
IRDC18337		0.82	1.00	0.68	3.11	0.91	2.45	0.26	≤0.02	≤0.02	1.27
IRDC18385		0.35	1.06	0.57	0.84	0.83	2.27	≤0.05	≤0.05	≤0.05	≤0.16
IRDC18437	7.13	≤0.04	1.04	0.36	≤0.04	0.47	2.41	≤0.06	≤0.06	≤0.06	≤0.16
IRDC18454.1		0.54	1.22	0.62	≤0.04	0.70	1.88	≤0.06	≤0.06	≤0.06	≤0.17
IRDC18454.3		2.13	2.75	1.89	2.43	2.74	3.37	≤0.05	≤0.05	≤0.05	≤0.16
IRDC19175		0.33	0.56	0.30	0.54	0.51	1.02	≤0.05	≤0.05	≤0.05	≤0.12
IRDC20081	6.90	0.35	1.32	0.31	0.22	1.10	2.64	≤0.06	≤0.06	≤0.06	2.42
HMPO18089		1.44	5.57	3.35	3.02	4.99	6.52	5.13	1.80	≤0.03	18.35
HMPO18102		4.23	2.93	2.83	4.25	3.20	4.26	0.87	0.82	≤0.03	2.92
HMPO18151	49.32	0.44	5.13	1.62	1.91	3.80	7.92	0.81	0.07	≤0.03	3.96
HMPO18182	34.55	1.32	4.53	2.08	2.60	4.06	7.41	2.37	0.66	≤0.03	8.67
HMPO18247	10.49	0.36	1.88	1.02	0.32	1.42	4.66	0.39	≤0.03	≤0.03	0.77
HMPO18264	76.18	1.04	6.93	2.04	6.32	5.17	13.61	1.35	0.70	≤0.03	17.25
HMPO18310		0.89	3.25	1.49	1.23	2.24	4.69	0.82	0.16	≤0.03	0.81
HMPO18488		1.10	3.94	1.29	3.49	2.65	6.12	1.21	0.27	≤0.06	8.43
HMPO18517	49.32	1.00	6.90	1.42	2.05	5.11	7.80	1.14	0.36	≤0.05	10.68
HMPO18566		2.09	3.26	2.09	3.85	3.34	5.71	1.77	0.46	≤0.05	7.36
HMPO19217		1.51	3.08	1.31	2.93	3.46	4.26	1.39	0.16	≤0.05	12.40
HMPO19410	39.12	0.57	6.01	1.82	0.83	3.21	15.50	1.80	0.13	≤0.05	6.03
HMPO20126	53.19	0.69	6.48	2.75	≤0.05	4.03	10.28	≤0.08	0.35	≤0.08	10.79
HMPO20216	16.24	≤0.05	2.42	0.60	≤0.05	1.33	2.50	≤0.07	≤0.07	≤0.07	0.61
HMPO20293	29.35	0.43	5.29	1.75	3.83	2.65	14.77	0.90	≤0.06	≤0.06	4.86
HMPO22134	13.64	0.12	2.81	0.30	≤0.03	1.14	2.55	0.32	≤0.04	≤0.03	2.79
HMPO23033	35.88	0.53	5.84	1.05	1.03	3.47	7.37	0.71	0.18	≤0.03	3.09
HMPO23139	30.56	0.59	4.17	0.46	1.43	1.57	4.60	0.89	≤0.03	≤0.03	14.17
HMPO23151	14.85	≤0.03	2.36	≤0.03	0.40	0.50	0.14	0.43	≤0.03	≤0.03	8.40
HMPO23545	6.68	≤0.03	1.38	≤0.03	≤0.03	0.82	0.39	≤0.03	≤0.03	≤0.03	1.16
HMC009.62		5.02	11.63	4.01	13.39	9.05	7.25	7.69	3.59	≤0.03	34.33
HMC010.47		8.92	13.14	6.07	9.11	10.40	6.67	10.83	10.61	1.45	45.61
HMC029.96		1.89	7.19	3.14	4.28	6.43	6.01	7.07	2.68	≤0.03	39.19
HMC031.41		5.76	6.66	2.60	5.85	2.99		8.39	6.05	1.66	41.68
HMC034.26		4.38	11.20	6.92	9.74	14.78	7.32	12.72	8.25	1.28	84.72
HMC045.47		2.28	5.31	2.68	4.81	6.21	7.63	1.70	0.58	≤0.03	12.56
HMC075.78		1.33	6.44	1.45	4.63	4.55	4.58	2.73	0.65	≤0.06	38.86
W3H2O	69.66	1.05	7.08	0.91	3.99	4.09	3.07	3.76	1.68	0.51	66.59
W3IRS5		≤0.02	7.58	0.41	1.21	1.73	0.22	0.71	≤0.03	≤0.03	69.46
NGC7538B		0.69	6.41	0.82	3.15	3.19	2.75	1.81	1.10	≤0.03	19.45
Orion-KL		24.47	7.96	1.96	410.83	3.22	0.51	9.43	59.54	5.57	2468.78
UCH005.89		2.68	21.91	12.18	23.42	16.05	18.64	10.24	4.41	≤0.03	
UCH010.10	4.84	≤0.02	≤0.02	0.71	≤0.02	0.57		0.87	≤0.02	≤0.02	≤0.06
UCH010.30		3.92	14.53	4.16	6.89	6.71	9.55	6.68	2.18	≤0.03	
UCH012.21		2.59	7.97	2.97	4.01	4.73	5.04	4.08	1.53	≤0.03	16.31
UCH013.87	32.39	0.98	6.60	1.20	≤0.03	3.77	4.33	3.67	0.44	≤0.03	6.06
UCH030.54	23.59	0.39	2.75	0.32	≤0.03	1.04	1.22	0.69	≤0.03	≤0.03	2.24
UCH035.20		0.31	3.46	1.14	≤0.03	2.66	4.17	2.17	0.50	≤0.03	11.69
UCH045.12	43.79	≤0.03	5.40	0.80	0.82	3.13	1.11	1.30	0.14	≤0.03	
UCH045.45	22.46	≤0.03	2.99	0.60	0.83	1.38	2.32	1.19	0.14	≤0.03	6.55

Table 2.17 Continuation of Table 2.16 with additional species. The integrated intensity $\int T_{\rm mb}$ in K km s^{-1}. Non-detections are indicated by $\leq$ and the 1σ rms value is given. A blank entry means that the molecule is detected, but rejected from the analysis due to reasons discussed in Section 2.3.2.

Source	$C^{18}O$	OCS(1)	H_2CO(1)	CH_3OH(1)	H_2CO(2)	CH_3OH(2)	OCS(2)	$C^{33}S$	$H_{2,29}$	$H_{2,\rm beam}$
IRDC011.1	7.98	$\leq$0.08	0.69	1.08	3.29	0.66	$\leq$0.10	$\leq$0.10	2.70	1.70
IRDC028.1	8.36	$\leq$0.09	1.29	2.38	5.54	1.15	$\leq$0.10	$\leq$0.10	2.34	1.40
IRDC028.2	16.84	2.38	7.19	15.38		13.38	1.65	$\leq$0.09	7.86	5.21
IRDC048.6	2.19	$\leq$0.07	$\leq$0.07	$\leq$0.07	0.37	$\leq$0.23	$\leq$0.23	$\leq$0.23	0.63	0.43
IRDC079.1	14.07	$\leq$0.21	$\leq$0.21	$\leq$0.21	3.57	$\leq$0.17	$\leq$0.17	$\leq$0.17	3.45	2.73
IRDC079.3	4.80	$\leq$0.19	$\leq$0.19	$\leq$0.19	1.24	$\leq$0.17	$\leq$0.17	$\leq$0.17	2.16	1.55
IRDC18151	13.34	$\leq$0.07	3.42	4.80	11.72	6.92	$\leq$0.10	$\leq$0.10	1.52	0.62
IRDC18182	6.03	$\leq$0.07	$\leq$0.07	$\leq$0.07	1.48	$\leq$0.10	$\leq$0.10	$\leq$0.10	0.40	0.14
IRDC18223	9.86	$\leq$0.07	0.78	1.07	3.35	1.96	$\leq$0.10	$\leq$0.10	0.61	0.29
IRDC18306	6.31	$\leq$0.07	$\leq$0.07	$\leq$0.07	0.40	$\leq$0.10	$\leq$0.10	$\leq$0.10	0.50	0.15
IRDC18308	6.86	$\leq$0.07	0.59	1.31	3.02	0.69	$\leq$0.07	$\leq$0.07	0.72	0.22
IRDC18310	4.43	$\leq$0.07	0.52	0.87	2.86	$\leq$0.10	$\leq$0.10	$\leq$0.10	0.48	0.13
IRDC18337	3.94	$\leq$0.05	1.59	2.59	5.87	1.95	$\leq$0.07	$\leq$0.07	0.23	0.12
IRDC18385	3.24	$\leq$0.16	$\leq$0.16	$\leq$0.16	2.56	$\leq$0.10	$\leq$0.10	$\leq$0.10	0.23	0.08
IRDC18437	6.94	$\leq$0.16	$\leq$0.16	$\leq$0.16	$\leq$0.16	$\leq$0.11	$\leq$0.11	$\leq$0.11	0.31	0.09
IRDC18454.1	6.75	$\leq$0.17	$\leq$0.17	$\leq$0.17	$\leq$0.17	$\leq$0.11	$\leq$0.11	$\leq$0.11	0.41	0.18
IRDC18454.3	15.88	$\leq$0.16	$\leq$0.16	1.37	4.62	$\leq$0.10	$\leq$0.10	$\leq$0.10	0.59	0.20
IRDC19175	4.39	$\leq$0.12	$\leq$0.12	$\leq$0.12	1.13	$\leq$0.24	$\leq$0.24	$\leq$0.24	0.27	0.09
IRDC20081	10.67	$\leq$0.19	$\leq$0.19	$\leq$0.19	2.42	$\leq$0.19	$\leq$0.19	$\leq$0.19	0.59	0.24
HMPO18089	37.63	6.01	7.65	12.39		4.81	2.75	2.96	3.80	2.37
HMPO18102	8.20	1.12	2.95	4.87	10.35	3.12	$\leq$0.10	$\leq$0.10	1.93	0.63
HMPO18151	20.0	$\leq$0.07	1.69	1.54	8.16	1.90	$\leq$0.10	0.74	2.00	0.98
HMPO18182	38.84	1.95	4.06	8.46	11.59	6.42	1.94	1.83	2.55	1.44
HMPO18247	18.50	$\leq$0.07	0.58	0.90	2.96	0.57	0.57	$\leq$0.11	1.28	0.60
HMPO18264	20.42	1.82	10.92	12.97	31.28	7.82	1.27	1.11	4.32	2.09
HMPO18310	18.79	$\leq$0.07	0.43	0.52	3.20	$\leq$0.10	$\leq$0.10	$\leq$0.10	1.35	0.37
HMPO18488	25.16	$\leq$0.10	2.99	6.06	12.85	3.81	1.23	0.88	1.48	0.56
HMPO18517	26.29	1.50	4.12	5.82	14.24	5.54	1.28	0.95	3.25	1.15
HMPO18566	16.62	1.84	2.63	5.54	9.41	5.65	3.44	2.39	1.17	0.62
HMPO19217	23.58	$\leq$0.08	4.65	8.87	13.54	8.03	1.72	$\leq$0.23	1.92	0.79
HMPO19410	13.58	0.68	2.56	3.02	9.86	2.30	0.40	0.74	3.11	0.96
HMPO20126	14.28	$\leq$0.19	5.99	4.54	15.81	5.61	$\leq$0.12	$\leq$0.12	2.61	1.34
HMPO20216	9.23	$\leq$0.24	$\leq$0.24	$\leq$0.24	2.73	$\leq$0.18	$\leq$0.18	$\leq$0.18	0.60	0.30
HMPO20293	11.50	$\leq$0.18	3.13	3.80	11.57	1.94	$\leq$0.18	$\leq$0.18	1.99	0.55
HMPO22134	12.63	$\leq$0.06	0.83	$\leq$0.06	3.39	$\leq$0.16	$\leq$0.16	$\leq$0.16	1.12	0.34
HMPO23033	13.12	$\leq$0.06	2.22	1.86	10.49	1.63	$\leq$0.17	$\leq$0.17	1.84	0.73
HMPO23139	15.22	0.73	4.31	4.22	14.95	2.56	$\leq$0.17	$\leq$0.17	1.39	0.59
HMPO23151	15.77	$\leq$0.06	1.23	0.93	4.42	$\leq$0.11	$\leq$0.11	$\leq$0.11	1.05	0.48
HMPO23545	10.22	$\leq$0.07	0.38	$\leq$0.07	1.92	$\leq$0.17	$\leq$0.17	$\leq$0.17	0.70	0.20
HMC009.62	72.23	7.25	9.71	19.93	27.00	6.71	1.78	1.82	16.63	11.71
HMC010.47	79.58	34.20	26.58	55.86		39.48	31.17	16.65	40.09	32.81
HMC029.96	69.00	12.11	14.25	15.96	36.67	9.94	10.65	8.68	16.49	12.01
HMC031.41	60.31	24.88	19.60	43.74		27.47	21.38	17.30	28.41	21.69
HMC034.26	110.54	40.34	40.66	64.47	67.23	46.42	36.10	26.00	72.36	51.50
HMC045.47	27.98	1.47	4.50	6.99	14.89	3.71	1.32	1.09	7.84	4.99
HMC075.78	39.72	3.07	7.58	8.08	22.05	6.65	3.85	3.11	12.03	10.32
W3H2O	44.78	11.89	14.69	18.70	33.35	27.64	18.67	15.87	13.99	12.52
W3IRS5	40.0	0.49	4.03	0.81	11.26	1.06	1.34	0.95	11.42	8.98
NGC7538B	29.60	1.76	7.64	4.91	21.93	5.82	2.07	2.85	23.60	19.59
Orion-KL	112.27	272.95	212.37	219.77	425.95	231.06	297.76	56.14	237.20	204.20
UCH005.89	80.78	12.59	31.45	24.53	77.61	16.57	9.61	10.40	32.87	23.75
UCH010.10	$\leq$0.06	$\leq$0.06	$\leq$0.06	$\leq$0.06	$\leq$0.06	$\leq$0.11	$\leq$0.11	$\leq$0.11	0.98	0.84
UCH010.30	49.32	1.91	5.62	9.59	25.68	4.67	0.59	2.28	12.29	7.29
UCH012.21	45.54	4.38	8.31	15.80	22.14	22.94	8.09	7.06	14.57	10.84
UCH013.87	42.76	$\leq$0.08	1.91	2.03	7.33	1.21	$\leq$0.10	1.47	8.07	5.08
UCH030.54	25.04	$\leq$0.07	0.91	$\leq$0.07	3.67	$\leq$0.08	$\leq$0.08	$\leq$0.08	3.18	2.06
UCH035.20	40.11	$\leq$0.07	3.52	1.13	12.05	$\leq$0.05	$\leq$0.05	1.55	18.15	14.29
UCH045.12	20.04	$\leq$0.07	1.80	$\leq$0.07	6.68	$\leq$0.03	$\leq$0.03	0.69	11.24	7.06
UCH045.45	21.85	$\leq$0.07	2.40	1.35	7.67	$\leq$0.03	$\leq$0.03	1.46	6.32	3.72

Table 2.18 Iteration 0 column densities in $a(x) = a \cdot 10^x$ cm^{-2} derived with the initially chosen typical temperatures (see Section 2.4.3 and Tables 2.3–2.6). Non-detections are indicated by $\leq$ and the upper limit derived with the 3σ rms value. A blank entry means that the molecule is detected, but rejected from the analysis due to reasons discussed in Section 2.3.2.

Source	HCN	HNCO	C_2H	$HN^{13}C$	SiO	$H^{13}CO^+$	N_2H^+	^{13}CS	CH_3CN	CH_3OCHO	SO
IRDC011.1		4.5(12)	4.2(14)	3.6(12)	5.5(12)	2.6(12)	2.8(13)	3.7(12)	9.3(12)	$\leq$4.9(12)	$\leq$3.9(12)
IRDC028.1		9.6(12)	5.6(14)	4.0(12)	1.0(13)	2.5(12)	4.0(13)	7.5(12)	$\leq$5.2(12)	$\leq$8.6(12)	2.7(13)
IRDC028.2		1.5(13)	9.2(14)	3.9(12)	1.8(13)	3.3(12)	6.5(13)	1.5(13)	3.1(13)	$\leq$8.9(12)	1.7(14)
IRDC048.6	2.1(13)	1.2(12)	6.7(13)	7.9(11)	$\leq$1.9(11)	1.0(12)	8.0(12)	$\leq$8.6(11)	$\leq$2.7(12)	$\leq$4.6(12)	4.5(12)
IRDC079.1		$\leq$4.3(11)	4.2(14)	1.7(12)	$\leq$2.7(11)	2.5(12)	2.3(13)	3.9(12)	$\leq$6.0(12)	$\leq$9.9(12)	5.5(13)
IRDC079.3	5.7(13)	1.6(12)	5.4(14)	2.6(12)	$\leq$2.6(11)	2.4(12)	2.5(13)	$\leq$1.8(12)	$\leq$5.7(12)	$\leq$9.5(12)	$\leq$9.5(12)
IRDC18151	1.3(14)	3.0(12)	1.5(15)	2.8(12)	4.4(12)	3.6(12)	4.9(13)	4.1(12)	$\leq$2.9(12)	$\leq$4.8(12)	5.7(13)
IRDC18182		1.7(12)	3.8(14)	1.7(12)	$\leq$2.1(11)	1.2(12)	1.6(13)	$\leq$9.0(11)	$\leq$2.9(12)	$\leq$4.8(12)	$\leq$3.8(12)
IRDC18223	9.5(13)	3.1(12)	6.4(14)	6.3(12)	5.7(12)	3.6(12)	3.7(13)	3.8(12)	$\leq$2.9(12)	$\leq$4.7(12)	2.0(13)
IRDC18306		1.4(12)	2.1(14)	1.6(12)	$\leq$2.0(11)	8.6(11)	1.6(13)	$\leq$8.8(11)	$\leq$2.8(12)	$\leq$4.6(12)	$\leq$3.6(12)
IRDC18308	1.6(14)	6.6(12)	3.9(14)	1.7(12)	4.7(12)	1.2(12)	2.2(13)	2.6(12)	$\leq$2.6(12)	$\leq$4.3(12)	$\leq$3.5(12)
IRDC18310		6.0(12)	2.3(14)	3.1(12)	5.6(12)	1.4(12)	2.6(13)	$\leq$8.6(11)	$\leq$2.7(12)	$\leq$4.5(12)	$\leq$3.8(12)
IRDC18337		2.9(12)	2.8(14)	1.4(12)	7.0(12)	1.1(12)	1.8(13)	2.6(12)	$\leq$2.1(12)	$\leq$3.4(12)	2.2(13)
IRDC18385		1.2(12)	2.9(14)	1.2(12)	1.9(12)	1.0(12)	1.5(13)	$\leq$1.7(12)	$\leq$5.3(12)	$\leq$8.9(12)	$\leq$8.4(12)
IRDC18437	1.6(13)	$\leq$4.0(11)	2.9(14)	7.3(11)	$\leq$2.5(11)	5.9(11)	8.9(12)	$\leq$1.7(12)	$\leq$5.4(12)	$\leq$8.9(12)	$\leq$8.2(12)
IRDC18454.1		1.9(12)	3.4(14)	1.3(12)	$\leq$2.6(11)	8.8(11)	1.9(13)	$\leq$1.7(12)	$\leq$5.5(12)	$\leq$9.1(12)	$\leq$8.9(12)
IRDC18454.3		7.6(12)	7.6(14)	3.9(12)	5.5(12)	3.5(12)	3.2(13)	$\leq$1.7(12)	$\leq$5.3(12)	$\leq$8.8(12)	$\leq$8.3(12)
IRDC19175		1.2(12)	1.5(14)	6.2(11)	1.2(12)	6.4(11)	5.6(12)	$\leq$1.5(12)	$\leq$4.7(12)	$\leq$7.7(12)	$\leq$6.2(12)
IRDC20081	9.1(13)	1.2(12)	3.7(14)	6.4(11)	5.0(11)	1.4(12)	6.5(12)	$\leq$1.8(12)	$\leq$5.7(12)	$\leq$9.5(12)	4.1(13)
HMPO18089		1.0(13)	3.9(15)	1.8(13)	1.7(13)	1.7(13)	4.9(13)	1.3(14)	2.5(13)	$\leq$4.2(12)	2.5(14)
HMPO18102		3.1(13)	2.0(15)	1.5(13)	2.3(13)	1.1(13)	6.5(13)	2.1(13)	1.1(13)	$\leq$4.2(12)	4.0(13)
HMPO18151	2.8(14)	3.2(12)	3.6(15)	8.8(12)	1.0(13)	1.3(13)	3.6(13)	2.0(13)	1.0(12)	$\leq$4.1(12)	5.4(13)
HMPO18182	2.0(14)	9.6(12)	3.1(15)	1.1(13)	1.4(13)	1.4(13)	1.0(14)	5.8(13)	9.1(12)	$\leq$4.1(12)	1.2(14)
HMPO18247	1.9(14)	2.6(12)	1.3(15)	5.6(12)	1.7(12)	4.8(12)	3.7(13)	9.5(12)	$\leq$1.2(12)	$\leq$4.0(12)	1.0(13)
HMPO18264	1.4(15)	7.6(12)	4.8(15)	1.1(13)	3.5(13)	1.7(13)	1.8(14)	3.3(13)	9.6(12)	$\leq$3.9(12)	2.3(14)
HMPO18310		6.5(12)	2.3(15)	8.1(12)	6.7(12)	7.5(12)	3.1(13)	2.0(13)	2.2(12)	$\leq$3.8(12)	1.1(13)
HMPO18488		8.0(12)	2.7(15)	7.0(12)	1.9(13)	8.9(12)	4.1(13)	3.0(13)	3.7(12)	$\leq$7.8(12)	1.1(14)
HMPO18517	2.8(14)	7.3(12)	4.8(15)	7.7(12)	1.1(13)	1.7(13)	7.6(13)	2.8(13)	5.0(12)	$\leq$7.3(12)	1.4(14)
HMPO18566		1.5(13)	2.3(15)	1.1(13)	2.1(13)	1.1(13)	8.5(13)	4.3(13)	6.3(12)	$\leq$7.3(12)	1.0(14)
HMPO19217		1.1(13)	2.1(15)	7.1(12)	1.6(13)	1.2(13)	7.4(13)	3.4(13)	2.2(12)	$\leq$7.1(12)	1.7(14)
HMPO19410	2.3(14)	4.1(12)	4.2(15)	9.9(12)	4.6(12)	1.1(13)	1.0(14)	4.4(13)	1.8(12)	$\leq$6.5(12)	8.2(13)
HMPO20126	3.1(14)	5.0(12)	4.5(15)	1.5(13)	$\leq$8.7(11)	1.4(13)	1.2(14)	$\leq$5.8(12)	4.7(12)	$\leq$1.1(13)	1.5(14)
HMPO20216	9.3(13)	$\leq$1.1(12)	1.7(15)	3.3(12)	$\leq$7.9(11)	4.5(12)	1.0(13)	$\leq$5.2(12)	$\leq$2.9(12)	$\leq$9.7(12)	8.3(12)
HMPO20293	1.7(14)	3.2(12)	3.7(15)	9.5(12)	2.1(13)	8.9(12)	1.1(14)	2.2(13)	$\leq$2.3(12)	$\leq$7.8(12)	6.6(13)
HMPO22134	1.8(14)	8.9(11)	1.9(15)	1.6(12)	$\leq$4.4(11)	3.8(12)	1.7(13)	7.9(12)	$\leq$1.5(12)	$\leq$3.6(12)	3.8(13)
HMPO23033	2.8(14)	3.9(12)	4.0(15)	5.7(12)	5.6(12)	1.2(13)	4.5(13)	1.7(13)	2.4(12)	$\leq$3.6(12)	4.2(13)
HMPO23139	4.7(14)	4.3(12)	2.9(15)	2.5(12)	7.8(12)	5.3(12)	4.7(13)	2.2(13)	$\leq$1.1(12)	$\leq$3.6(12)	1.9(14)
HMPO23151	8.5(13)	$\leq$5.8(11)	1.6(15)	$\leq$4.2(11)	2.2(12)	1.7(12)	1.7(12)	1.1(13)	$\leq$1.0(12)	$\leq$3.5(12)	1.1(14)
HMPO23545	3.8(13)	$\leq$6.1(11)	9.6(14)	$\leq$4.5(11)	$\leq$4.6(11)	2.8(12)	2.3(12)	$\leq$2.0(12)	$\leq$1.1(12)	$\leq$3.7(12)	1.6(13)
HMC009.62		1.4(14)	1.7(16)	4.2(13)	1.4(14)	5.8(13)	2.4(14)	3.5(14)	1.6(14)	$\leq$2.8(13)	7.1(14)
HMC010.47		2.5(14)	1.9(16)	6.3(13)	9.4(13)	6.6(13)	3.6(14)	4.9(14)	4.8(14)	4.6(14)	9.4(14)
HMC029.96		5.2(13)	1.0(16)	3.3(13)	4.4(13)	4.1(13)	1.3(14)	3.2(14)	1.2(14)	$\leq$2.9(13)	8.1(14)
HMC031.41		1.6(14)	9.6(15)	2.7(13)	6.0(13)	1.9(13)	4.4(13)	3.8(14)	2.7(14)	5.3(14)	8.6(14)
HMC034.26		1.2(14)	1.6(16)	7.2(13)	1.0(14)	9.4(13)	9.7(13)	5.8(14)	3.7(14)	4.1(14)	1.7(15)
HMC045.47		6.3(13)	7.6(15)	2.8(13)	4.9(13)	4.0(13)	7.3(13)	7.7(13)	2.6(13)	$\leq$2.6(13)	2.6(14)
HMC075.78		3.7(13)	9.3(15)	1.5(13)	4.8(13)	2.9(13)	1.3(14)	1.2(14)	2.9(13)	$\leq$5.7(13)	8.0(14)
W3H_2O	1.3(15)	2.9(13)	1.0(16)	9.4(12)	4.1(13)	2.6(13)	2.0(13)	1.7(14)	7.6(13)	1.6(14)	1.4(15)
W3IRS5		$\leq$1.6(12)	1.1(16)	4.2(12)	1.2(13)	1.1(13)	5.0(12)	3.3(13)	$\leq$3.8(12)	$\leq$2.7(13)	1.4(15)
NGC7538B		1.9(13)	9.2(15)	8.5(12)	3.2(13)	2.0(13)	1.3(13)	8.2(13)	5.0(13)	$\leq$2.5(13)	4.0(14)
Orion-KL		6.7(14)	1.1(16)	2.0(13)	4.2(15)	2.1(13)	4.3(12)	4.3(14)	2.7(15)	1.8(15)	5.1(16)
UCH005.89		7.4(13)	3.2(16)	1.3(14)	2.4(14)	1.0(14)	5.2(14)	4.7(14)	2.0(14)	$\leq$3.1(13)	
UCH010.10	9.1(13)	$\leq$1.9(12)	$\leq$9.9(13)	7.3(12)	$\leq$7.1(11)	3.7(12)	2.1(13)	4.0(13)	$\leq$3.0(12)	$\leq$2.1(13)	$\leq$3.5(12)
UCH010.30		1.1(14)	2.1(16)	4.3(13)	7.1(13)	4.3(13)	3.2(14)	3.0(14)	9.9(13)	$\leq$2.9(13)	
UCH012.21		7.1(13)	1.1(16)	3.1(13)	4.1(13)	3.0(13)	7.3(13)	1.9(14)	6.9(13)	$\leq$2.8(13)	3.4(14)
UCH013.87	1.0(15)	2.7(13)	9.5(15)	1.2(13)	$\leq$9.2(11)	2.4(13)	9.8(13)	1.7(14)	2.0(13)	$\leq$2.9(13)	1.2(14)
UCH030.54	2.6(14)	1.1(13)	4.0(15)	3.3(12)	$\leq$9.2(11)	6.7(12)	5.7(12)	3.2(13)	$\leq$3.8(12)	$\leq$2.7(13)	4.6(13)
UCH035.20		8.6(12)	5.0(15)	1.2(13)	$\leq$8.9(11)	1.7(13)	9.2(13)	9.9(13)	2.3(13)	$\leq$2.8(13)	2.4(14)
UCH045.12	1.4(15)	$\leq$2.4(12)	7.8(15)	8.3(12)	8.5(12)	2.0(13)	8.8(12)	5.9(13)	6.2(12)	$\leq$2.9(13)	
UCH045.45	3.7(14)	$\leq$2.4(12)	4.3(15)	6.2(12)	8.5(12)	8.8(12)	5.3(13)	5.4(13)	6.1(12)	$\leq$2.6(13)	1.3(14)

Table 2.19 Continuation of Table 2.18 with additional species. Iteration 0 column densities in $a(x) = a \cdot 10^x$ cm^{-2} derived with the initially chosen typical temperatures (see Section 2.4.3 and Tables 2.3–2.6). Non-detections are indicated by $\leq$ and the upper limit derived with the 3σ rms value. A blank entry means that the molecule is detected, but rejected from the analysis due to reasons discussed in Section 2.3.2. The last column gives the lower limit for the ionization degree x(e).

Source	$C^{18}O$	OCS(1)	$H_2CO(1)$	$CH_3OH(1)$	$H_2CO(2)$	$CH_3OH(2)$	OCS(2)	$C^{33}S$	$H_{2,29}$	$H_{2,\mathrm{beam}}$	x(e)
IRDC011.1	4.3(15)	≤7.6(14)	1.2(14)	1.1(14)	7.6(12)	4.1(13)	≤3.8(15)	≤6.0(12)	6.1(22)	8.8(22)	4.3(-09)
IRDC028.1	4.5(15)	≤8.8(14)	2.2(14)	2.3(14)	1.3(13)	7.1(13)	≤3.6(15)	≤5.7(12)	5.3(22)	7.2(22)	4.9(-09)
IRDC028.2	9.1(15)	7.9(15)	1.3(15)	1.5(15)		8.3(14)	2.0(16)	≤5.5(12)	1.8(23)	2.7(23)	2.0(-09)
IRDC048.6	1.2(15)	≤6.8(14)	≤3.5(13)	≤2.0(13)	8.5(11)	≤4.3(13)	≤8.5(15)	≤1.3(13)	1.4(22)	2.2(22)	6.8(-09)
IRDC079.1	7.6(15)	≤2.1(15)	≤1.1(14)	≤6.2(13)	8.3(12)	≤3.2(13)	≤6.4(15)	≤1.0(13)	7.3(22)	9.2(22)	3.4(-09)
IRDC079.3	2.6(15)	≤1.9(15)	≤9.8(13)	≤5.5(13)	2.9(12)	≤3.2(13)	≤6.5(15)	≤1.0(13)	4.6(22)	5.2(22)	5.2(-09)
IRDC18151	7.2(15)	≤7.4(14)	6.0(14)	4.7(14)	2.7(13)	4.3(14)	≤3.7(15)	≤5.9(12)	8.1(22)	2.3(23)	4.6(-09)
IRDC18182	3.3(15)	≤7.4(14)	≤3.9(13)	≤2.2(13)	3.4(12)	≤1.8(13)	≤3.6(15)	≤5.7(12)	2.1(22)	5.3(22)	5.6(-09)
IRDC18223	5.3(15)	≤7.3(14)	1.4(14)	1.1(14)	7.8(12)	1.2(14)	≤3.7(15)	≤5.9(12)	3.2(22)	1.1(23)	1.1(-08)
IRDC18306	3.4(15)	≤7.1(14)	≤3.7(13)	≤2.1(13)	9.4(11)	≤1.8(13)	≤3.6(15)	≤5.7(12)	2.7(22)	5.6(22)	3.5(-09)
IRDC18308	3.7(15)	≤6.8(14)	1.0(14)	1.3(14)	7.0(12)	4.3(13)	≤2.7(15)	≤4.3(12)	3.8(22)	8.0(22)	3.3(-09)
IRDC18310	2.4(15)	≤7.3(14)	9.1(13)	8.6(13)	6.7(12)	≤1.9(13)	≤3.7(15)	≤5.9(12)	2.5(22)	4.9(22)	6.0(-09)
IRDC18337	2.1(15)	≤5.4(14)	2.8(14)	2.6(14)	1.4(13)	1.2(14)	≤2.7(15)	≤4.2(12)	1.2(22)	4.5(22)	9.7(-09)
IRDC18385	1.8(15)	≤1.6(15)	≤8.6(13)	≤4.9(13)	5.9(12)	≤1.8(13)	≤3.7(15)	≤5.8(12)	1.2(22)	2.8(22)	8.9(-09)
IRDC18437	3.7(15)	≤1.6(15)	≤8.4(13)	≤4.7(13)	≤1.1(12)	≤2.0(13)	≤4.0(15)	≤6.3(12)	1.6(22)	3.4(22)	3.8(-09)
IRDC18454.1	3.6(15)	≤1.7(15)	≤9.1(13)	≤5.1(13)	≤1.2(12)	≤2.0(13)	≤3.9(15)	≤6.2(12)	2.2(22)	6.5(22)	4.4(-09)
IRDC18454.3	8.6(15)	≤1.6(15)	≤8.4(13)	1.4(14)	1.1(13)	≤1.9(13)	≤3.9(15)	≤6.1(12)	3.1(22)	7.5(22)	1.1(-08)
IRDC19175	2.4(15)	≤1.2(15)	≤6.3(13)	≤3.6(13)	2.6(12)	≤4.5(13)	≤9.0(15)	≤1.4(13)	1.4(22)	3.2(22)	4.3(-09)
IRDC20081	5.8(15)	≤1.9(15)	≤9.7(13)	≤5.5(13)	5.6(12)	≤3.6(13)	≤7.1(15)	≤1.1(13)	3.1(22)	9.0(22)	4.2(-09)
HMPO18089	3.1(16)	6.3(14)	2.1(14)	5.6(14)		7.7(13)	3.7(14)	3.7(13)	4.5(22)	1.9(23)	3.5(-08)
HMPO18102	6.8(15)	1.2(14)	8.3(13)	2.2(14)	3.5(13)	5.0(13)	≤4.1(13)	≤3.9(12)	2.3(22)	5.1(22)	4.5(-08)
HMPO18151	1.7(16)	≤2.3(13)	4.7(13)	6.9(13)	2.8(13)	3.0(13)	≤4.0(13)	9.3(12)	2.3(22)	8.0(22)	5.0(-08)
HMPO18182	3.2(16)	2.0(14)	1.1(14)	3.8(14)	3.9(13)	1.0(14)	2.6(14)	2.3(13)	3.0(22)	1.2(23)	4.4(-08)
HMPO18247	1.5(16)	≤2.2(13)	1.6(13)	4.1(13)	1.0(13)	9.2(12)	7.6(13)	≤4.0(12)	1.5(22)	4.9(22)	3.1(-08)
HMPO18264	1.7(16)	1.9(14)	3.1(14)	5.8(14)	1.1(14)	1.3(14)	1.7(14)	1.4(13)	5.1(22)	1.7(23)	3.4(-08)
HMPO18310	1.6(16)	≤2.2(13)	1.2(13)	2.3(13)	1.1(13)	≤4.7(12)	≤3.9(13)	≤3.7(12)	1.6(22)	3.0(22)	4.4(-08)
HMPO18488	2.1(16)	≤3.1(13)	8.4(13)	2.7(14)	4.4(13)	6.1(13)	1.6(14)	1.1(13)	1.7(22)	4.5(22)	4.8(-08)
HMPO18517	2.2(16)	1.6(14)	1.2(14)	2.6(14)	4.8(13)	8.9(13)	1.7(14)	1.2(13)	3.8(22)	9.4(22)	4.2(-08)
HMPO18566	1.4(16)	1.9(14)	7.4(13)	2.5(14)	3.2(13)	9.1(13)	4.6(14)	3.0(13)	1.4(22)	5.1(22)	7.9(-08)
HMPO19217	1.9(16)	≤2.4(13)	1.3(14)	4.0(14)	4.6(13)	1.3(14)	2.3(14)	≤8.7(12)	2.2(22)	6.5(22)	4.9(-08)
HMPO19410	1.1(16)	7.1(13)	7.2(13)	1.4(14)	3.3(13)	3.7(13)	5.3(13)	9.2(12)	3.7(22)	7.8(22)	2.9(-08)
HMPO20126	1.2(16)	≤5.9(13)	1.7(14)	2.0(14)	5.4(13)	9.0(13)	≤4.8(13)	≤4.5(12)	3.1(22)	1.1(23)	4.3(-08)
HMPO20216	7.6(15)	≤7.4(13)	≤2.0(13)	≤3.2(13)	9.2(12)	≤8.5(12)	≤7.1(13)	≤6.6(12)	7.1(21)	2.5(22)	5.8(-08)
HMPO20293	9.5(15)	≤5.7(13)	8.8(13)	1.7(14)	3.9(13)	3.1(13)	≤7.3(13)	≤6.8(12)	2.3(22)	4.5(22)	3.9(-08)
HMPO22134	1.0(16)	≤2.0(13)	2.3(13)	≤8.6(12)	1.1(13)	≤7.8(12)	≤6.5(13)	≤6.1(12)	1.3(22)	2.7(22)	2.7(-08)
HMPO23033	1.1(16)	≤1.9(13)	6.2(13)	8.4(13)	3.6(13)	2.6(13)	≤6.8(13)	≤6.4(12)	2.2(22)	6.0(22)	5.0(-08)
HMPO23139	1.3(16)	7.6(13)	1.2(14)	1.9(14)	5.1(13)	4.1(13)	≤6.9(13)	≤6.4(12)	1.6(22)	4.8(22)	3.2(-08)
HMPO23151	1.3(16)	≤1.9(13)	3.4(13)	4.2(13)	1.5(13)	≤5.1(12)	≤4.2(13)	≤3.9(12)	1.2(22)	3.9(22)	1.2(-08)
HMPO23545	8.4(15)	≤2.1(13)	1.1(13)	≤8.8(12)	6.5(12)	≤8.2(12)	≤6.9(13)	≤6.4(12)	8.2(21)	1.6(22)	3.0(-08)
HMC009.62	1.0(17)	5.6(14)	5.6(14)	4.9(15)	3.0(14)	5.2(14)	1.4(14)	3.2(13)	3.4(22)	5.4(22)	1.6(-07)
HMC010.47	1.1(17)	2.6(15)	1.5(15)	1.4(16)		3.1(15)	2.4(15)	2.9(14)	8.1(22)	1.5(23)	7.7(-08)
HMC029.96	9.6(16)	9.3(14)	8.3(14)	4.0(15)	4.1(14)	7.8(14)	8.4(14)	1.5(14)	3.3(22)	5.5(22)	1.1(-07)
HMC031.41	8.4(16)	1.9(15)	1.1(15)	1.1(16)		2.1(15)	1.7(15)	3.0(14)	5.8(22)	1.0(23)	3.0(-08)
HMC034.26	1.5(17)	3.1(15)	2.4(15)	1.6(16)	7.5(14)	3.6(15)	2.8(15)	4.6(14)	1.5(23)	2.4(23)	5.8(-08)
HMC045.47	3.9(16)	1.1(14)	2.6(14)	1.7(15)	1.7(14)	2.9(14)	1.0(14)	1.9(13)	1.6(22)	2.3(22)	2.3(-07)
HMC075.78	5.6(16)	2.4(14)	4.4(14)	2.0(15)	2.5(14)	5.2(14)	3.0(14)	5.5(13)	2.2(22)	3.1(22)	1.2(-07)
W3H_2O	6.3(16)	9.2(14)	8.5(14)	4.6(15)	3.7(14)	2.2(15)	1.5(15)	2.8(14)	2.6(22)	3.7(22)	9.0(-08)
W3IRS5	5.6(16)	3.8(13)	2.3(14)	2.0(14)	1.3(14)	8.3(13)	1.1(14)	1.7(13)	2.1(22)	2.7(22)	4.7(-08)
NGC7538B	4.1(16)	1.4(14)	4.4(14)	1.2(15)	2.5(14)	4.5(14)	1.6(14)	5.0(13)	4.4(22)	5.8(22)	4.2(-08)
Orion-KL	1.6(17)	2.1(16)	1.2(16)	5.4(16)	4.8(15)	1.8(16)	2.3(16)	9.8(14)	4.4(23)	6.1(23)	4.2(-09)
UCH005.89	1.1(17)	9.7(14)	1.8(15)	6.1(15)	8.7(14)	1.3(15)	7.5(14)	1.8(14)	6.7(22)	1.1(23)	1.4(-07)
UCH010.10	≤2.3(14)	≤1.3(13)	≤9.7(12)	≤4.2(13)	≤1.9(12)	≤2.6(13)	≤2.6(13)	≤5.8(12)	2.0(21)	3.9(21)	1.8(-07)
UCH010.30	6.9(16)	1.5(14)	3.3(14)	2.4(15)	2.9(14)	3.6(14)	4.6(13)	4.0(13)	2.5(22)	3.4(22)	1.7(-07)
UCH012.21	6.4(16)	3.4(14)	4.8(14)	3.9(15)	2.5(14)	1.8(15)	6.4(14)	1.2(14)	3.0(22)	5.0(22)	9.4(-08)
UCH013.87	6.0(16)	≤1.8(13)	1.1(14)	5.0(14)	8.2(13)	9.5(13)	≤2.3(13)	2.6(13)	1.6(22)	2.3(22)	1.4(-07)
UCH030.54	3.5(16)	≤1.7(13)	5.3(13)	≤5.4(13)	4.1(13)	≤2.0(13)	≤2.0(13)	≤4.4(12)	6.4(21)	9.5(21)	9.3(-08)
UCH035.20	5.6(16)	≤1.7(13)	2.0(14)	2.8(14)	1.4(14)	≤1.2(13)	≤1.2(13)	2.7(13)	3.4(22)	4.3(22)	4.8(-08)
UCH045.12	2.8(16)	≤1.6(13)	1.0(14)	≤5.1(13)	7.5(13)	≤6.8(12)	≤6.8(12)	1.2(13)	2.3(22)	3.3(22)	7.8(-08)
UCH045.45	3.1(16)	≤1.6(13)	1.4(14)	3.4(14)	8.6(13)	≤6.8(12)	≤6.8(12)	2.6(13)	1.3(22)	1.7(22)	6.6(-08)

Table 2.20 Iteration 1 column densities in $a(x) = a \cdot 10^x$ cm^{-2} derived with the mean temperatures from the best-fit models of iteration 0 (see Section 2.4.3 and Tables 2.3–2.6). Non-detections are indicated by $\leq$ and the upper limit derived with the 3σ rms value. A blank entry means that the molecule is detected, A but rejected from the analysis due to reasons discussed in Section 2.3.2.

Source	HCN	HNCO	C_2H	$HN^{13}C$	SiO	$H^{13}CO^+$	N_2H^+	^{13}CS	CH_3CN	CH_3OCHO	SO
IRDC011.1		5.6(12)	5.4(14)	4.6(12)	6.8(12)	3.3(12)	2.8(13)	4.6(12)	6.7(12)	≤5.4(12)	≤3.0(12)
IRDC028.1		1.2(13)	7.1(14)	5.1(12)	1.2(13)	3.1(12)	4.0(13)	9.1(12)	≤3.7(12)	≤9.6(12)	2.1(13)
IRDC028.2		1.9(13)	1.2(15)	5.0(12)	2.2(13)	4.1(12)	6.5(13)	1.8(13)	2.2(13)	≤9.9(12)	1.3(14)
IRDC048.6	2.7(13)	1.5(12)	8.5(13)	1.0(12)	≤2.3(11)	1.3(12)	8.0(12)	≤1.1(12)	≤2.0(12)	≤5.1(12)	3.5(12)
IRDC079.1		≤5.4(11)	5.4(14)	2.2(12)	≤3.3(11)	3.2(12)	2.3(13)	4.8(12)	≤4.3(12)	≤1.1(13)	4.3(13)
IRDC079.3	7.2(13)	2.0(12)	6.9(14)	3.3(12)	≤3.2(11)	3.0(12)	2.5(13)	≤2.2(12)	≤4.1(12)	≤1.1(13)	≤7.4(12)
IRDC18151	1.6(14)	3.8(12)	1.9(15)	3.6(12)	5.4(12)	4.6(12)	4.9(13)	4.9(12)	≤2.1(12)	≤5.4(12)	4.4(13)
IRDC18182		2.2(12)	4.8(14)	2.1(12)	≤2.5(11)	1.5(12)	1.6(13)	≤1.1(12)	≤2.1(12)	≤5.3(12)	≤2.9(12)
IRDC18223	1.2(14)	3.9(12)	8.2(14)	7.9(12)	7.1(12)	4.5(12)	3.7(13)	4.6(12)	≤2.0(12)	≤5.3(12)	1.5(13)
IRDC18306		1.7(12)	2.7(14)	2.0(12)	≤2.4(11)	1.1(12)	1.6(13)	≤1.1(12)	≤2.0(12)	≤5.2(12)	≤2.8(12)
IRDC18308	2.0(14)	8.4(12)	5.0(14)	2.2(12)	5.8(12)	1.5(12)	2.2(13)	3.1(12)	≤1.9(12)	≤4.8(12)	≤2.7(12)
IRDC18310		7.6(12)	2.9(14)	4.0(12)	6.9(12)	1.8(12)	3.3(13)	≤1.0(12)	≤2.0(12)	≤5.1(12)	≤2.9(12)
IRDC18337		3.7(12)	3.5(14)	1.8(12)	8.6(12)	1.5(12)	1.8(13)	3.2(12)	≤1.5(12)	≤3.8(12)	1.7(13)
IRDC18385		1.6(12)	3.7(14)	1.5(12)	2.3(12)	1.3(12)	1.5(13)	≤2.0(12)	≤3.8(12)	≤9.9(12)	≤6.6(12)
IRDC18437	2.0(13)	≤5.0(11)	3.7(14)	9.3(11)	≤3.1(11)	7.6(11)	1.1(13)	≤2.1(12)	≤3.8(12)	≤9.9(12)	≤6.4(12)
IRDC18454.1		2.4(12)	4.3(14)	1.6(12)	≤3.1(11)	1.1(12)	1.9(13)	≤2.1(12)	≤3.9(12)	≤1.0(13)	≤6.9(12)
IRDC18454.3		9.6(12)	9.7(14)	4.9(12)	6.7(12)	4.4(12)	3.2(13)	≤2.0(12)	≤3.8(12)	≤9.8(12)	≤6.4(12)
IRDC19175		1.5(12)	2.0(14)	7.9(11)	1.5(12)	8.2(11)	5.6(12)	≤1.8(12)	≤3.3(12)	≤8.6(12)	≤4.8(12)
IRDC20081	1.2(14)	1.6(12)	4.7(14)	8.1(11)	6.1(11)	1.8(12)	6.5(12)	≤2.2(12)	≤4.1(12)	≤1.1(13)	3.2(13)
HMPO18089		8.5(12)	2.6(15)	1.2(13)	1.1(13)	1.1(13)	4.9(13)	8.2(13)	3.6(13)	≤6.4(12)	2.2(14)
HMPO18102		2.5(13)	1.4(15)	9.7(12)	1.5(13)	6.8(12)	6.5(13)	1.4(13)	1.6(13)	≤6.4(12)	3.6(13)
HMPO18151	1.8(14)	2.6(12)	2.4(15)	5.6(12)	6.8(12)	8.0(12)	3.6(13)	1.3(13)	1.5(12)	≤6.3(12)	4.8(13)
HMPO18182	1.3(14)	7.8(12)	2.1(15)	7.1(12)	9.2(12)	8.6(12)	6.4(13)	3.8(13)	1.3(13)	≤6.3(12)	1.1(14)
HMPO18247	1.2(14)	2.1(12)	8.7(14)	3.5(12)	1.1(12)	3.0(12)	3.7(13)	6.2(12)	≤1.7(12)	≤6.2(12)	9.4(12)
HMPO18264	8.6(14)	6.1(12)	3.2(15)	7.0(12)	2.2(13)	1.1(13)	1.1(14)	2.2(13)	1.4(13)	≤6.0(12)	2.1(14)
HMPO18310		5.2(12)	1.5(15)	5.1(12)	4.4(12)	4.7(12)	3.1(13)	1.3(13)	3.2(12)	≤5.9(12)	9.9(12)
HMPO18488		6.5(12)	1.8(15)	4.4(12)	1.2(13)	5.6(12)	4.1(13)	1.9(13)	5.3(12)	≤1.2(13)	1.0(14)
HMPO18517	1.8(14)	5.9(12)	3.2(15)	4.9(12)	7.3(12)	1.1(13)	7.6(13)	1.8(13)	7.2(12)	≤1.1(13)	1.3(14)
HMPO18566		1.2(13)	1.5(15)	7.2(12)	1.4(13)	7.1(12)	5.5(13)	2.8(13)	9.0(12)	≤1.1(13)	9.0(13)
HMPO19217		8.9(12)	1.4(15)	4.5(12)	1.0(13)	7.3(12)	4.7(13)	2.2(13)	3.2(12)	≤1.1(13)	1.5(14)
HMPO19410	1.4(14)	3.3(12)	2.8(15)	6.3(12)	2.9(12)	6.8(12)	1.0(14)	2.9(13)	2.6(12)	≤9.9(12)	7.3(13)
HMPO20126	1.9(14)	4.0(12)	3.0(15)	9.4(12)	≤5.7(11)	8.5(12)	7.6(13)	≤3.7(12)	6.8(12)	≤1.7(13)	1.3(14)
HMPO20216	5.9(13)	≤8.5(11)	1.1(15)	2.1(12)	≤5.1(11)	2.8(12)	1.0(13)	≤3.4(12)	≤4.2(12)	≤1.5(13)	7.5(12)
HMPO20293	1.1(14)	2.5(12)	2.4(15)	6.0(12)	1.4(13)	5.6(12)	1.1(14)	1.4(13)	≤3.4(12)	≤1.2(13)	5.9(13)
HMPO22134	1.2(14)	7.2(11)	1.3(15)	1.0(12)	≤2.8(11)	2.4(12)	1.1(13)	5.1(12)	≤2.2(12)	≤5.6(12)	3.4(13)
HMPO23033	1.8(14)	3.1(12)	2.7(15)	3.6(12)	3.6(12)	7.3(12)	4.5(13)	1.1(13)	3.5(12)	≤5.5(12)	3.8(13)
HMPO23139	3.0(14)	3.5(12)	1.9(15)	1.6(12)	5.1(12)	3.3(12)	3.0(13)	1.4(13)	≤1.6(12)	≤5.5(12)	1.7(14)
HMPO23151	5.4(13)	≤4.7(11)	1.1(15)	≤2.6(11)	1.4(12)	1.1(12)	1.1(12)	6.8(12)	≤1.5(12)	≤5.4(12)	1.0(14)
HMPO23545	2.4(13)	≤4.9(11)	6.4(14)	≤2.9(11)	≤3.0(11)	1.7(12)	2.3(12)	≤1.3(12)	≤1.6(12)	≤5.7(12)	1.4(13)
HMC009.62		3.8(13)	7.0(15)	1.8(13)	6.1(13)	2.5(13)	1.0(14)	1.6(14)	7.0(13)	≤7.6(12)	4.3(14)
HMC010.47		6.8(13)	7.9(15)	2.7(13)	4.2(13)	2.9(13)	1.6(14)	2.2(14)	2.1(14)	1.2(14)	5.7(14)
HMC029.96		1.4(13)	4.3(15)	1.4(13)	1.9(13)	1.8(13)	5.9(13)	1.4(14)	5.2(13)	≤7.7(12)	4.9(14)
HMC031.41		4.4(13)	4.0(15)	1.2(13)	2.7(13)	8.2(12)	4.4(13)	1.7(14)	1.2(14)	1.4(14)	5.2(14)
HMC034.26		3.3(13)	6.8(15)	3.1(13)	4.4(13)	4.1(13)	9.7(13)	2.6(14)	1.6(14)	1.1(14)	1.1(15)
HMC045.47		1.7(13)	3.2(15)	1.2(13)	2.2(13)	1.7(13)	7.3(13)	3.4(13)	1.1(13)	≤7.0(12)	1.6(14)
HMC075.78		1.0(13)	3.9(15)	6.5(12)	2.1(13)	1.3(13)	5.5(13)	5.6(13)	1.3(13)	≤1.5(13)	4.9(14)
W3H2O	5.5(14)	8.0(12)	4.3(15)	4.1(12)	1.8(13)	1.1(13)	2.0(13)	7.6(13)	3.3(13)	4.3(13)	8.3(14)
W3IRS5		≤4.5(11)	4.6(15)	1.8(12)	5.5(12)	4.8(12)	2.2(12)	1.5(13)	≤1.6(12)	≤7.1(12)	8.7(14)
NGC7538B		5.3(12)	3.9(15)	3.7(12)	1.4(13)	8.8(12)	1.3(13)	3.7(13)	2.1(13)	≤6.7(12)	2.4(14)
Orion-KL		1.9(14)	4.8(15)	8.8(12)	1.9(15)	8.9(12)	4.3(12)	1.9(14)	1.2(15)	4.8(14)	3.1(16)
UCH005.89		1.9(13)	1.2(16)	5.0(13)	9.7(13)	4.0(13)	2.1(14)	1.9(14)	8.5(13)	≤7.7(12)	
UCH010.10	3.6(13)	≤4.8(11)	≤3.8(13)	2.9(12)	≤2.9(11)	1.4(12)	2.1(13)	1.6(13)	≤1.3(12)	≤5.2(12)	≤2.1(12)
UCH010.30		2.7(13)	8.0(15)	1.7(13)	2.9(13)	1.7(13)	1.3(14)	1.2(14)	4.2(13)	≤7.1(12)	
UCH012.21		1.8(13)	4.4(15)	1.2(13)	1.7(13)	1.2(13)	7.3(13)	7.6(13)	3.0(13)	≤7.1(12)	2.0(14)
UCH013.87	4.1(14)	6.8(12)	3.6(15)	4.9(12)	≤3.7(11)	9.4(12)	3.9(13)	6.8(13)	8.6(12)	≤7.3(12)	7.4(13)
UCH030.54	1.0(14)	2.7(12)	1.5(15)	1.3(12)	≤3.7(11)	2.6(12)	5.8(12)	1.3(13)	≤1.6(12)	≤6.7(12)	2.7(13)
UCH035.20		2.2(12)	1.9(15)	4.7(12)	≤3.6(11)	6.7(12)	3.7(13)	4.0(13)	9.6(12)	≤6.9(12)	1.4(14)
UCH045.12	5.6(14)	≤6.1(11)	3.0(15)	3.2(12)	3.4(12)	7.8(12)	8.7(12)	2.4(13)	2.6(12)	≤7.1(12)	
UCH045.45	1.4(14)	≤6.0(11)	1.6(15)	2.4(12)	3.4(12)	3.5(12)	2.1(13)	2.2(13)	2.6(12)	≤6.6(12)	8.0(13)

Table 2.21 Continuation of Table 2.20 with additional species. Iteration 1 column densities in $a(x) = a \cdot 10^x$ cm^{-2} derived with the mean temperatures from the best-fit models of iteration 0 (see Section 2.4.3 and Tables 2.3–2.6). Non-detections are indicated by $\leq$ and the upper limit derived with the 3σ rms value. A blank entry means that the molecule is detected, but rejected from the analysis due to reasons discussed in Section 2.3.2. The last column gives the lower limit for the ionization degree x(e).

Source	C^{18}O	OCS(1)	H$_2$CO(1)	CH$_3$OH(1)	H$_2$CO(2)	CH$_3$OH(2)	OCS(2)	C^{33}S	H$_{2,29}$	H$_{2,\mathrm{beam}}$	x(e)
IRDC011.1	4.4(15)	≤1.6(14)	5.5(13)	9.1(13)	8.5(12)	2.7(13)	≤5.2(14)	≤4.3(12)	3.7(22)	5.3(22)	8.9(-09)
IRDC028.1	4.6(15)	≤1.9(14)	1.0(14)	2.0(14)	1.4(13)	4.8(13)	≤5.0(14)	≤4.1(12)	3.2(22)	4.3(22)	1.0(-08)
IRDC028.2	9.3(15)	1.7(15)	5.8(14)	1.3(15)		5.6(14)	2.8(15)	≤3.9(12)	1.1(23)	1.6(23)	4.1(-09)
IRDC048.6	1.2(15)	≤1.4(14)	≤1.6(13)	≤1.7(13)	9.5(11)	≤2.9(13)	≤1.2(15)	≤9.6(12)	8.6(21)	1.3(22)	1.4(-08)
IRDC079.1	7.7(15)	≤4.4(14)	≤5.0(13)	≤5.3(13)	9.3(12)	≤2.2(13)	≤8.9(14)	≤7.3(12)	4.3(22)	5.5(22)	7.1(-09)
IRDC079.3	2.6(15)	≤4.0(14)	≤4.5(13)	≤4.7(13)	3.2(12)	≤2.2(13)	≤8.9(14)	≤7.3(12)	2.7(22)	3.1(22)	1.1(-08)
IRDC18151	7.3(15)	≤1.6(14)	2.7(14)	4.0(14)	3.0(13)	2.9(14)	≤5.1(14)	≤4.2(12)	5.1(22)	1.4(23)	9.0(-09)
IRDC18182	3.3(15)	≤1.6(14)	≤1.8(13)	≤1.9(13)	3.8(12)	≤1.2(13)	≤5.0(14)	≤4.1(12)	1.3(22)	3.4(22)	1.1(-08)
IRDC18223	5.4(15)	≤1.6(14)	6.2(13)	9.0(13)	8.7(12)	8.2(13)	≤5.1(14)	≤4.2(12)	2.0(22)	6.7(22)	2.2(-08)
IRDC18306	3.5(15)	≤1.5(14)	≤1.7(13)	≤1.8(13)	1.0(12)	≤1.2(13)	≤5.0(14)	≤4.1(12)	1.7(22)	3.6(22)	6.8(-09)
IRDC18308	3.8(15)	≤1.5(14)	4.7(13)	1.1(14)	7.8(12)	2.9(13)	≤3.7(14)	≤3.0(12)	2.4(22)	5.1(22)	6.3(-09)
IRDC18310	2.4(15)	≤1.6(14)	4.2(13)	7.3(13)	7.4(12)	≤1.3(13)	≤5.2(14)	≤4.2(12)	1.6(22)	3.1(22)	1.2(-08)
IRDC18337	2.2(15)	≤1.2(14)	1.3(14)	2.2(14)	1.5(13)	8.1(13)	≤3.7(14)	≤3.0(12)	7.8(21)	2.9(22)	1.9(-08)
IRDC18385	1.8(15)	≤3.5(14)	≤4.0(13)	≤4.1(13)	6.6(12)	≤1.2(13)	≤5.1(14)	≤4.2(12)	7.7(21)	1.8(22)	1.7(-08)
IRDC18437	3.8(15)	≤3.4(14)	≤3.8(13)	≤4.0(13)	≤1.2(12)	≤1.3(13)	≤5.5(14)	≤4.5(12)	1.0(22)	2.1(22)	7.6(-09)
IRDC18454.1	3.7(15)	≤3.7(14)	≤4.2(13)	≤4.3(13)	≤1.3(12)	≤1.3(13)	≤5.4(14)	≤4.4(12)	1.4(22)	4.1(22)	8.6(-09)
IRDC18454.3	8.7(15)	≤3.4(14)	≤3.9(13)	1.1(14)	1.2(13)	≤1.3(13)	≤5.4(14)	≤4.4(12)	2.0(22)	4.8(22)	2.1(-08)
IRDC19175	2.4(15)	≤2.6(14)	≤2.9(13)	≤3.0(13)	2.9(12)	≤3.1(13)	≤1.2(15)	≤1.0(13)	9.1(21)	2.0(22)	8.6(-09)
IRDC20081	5.9(15)	≤3.9(14)	≤4.5(13)	≤4.7(13)	6.3(12)	≤2.4(13)	≤9.8(14)	≤8.0(12)	2.0(22)	5.7(22)	8.2(-09)
HMPO18089	2.3(16)	1.5(15)	3.7(14)	9.9(14)		1.6(14)	1.2(15)	3.6(13)	8.2(22)	3.6(23)	1.2(-08)
HMPO18102	5.0(15)	2.8(14)	1.4(14)	3.9(14)	3.2(13)	1.0(14)	≤1.3(14)	≤3.7(12)	4.2(22)	9.5(22)	1.6(-08)
HMPO18151	1.2(16)	≤5.4(13)	8.2(13)	1.2(14)	2.5(13)	6.4(13)	≤1.3(14)	8.9(12)	4.3(22)	1.5(23)	1.7(-08)
HMPO18182	2.4(16)	4.8(14)	2.0(14)	6.7(14)	3.5(13)	2.2(14)	8.4(14)	2.2(13)	5.5(22)	2.2(23)	1.5(-08)
HMPO18247	1.1(16)	≤5.3(13)	2.8(13)	7.2(13)	9.0(12)	1.9(13)	2.5(14)	≤3.9(12)	2.8(22)	9.1(22)	1.1(-08)
HMPO18264	1.3(16)	4.5(14)	5.3(14)	1.0(15)	9.6(13)	2.6(14)	5.5(14)	1.3(13)	9.4(22)	3.2(23)	1.2(-08)
HMPO18310	1.2(16)	≤5.2(13)	2.1(13)	4.1(13)	9.8(12)	≤9.8(12)	≤1.3(14)	≤3.5(12)	2.9(22)	5.5(22)	1.5(-08)
HMPO18488	1.5(16)	≤7.3(13)	1.5(14)	4.8(14)	3.9(13)	1.3(14)	5.4(14)	1.1(13)	3.2(22)	8.4(22)	1.7(-08)
HMPO18517	1.6(16)	3.7(14)	2.0(14)	4.6(14)	4.4(13)	1.9(14)	5.5(14)	1.1(13)	7.0(22)	1.7(23)	1.5(-08)
HMPO18566	1.0(16)	4.6(14)	1.3(14)	4.4(14)	2.9(13)	1.9(14)	1.5(15)	2.9(13)	2.5(22)	9.4(22)	2.7(-08)
HMPO19217	1.4(16)	≤5.8(13)	2.3(14)	7.1(14)	4.1(13)	2.7(14)	7.5(14)	≤8.4(12)	4.2(22)	1.2(23)	1.7(-08)
HMPO19410	8.3(15)	1.7(14)	1.3(14)	2.4(14)	3.0(13)	7.7(13)	1.7(14)	8.9(12)	6.8(22)	1.4(23)	1.0(-08)
HMPO20126	8.8(15)	≤1.4(14)	2.9(14)	3.6(14)	4.8(13)	1.9(14)	≤1.6(14)	≤4.3(12)	5.7(22)	2.0(23)	1.5(-08)
HMPO20216	5.7(15)	≤1.8(14)	≤3.5(13)	≤5.6(13)	8.3(12)	≤1.8(13)	≤2.3(14)	≤6.4(12)	1.3(22)	4.6(22)	2.0(-08)
HMPO20293	7.1(15)	≤1.4(14)	1.5(14)	3.0(14)	3.5(13)	6.5(13)	≤2.4(14)	≤6.6(12)	4.3(22)	8.3(22)	1.4(-08)
HMPO22134	7.8(15)	≤4.7(13)	4.0(13)	≤1.5(13)	1.0(13)	≤1.6(13)	≤2.1(14)	≤5.8(12)	2.4(22)	5.1(22)	9.3(-09)
HMPO23033	8.1(15)	≤4.5(13)	1.1(14)	1.5(14)	3.2(13)	5.5(13)	≤2.2(14)	≤6.2(12)	4.0(22)	1.1(23)	1.7(-08)
HMPO23139	9.4(15)	1.8(14)	2.1(14)	3.4(14)	4.6(13)	8.6(13)	≤2.2(14)	≤6.2(12)	3.0(22)	8.8(22)	1.1(-08)
HMPO23151	9.7(15)	≤4.6(13)	6.0(13)	7.4(13)	1.4(13)	≤1.1(13)	≤1.4(14)	≤3.8(12)	2.3(22)	7.2(22)	4.2(-09)
HMPO23545	6.3(15)	≤4.9(13)	1.8(13)	≤1.6(13)	5.9(12)	≤1.7(13)	≤2.2(14)	≤6.2(12)	1.5(22)	3.1(22)	1.0(-08)
HMC009.62	5.2(16)	9.9(14)	3.7(14)	1.7(15)	9.9(13)	2.1(14)	3.5(14)	2.2(13)	9.5(22)	1.5(23)	2.4(-08)
HMC010.47	5.7(16)	4.7(15)	1.0(15)	4.7(15)		1.2(15)	6.1(15)	2.0(14)	2.3(23)	4.3(23)	1.2(-08)
HMC029.96	5.0(16)	1.7(15)	5.5(14)	1.3(15)	1.3(14)	3.1(14)	2.1(15)	1.0(14)	9.4(22)	1.6(23)	1.7(-08)
HMC031.41	4.3(16)	3.4(15)	7.5(14)	3.7(15)		8.7(14)	4.2(15)	2.1(14)	1.6(23)	2.8(23)	4.8(-09)
HMC034.26	8.0(16)	5.5(15)	1.6(15)	5.4(15)	2.5(14)	1.5(15)	7.1(15)	3.1(14)	4.1(23)	6.7(23)	9.0(-09)
HMC045.47	2.0(16)	2.0(14)	1.7(14)	5.8(14)	5.5(13)	1.2(14)	2.6(14)	1.3(13)	4.5(22)	6.5(22)	3.6(-08)
HMC075.78	2.9(16)	4.2(14)	2.9(14)	6.7(14)	8.1(13)	2.1(14)	7.5(14)	3.7(13)	6.3(22)	8.7(22)	1.8(-08)
W3H2O	3.2(16)	1.6(15)	5.6(14)	1.6(15)	1.2(14)	8.7(14)	3.7(15)	1.9(14)	7.4(22)	1.1(23)	1.4(-08)
W3IRS5	2.9(16)	6.7(13)	1.5(14)	6.8(13)	4.1(13)	3.4(13)	2.6(14)	1.1(13)	6.0(22)	7.6(22)	7.1(-09)
NGC7538B	2.1(16)	2.4(14)	2.9(14)	4.1(14)	8.1(13)	1.8(14)	4.1(14)	3.4(13)	1.2(23)	1.7(23)	6.4(-09)
Orion-KL	8.1(16)	3.7(16)	8.2(15)	1.8(16)	1.6(15)	7.3(15)	5.8(16)	6.7(14)	1.3(24)	1.7(24)	6.4(-10)
UCH005.89	5.5(16)	2.1(15)	1.3(15)	2.0(15)	2.7(14)	5.3(14)	2.4(15)	1.2(14)	2.2(23)	3.6(23)	1.8(-08)
UCH010.10	≤1.1(14)	≤2.8(13)	≤6.9(12)	≤1.4(13)	≤5.8(11)	≤1.1(13)	≤8.3(13)	≤3.9(12)	6.4(21)	1.3(22)	2.3(-08)
UCH010.30	3.3(16)	3.1(14)	2.3(14)	7.8(14)	8.8(13)	1.5(14)	1.5(14)	2.7(13)	8.1(22)	1.1(23)	2.0(-08)
UCH012.21	3.1(16)	7.2(14)	3.4(14)	1.3(15)	7.6(13)	7.3(14)	2.0(15)	8.4(13)	9.6(22)	1.6(23)	1.2(-08)
UCH013.87	2.9(16)	≤3.8(13)	7.8(13)	1.6(14)	2.5(13)	3.9(13)	≤7.3(13)	1.7(13)	5.3(22)	7.6(22)	1.7(-08)
UCH030.54	1.7(16)	≤3.6(13)	3.7(13)	≤1.8(13)	1.3(13)	≤8.0(12)	≤6.3(13)	≤3.0(12)	2.1(22)	3.1(22)	1.1(-08)
UCH035.20	2.7(16)	≤3.6(13)	1.4(14)	9.2(13)	4.1(13)	≤5.0(12)	≤3.9(13)	1.8(13)	1.1(23)	1.4(23)	5.7(-09)
UCH045.12	1.4(16)	≤3.4(13)	7.4(13)	≤1.7(13)	2.3(13)	≤2.8(12)	≤2.2(13)	8.1(12)	7.4(22)	1.1(23)	9.6(-09)
UCH045.45	1.5(16)	≤3.4(13)	9.9(13)	1.1(14)	2.6(13)	≤2.8(12)	≤2.2(13)	1.7(13)	4.2(22)	5.6(22)	7.9(-09)

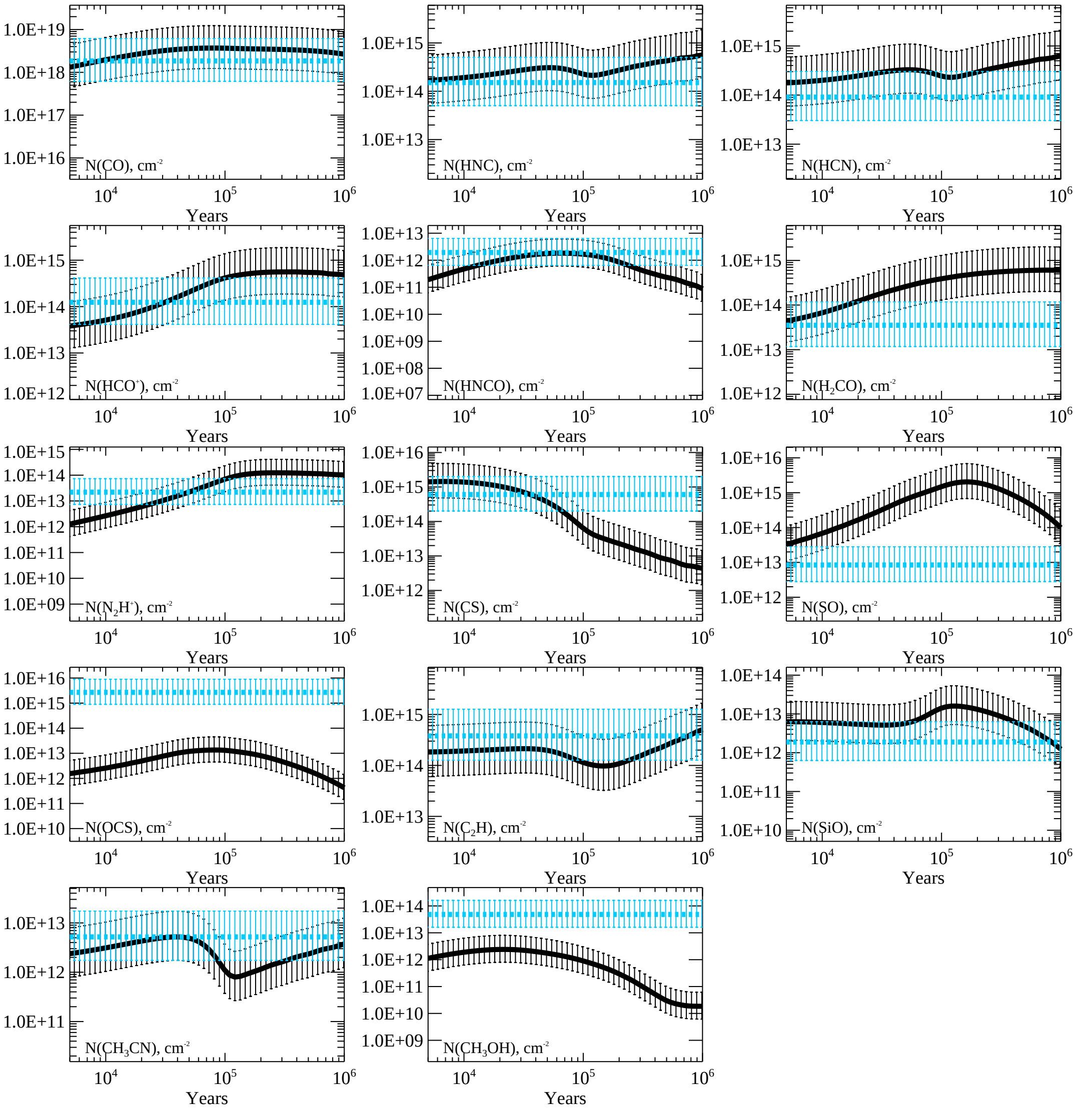

Figure 2.8 Modeled and observed median column densities in cm^{-2} in the IRDC stage. The modeled values are shown in black and the observed values in blue. The error bars are given by the vertical marks. The molecule name is labeled in the plot.

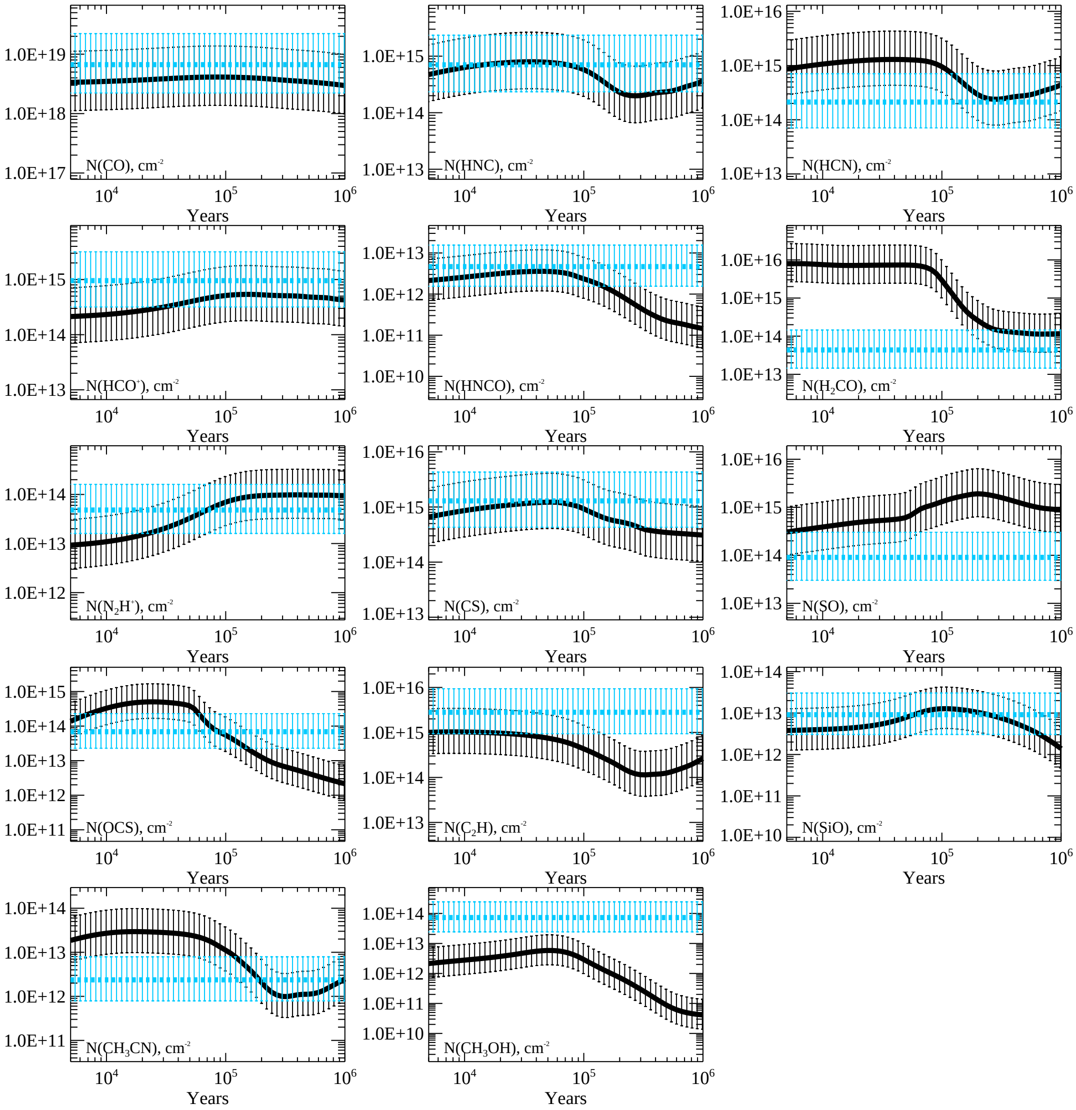

Figure 2.9 Modeled and observed median column densities in cm^{-2} in the HMPO stage. The modeled values are shown in black and the observed values in blue. The error bars are given by the vertical marks. The molecule name is labeled in the plot.

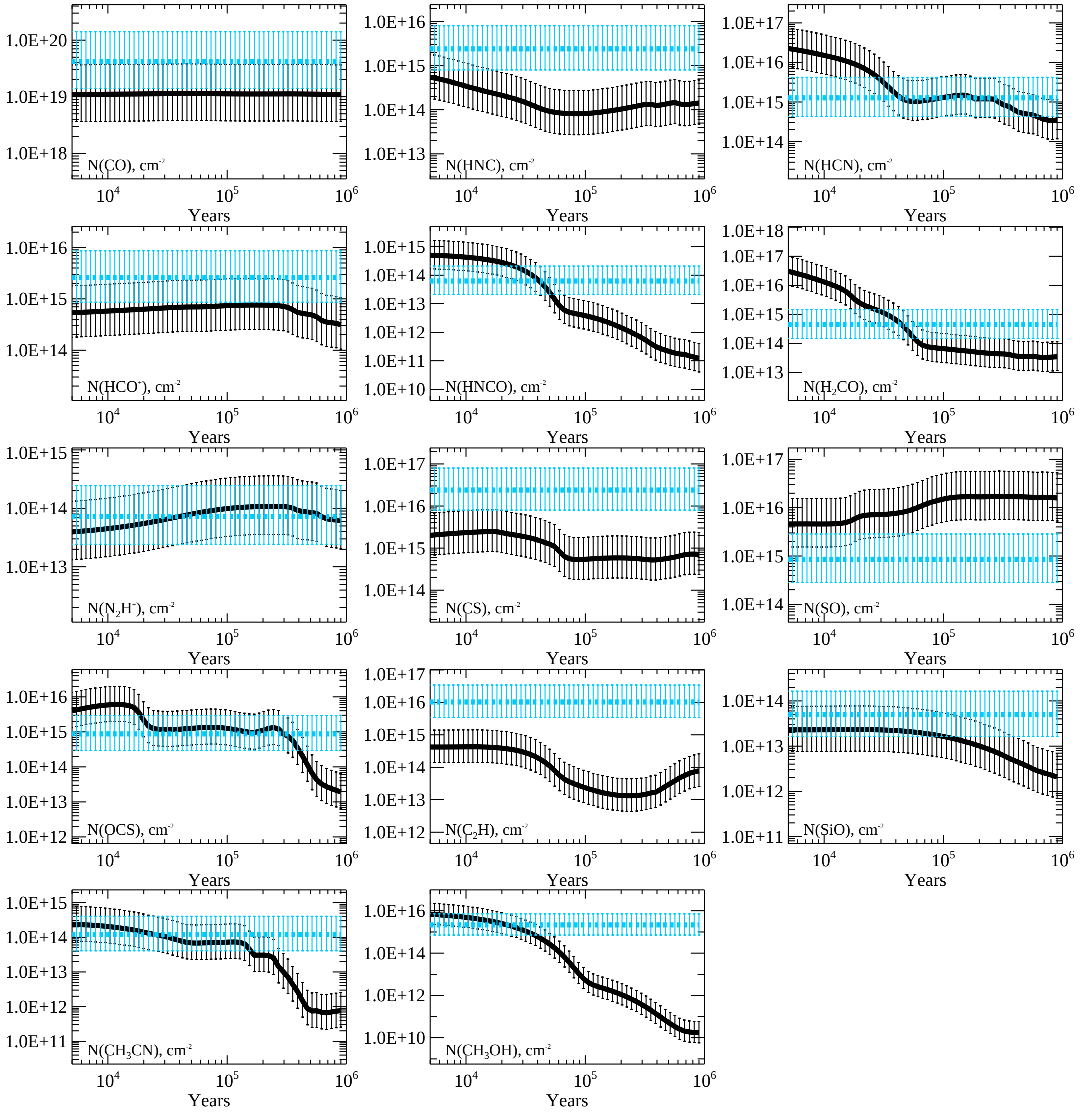

Figure 2.10 Modeled and observed median column densities in cm^{-2} in the HMC stage. The modeled values are shown in black and the observed values in blue. The error bars are given by the vertical marks. The molecule name is labeled in the plot.

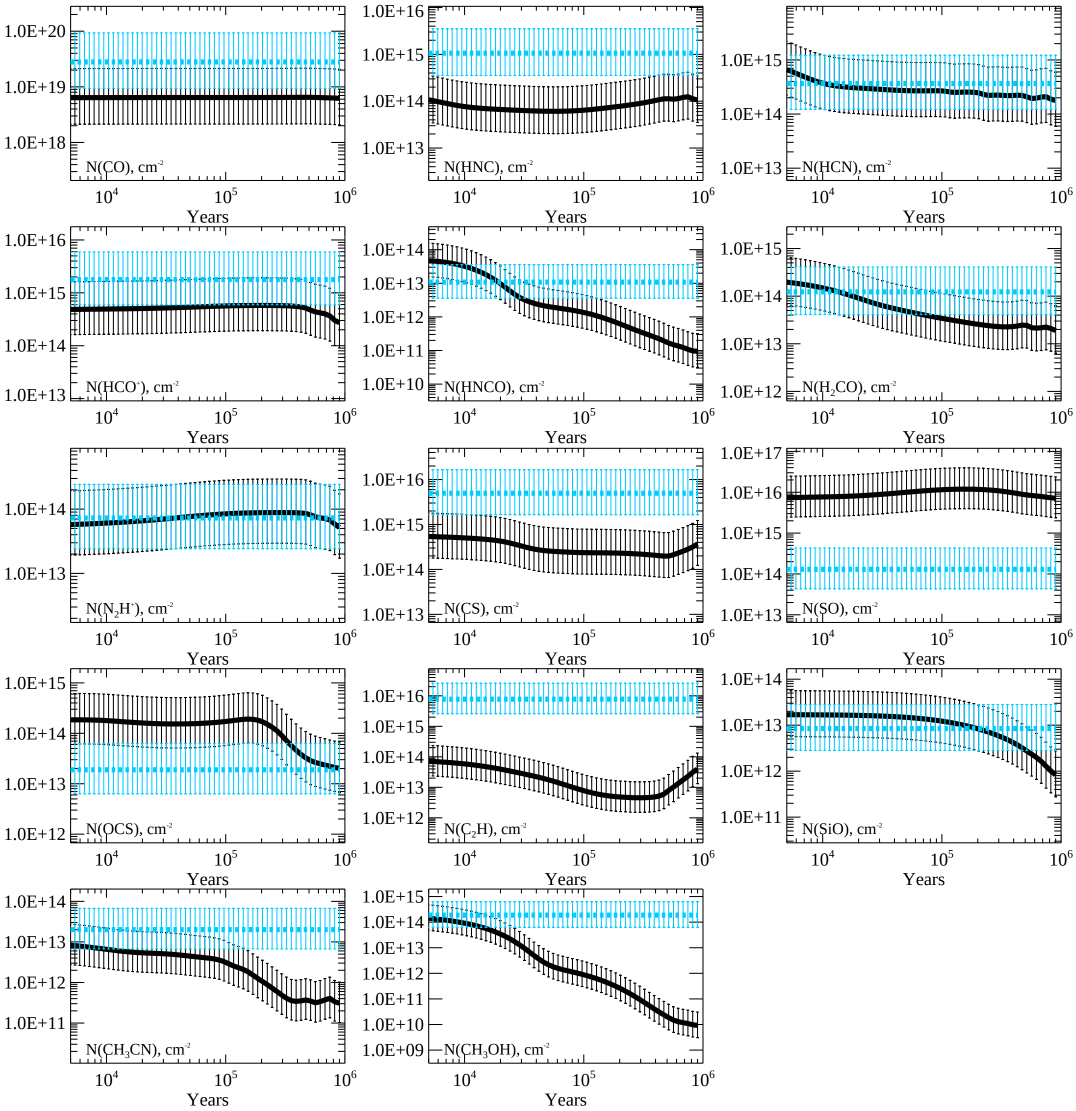

Figure 2.11 Modeled and observed median column densities in cm^{-2} in the UCHII stage. The modeled values are shown in black and the observed values in blue. The error bars are given by the vertical marks. The molecule name is labeled in the plot.

Chapter 3

Chemical evolution in the early phases of massive star formation: Deuteration

This Chapter has been submitted to A&A. (Gerner, Shirley, Beuther, Semenov, Linz, Albertsson and Henning, subm.)[1]

In the previous chapter we studied the chemical characterization of the single stages of the assumed high-mass star formation sequence and described the comparison of the observational findings with best-fit models. In that part the characterization was only based on non-deuterated molecules. However, due to its special features, deuterated chemistry (chemistry involving deuterium atoms) is believed to be a useful tool in order to differentiate the varying conditions in the different evolutionary stages. Thus, in a next step, we included observations of deuterated molecules and incorporated them in the analysis. This chapter includes a description of the observations and its results as well as a comparison with two different models.

3.1 Introduction

The chemical evolution in high-mass star formation is still poorly understood and a field of intense investigations. The question of which molecules are to be used to distinguish between different evolutionary stages is of great interest. Those so called chemical clocks could be used to derive lifetimes of the different stages and help to infer the absolute ages of those objects. In addition, studying deuterium chemistry is also very useful to constrain physical parameters as for example the ionization fraction, temperature and density (e.g., Crapsi et al. 2005; Chen et al. 2011). In particular, deuterated molecules are very prominent candidates for probing this evolutionary sequence, since their chemistry depends highly on the temperature and the thermal

---

[1] The model used in this publication and Section 3.6.4 as well as Figures 3.9, 3.10, 3.11, 3.12, 3.13, 3.14, 3.15, 3.16, 3.17, 3.18, 3.19, 3.20, 3.21, 3.22 were provided by Dmitry Semenov. All other parts were done and written by me.

history of an object (Caselli & Ceccarelli 2012; Albertsson et al. 2013). The deuteration fraction (the ratio between the column density of a deuterated molecule and its non-deuterated counterpart) is therefore an important parameter in order to study these evolutionary effects.

Theoretical and observational deuteration studies of low-mass star-forming regions revealed a large increase by several orders of magnitude in the deuteration fraction of starless cores with respect to the cosmic atomic D/H ratio of $\sim 10^{-5}$ (Linsky 2003; Oliveira et al. 2003) and discussed possible trends with the evolutionary state of the star-forming region (e.g., Caselli et al. 2002a; Crapsi et al. 2005; Bourke et al. 2012; Friesen et al. 2013). Correlations of the deuteration fraction were seen, e.g., with the dust temperature and the level of CO depletion (Emprechtinger et al. 2009) or with the density (Daniel et al. 2007). Whether the deuterium chemistry during high-mass star formation behaves similar to that of low-mass cores is poorly constrained by observations so far. The current studies mostly target single deuterated species instead of a larger set of molecules, or are focused on a limited number of sources. Miettinen et al. (2011) found deuteration fractions in a sample of seven massive clumps associated with IRDCs that are lower than the values found in low-mass starless cores. Early studies of very young IRDCs by Pillai et al. (2007) and more evolved HMPOs by Fontani et al. (2006) indicated a trend of higher deuteration fractions for the younger, cooler sources. A recent attempt to systematically study a larger sample of different evolutionary stages by Fontani et al. (2011) revealed that the N_2D^+/N_2H^+ column density ratio is an indicator for the evolutionary stage in high-mass star formation. Chen et al. (2011) observed several dense cores covering different evolutionary stages in three massive star-forming clouds and studied the deuteration fraction of N_2H^+ and the role of CO depletion in this context. They found a clear trend of decreasing deuteration fraction with increasing gas temperature tracing different evolutionary stages. They also found an increasing trend of the deuteration fraction with the CO depletion factor, which is similarly seen in low-mass protostellar cores.

In order to study the deuteration in high-mass star forming regions in an evolutionary sense, we divide the high-mass star formation sequence into different stages (see also Gerner et al. 2014, hereafter Paper I). Beuther et al. (2007a); Zinnecker & Yorke (2007); Tan et al. (2014) divided the evolutionary sequence into different phases based on their physical conditions. We describe the evolutionary picture from an observationally point of view and distinguish between 4 observationally motivated stages based on the underlying physical sequence. First, our picture starts with an initially starless infrared dark cloud phase (IRDC). At this point these objects are close to isothermal and consist of cold and dense gas and dust. In this approach we do not consider a long living pre-IRDC phase, which is proposed in theoretical works (e.g., Narayanan et al. 2008; Heitsch et al. 2008) and also supported by observations (e.g., Barnes et al. 2011). This phase should be less dense and in our model we define the year zero of our evolutionary sequence when the densities start to be higher than 10^4 cm^{-3}. According to our modeling, these densities are enough to transform almost all atomic gas within several thousand years into molecular gas and the cloud reaches the molecular gas IRDC phase. While starless IRDCs only emit in the (sub-)millimeter regime, places of beginning star-formation start to show up as point sources at μm-wavelengths. Eventually, the overdensities within the IRDC begin to collapse and form one or several accreting protostars with $> 8\,M_\odot$ in the next phase, that is a high-mass protostellar object (HMPO). The internal sources of HMPOs emit at mid-infrared wavelengths and their radiation starts to heat up the environment, leading to non-isothermal temperature profiles. The higher temperatures boost the molecular complexity leading to the hot molecular core phase (HMC). This phase is from a physical point a sub-group of the HMPO phase, but clearly distinguishes from a chemical point of view, driven by the higher temperatures that liberate molecules from molecular-rich ices and increase the molecular complexity of the source. Finally, the UV-radiation of the central star(s) ionizes the ambient gas and create an ultra-compact HII region (UCHII). That is the last stage considered in our evolutionary picture. These objects presumably have stopped accreting and complex molecules seen in the HMC phase are not longer detectable. It is possible that overlaps occur between these stages, leading to HMCs associated with UCHII regions and even still accreting protostars within UCHII regions. High-mass star-forming sites are complex objects. In order to circumvent the problem of the coexistence of different stages in one object, we want to statistically characterize the evolution along the different stages.

In this work we continue and extend an investigation of the chemical evolution in 59 high-mass star forming regions in different evolutionary stages (Paper I) towards deuterated molecules. In the previous work we measured the beam averaged column densities of 14 different molecular species and derived a chemical evolutionary picture across the evolutionary sequence in high-mass star formation starting with IRDCs via HMPOs to HMCs and finally UCHII regions. We found that overall the chemical complexity, column densities and abundances increase with evolutionary stage. We fitted the data with a 1D physico-chemical modeling approach and found good agreement with the observations. Here we want to measure the deuteration fractions of the four deuterated molecules DCN, DNC, DCO^+ and N_2D^+ and test their correlations with evolutionary stage and with physical parameters such as the luminosity of the objects. Furthermore, we model the derived column densities with a state-of-the-art 1D deuterium chemical model along the evolutionary sequence from IRDCs via HMPOs to HMCs and UCHII regions.

The structure of the chapter is the following. In Section 3.2 we introduce the source sample, followed by a description of the observations in Section 3.3 and an introduction to deuterium fractionation in Section 3.4. In Section 3.5 we present the results of the analyzed observational data. In Section 3.6 we introduce the model used to fit the data and discuss the modeling results as well as their implications. We conclude with a summary in Section 3.7.

3.2 Source sample

The sources are taken from Paper I and initially selected from different source lists. The total sample contains 59 high-mass star-forming regions, consisting of 19 IRDCs and 20 HMPOs as well as 11 HMCs and 9 UCHIIs. The sources were selected from well known source catalogs of the literature without specific selection criteria such as spherical symmetry. The lists of the IRDCs were first presented in Carey et al. (2000)

and Sridharan et al. (2005) and are part of the *Herschel* guaranteed time key project EPOS (The Early Phase of Star Formation, Ragan et al. 2012). This sample consists of 6 IRDCs showing no internal point sources below 70μm and 13 IRDCs that have internal point sources at 24μm and 70μm. The HMPOs are taken from the well-studied sample by Sridharan et al. (2002) and Beuther et al. (2002b,c). HMC sources are selected from the line-rich sample of Hatchell et al. (1998), including a few additional well-known HMCs: W3IRS5, W3H_2O and Orion-KL. For the UCHII regions, we selected line-poor high-mass star-forming regions from Hatchell et al. (1998), and additional sources from Wood & Churchwell (1989b). Recent studies towards single sources of the ones included in this work overall confirm the evolutionary classification given in the referenced papers. The source list is the same as the list that is given in Table 2.1 of Chapter 2.

3.3 Observations

The 59 sources were observed with the Arizona Radio Observatory Submillimeter Telescope (SMT) in 2013 between February 12-15, March 10-13 and on March 31 and April 1 with $\sim$ 100 h total observing time. For the observations we used the ALMA type 1.3 mm dual polarization sideband separating heterodyne receiver and the filterbanks as backends with a resolution of 250 kHz which corresponds to $\sim$ 0.3 km s^{-1} resolution in velocity. The beam size of the SMT at 1.3 mm is $\sim$ 30$''$. One single integration took 5 min in position-switching mode, with 2.5 minutes on-source time. The emission in the deuterated lines were integrated 2-3 times and the emission in the non-deuterated lines 1-2 times, depending on the observing conditions. The data was calibrated using data of Jupiter from the same observation runs assuming a sideband rejection of 13db. The mean system temperatures of the spectra T_{sys} is 380 K. The data reduction was conducted with the standard GILDAS[2] software package CLASS. All spectra from each source were baseline subtracted, calibrated to T_{mb} scale with typical beam efficiencies of 0.6 and averaged. In few cases we used the 1 MHz filterbanks spectra due to very broad lines (e.g., in Orion-KL) or when the line was not detected in the 250 kHz filterbanks but in the 1 MHz filterbanks. The line integrals were measured by summing the line emission channel by channel for detected lines. The detection criteria is S/N $>$ 3.

3.3.1 RMS

The median 1σ rms values for the deuterated molecules are 0.031 K for DCN, 0.024 K for DNC, 0.025 K for DCO^+ and 0.035 K for N_2D^+. DCN was observed in the later shifts and the higher rms value is due to worse observing conditions during that period. The higher rms value for N_2D^+ is due to problems at this specific transition frequency and described in the following Section. An overview of all rms values is given in Figure 3.1. The strong outlier in DCN is from Orion-KL which is still a detection.

---

[2] http://www. iram.fr/IRAMFR/GILDAS

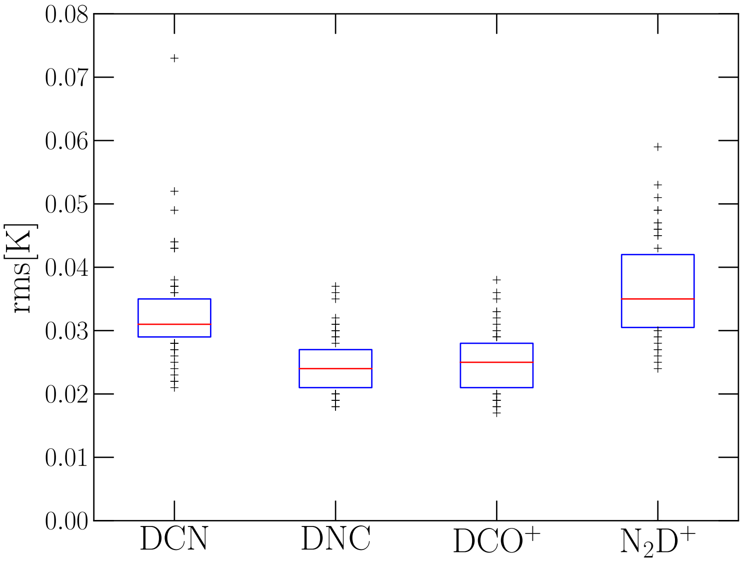

Figure 3.1 1σ rms values of spectra of the deuterated molecules. The red solid line shows the median, the blue box the 25%-75% range and the crosses mark the outliers.

3.3.2 Problems with N_2D^+ spectra

Reducing and analyzing the spectra of the N_2D^+ (3-2) transition at 231.32 GHz was problematic due to blending by an overlaying pressure broadened ozone line in the atmosphere. This ozone line depends on the elevation of the source and time of the observation and affects the different sources with varying strength. Due to this contamination, the mean 1σ rms value of the N_2D^+ line is 40% higher than for the other deuterated spectral lines and thus the threshold for a detection is higher. Another factor leading to higher rms-value might be the higher frequency of the N_2D^+ (3-2), although this effect is likely of minor importance. In the 5 sources IRDC18454.1, IRDC18454.3, Orion-KL, HMC010.47 and HMC031.41 the ozone line makes it impossible to discriminate between a detection or a non-detection.

3.4 Deuterium fractionation

Under cold conditions, the deuteration fraction of molecules can be enhanced through reactions with, e.g., deuterated H_3^+, H_2D^+. While the chemical reaction that deuterates H_3^+ proceeds without a thermal barrier, the backward reaction is endothermic and has a thermal energy barrier (Watson 1974; Caselli & Ceccarelli 2012; Albertsson et al. 2013). This energy barrier leads to an enhanced formation fraction at low temperatures, but becomes negligible for higher temperatures at which the backward reaction becomes as efficient as the forward reaction. The chemical reactions and their energy barriers that introduce deuterium into some of the key molecules are the following:

$$
\begin{aligned}
\mathrm{H_3^+ + HD} &\rightleftarrows \mathrm{H_2D^+ \ \ + H_2 + 230K} \quad (3.1)\\
\mathrm{CH_3^+ + HD} &\rightleftarrows \mathrm{CH_2D^+ + H_2 + 370K} \quad (3.2)\\
\mathrm{C_2H_2^+ + HD} &\rightleftarrows \mathrm{C_2HD^+ + H_2 + 550K} \quad (3.3)
\end{aligned}
$$

The temperature range for an effective D-enhancement for the pathway via H_3^+ isotopologues is $\sim 10 - 30$ K, whereas it is $\sim 10 - 80$ K for pathways via light hydrocarbons (Millar et al. 1989; Albertsson et al. 2013). This enhances the deuteration fraction of the key molecules H_3^+ and CH_3^+ in different temperature regimes. Another effect that increases the H_2D^+/H_3^+ ratio is the depletion of neutral gas-phase species (e.g., CO, N_2) (see Dalgarno & Lepp 1984; Roberts & Millar 2000). This enhancement is then imprinted on the molecules formed through these reaction partners.

In the literature different models exist describing the formation routes of deuterated molecules and their relative importance. The dominant formation pathways of DCO^+ and N_2D^+ are via a low-temperature route through H_3^+ isotopologues, whereas DCN can be formed via a fractionation route involving light hydrocarbons. The back-reaction of the route via H_3^+ isotopologues sets in at temperatures around 30 K and their deuteration fractions decrease with rising temperature. According to Roueff et al. (2007), both DCN and DNC can still be formed efficiently at temperatures > 30 K, although at higher temperatures DCN and DNC are not formed equally anymore, because of the interconversion of DNC to the more energetically favorable DCN. Whereas, the chemical models of Turner (2001) indicate that only DCN is also formed via reactions with light hydrocarbons involved, but not DNC. Following the Turner (2001) scheme, molecules such as C_2D, HDCO or C_3HD should show a similar behavior like DCN with temperature, since they are also formed via CH_2D^+ and C_2HD^+.

Parise et al. (2009) found a low DCO^+/HCO^+ column density ratio but significant deuteration fractions for HCN and H_2CO under temperature conditions of ~ 70 K towards the Orion Bar PDR. Model calculations by Roueff et al. (2007) predicted that in general the DNC/HNC, DCO^+/HCO^+ and N_2D^+/N_2H^+ column density ratios decrease with temperature, but are almost constant with density. The DCN/HCN column density ratio shows a more complex behavior with temperature, reaching the largest ratio for ~ 30 K, and shows a stronger increase with density. They found that the reason for this behavior is twofold. First, due to the enhanced abundance of radicals (e.g., CHD and CD_2) that form DCN. Second, the main destruction pathways of DCN are reactions with the ions HCO^+ and H_3O^+, that leads to $DCNH^+$ which subsequently returns to DCN via dissociative recombination. The deuteration fractions also strongly depend on the assumed elemental abundances.

3.5 Results

3.5.1 Detection fractions for DCN, DNC, DCO^+ and N_2D^+

The detection fractions of DCN, DNC, DCO^+ and N_2D^+ in the single stages are shown in Figure 3.2. In this figure, the IRDC stage is split into the two categories of sources mentioned in Sect. 2.2, without and with an embedded point source. From that figure we identify three trends:

1) N_2D^+ is only detected towards IRDCs and HMPOs (see also Fontani et al. 2014). Since the N_2H^+ abundance is almost constant over the full evolutionary sequence (Paper I), most likely a strong temperature dependence of the N_2D^+ production leading to its disappearance at $T \gtrsim 30$ K is the answer to its apparent absence in the HMC and UCHII stages. Another complication is problems with the particular bandpass of its (3-2) transition mentioned in Sect. 2.3.2 which lead to a higher mean 1σ rms value. 2) The only deuterated molecule detected in the coldest IRDCs without an embedded 70μm point source is DCO^+ which has also the highest detection fraction in the more evolved IRDCs. 3) The detection fractions of DCN, DNC and DCO^+ in warm IRDCs up to UCHII regions are comparable and peak at the HMC stage. In general the detection fractions towards the observed high-mass star-forming regions are high, $\gtrsim 60\%$. It is important to mention here that the strength of a transition is the product of column density and temperature and thus detections at the lower temperatures present in the earlier stages are more difficult. A lower detection fraction does not necessarily mean that the column densities in the earlier stages are lower compared to the later stages. The differences in column densities along the evolutionary sequence is discussed in Sect 3.6.1.

3.5.2 Molecular column densities

We calculated the molecular column densities of the upper level of a particular transition following the equation for optically thin emission:

$$N_u = \frac{8\pi k \nu^2}{hc^3 A_{ul}} \frac{J_\nu(T_{\rm ex})}{[J_\nu(T_{\rm ex}) - J_\nu(T_{\rm cmb})]} \cdot \int T_{mb} \delta\nu \tag{3.4}$$

where the integrated intensity is in K km s^{-1}, and the Einstein coefficient A_{ul} is in s^{-1} and with:

$$J_\nu(T) = \frac{h\nu/k}{\exp[h\nu/kT] - 1} \tag{3.5}$$

where ν is the frequency of the observed transition. Then the total column density (which we will refer from now on as column density) can be calculated:

$$N_{tot} = N_u \cdot \frac{Q}{g_u \exp[-E_u/kT_{ex}]} \tag{3.6}$$

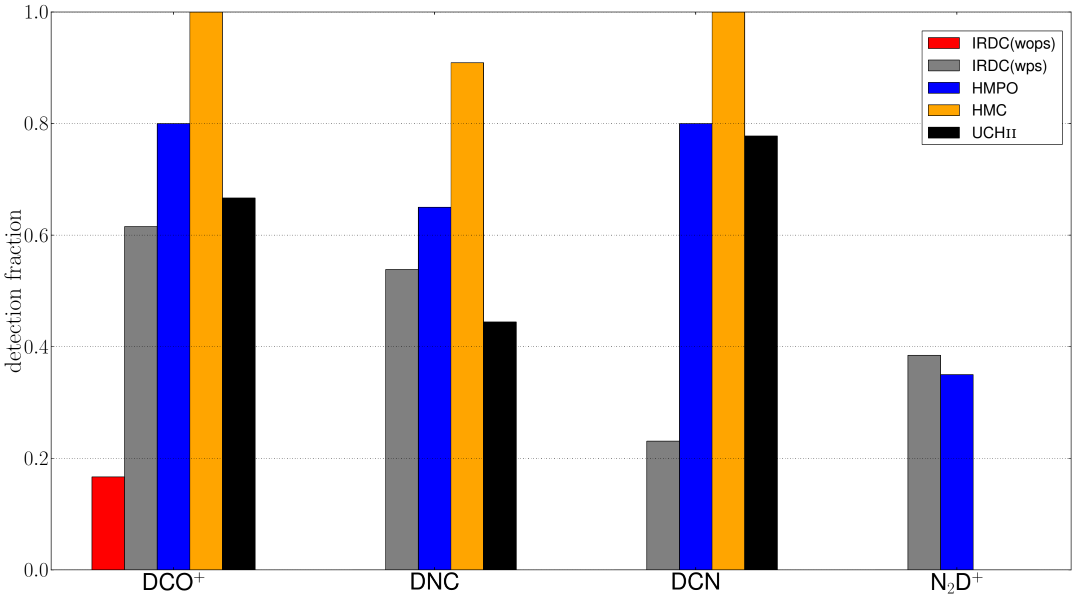

Figure 3.2 Detection fraction of the 4 observed deuterated species in the different evolutionary stages. Here the IRDC stage is divided into the two subsamples without and with an embedded point source at 24 or 70μ m, indicated in the caption as IRDC(wops) and IRDC(wps), respectively.

In the cases where we could derive the optical depth τ either due to hyperfine splitting or by comparing the same transitions of the main isotopologue with its rarer isotopologue (e.g., HCO^+ and $H^{13}CO^+$) we corrected the column density using:

$$N_{\mathrm{corr}} = N_{\mathrm{tot}} \cdot \frac{\tau}{1 - \exp[-\tau]} \tag{3.7}$$

In order to obtain abundances we derived H_2 column densities either from dust maps obtained with Mambo with the IRAM 30m telescope at 1.2 mm (Beuther et al. 2002b) and a resolution of 11″, or the galactic plane survey ATLASGAL (Schuller et al. 2009) at 870μm and a resolution of 19.2″, or the SCUBA Legacy Catalog (Di Francesco et al. 2008) at 850μm and a resolution of 22.9″ (see Table 2.1). The continuum data were smoothed to 29″ resolution in order to be beam matched with the IRAM 30m observations at 3 mm and the SMT molecular line data. H_2 column densities were calculated from the observed peak intensities assuming optically thin emission and LTE following Equation 3.8 (Schuller et al. 2009). The dust opacities used were $\kappa_{850\mu\mathrm{m}} = 1.48$, $\kappa_{870\mu\mathrm{m}} = 1.42$, $\kappa_{1.2\mathrm{mm}} = 0.97$, interpolated values from Ossenkopf & Henning (1994), assuming grains with thin ice mantles, gas densities of $n = 10^5$ cm^{-3}, and a gas-to-dust mass ratio $R = 100$. With these assumptions the H_2 column density is calculated as:

$$N_{H_2} = \frac{F_\nu \cdot R}{B_\nu \cdot \Omega \cdot \kappa_\nu \cdot \mu \cdot m_H} \tag{3.8}$$

Table 3.1 List of analyzed molecules with transitions, frequencies, energies of the upper level, and Einstein coefficients $A_{\rm ul}$.

Molecule	Transition	Frequency [GHz]	E_u/k [K]	$A_{\rm ul}$ [$10^{-3} \times s^{-1}$]
DCO^+	3-2	216.1126	20.74	0.772
DCN	3-2	217.2385	20.85	0.457
DNC	3-2	228.9105	21.97	0.557
N_2D^+	3-2	231.3218	22.20	0.712
$H^{13}CO^+$	3-2	260.2553	24.98	1.337
HCN	3-2	265.8864	25.52	0.836
HCO^+	3-2	267.5576	25.68	1.476
HNC	3-2	271.9811	26.11	0.934
N_2H^+	3-2	279.5117	26.82	1.259

Notes. Values are taken from LAMDA database (Schöier et al. 2005).

The uncertainties in the derived H_2 column densities are based largely on the dust and temperature properties and are approximately about factor of 3. A more detailed description of the derivation is given in Paper I.

The molecular column densities are then divided by the H_2 column densities and the averaged abundances are derived. The line parameters of the observed molecules are given in Table 3.1.

3.5.3 Excitation temperatures and final column densities

In this section we discuss the excitation temperatures used to derive the column densities and how we combined the data from Paper I and this work to obtain the final column densities.

The column densities for the non-deuterated species were partly taken from Paper I and partly calculated from the new observations. A detailed overview on the exact combination of the previous work and this one is given below. In the previous study we used likely optically thin (1-0) transitions of $H^{13}CO^+$ and $HN^{13}C$ and, due to their hyperfine structure, optical depth corrected N_2H^+ and HCN to derive their column densities. The spectra of the first study were partly affected by source emission at the present off-positions and strong optical depth effects. In these cases the optical depth and the integrated intensity could not be reliably determined. Thus we refrained from using those lines in the analysis. In this work we have additional information from the (3-2) transitions to complement the missing column densities. In order to obtain consistent results from both observation runs we compared the column densities of $H^{13}CO^+$(1-0) with the column densities of $H^{13}CO^+$(3-2) derived with $T_{\rm ex} = 20.9$ K (IRDC), $T_{\rm ex} = 29.5$ K (HMPO), $T_{\rm ex} = 40.2$ K (HMC) and $T_{\rm ex} = 36.0$ K (UCH II). Those are the mean temperatures of the best-fit models from Paper I. The comparison is shown in Figure 3.3.

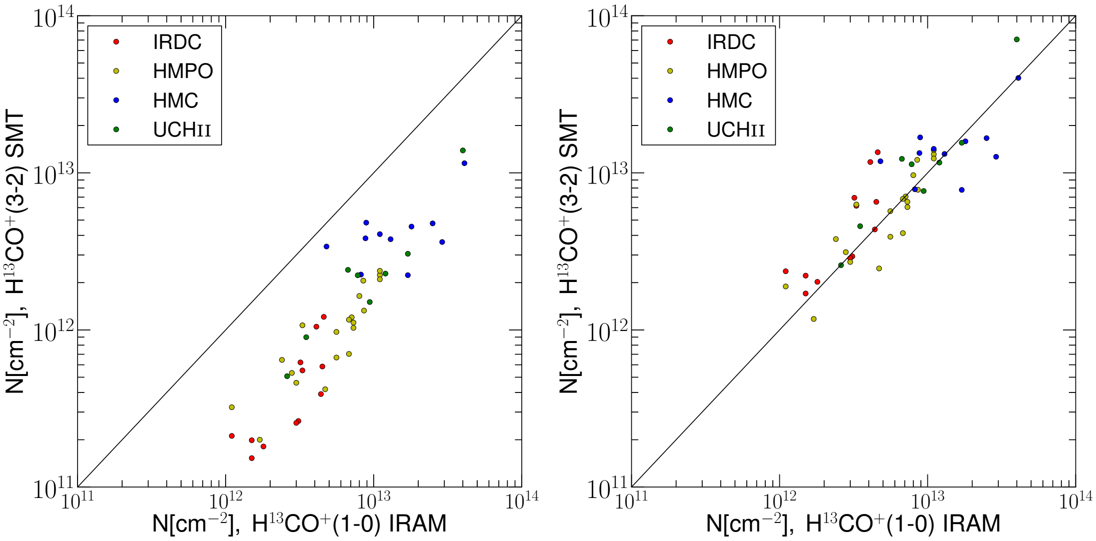

Figure 3.3 Left: Comparison of column densities derived from H^{13}CO$^+$(1-0) and H^{13}CO$^+$(3-2) transitions assuming the same excitation temperatures for both transitions. Right: Comparison of column densities derived from H^{13}CO$^+$(1-0) and H^{13}CO$^+$(3-2) transitions assuming different excitation temperatures for both transitions.

The derived column densities for the IRAM data are clearly all higher. Excluding problems in the quality of the data and the calibration leads to the assumption that, while the (1-0) transitions are in LTE, the upper levels are sub-thermally populated and thus the (3-2) transitions are not in LTE. This implies that the average densities of the gas should be below $\sim 10^6 - 10^7 \mathrm{cm}^{-3}$. Since the two different lines trace gas with different excitation conditions, the spatial extend probed by both transitions might be different. However, we do not know the beam filling factors for the different molecules and their different transitions. In order to compensate for the differences in the excitation conditions, we calculated the excitation temperature of the (3-2) transition for each source which would be necessary to derive the total column densities derived from the (1-0) transition. From those excitation temperatures we computed the median value for each stage. That resulted in $T_{\mathrm{ex}} = 5.2$ (IRDC), $T_{\mathrm{ex}} = 6.2$ (HMPO), $T_{\mathrm{ex}} = 7.2$ (HMC) and $T_{\mathrm{ex}} = 6.4$ (UCH II) for the (3-2) transitions. The comparison of the calibrated H^{13}CO$^+$(3-2) column densities derived with the lower, non-thermal excitation temperatures and the (1-0) data is shown in Figure 3.3. This correction should also reduce the error in the beam filling fraction and make the different transitions comparable.

For the four different molecules we derived the column densities in the following way.

HCO^+ and N_2H^+

For HCO^+ we derived optical depths using the HCO^+(3-2) and $H^{13}CO^+$(3-2) transitions assuming the relative isotopic ratio representative of the Sun and the local ISM of $^{12}C/^{13}C$=89 (Lodders 2003) and calculated optical depth corrected column densities. The values of τ derived with this method and their uncertainties are given in Table 3.8.

For N_2H^+ we took the column densities from the (1-0) transitions from Paper I, for which we used, in case of optically thick lines, the optical depth and the excitation temperature from the hyperfine fits made with CLASS[3]. The hyperfine structure fitting routine (METHOD HFS) assumes that all components of the hyperfine structure have the same excitation temperature and the same width and that the components are separated in frequency by the laboratory values. From the comparison of the ratios of the line intensities of the hyperfine components to the theoretically expected ratios, the fit routine estimates the optical depth of the line. In the optically thick case that allows to determine the excitation temperature. In the optically thin case we assumed the excitation temperatures given in Section 3.5.3.

HNC

For HNC we derived optical depths using the HNC(1-0) and $HN^{13}C$(1-0) transitions and calculated optical depth corrected column densities. Furthermore we calculated from the (3-2) transitions column densities without optical depth correction. We compared the resulting column densities and found an offset of a factor ~ 11.6. For the sources for which the optical depth could not be determined reliably, meaning the calculation resulted in $\tau > 50$, or no data of the (1-0) transition were available, we used the column densities derived from the (3-2) transitions and multiplied with the correction factor of 11.6. The values of τ derived with this method and their uncertainties are given in Table 3.8.

HCN

For HCN we used the optical depth corrected column densities from the (1-0) transitions when available. In all other cases we computed the mean difference between column densities derived from the (1-0) transitions and the (3-2) transitions and applied this factor of ~ 1.7 to the derived column densities from the (3-2) transitions.

All column densities are beam averaged quantities. The resulting median abundances including all detections and upper limits for each subsequent evolutionary phase are given in Tables 3.2. In the derivation of the column densities we assumed the excitation temperatures of the deuterated and non-deuterated molecule of the same transition to be equal. This assumption is valid for high densities and high excitation temperatures, but might lead to an underestimation of the deuteration column density ratios D_{frac} by a factor of $\sim 2-4$ (Shirley 2014, in prep.).

---

[3] `http://www.iram.fr/IRAMFR/GILDAS/doc/pdf/class.pdf`

Table 3.2 Observed median column densities (N) and the standard deviation (SD) for IRDCs, HMPOs, HMCs and UCHII regions as $a(x) = a \times 10^x$. The median includes detections and upper limits of non-detections. Species detected in less than 50% of the sources are indicated by an upper limit.

	IRDC		HMPO		HMC		UCHII	
	N	SD	N	SD	N	SD	N	SD
	cm^{-2}	cm^{-2}	cm^{-2}	cm^{-2}	cm^{-2}	cm^{-2}	cm^{-2}	cm^{-2}
HCO^+	3.9(14)	4.8(14)	8.3(14)	6.7(14)	2.2(15)	1.2(15)	1.6(15)	3.5(15)
HCN	6.9(13)	6.0(13)	1.3(14)	1.7(14)	3.5(14)	3.4(15)	3.4(14)	3.6(14)
HNC	3.8(14)	2.2(14)	6.2(14)	4.7(14)	1.5(15)	7.9(14)	5.0(14)	2.1(15)
N_2H^+	2.2(13)	1.5(13)	4.6(13)	3.2(13)	5.5(13)	4.6(13)	3.7(13)	6.4(13)
DCO^+	≤3.1(11)	1.1(12)	6.7(11)	6.5(11)	2.0(12)	7.6(12)	4.6(11)	3.4(11)
DCN	≤6.1(11)	7.3(11)	2.0(12)	2.2(12)	8.0(12)	3.6(13)	1.9(12)	6.0(12)
DNC	≤6.1(11)	9.2(11)	1.0(12)	1.2(12)	8.7(11)	7.1(11)	≤3.0(11)	1.9(12)
N_2D^+	≤6.8(11)	4.3(11)	≤3.8(11)	4.0(11)	≤2.2(11)	6.6(10)	≤3.3(11)	4.6(10)

3.6 Discussion

3.6.1 Deuteration fractions

The spread of the deuteration fractions D_{frac} for each stage is shown in Figure 3.4. These values include only detections and only in the case of N_2D^+ the median 3σ-limits of non-detections for the HMC-stage and UCHII-stage are given, since the detection fraction is zero. These values can be considered as a sensitivity limit.

The ratios of the column densities of DNC, DCO^+ and N_2D^+ with their non-deuterated counterparts HNC, HCO^+ and N_2H^+ all show decreasing trends with evolutionary stage, despite the large spread of ratios within individual stages. Only HCN shows an increase in the ratio with the maximum reached in the HMC-stage. We perform the one-way ANOVA test from the Python package SciPy[4] for all four deuteration fractions. This statistically tests the null hypothesis that the ratios among the different evolutionary groups have the same mean value. In addition, we performed a two-sided Kolmogorov-Smirnov (KS2) test (e.g., Conover 1971) for each two consecutive stages. The KS2 can be used to test whether two data samples come from the same parent distribution. For both tests we only use the detections and no upper limits.

The one-way ANOVA test yields probability values p of 0.005, 0.007, 0.01 and 0.07 for N_2H^+, HNC, HCO^+ and HCN, respectively. Thus, the results are significant on a 5% significance level for the three molecules N_2H^+, HNC, HCO^+ and on a 10% significance level for HCN. We conclude that the null hypothesis of a constant deuteration value among all stages can be ruled out and the described trends along the evolutionary path are real. This implies a different chemistry for DCN and the other three deuterated molecules in our setup (N_2D^+, DNC, DCO^+). The resulting p-values of

---

[4] `http://docs.scipy.org/doc/scipy-dev/reference/generated/scipy.stats.f_oneway.html`

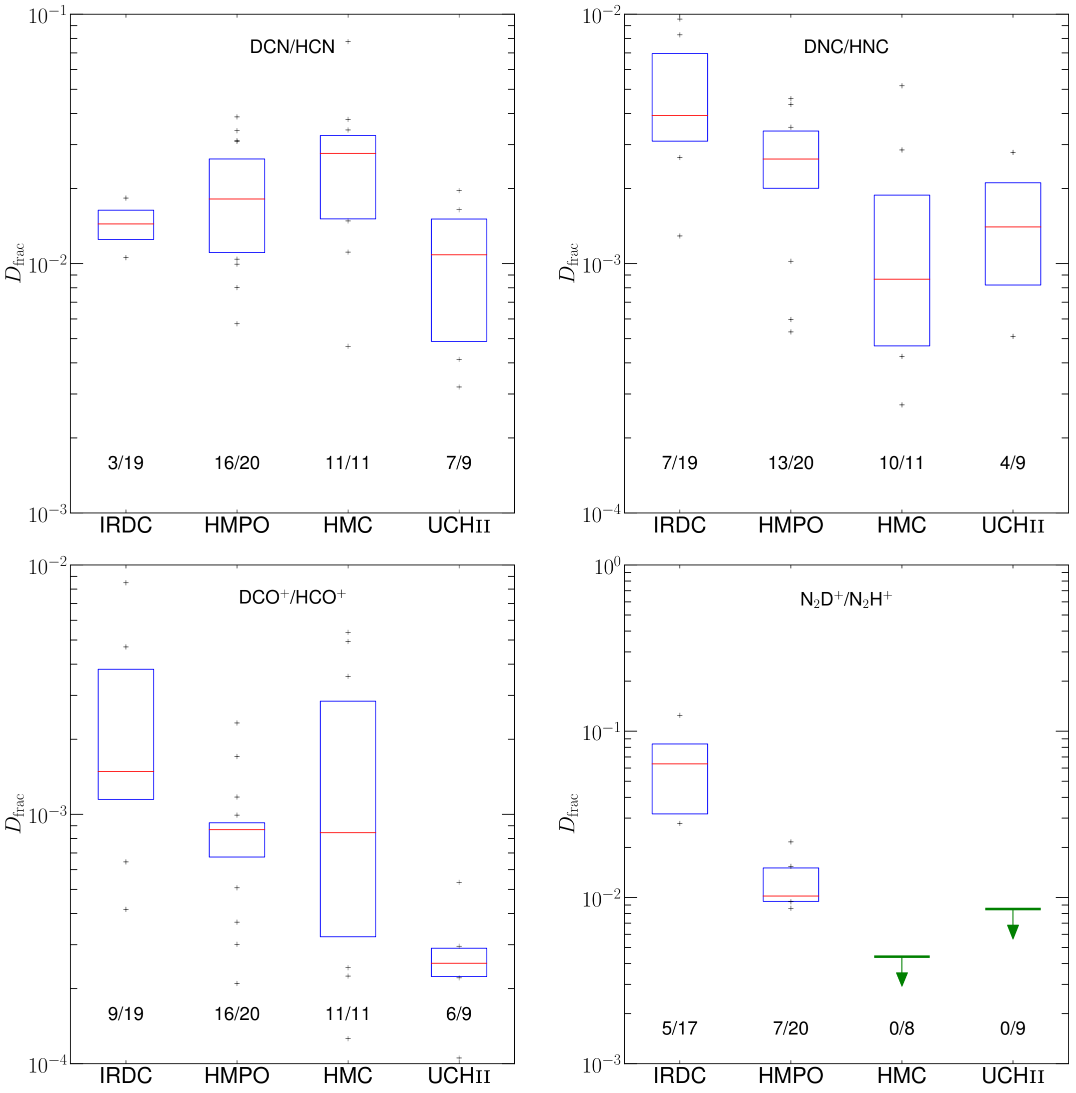

Figure 3.4 Spread in deuteration fractions $D_{\rm frac}$ among the 4 evolutionary stages for HCN, HNC, HCO^+ and N_2H^+. The red solid line shows the median, the blue box the 25%-75% range and the crosses mark the outliers. The green lines for the HMCs and UCHIIs for N_2H^+ give the median of their limits. The numbers at the bottom of each stage give the detection rate.

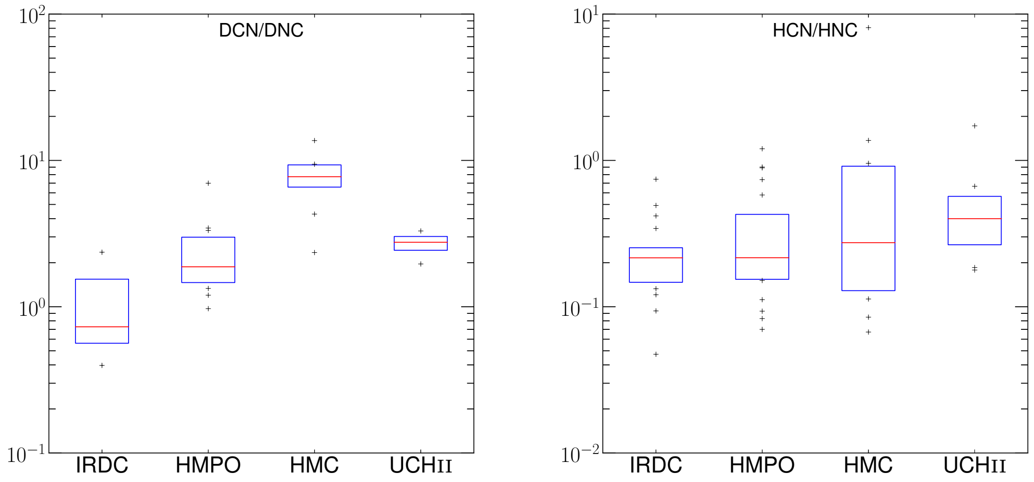

Figure 3.5 Spread in the fractions among the 4 evolutionary stages for DCN/DNC and HCN/HNC. The red solid line shows the median, the blue box the 25%-75% range and the crosses mark the outliers.

the KS2 test are shown in Table 3.3. High p-values cannot reject the null hypothesis that the two samples are drawn from the same distribution. The computed probabilities from the KS2 test are consistent with the picture that the deuteration fraction of HCO^{+}, HNC and N_2H^{+} in general decreases with evolutionary stage, although in some cases the consecutive stages are statistically not different from each other (e.g., HMPO-HMC of DCO^{+}/HCO^{+}, HMC-UCHII of DNC/HNC). The reason for this is that the evolution along the sequence is continuous. However, there might be overlaps between consecutive stages like, for example, some of the HMCs are associated with UCHII regions. One can distinguish between two different scenarios that can lead to an overlap between consecutive stages. In the cases like HMC029.96 (G29.96), high spatial resolution observations show a separation of the actual UCHII region and the neighboring HMC of $2''$ (Cesaroni et al. 1994; Beuther et al. 2007b). The HMC and the UCHII region are two (or more) distinct entities. The second scenario are cases like HMC009.62 (G9.62), where also a separate UCHII region exists, but in addition a small hypercompact HII region is present at the location of the HMC itself (Testi et al. 2000). This is a general caveat in single-dish observations of HMCs that might be contaminated by UCHII regions in the beam. Here, the sources are classified based on their chemistry and that is likely dominated by the HMC. However, that does not totally cancel this effect and differences in the measured ratios between different stages are in some cases weaker. Nevertheless, the global trends are clearly visible. The KS2 test also confirms the trend seen in the ratio of DCN/HCN, although an increase in the ratio of DCN/HCN in the first three stages is not strongly supported. That is pointing towards a rather flat DCN/HCN ratio during the IRDC to HMC stages which drops in the latest considered stage.

Furthermore, Figure 3.5 shows the observed column density ratios of DCN/DNC and HCN/HNC. While the ratio of the non-deuterated molecules is almost constant,

Table 3.3 Resulting p-values of the KS2 test.

	IRDC-HMPO	HMPO-HMC	HMC-UCHII
DCO^+/HCO^+	0.02	0.40	0.11
DCN/HCN	0.41	0.54	0.10
DNC/HNC	0.07	0.09	0.74
N_2D^+/N_2H^+	< 0.01		
DCN/DNC	0.14	< 0.01	0.01
HCN/HNC	0.74	0.82	0.43

the ratio of the deuterated molecules shows clearly a peak at the HMC stage. That qualitative behavior is reflected by the results of the one-way ANOVA tests that yield probability values $p < 10^{-4}$ for DCN/DNC and $p = 0.17$ in the case of HCN/HNC . The KS2 test of the consecutive stages confirms these findings. This leads to the conclusion that DCN can be formed more efficiently in the more evolved sources than DNC. The observed behavior can be understood according to the dominant formation pathways scenario stated by Turner (2001). He claimed that all four deuterated molecules can be efficiently formed at low temperatures via H_2D^+, but only DCN can be formed at higher temperature via CH_2D^+. That would lead to the observed trends in the deuteration fractions, since DCN can still be formed in the more evolved stages, in contrary to the other observed deuterated molecules.

However, newer chemical models, e.g., from Roueff et al. (2007) or the updated model we use, do not support this scenario of a difference in dominant formation pathways between DCN and DNC. According to these new models, both isomers are formed from light hydrocarbons and thus exhibit a similar evolution in the abundance ratios with temperature. Hiraoka et al. (2006) were studying the association reactions of CN with D in laboratory experiments and found at a temperature of 10 K an intensity ratio of DNC/DCN of ~ 3. At temperatures > 20 K, the formation of DNC and DCN became negligible. This is consistent with the derived value for the IRDC stage in this work on the order of unity, but contradicts the higher DCN/DNC ratios found in the HMC stage, suggesting another possible formation route.

3.6.2 Relation between deuteration and other parameters

We measured the full width at half maximum (FWHM) of HCN, $HN^{13}C$, $H^{13}CO^+$ and N_2H^+. The minor isotopologues are assumed to be optically thin. For N_2H^+ and HCN we corrected the measured optically thick FWHM $\Delta\nu_{\mathrm{thick}}$ according to Phillips et al. (1979) using the relation:

$$\frac{\mathrm{FWHM_{thick}}}{\mathrm{FWHM_{thin}}} = \frac{1}{\sqrt{\ln 2}}\sqrt{\ln\frac{\tau}{\ln\frac{2}{\exp(-\tau)+1}}} \tag{3.9}$$

where τ is the optical depth of the line center and $\mathrm{FWHM_{thin}}$ the optically thin FWHM. The correlation plots are shown in Figure 3.6 with the Spearman's rank correlation coefficient ρ given in the upper left corner. By definition, the absolute value of ρ is ≤ 1 with a stronger correlation for larger ρ. The sign indicates a positive or negative correlation between the two quantities. The plots show that earlier phases have smaller FWHM. In the derivation of the Spearman coefficient we only consider the detections. The resulting coefficient is consistent with the data being uncorrelated for all four molecules. The FWHM of N_2H^+ might be an exception and correlated, but with only few detections of N_2H^+ no conclusive answer can be given.Although the correlation with the FWHM is weak, the decrease of the deuterium ratio with increasing FWHM is consistent with the picture of more quiescent, early stages with lower FWHM and higher deuteration fractions followed by more turbulent stages with higher FWHM and lower deuterium ratios. As we will see below, correlations of the deuterium ratio with other quantities than the FWHM are stronger.

Furthermore, we studied the correlation of the deuteration with the H_2 column density and luminosity L. The luminosities and H_2 column densities are shown in Tables 3.6–3.7 and the corresponding correlation plots in Figure 3.7 and Figure 3.8. In general, the deuteration fraction shows an anti-correlation with the luminosities of the sources and a lack of correlation with H_2 column densities. The strongest correlation is found for N_2D^+, but with only few detections of N_2D^+ the correlation is not very reliable. The luminosity of a source is not necessarily a tracer of its evolutionary stage, but Figure 3.7 shows that the four different evolutionary stages are nicely separated with respect to the luminosity. Taking into account that the temperature of the objects increases with evolutionary stage, the luminosity can be used as a proxy for the temperature in the case of our source sample. Since higher luminosities indicate higher temperatures and smaller regions with $T \lesssim 20$ K, where CO is frozen out, it reduces the overall abundance as well as the D/H ratio of N_2H^+. Thus the deuteration fraction is not so much sensitive to the total amount of gas rather than to the fraction of high-temperature to cold-temperature gas and the degree of CO depletion onto dust grain surfaces. Among all four molecular deuteration fractions, DCN shows the weakest correlation with any of the shown parameters. This seems to be an effect of its high temperature formation route.

3.6.3 Modeling the chemical evolution

With the observed column densities of 18 species (14 from Paper I) including 4 deuterated species in different stages of massive star formation at hand, we applied the iterative physico-chemical fitting model “MUSCLE-D” (“MUlti Stage CLoud codE with D-chemistry”) to these data. A list of all fitted species is given in Table 3.4. The model fits the evolution of the observed chemical data and thereby constrains basic physical properties in the assumed evolutionary path of high-mass star formation, such as mean temperatures and mean chemical ages. The chemical ages can be interpreted as typical lifetimes of the various stages. This model is the extended version of the iterative fitting model “MUSCLE” (“MUlti Stage CLoud codE”) already used and described in Paper I and includes a physical and a chemical model. Here we will give a short summary of the main characteristics of the two parts of “MUSCLE-D”, the physical model in Section 3.6.3 and the chemical model “ALCHEMIC” in Section 3.6.3.

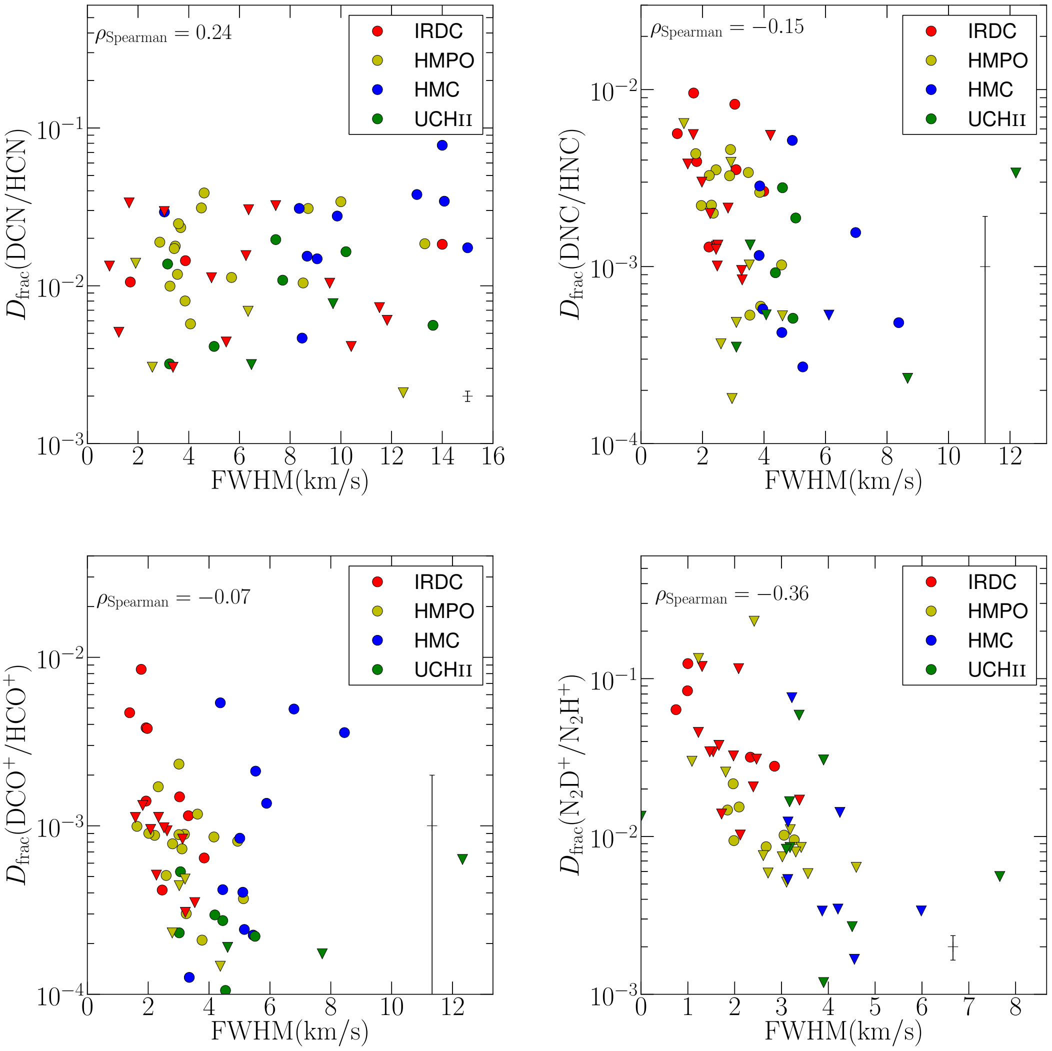

Figure 3.6 Deuteration fractions of HCN, HNC, HCO^+ and N_2H^+ vs. FWHM of non-deuterated species from HCN (or $H^{13}CN$ in case HCN is not available), $HN^{13}C$, $H^{13}CO^+$ and N_2H^+, respectively. The dots mark detections, the triangles upper limits. The typical size of an error bar from the uncertainty in the integrated flux is given in the lower right.

Table 3.4 List of species fitted with the model.

Molecules
CO^a, HNC^a, HCN, HCO^{+a}, HNCO, H_2CO, N_2H^+, CS^a, SO OCS, C_2H, SiO, CH_3CN, CH_3OH, DCO^+, DCN, DNC, N_2D^+

Notes. [a] Minor isotopologue observed.

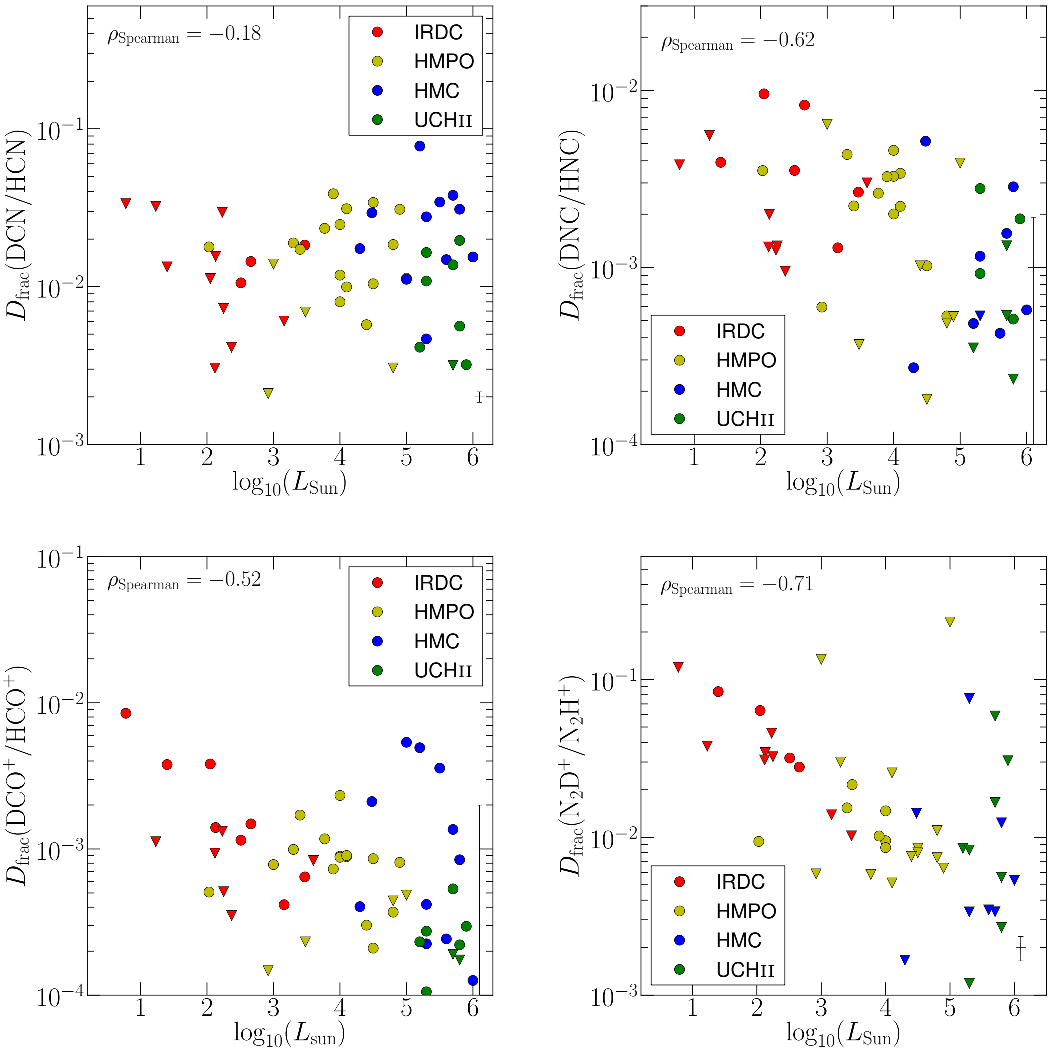

Figure 3.7 Deuteration fractions of HCN, HNC, HCO$^+$ and N$_2$H$^+$ vs. the luminosity of the source. The dots mark detections, the triangles upper limits. The typical size of an error bar from the uncertainty in the integrated flux is given in the lower right.

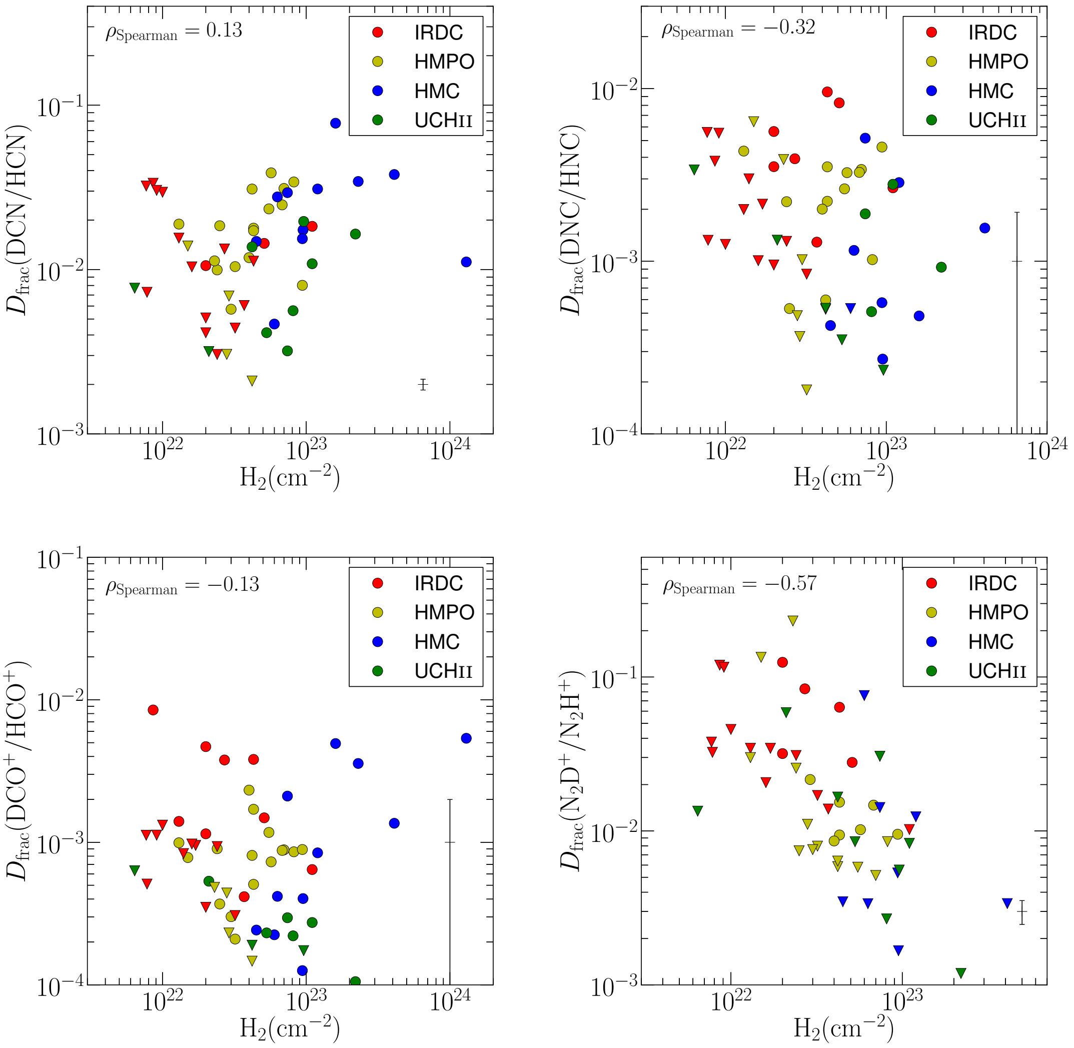

Figure 3.8 Deuteration fractions of HCN, HNC, HCO^+ and N_2H^+ vs. the H_2 column density of the source. The typical size of an error bar from the uncertainty in the integrated flux is given in the lower right.

Physical model

The physical model treats the star-forming region as spherically symmetric 1D-clouds with a fixed outer radius of $r_{\text{out}} = 0.5$ pc. That is based on the largest beam size of our observations of $30''$ and is also the typical size of high-mass star forming regions. High angular resolution studies revealed in some of the sources complex structures that deviate from the spherically symmetric case (e.g., Beuther et al. 2002a). However, in single-dish maps these sources appear to be symmetric (e.g., Beuther et al. 2002b). Since we are analyzing single-dish data, a 1D-model physical model appears to be sufficient for us. More sophisticated models, that take into account complicated substructures, would increase the number of fitting parameters and might lead to an over-interpretation of the data. The radial density and temperature structure is modeled with

$$\begin{aligned} \rho(r) &= \rho_{\text{in}}(r/r_{\text{in}})^{-p}, & r &\geq r_{\text{in}}; \\ \rho(r) &= \rho_{\text{in}}, & r &< r_{\text{in}} \end{aligned} \tag{3.10}$$

and

$$\begin{aligned} T(r) &= T_{\text{in}}(r/r_{\text{in}})^{-q}, & r &\geq r_{\text{in}}; \\ T(r) &= T_{\text{in}}, & r &< r_{\text{in}}, \end{aligned} \tag{3.11}$$

respectively. The fitted physical quantities are the inner radius r_{in}, the temperature and density at the inner radius, T_{in} and ρ_{in} and the power law index of the density p. The inner radius is limited between $5 \times 10^{-5} - 5 \times 10^{-2}$ pc. While we assume the IRDC is an isothermal sphere, the temperature structure of the more evolved stages is modeled by a inner flat plateau with T_{in} and a power-law with slope $q = 0.4$ as a standard value for $r > r_{\text{in}}$ (see van der Tak et al. 2000). The radial density profile within r_{in} is flat with ρ_{in} and decreases for $r > r_{\text{in}}$ as a power law with slope p. The value of p is limited to values between 1.5 and 2.0 in order to save computing time. That range is supported by several observations, e.g. Guertler et al. (1991); Beuther et al. (2002b); Mueller et al. (2002); Hatchell & van der Tak (2003). The temperature and density profiles are simultaneously fitted. The model does not take into account radiative transport. In the model, the whole cloud is embedded in a larger diffuse low-density medium that shields the high-mass star forming cloud from the interstellar FUV radiation.

Chemical model

The chemical model is an updated version of the time-dependent gas-grain chemical model "ALCHEMIC" described in Semenov et al. (2010) with the updates described in Paper I. In addition, the deuterium network from Albertsson et al. (2013) was added and extended with high-temperature reactions (Harada et al. 2010, 2012; Albertsson et al. 2014b) and ortho/para states of H_2, H_2^+ and H_3^+ and their isotopologues (Albertsson et al. 2014a). In total, the chemical network comprises 15 elements that can form 1260 different species from 38 500 reactions.

The initial abundances prior to the IRDC stage are taken from the "low metals" set given in Lee et al. (1998) with changed elemental abundance of Si (3×10^{-9} with respect to H) and S (8×10^{-7} with respect to H). The changes were needed in order to achieve proper fits to the IRDC phase. The initial ortho-para ratio of H_2 is assumed to be the statistical value of 3:1. In another realization of the model we assume all H_2 to be in the para state, due to the cold conditions. A comparison of these two extreme cases is given in Sect. 3.6.4. For the subsequent stages, the chemical outcome of the previous best-fit model is used as input initial abundances.

The fitting procedure

The fitting for the different stages is done iteratively using the physical and chemical model described above. In this sense we modeled the observed column densities for the IRDC, HMPO and HMC stage by varying the parameters $r_{\rm in}$, $T_{\rm in}$, $\rho_{\rm in}$ and p. While keeping all other parameters fixed, we vary these four parameters and run the model over 10^5 yr for each of the realizations. Then we compute the χ^2-value for each time step and model realization, given the observed mean column densities and computed model column densities. We assumed the standard deviation between modeled and observed values to be one order of magnitude as a typical value. Molecules that were detected in less than 50% of the sources within one stage were considered as upper limits. Finally, the model with the minimum χ^2-value is found as the best-fit model which matches best with the calculated mean column densities for each stage.

Due to the iterative fitting along the evolutionary sequence, the introduced uncertainties increase with evolutionary stage leading to a limited confidence in the obtained results for the later stages. Thus, we refrained from fitting the UCHII stage.

3.6.4 The importance of initial ortho-para H_2 ratio for deuterium fractionation and modeling the observations

The importance of the ortho-para ratio of molecular hydrogen for deuterium fractionation via H_3^+ isotopologues has been realized more than two decades ago in a pioneering study by Pagani et al. (1992) and later experimentally confirmed by Gerlich et al. (2002). Ortho-H_2 in its ground rotational level has an energy higher by ~ 170 K compared to the ground state energy of para-H_2 of 0 K. Consequently, ortho-H_2 is able to react more readily with deuterated H_3^+ isotopologues even at low temperatures, $\lesssim 20 - 30$ K, lowering their abundances and hence the deuterium enrichment via H_3^+-induced ion-molecule chemistry (Flower et al. 2006).

The importance of nuclear spin states of molecular hydrogen for deuterium fractionation has also been revealed in observations of low- and high-mass star-forming regions. For example, Maret & Bergin (2007) have observed the classical low-mass pre-stellar core Barnard 68 in lines of $H^{13}CO^+$ and DCO^+. They found that the DCO^+ emission is dependent of the ortho-para H_2 ratio and indicates a non-thermal value of 1% (the thermal value being several orders of magnitude lower). Pagani et al. (2009) have studied another low-mass cloud L183, estimated the H_2D^+ ortho-para ratio and derived the ortho-para H_2 ratio. This ratio varies across the core by at least an order of magnitude, with a median value of 0.1 (which is also non-thermal). In a later work, Pagani et al. (2011) found that ortho-para H_2 ratios > 0.1 are required to explain the observed DCO^+ emission in pre-stellar cores, and that the conversion of ortho- to para-H_2 is a long process ($\gtrsim$ 1 Myr). Finally, recently Taquet et al. (2013) have observed heavy water in a more evolved, low-mass protostellar envelope, IRAS 16293, and found by modeling that the deuteration of water is sensitive to the ortho-para H_2 ratio and to the total cloud density, but it also depends on the temperatures and the visual extinction. Their observations suggest that water is formed in predominantly solid form under warmer conditions than those in dense cloud cores.

We have taken such a strong dependence of the deuterium fractionation into consideration in our modeling. For that, we performed the fitting of the IRDC-HMPO-HMC-UCHII evolutionary sequence using the same initial elemental abundances but the two radically different initial ortho-para H_2 ratios. As initial ortho-para H_2 values we have considered the equilibrium value of 3:1 and the case when only para-H_2 is present (representative of an extremely cold, dense and dark environment). In reality, the formation of IRDCs will begin from fragmentation and contraction of low-density gas where this ratio is somewhere between these two extremes. It is important to note that the H_2 ortho-para ratio upon its formation on dust grain surfaces was experimentally found to be thermal, 3:1 (Gavilan et al. 2012). This value should be representative of the environments where predominantly atomic gas is/has converted to molecular gas (e.g., Giant Molecular Clouds), and which could also be representative of pre-IRDC gas.

We have found in both cases similarly accurate modeling results with a maximum of 5 of 18 misfitted species in one stage. In case of the ratio being 3:1 we obtain a lower best-fit temperature for the IRDC stage (11 K compared to 20 K). This result better resembles typical IRDC temperatures. The modeling results and their differences are described and discussed in the next section in more detail.

3.6.5 The modeling results

We fitted the combined data from Paper I and this work with the above described model assuming two extreme ortho-para H_2 ratios (hereafter: model *A*: o/p=3:1; model *B*: p=100%). The resulting best-fit model parameters for the IRDC, HMPO, HMC and UCHII stage for model *A* and model *B* are shown in Tables 3.9 – 3.12. The evolution of the best-fits with time of model *A* are shown in Figure 3.9 and for model *B* in Figure 3.10. These distributions give a good sense of its uncertainty. The best-fit lifetimes for model *A* are 5 300 years for the IRDC with a range of several thousand years up to several 10^4 years, and 38 400 years for the HMPO and 32 400 years for the HMC stage with values below $\sim$ 10 000 years being unlikely and for the UCHII stage of 8 000 years. For model *B* we find 19 000 years for the IRDC with a likely range between $sim 15\,000 - 35\,000$ years, 6 400 years for the HMPO with a likely range between $\sim 3\,000 - 20\,000$ years and 85 700 years for the HMC stage with values below $\sim$ 75 000 years being unlikely. The best-fit lifetime for the UCHII stage is $\sim$ 2 000 years, with values between $2\,000 - 20\,000$ years leading to equally good fits.

Table 3.5 List of misfitted species.

Stage	Model *A*	Model *B*	Paper I
IRDC	N_2H^+	-	-
HMPO	SO, CH_3OH	HCO^+, HNCO, C_2H	H_2CO, CH_3OH
HMC	HNCO, SO, C_2H, CH_3OH	HNCO, SO, CH_3OH, DCO^+	HNC, CS, C_2H
UCHII	HNCO, SO, C_2H, SiO, DCO^+	HNCO, SO, C_2H, DCO^+	HNC, SO, C_2H

The observed and modeled column densities are shown in Tables 3.13 – 3.16 for both models. The best-fit of model *A* (o/p=3:1) of the IRDC stage reproduces 17 of 18 molecules within the assumed combined (observational + chemical) uncertainty of one order of magnitude. N_2H^+ is underproduced by a factor of ~ 60. This is possibly connected to the short lifetime and the lack of sufficient CO depletion. In the HMPO stage the model is able to reproduce 16 of 18 molecules. SO is overproduced by a factor of ~ 30 and CH_3OH underproduced by a factor of ~ 50. The underproduction of methanol is possibly due to shock- or outflow-triggered enhanced desorption of methanol ice from grains, which is not taken into account in the model. The reason for the misfit of SO might be a poorly implemented chemistry of sulfur-bearing species in modern astrochemical models in general. In the HMC stage the model could fit 14 of 18 species. Besides C_2H, which is ~ 20 times underproduced, HNCO, SO and CH_3OH are misfitted by more than a factor of 100. The underproduction of CH_3OH and overproduction of SO in the HMPO stage is continuing in the HMC phase. The overproduction of HNCO might be connected to not well enough understood shock- and surface chemistry. The difference in C_2H between the model and observations might be influenced by UV-radiation of the central star(s) or a clumpy structure of the environment, which is not considered in the model. That is especially important for the UCHII regions, but it is also already present in some HMCs. For the last considered stage of an UCHII region the model reproduces 13 of 18 species. As in the HMC stage, the molecules HNCO, SO and C_2H are misfitted in the UCHII stage. In addition, SiO and DCO^+ are slightly overproduced.

The best-fit of model *B* (only para-H_2) of the IRDC stage agrees with all observed column densities within the assumed uncertainty of one order of magnitude. The model results for the HMPOs agrees for 15 of 18 molecules with the observed values. The modeled HCO^+ value is about 20 times lower, HNCO about 20 times higher and C_2H only slightly exceeds the assumed uncertainty of one order of magnitude difference. The best-fit model of the HMCs agrees with 14 of 18 molecules with the observed values. The molecules HNCO, SO are about 100 times higher in the model, CH_3OH about 20 times lower and DCO^+ only slightly above the one order of magnitude uncertainty. In the UCHII stage 14 of 18 species are fitted well. Similar to model *A*, the misfitted species are HNCO, SO, C_2H and DCO^+. In total the best-fit add up to $\sim 85,000$ years for model *A* and $\sim 115,000$ years for model *B*, which is on the same order as typical models of high-mass star formation (e.g., McKee & Tan 2003; Tan et al. 2014).

The comparison of model *A* and model *B* shows especially differences in the lifetimes and best-fit temperatures. The IRDC stage of model *A* is 4 times shorter than in

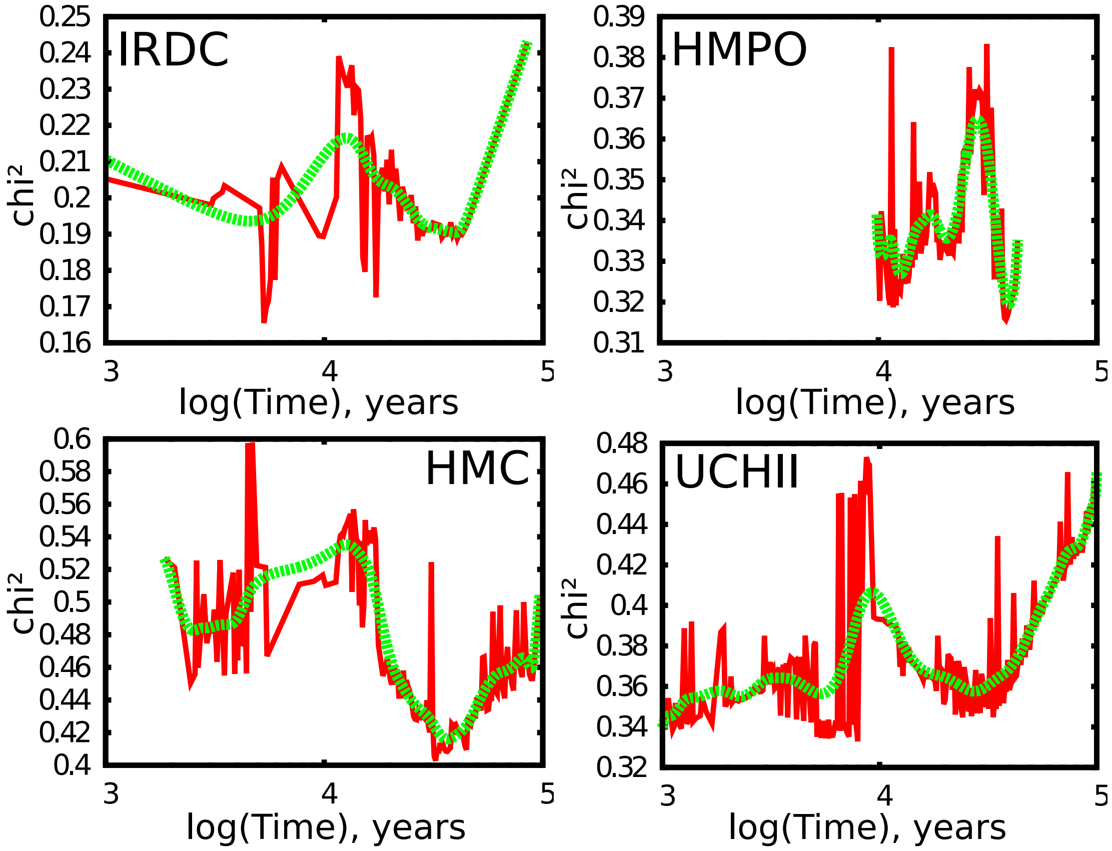

Figure 3.9 Evolution of the minimum χ^2 of the best-fit models with time with ortho-para H_2 ratio of 3:1. The four panels show the four different stages IRDC (upper left), HMPO (upper right), HMC (lower left) and UCHII (lower right). The red curve marks the calculated values at all 299 time moments, whereas the green curve shows their smoothed spline interpolation.

model *B* and the temperature of model *A* of $\sim$ 11 K is much lower than the $\sim$ 20 K of model *B*. The general chemical fits are similar, with N_2H^+ and the four included deuterated species being less abundant in the colder and younger model *A*. The other stages are in general similarly well fitted. However, the well fitted species are different. In Table 3.5 we compare the misfitted species from the best-fit model of Paper I with this work. We conclude that the initial o/p H_2 ratio is between the two extreme cases considered in model *A* and model *B*. The lower and more favorable best-fit temperature of the IRDC stage obtained with model *A* and taking into account relatively long timescales for the conversion of an initially thermal ratio into predominantly para-H_2 at typical cloud temperatures and densities, a value closer to an ortho-para H_2 ratio of 3:1 is more likely.

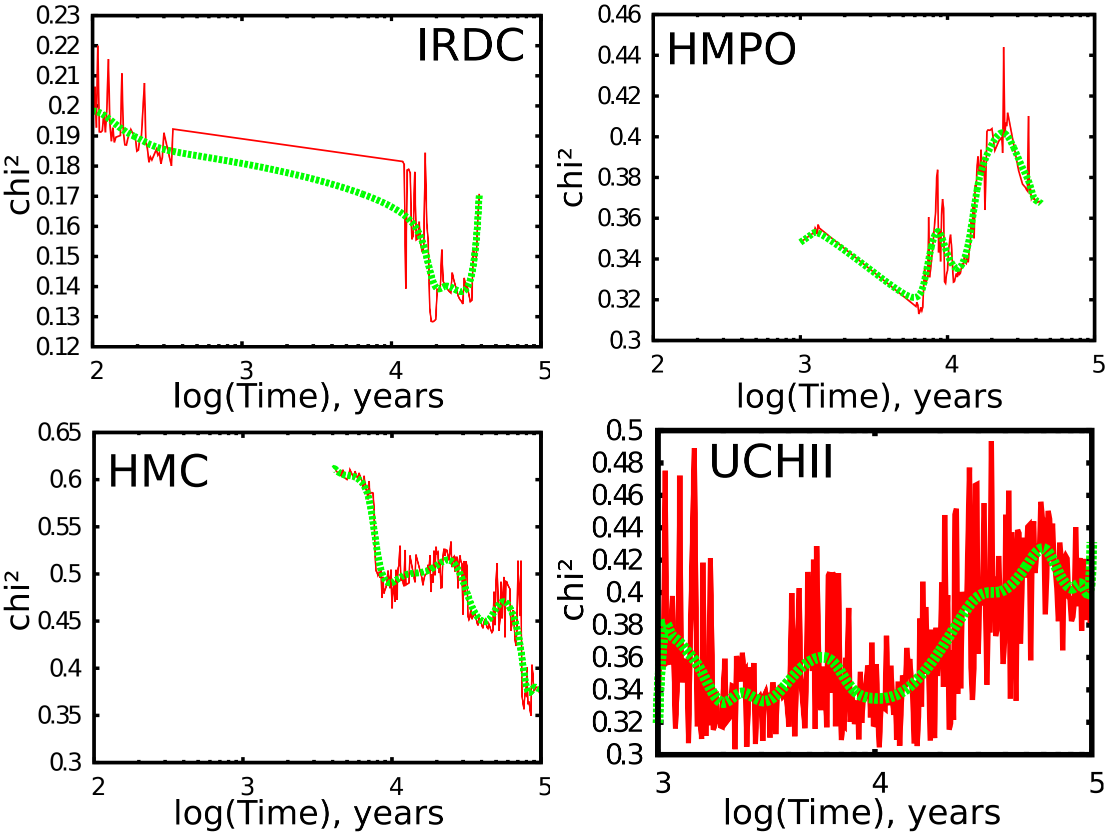

Figure 3.10 Evolution of the minimum χ^2 of the best-fit models with time with only para-H_2 present. The four panels show the four different stages IRDC (upper left), HMPO (upper right), HMC (lower left) and UCHII (lower right). The red curve marks the calculated values at all 299 time moments, whereas the green curve shows their smoothed spline interpolation.

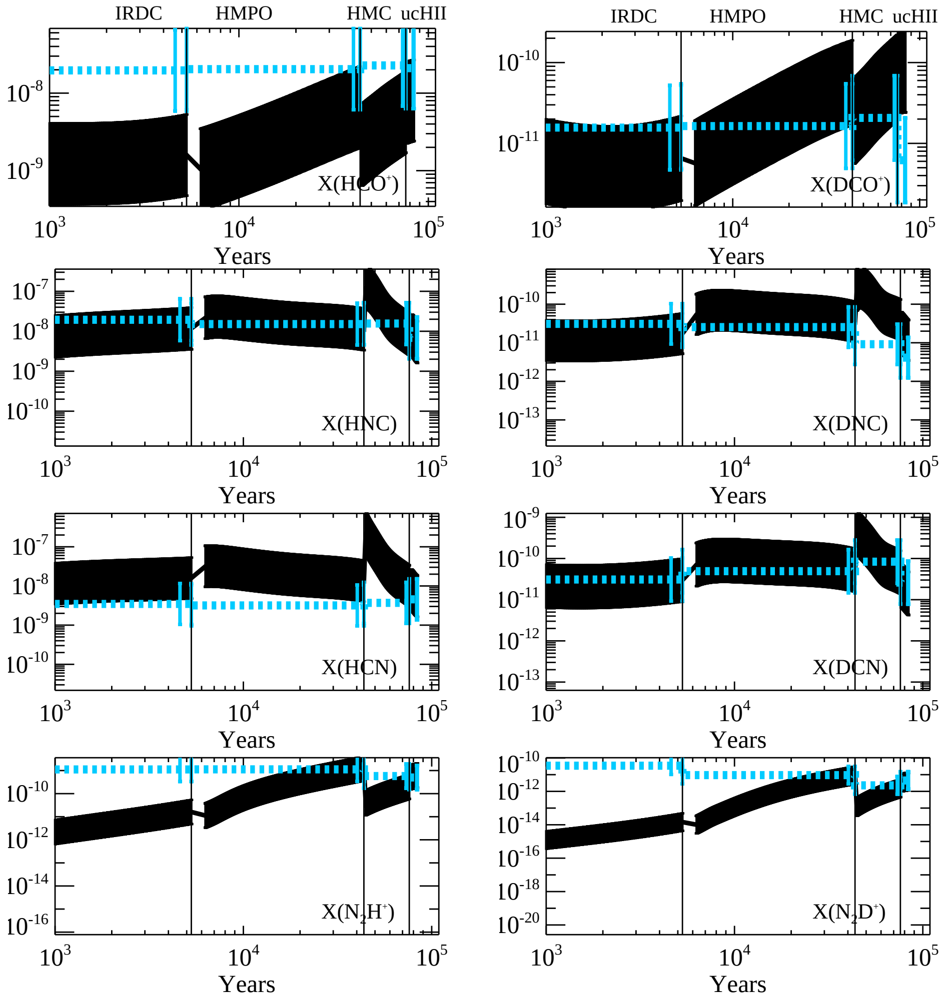

Figure 3.11 The modeled and observed relative abundances to H_2 are plotted for the IRDC-UCHII stages for the model with an ortho-para H_2 ratio of 3:1. The modeled values are shown by the black solid line, the observed values show the median of all detections and upper limits and are depicted by the blue dashed line. The error bars are indicated by the vertical marks.

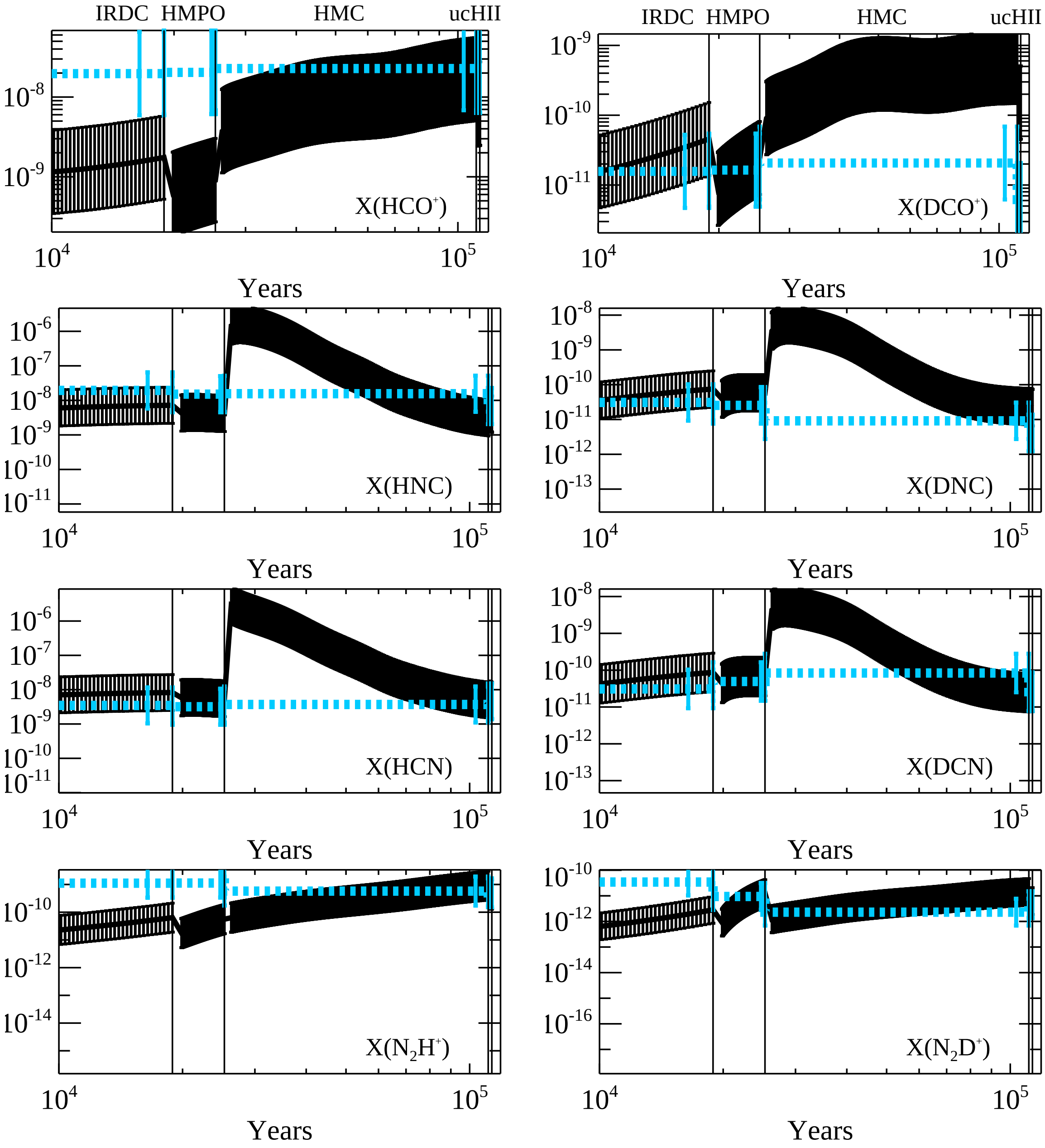

Figure 3.12 The modeled and observed relative abundances to H_2 are plotted for the IRDC-HMC stages for the model with only para-H_2 present. The modeled values are shown by the black solid line, the observed values show the median of all detections and upper limits and are depicted by the blue dashed line. The error bars are indicated by the vertical marks.

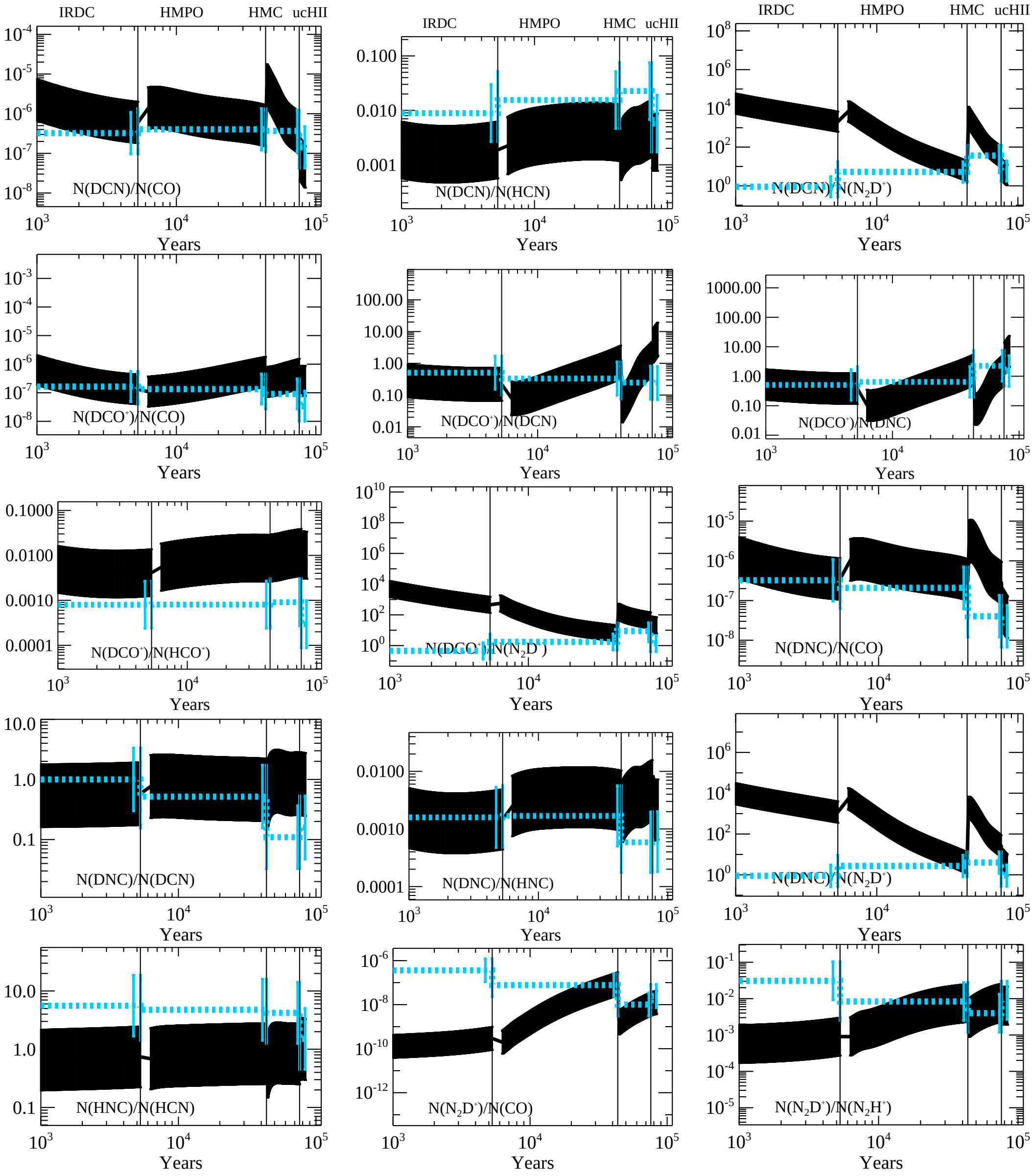

Figure 3.13 The modeled and observed column density ratios are plotted for all stages for the model with an ortho-para H_2 ratio of 3:1. The modeled values are shown by the black solid line, the observed values show the median of all detections and upper limits and are depicted by the blue dashed line. The error bars are indicated by the vertical marks.

In general, the overall fit of all 18 molecules of the four fitted phases is good for both models. The specific time dependent evolution of the best-fit abundances of molecules DCN, DNC, DCO^+, N_2D^+ and their non-deuterated counterparts for model *A* are shown in Figure 3.11 and for model *B* in Figure 3.12. Between two consecutive stages, the physical parameters are instantly changed and the molecular species show a quick response to that change, followed by a slower evolution under the new constant conditions. The difference in the formation pathways of the ions DCO^+ and N_2D^+ plus isotopologues and DNC, DCN, HNC and HCN discussed in Sect. 3.6.2 can be seen in the best-fit plots in Figure 3.12 and in Figures 3.15–3.18 of model *B*. The molecular ions show a strong increase of about two orders of magnitude under the constant and cool conditions during the IRDC and HMPO stage compared to an increase of not even one order of magnitude in the warmer HMC stage. Whereas the non-ions are almost constant during the first two stages, besides a slight increase of DCN and HCN in the IRDC stage and show a strong decrease by more than two orders of magnitude in the warmer HMC stage. For completion, Figures 3.19–3.22 show the column densities for model *A* in each stage separately.

The evolution for the different molecular ratios are shown in Figure 3.13 and Figure 3.14 for model *A* and model *B*, respectively. The modeled abundance ratios show partly larger deviations from the observed values, since the uncertainties from both molecules add up. In Sect. 3.6.1 we discussed the ratio of DCN/DNC and a possible chemical explanation based on a chemical network by Turner (2001). However, the chemical network used in our work shows a different trend with a constant ratio rather than an increase of DCN/DNC with temperature. It agrees with the constant ratio of HNC/HCN of unity with recent developments in the collisional rates by Sarrasin et al. (2010). Thus the observed trend disagrees with our model predictions and the possibility of different chemical formation pathways needs to be tested by future observations of more deuterated molecules sharing the same formation pathways as DCN (e.g., light hydrocarbons with 2 or 3 C-atoms).

3.6.6 Comparison with best-fit models of Paper I

In Paper I we iteratively fitted our model to an observational dataset containing the median column densities of 14 different non-deuterated species. The column densities were derived with typical temperatures for each stage. The model followed the observed evolution and successfully fit most of the species with few exceptions in individual stages. The fits also constrained the physical structure of the model and yielded mean best-fit temperatures for each stage. The mean temperatures deviated from the temperatures used to derive the observed column densities for the later stages. In a second step we fitted the newly derived column densities. The temperature in the best-fit models decreased again and we could not find a converging solution.

In this work we used the best-fit temperatures of the first model from Paper I to recalculate the median column densities for the previously analyzed 14 species and additional four deuterated species. The temperatures in the best-fit models of the IRDC stage are similar for the model in Paper I and model *B* of this work, but the mean density increased by about an order of magnitude. The best-fit lifetime in this

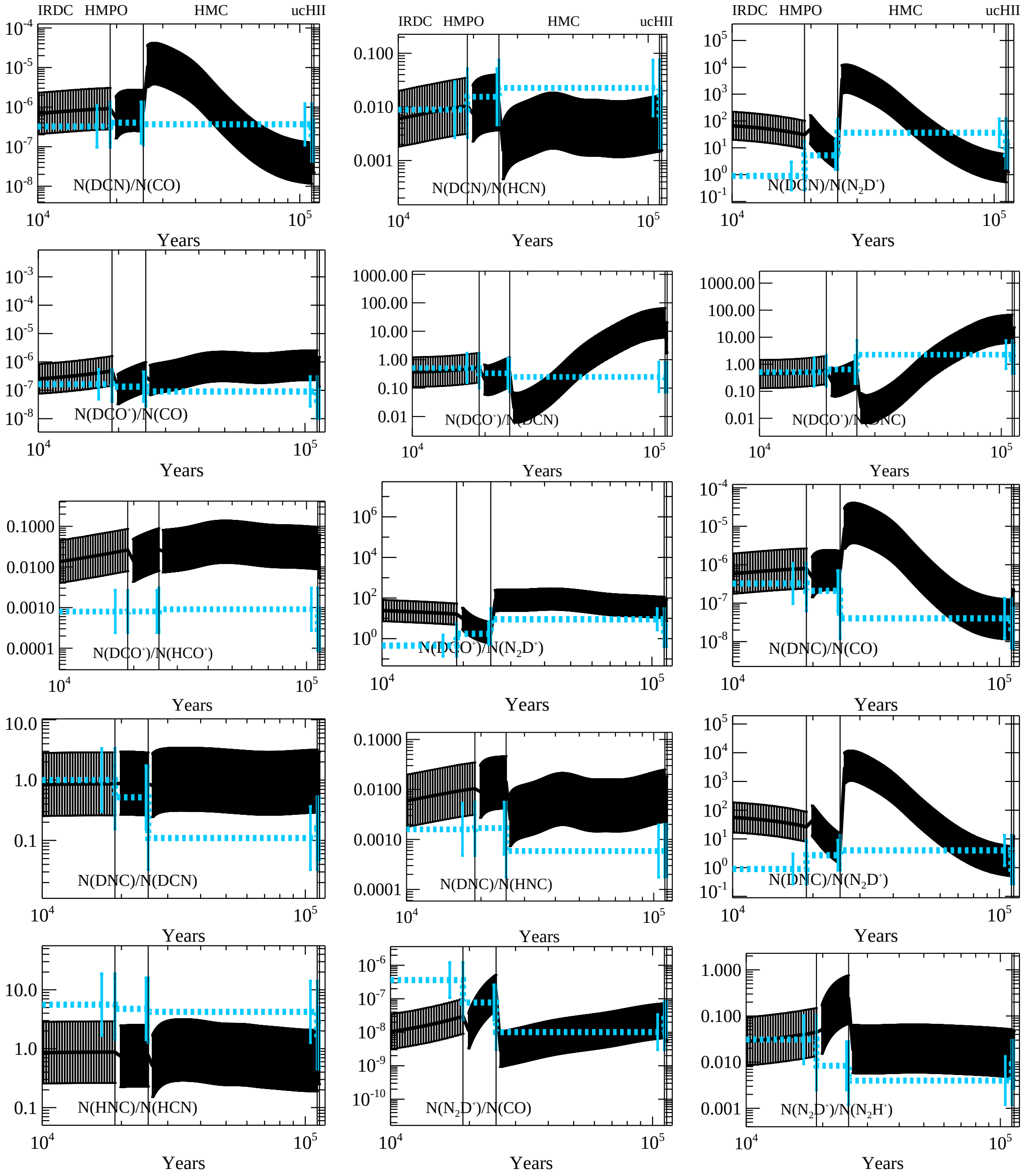

Figure 3.14 The modeled and observed column density ratios are plotted for all stages for the model with only para-H_2 present. The modeled values are shown by the black solid line, the observed values show the median of all detections and upper limits and are depicted by the blue dashed line. The error bars are indicated by the vertical marks.

work is a factor of ~ 2 longer, but agrees within the assumed uncertainties. However, model *A* lead to a much lower best-fit temperature and a shorter lifetime of the IRDC stage. The HMPO best-fit mean temperature in this work is lower by 30% for both models. The mean density increased by a factor $3-4$. The best-fit lifetime is shorter by a factor of ~ 2 for model *A* and almost a magnitude in case of model *B*. The HMC best-fit mean temperature in this work is higher by 25% for model *A* and 50% for model *B*. The mean densities are similar. In comparison to Paper I, the best-fit lifetime is about 25% lower for model *A*, but ~ 2 times larger for model *B*.

The total lifetimes from the IRDC to the UCHII phase in Paper I and model *B* add up to $\sim 110,000$ years. Model *A* total lifetime is slightly lower with $\sim 65,000$ years. The molecules that could not be reproduced in Paper I and this work are not the same (see list of misfitted species in Table 3.5). Possible reasons are the additional four deuterated molecules as free fit parameters that were treated with equal weight as well as the revised excitation temperatures in order to derive column densities compared to Paper I (see Section 3.5.3). Although D-chemistry is seen as a tracer of the thermal history and conditions of an object and we see correlations with luminosity as an evolutionary tracer, the model fits did not improve substantially. Increasing the number of fitted molecules from 14 to 18 species did not improve the achieved results strongly, probably due to the less statistical importance of the deuterated molecules within the total number of 18 species.

3.6.7 Comparison with literature

In low-mass star formation both observations and theory show that it is possible to use the deuteration fraction of a molecule as an evolutionary tracer (e.g., Crapsi et al. 2005; Aikawa et al. 2005; Emprechtinger et al. 2009). In a recent work, Fontani et al. (2011) observed 27 cores within high-mass star-forming regions and derived the deuteration fraction of N_2D^+/N_2H^+. They found a similar behavior as in the low-mass regime. The deuteration fraction is the highest in the starless cores with $D_{\rm frac} = 0.26$ and decreases during the formation of the protostellar objects to $D_{\rm frac} = 0.04$. We find in our work a similar trend, but the median deuteration fraction we measure in our IRDC sample is lower by a factor of four compared to their high-mass starless core sample. That might be due to the fact that our IRDC sample contains starless as well as already more evolved objects inhabiting 24μm sources. The same is true for the HMPO samples of Fontani et al. (2011) and this work. We find lower ratios by about a factor of four. The largest D/H ratio we see is the N_2D^+/N_2H^+ ratio in IRDC20081 of $D_{\rm frac} = 0.12$. This source inhabits no point sources below 70μm, but it is close to a nearby source with extended emission. It is presumably in a very early pre-stellar phase.

Miettinen et al. (2011) studied seven massive clumps within IRDCs and derived deuteration fractions for N_2H^+ between $0.002-0.028$ and for HCO^+ between $0.0002-0.014$. While the range of values for HCO^+ is comparable with the IRDCs in our sample, the deuteration fractions for N_2H^+ are about one order of magnitude higher in this work. Chen et al. (2011) observed several cores in various evolutionary stages and found deuteration values of N_2H^+ between $0.004-0.1$. The source lists have three targets common. For the HMPO18151 both works agree on a value of $D_{\text{frac}} = 0.01$. For the other two sources in common, IRDC18151 and IRDC18223, we find a slightly higher value of $D_{\text{frac}} = 0.03$ instead of $D_{\text{frac}} = 0.02$. While the highest value they found is similar to the maximum value we observe, they detected N_2D^+ in a larger number of sources and found also lower deuteration fractions, especially in the more evolved sources for which we have no detections of N_2D^+.

Work by Crapsi et al. (2005) studying the N_2D^+/N_2H^+ ratio in low-mass starless cores revealed deuteration fractions on the percentage level up to almost 50% in the most extreme case of Oph D. The maximum ratio observed in our survey is ~ 0.1.

Sakai et al. (2012) measured deuteration fractions of DNC/HNC for IRDCs and HMPOs. They find $D_{\text{frac}} = 0.003 - 0.03$ for MSX (Midcourse Space Experiment) dark sources at 8μm and $D_{\text{frac}} = 0.005 - 0.0.01$ for HMPOs. These ratios agree well with $D_{\text{frac}} = 0.001 - 0.01$ for our IRDC sample, but are higher compared to $D_{\text{frac}} = 0.0005 - 0.005$ for our HMPO sample. This is probably due to the fact that Sakai et al. derived the ratio of DNC(1-0) and HN^{13}C(1-0) with a conversion factor $^{12}C/^{13}C = 40 - 62$, while we derive it from HNC(1-0) observations and use HN^{13}C(1-0) observations to derive optical depths, assuming $^{12}C/^{13}C = 89$. This leads to higher HNC column densities in our case and thus lower deuteration fractions compared to their findings.

In a recent study, Kong et al. (2013) explored the effect of different parameters on the deuteration fraction of N_2H^+ in dense and cold environments. They found an increase of the deuteration fraction with decreasing temperature. However, they also found a positive correlation with the density, which is not clearly seen in our data. They employed a 0D model to study deuteration in star-forming clouds and found that the timescales to reach equilibrium in the abundances is on the order of several free-fall times ($\sim 10^6$ years) for typical densities of high-mass cores. In contrast, the best-fit models in our work are not supposed to reach chemical equilibrium and thus our model predicts a total timescale of $\sim 10^5$ years for the best-fit models. This is likely due to the fact that in a 1D model with a power law density profile with higher densities in the inner region timescales in the chemical evolution are shorter than in a 0D model.

3.7 Conclusion

In this work we extended the analysis from Paper I of the chemical evolution in 59 high-mass star forming regions for deuterated molecules. We measured beam averaged column densities and deuteration fractions of the four deuterated species DCO^+, DCN, DNC, and N_2H^+. We find an overall high detection fraction towards the high-mass star-forming regions, except for N_2D^+, which is likely due to the limited sensitivity of our survey. The detection fraction of DCO^+, DCN and DNC increases from IRDCs to HMPOs and peaks at the HMC sample, where we detect all three molecules in all sources but one, and drops again towards the UCHII stage.

The (3-2) lines are sub-thermally populated. The median deuteration fractions we find are 0.02 for DCN, 0.002 for DNC, 0.0009 for DCO^+ and 0.02 for N_2D^+. The deuteration fractions of DNC, DCO^+ and N_2D^+ show a decreasing trend from IRDCs over HMPOs and HMCs to UCHII regions, which supports the hypothesis that deuterated molecules may be used as indicators of the evolutionary stage in high-mass star-forming regions.

In general, we find the strongest correlations between the deuteration fraction of the various molecules and physical parameters in case of N_2H^+. The FWHM of N_2H^+ shows a slight anti-correlation with the observed N_2D^+/N_2H^+ column density ratio. We also find that, in general, the deuteration fraction of all four observed deuterated species anti-correlates with the luminosity of the sources, especially with the N_2D^+/N_2H^+ column density ratio. However, the total measured column density of the gas does not have a strong effect on the deuteration fraction. That leads to the interpretation that, within the range of probed densities, deuteration depends on the temperature of the environment more than on the column density and is enhanced in colder, less luminous regions. However, for example Albertsson et al. (2013) found in their models differences in the deuteration with density at lower densities.

The anti-correlation with luminosity, which is related to the evolutionary stage, indicates that evolutionary stage plays an important role for the deuteration fraction. But its huge scatter within single stages leads to the assumption that the evolution might not be the only factor. Furthermore, we fitted the observed data with a chemical model and find reasonable physical model fits. Combining observations of non-deuterated and deuterated species to obtain best-fits lead to reasonable chemical and physical models. For the model we assumed two extreme ortho-para H_2 ratios of 3:1, resembling conditions of thermal equilibrium, and with only para-H_2 present, taking into account a cold long lived pre-IRDC stage. The best-fit models differ most in their lifetimes and their temperature, but produce both reasonably good results. We cannot deduce the better ortho-para H_2 ratio from our two different models. However, from a chemical and physical point of view, converting all ortho-H_2 into para-H_2 during a pre-IRDC phase takes several million years. The lower best-fit temperature for the IRDC stage in case of the ratio being 3:1 better resembles typical IRDC temperatures. Thus, we favor a true initial ortho-para H_2 ratio closer to 3:1. Due to large uncertainties in the observations and the model and a large spread of observed values within the 4 subsamples we could not substantially improve the best-fit model results compared to Paper I. Another reason is that the combination of the 4 deuterated molecules with the 14 non-deuterated species probably reduced the statistical importance of each molecule and thus the effect on the best-fit of the model.

3.8 Appendix material

Table 3.6 Luminosity, H_2, DCO^+, DCN, DNC and N_2D+ column density and the corresponding error (Δ) for each source. The errors show the uncertainties in the measured integrated flux.

Source	Luminosity log L_{Sun}	H_2 cm^{-2}	DCO^+ cm^{-2}	$\Delta(DCO^+)$ cm^{-2}	DCN cm^{-2}	Δ(DCN) cm^{-2}	DNC	Δ(DNC)	N_2D+	$\Delta(N_2D+)$
IRDC011.1	3.16[a]	3.7(22)	4.5(11)	1.2(11)	≤4.1(11)	3.7(11)	9.3(11)	1.4(11)	≤3.9(11)	9.6(10)
IRDC028.1		3.2(22)	≤1.9(11)	4.8(10)	≤5.4(11)	1.1(11)	≤4.3(11)	9.7(10)	≤6.8(11)	9.6(10)
IRDC028.2	3.47[a]	1.1(23)	9.3(11)	1.1(11)	3.4(12)	3.2(11)	1.5(12)	2(11)	≤6.6(11)	1.9(11)
IRDC048.6	0.78[a]	8.6(21)	1.2(12)	7.1(10)	≤9(11)	1.9(11)	≤4.7(11)	2(11)	≤9.6(11)	2.5(11)
IRDC079.1	2.05[a]	4.3(22)	3.9(12)	8.9(10)	≤8.1(11)	5.1(11)	2.7(12)	1.5(11)	1.5(12)	2.4(11)
IRDC079.3	1.4[a]	2.7(22)	3(12)	1(11)	≤9.6(11)	6.9(11)	1.9(12)	1.5(11)	2.1(12)	3.3(11)
IRDC18151	2.66[a]	5.1(22)	3(12)	1.3(11)	2.3(12)	2.8(11)	3.2(12)	2.3(11)	1.4(12)	2.1(11)
IRDC18182	2.13[a]	1.3(22)	5.4(11)	8(10)	≤5.4(11)	4.3(11)	≤5.7(11)	1.2(11)	≤5.5(11)	8.2(10)
IRDC18223	2.51[a]	2(22)	9.7(11)	1.4(11)	1.3(12)	3.4(11)	3.2(12)	2.5(11)	1.2(12)	1.8(11)
IRDC18306		1.7(22)	≤3(11)	9.8(10)	≤5.7(11)	2(11)	≤6.3(11)	1(11)	≤5.5(11)	2.1(11)
IRDC18308	2.12[a]	2.4(22)	≤2.8(11)	9.3(10)	≤6.1(11)	1.5(11)	≤5.3(11)	2(11)	≤6.8(11)	3.6(11)
IRDC18310		1.6(22)	≤2.9(11)	1.9(11)	≤6.8(11)	2.9(11)	≤4.5(11)	3.1(11)	≤6.8(11)	3.6(11)
IRDC18337	2.25[a]	7.8(21)	≤2.8(11)	1(11)	≤5(11)	2.9(11)	≤3.9(11)	2.2(11)	≤5.8(11)	1.5(11)
IRDC18385	1.23[a]	7.7(21)	≤3.1(11)	9.8(10)	≤6.1(11)	1.2(11)	≤5.9(11)	2.2(11)	≤5.7(11)	1(11)
IRDC18437	2.23[a]	1(22)	≤3.1(11)	1.4(11)	≤5.9(11)	1.2(11)	≤5.3(11)	1.6(11)	≤5(11)	3.7(11)
IRDC18454.1	3.6[b]	1.4(22)	≤2.9(11)	1.1(11)	≤5.2(11)	1.5(11)	≤6.1(11)	1.3(11)		6.9(11)
IRDC18454.3	2.37[a]	2(22)	≤3.1(11)	7.3(10)	≤5.5(11)	2.5(11)	≤7.3(11)	1.7(11)		5.9(11)
IRDC19175	-1[a]	9.1(21)	≤2.7(11)	9.2(10)	≤5.4(11)	2.8(11)	≤4.5(11)	1.3(11)	≤6.5(11)	1.6(11)
IRDC20081		2(22)	1.4(12)	7.4(10)	≤6.1(11)	4(11)	9.1(11)	1.3(11)	8.1(11)	1.3(11)
HMPO18089	4.5[c]	8.2(22)	1.7(12)	9(10)	6.8(12)	2.5(11)	9.7(11)	1.3(11)	≤4.2(11)	9.1(10)
HMPO18102	2.92[c]	4.2(22)	≤1.2(11)	9.7(10)	≤3.8(11)	2.6(11)	1.1(12)	1.2(11)	≤3.8(11)	2.1(11)
HMPO18151	2.03[c]	4.3(22)	8.1(11)	4.4(10)	3.2(12)	1.3(11)	2.1(12)	9.5(10)	3.4(11)	7.6(10)
HMPO18182	3.77[c]	5.5(22)	9.5(11)	7.8(10)	3(12)	2.1(11)	1.7(12)	1.6(11)	≤3.7(11)	6.4(10)
HMPO18247	4.8[c]	2.8(22)	≤1.3(11)	2.2(10)	≤3.7(11)	1.8(11)	≤2(11)	1.2(11)	≤4.1(11)	6.6(10)
HMPO18264	4[c]	9.4(22)	2.4(12)	6.4(10)	6.9(12)	1.6(11)	4.4(12)	1.1(11)	1(12)	1.5(11)
HMPO18310	3.48[c]	2.9(22)	≤1.6(11)	1(11)	≤4.1(11)	3.3(11)	≤3.1(11)	1.5(11)	6.7(11)	1.3(11)
HMPO18488	4.5[c]	3.2(22)	2.4(11)	5.2(10)	1.4(12)	1.8(11)	≤2.1(11)	9.4(10)	≤3.3(11)	1.2(11)
HMPO18517	4.1[c]	7(22)	2(12)	5.6(10)	5.6(12)	2.3(11)	1.6(12)	1.3(11)	≤3.9(11)	1.2(11)
HMPO18566	4.8[c]	2.5(22)	3.8(11)	1.4(11)	2.3(12)	2.4(11)	8.1(11)	1.3(11)	≤4.1(11)	1.6(07)
HMPO19217	4.9[c]	4.2(22)	6.4(11)	9.6(10)	2.6(12)	2.3(11)	≤2.9(11)	2.4(11)	≤3(11)	7.6(10)
HMPO19410	4[c]	6.8(22)	1.3(12)	6.2(10)	3.5(12)	1.5(11)	2.6(12)	1.1(11)	1.5(12)	1.1(11)
HMPO20126	3.9[c]	5.7(22)	1.3(12)	8(10)	7.4(12)	1.8(11)	3.6(12)	1.3(11)	7.7(11)	1.2(11)
HMPO20216	3.3[c]	1.3(22)	4.9(11)	6.4(10)	1.1(12)	1.4(11)	1.2(12)	9.8(10)	≤3(11)	1.4(11)
HMPO20293	3.4[c]	4.3(22)	9.9(11)	7(10)	1.9(12)	2.4(11)	1.6(12)	1(11)	1.7(12)	1.6(11)
HMPO22134	4.1[c]	2.4(22)	6.9(11)	5.3(10)	1.2(12)	1.4(11)	3.6(11)	6.3(10)	≤2.8(11)	1.6(11)
HMPO23033	4[c]	4(22)	1.2(12)	7.9(10)	2.1(12)	2.6(11)	1.1(12)	1.6(11)	3.9(11)	1(11)
HMPO23139	4.4[c]	3(22)	2.8(11)	7.9(10)	1.7(12)	1.5(11)	≤2.5(11)	5.6(10)	≤2.3(11)	1.6(11)
HMPO23151	5[c]	2.3(22)	≤1.2(11)	5.4(10)	6.1(11)	1.1(11)	≤2.3(11)	9(10)	≤2.5(11)	1.6(11)
HMPO23545	3[c]	1.5(22)	1.5(11)	5.2(10)	≤3.3(11)	1.6(11)	≤2.7(11)	9(10)	≤3.1(11)	1.7(11)
HMC009.62	4.3[d]	9.5(22)	8.7(11)	9.6(10)	5.6(12)	1.1(11)	6.1(11)	7.6(10)	≤1.7(11)	1.4(11)
HMC010.47	5.5[e]	2.3(23)	6(12)	7(10)	1.2(13)	2.9(11)		3(11)		5.4(11)
HMC029.96	6[e]	9.4(22)	3.6(11)	1.2(11)	6.4(12)	1.7(11)	8.7(11)	8.6(10)	≤3.1(11)	1.4(11)
HMC031.41	5.2[e]	1.6(23)	5(12)	7.8(10)	8(12)	1.4(11)	5.8(11)	1.3(11)		1.8(11)
HMC034.26	5.7[e]	4.1(23)	5.9(12)	8.7(10)	1.9(13)	1.7(11)	2.5(12)	1.5(11)	≤3.3(11)	1.7(11)
HMC045.47	5.6[e]	4.5(22)	2.8(11)	5.5(10)	1.7(12)	1.3(11)	7.3(11)	1.3(11)	≤2.5(11)	2(11)
HMC075.78	5.3[e]	6.3(22)	1.1(12)	5.5(10)	4.9(12)	1.3(11)	1.1(12)	7.7(10)	≤1.9(11)	1.2(11)
W3H2O	4.48[f]	7.4(22)	3.4(12)	9.1(10)	1.6(13)	1.5(11)	2.1(12)	7.8(10)	≤2.8(11)	5.8(10)
W3IRS5	5.3[g]	6(22)	4.2(11)	7.6(10)	1.5(12)	1.1(11)	≤1.8(11)	1.2(11)	≤1.7(11)	7.1(10)
NGC7538B	5.8[e]	1.2(23)	2(12)	7.8(10)	1.4(13)	1.5(11)	1.5(12)	1(11)	≤1.6(11)	7.1(10)
Orion-KL	5[h]	1.3(24)	2.8(13)	1.6(11)	1.3(14)	1.6(12)		4.3(11)		1.2(12)
UCH005.89	5.3[e]	2.2(23)	1.3(12)	1.6(11)	2.1(13)	1.5(11)	6.3(12)	2.3(11)	≤2.5(11)	5.8(10)
UCH010.10		6.4(21)	≤1.9(11)	2.2(10)	≤2.8(11)	1.5(11)	≤3(11)	1.8(11)	≤2.8(11)	6.9(10)
UCH010.30	5.8[e]	8.1(22)	7(11)	1.1(11)	3.7(12)	2.1(11)	1.9(12)	1.4(11)	≤3.5(11)	1.2(11)
UCH012.21	5.8[e]	9.6(22)	≤2.1(11)	2.5(10)	5.2(12)	2.6(11)	≤2.3(11)	1.3(11)	≤4.1(11)	1.6(11)
UCH013.87	5.2[e]	5.3(22)	4.7(11)	6.4(10)	1.7(12)	1.6(11)	≤3(11)	5.5(10)	≤3.3(11)	3.2(11)
UCH030.54	5.7[i]	2.1(22)	2.4(11)	8.3(10)	≤3.2(11)	2.2(11)	≤2.3(11)	1.1(11)	≤3.4(11)	1.8(11)
UCH035.20	5.3[e]	1.1(23)	5.6(11)	1(11)	3.6(12)	1.9(11)	1.4(12)	2(11)	≤3.1(11)	1.3(11)
UCH045.12	5.9[e]	7.4(22)	4.6(11)	8.5(10)	1.8(12)	2.1(11)	6.1(11)	1.3(11)	≤2.7(11)	1.9(11)
UCH045.45	5.7[e]	4.2(22)	≤1.2(11)	1(11)	1.9(12)	2.2(11)	≤1.9(11)	1.8(11)	≤3.5(11)	1.9(11)

Notes. Column densities written as $a(x) = a \times 10^x$. H_2 column density is averaged over a 29″-beam and for all other molecules over a 30″-beam.
[a] Ragan et al. (2012), [b] Beuther et al. (2012), [c] Sridharan et al. (2002), [d] Linz et al. (2005), [e] Churchwell et al. (1990), [f] Chen et al. (2006), [g] Campbell et al. (1995), [h] Beuther et al. (2004), [i] Wood & Churchwell (1989a)

Table 3.7 HCO^+, HCN, HNC and N_2H^+ column density and corresponding error (Δ) for each source. The errors show the uncertainties in the measured integrated fluxes and determined optical depths.

Source	HCO^+ cm^{-2}	Δ(HCO^+) cm^{-2}	HCN cm^{-2}	Δ(HCN) cm^{-2}	HNC	Δ(HNC)	N_2H^+	Δ(N_2H^+)
IRDC011.1	1.1(15)	3.3(15)	6.7(13)	4.2(12)	7.2(14)	1.6(15)	2.8(13)	9.5(11)
IRDC028.1	6.3(14)	1.1(15)	1.2(14)	4.9(12)	5.1(14)	6.9(14)	4(13)	3.2(11)
IRDC028.2	1.4(15)	6.9(15)	1.9(14)	8(12)	5.5(14)	1.9(15)	6.5(13)	2.5(12)
IRDC048.6	1.4(14)	5.5(14)	2.7(13)	3(13)	1.2(14)	3.3(14)	8(12)	8.4(11)
IRDC079.1	1(15)	1.5(15)	7.2(13)	2.4(12)	2.9(14)	8(14)	2.3(13)	1.8(12)
IRDC079.3	7.9(14)	3.7(15)	7.2(13)	7.1(13)	4.7(14)	1.4(15)	2.5(13)	2.2(12)
IRDC18151	2(15)	1.3(15)	1.6(14)	2.8(14)	3.8(14)	2.1(14)	4.9(13)	1(12)
IRDC18182	3.9(14)	2(15)	3.4(13)	2.4(12)	2.9(14)	1(15)	1.6(13)	5.8(11)
IRDC18223	8.5(14)	1.2(15)	1.2(14)	1.4(14)	9(14)	1.1(15)	3.7(13)	2.2(11)
IRDC18306	3.1(14)	5(15)	$\leq$2.3(12)	3.4(12)	2.9(14)	2.8(15)	1.6(13)	1.8(12)
IRDC18308	3(14)	2(15)	2(14)	1.1(14)	4.1(14)	7.4(14)	2.2(13)	3.9(10)
IRDC18310	3(14)	1.3(15)	6.6(13)	3.4(12)	4.5(14)	9.4(12)	3.3(13)	6.9(11)
IRDC18337	5.4(14)	2.8(15)	6.9(13)	3(12)	3(14)	8.6(12)	1.8(13)	3.6(11)
IRDC18437	2.8(14)	1.7(15)	1.9(13)	7.2(13)	1.1(14)	5.7(15)	1.5(13)	1.8(13)
IRDC18385	2.3(14)	1.7(15)	2(13)	3(12)	4.2(14)	3.1(14)	1.1(13)	1.5(12)
IRDC18454.	3.4(14)	2.4(15)	$\leq$2.9(12)	3.2(12)	2(14)	6.7(12)	1.9(13)	2.2(12)
IRDC18454.	8.8(14)	2.3(15)	1.3(14)	5(12)	7.6(14)	2.3(15)	3.2(13)	7.9(11)
IRDC19175	2.4(14)	3.1(15)	1.8(13)	1.6(12)	8.2(13)	4.8(14)	5.6(12)	2.3(12)
IRDC20081	3.1(14)	6.6(14)	1.2(14)	1.1(14)	1.6(14)	7.3(14)	6.5(12)	1.5(12)
HMPO18089	1.9(15)	4.6(15)	2(14)	1.5(12)	9.5(14)	2.1(15)	4.9(13)	3.7(11)
HMPO18102	8.5(14)	1.4(15)	1.8(14)	1.7(12)	1.9(15)	3.3(15)	6.5(13)	1.2(12)
HMPO18151	1.6(15)	8.4(14)	1.8(14)	1.6(12)	6.1(14)	2.6(14)	3.6(13)	4.1(12)
HMPO18182	8.1(14)	6.7(14)	1.3(14)	7(14)	6.3(14)	5.3(14)	6.4(13)	2.4(11)
HMPO18247	3(14)	6.1(14)	1.2(14)	8(13)	4.1(14)	6.4(14)	3.7(13)	4.4(12)
HMPO18264	2.7(15)	9.7(14)	8.6(14)	4.1(14)	9.7(14)	4.8(14)	1.1(14)	3.1(12)
HMPO18310	6.7(14)	3.4(15)	5.9(13)	1.2(12)	8.5(14)	1.8(15)	3.1(13)	1.5(11)
HMPO18488	1.1(15)	1.8(15)	1.3(14)	1.4(12)	1.2(15)	5.5(15)	4.1(13)	1.5(13)
HMPO18517	2.2(15)	1.5(15)	1.8(14)	8.2(11)	4.8(14)	3.4(14)	7.6(13)	9.6(12)
HMPO18566	1(15)	2.1(15)	1.3(14)	1.5(12)	1.5(15)	7.3(15)	5.5(13)	1.2(12)
HMPO19217	7.9(14)	1.3(15)	8.3(13)	1.8(12)	5.5(14)	1.4(15)	4.7(13)	5.2(11)
HMPO19410	1.5(15)	1.2(15)	1.4(14)	7.5(11)	7.9(14)	4.7(14)	1(14)	1.3(12)
HMPO20126	1.7(15)	8.8(14)	1.9(14)	1.2(15)	1.1(15)	8.7(14)	7.6(13)	6.4(11)
HMPO20216	4.9(14)	5.1(14)	5.9(13)	1.4(12)	2.6(14)	4.3(14)	1(13)	3(12)
HMPO20293	5.8(14)	3.3(14)	1.1(14)	3.7(14)	7.1(14)	4.2(14)	1.1(14)	3.7(12)
HMPO22134	7.7(14)	7.5(14)	1.2(14)	4.7(13)	1.6(14)	3.1(14)	1.1(13)	4(11)
HMPO23033	5.4(14)	3.7(14)	1.8(14)	1.9(13)	5.5(14)	3.2(14)	4.5(13)	1.2(12)
HMPO23139	9.2(14)	1.1(15)	3(14)	1.4(14)	2.5(14)	3(14)	3(13)	1.3(12)
HMPO23151	2.5(14)	4.3(14)	5.4(13)	4(13)	6(13)	1.4(14)	1.1(12)	8(12)
HMPO23545	1.9(14)	2.7(14)	2.4(13)	5(12)	4.1(13)	1.1(14)	2.3(12)	1.2(12)
HMC009.62	2.2(15)	1.4(15)	3.2(14)	1.1(13)	2.2(15)	1.2(15)	1(14)	3.8(11)
HMC010.47	1.7(15)	1.6(15)	3.5(14)	1.9(12)	3.1(15)	2.1(15)	1.6(14)	3.9(12)
HMC029.96	2.8(15)	2.1(15)	4.2(14)	1.8(12)	1.5(15)	7.3(14)	5.9(13)	5.6(11)
HMC031.41	1(15)	5.1(15)	1(14)	3.9(12)	1.2(15)	2.8(15)	4.4(13)	2.3(12)
HMC034.26	4.3(15)	2(15)	5(14)	1.4(13)	1.6(15)	4.6(14)	9.7(13)	1.5(12)
HMC045.47	1.2(15)	1.4(15)	1.2(14)	1(12)	1.7(15)	1.9(15)	7.3(13)	6.4(11)
HMC075.78	2.7(15)	1.8(15)	1.8(14)	1.3(12)	9.8(14)	1.3(15)	5.5(13)	9.5(11)
W3H2O	1.6(15)	8.1(14)	5.5(14)	5.6(14)	4(14)	3(14)	2(13)	2(12)
W3IRS5	1.9(15)	5.1(14)	3.3(14)	1.6(12)	3.4(14)	5.6(14)	2.2(12)	4.4(11)
NGC7538B	2.3(15)	1.1(15)	4.5(14)	3.1(12)	5.2(14)	3.7(14)	1.3(13)	1(12)
Orion-KL	5.2(15)	1.4(16)	1.2(16)	3.1(13)	1.5(15)	7.4(14)	4.3(12)	1.5(12)
UCH005.89	1.2(16)	6.1(15)	1.3(15)	5.3(12)	6.8(15)	1.8(15)	2.1(14)	7.2(11)
UCH010.10	3(14)	1.4(16)	3.6(13)	2.8(13)	9(13)	8.5(12)	2.1(13)	7.3(13)
UCH010.30	3.2(15)	1.6(15)	6.7(14)	2.9(12)	3.7(15)	2.6(15)	1.3(14)	6(11)
UCH012.21	1.2(15)	1.3(15)	2.6(14)	3.7(12)	1(15)	9.2(14)	7.3(13)	3.1(13)
UCH013.87	2(15)	3(15)	4.1(14)	2.5(12)	8.7(14)	1.3(15)	3.9(13)	3.3(11)
UCH030.54	4.6(14)	6.8(14)	1(14)	8.5(11)	1.8(14)	2.5(14)	5.8(12)	2(12)
UCH035.20	2.1(15)	9.2(14)	3.4(14)	1.3(12)	5(14)	5(14)	3.7(13)	3.4(11)
UCH045.12	1.5(15)	9.9(14)	5.6(14)	2.5(12)	3.2(14)	2.7(14)	8.7(12)	1.7(12)
UCH045.45	6.3(14)	6.2(14)	1.4(14)	1.1(12)	3.6(14)	6.9(14)	2.1(13)	4.3(11)

Notes. Column densities written as $a(x) = a \times 10^x$. H_2 column density is averaged over a 29″-beam and for all other molecules over a 30″-beam. The given errors are uncertainties in the measured integrated fluxes and the optical depth τ. The high uncertainties in some cases are due to high uncertainties in the determined optical depth.

Table 3.8 Derived values for the optical depth τ for HNC and HCO^+ for each source.

Source	$\tau(HNC^+)$	$\tau(HCO^+)$
IRDC011.1	$38.0^{+2.3}_{-2.2}$	$20.4^{+3.1}_{-2.8}$
IRDC028.1	$16.6^{+1.3}_{-1.3}$	$9.9^{+1.7}_{-1.6}$
IRDC028.2	$27.8^{+3.5}_{-3.2}$	$32.6^{+4.8}_{-4.3}$
IRDC048.6	$17.5^{+2.7}_{-2.5}$	$11.3^{+0.6}_{-0.6}$
IRDC079.1	$22.9^{+2.8}_{-2.6}$	$16.1^{+5.1}_{-4.4}$
IRDC079.3	$31.6^{+3.0}_{-2.8}$	$9.5^{+1.5}_{-1.4}$
IRDC18151	$7.5^{+0.5}_{-0.5}$	$27.2^{+15.8}_{-11.5}$
IRDC18182	$29.1^{+3.5}_{-3.3}$	$13.0^{+6.6}_{-5.2}$
IRDC18223	$29.0^{+1.3}_{-1.2}$	$9.8^{+4.3}_{-3.7}$
IRDC18306	$44.7^{+9.4}_{-7.9}$	$18.5^{+5.2}_{-4.5}$
IRDC18308	$18.2^{+1.8}_{-1.7}$	$13.8^{+6.2}_{-5.3}$
IRDC18310		$22.4^{+12.9}_{-9.4}$
IRDC18337		$9.1^{+3.8}_{-3.4}$
IRDC18385	$36.2^{+4.7}_{-4.2}$	
IRDC18437	$9.6^{+2.9}_{-2.6}$	$23.7^{+1.5}_{-1.4}$
IRDC18454.1	$8.8^{+1.2}_{-32.3}$	$14.1^{+2.2}_{-2.0}$
IRDC18454.3	$22.7^{+3.0}_{-2.7}$	$15.7^{+7.5}_{-6.1}$
IRDC19175	$12.3^{+5.8}_{-4.8}$	$17.8^{+6.9}_{-5.8}$
IRDC20081	$21.0^{+4.5}_{-3.9}$	$9.8^{+2.6}_{-2.4}$
HMPO18089	$32.8^{+2.2}_{-2.1}$	$29.8^{+5.1}_{-4.4}$
HMPO18102	$29.7^{+1.7}_{-1.7}$	$11.2^{+0.7}_{-0.7}$
HMPO18151	$9.0\ ^{+0.4}_{-0.4}$	$13.1^{+0.5}_{-0.5}$
HMPO18182	$12.5^{+0.8}_{-0.8}$	$14.0^{+1.0}_{-1.0}$
HMPO18247	$14.8^{+1.5}_{-1.5}$	$7.9^{+0.6}_{-0.6}$
HMPO18264	$10.6^{+0.5}_{-0.5}$	$14.5^{+1.7}_{-1.6}$
HMPO18310	$29.3^{+2.1}_{-2.0}$	$15.1^{+0.8}_{-0.8}$
HMPO18488	$32.9^{+4.7}_{-4.1}$	$36.3^{+2.4}_{-2.2}$
HMPO18517	$7.0\ ^{+0.7}_{-0.7}$	$15.0^{+1.6}_{-1.5}$
HMPO18566	$41.5^{+4.8}_{-4.3}$	$15.9^{+0.5}_{-0.5}$
HMPO19217	$16.7^{+2.6}_{-2.4}$	$14.3^{+0.8}_{-0.8}$
HMPO19410	$13.0^{+0.6}_{-0.6}$	$13.4^{+2.1}_{-1.9}$
HMPO20126	$13.0^{+0.8}_{-0.8}$	$13.5^{+0.4}_{-0.4}$
HMPO20216	$10.2^{+1.6}_{-1.5}$	$15.7^{+1.0}_{-1.0}$
HMPO20293	$11.1^{+0.6}_{-0.6}$	$15.7^{+1.2}_{-1.2}$
HMPO22134	$9.9^{+1.9}_{-1.8}$	$8.7^{+1.8}_{-1.7}$
HMPO23033	$9.7^{+0.6}_{-0.6}$	$8.2^{+1.4}_{-1.4}$
HMPO23139	$7.8^{+1.2}_{-1.2}$	$18.2^{+1.6}_{-1.5}$
HMPO23151	$5.2^{+2.3}_{-2.3}$	$18.4^{+0.7}_{-0.7}$
HMPO23545	$5.7^{+2.6}_{-2.5}$	$19.1^{+2.1}_{-1.9}$
HMC009.62	$13.4^{+0.5}_{-0.5}$	$20.2^{+0.6}_{-0.6}$
HMC010.47	$14.1^{+0.7}_{-0.7}$	$13.1^{+0.9}_{-0.9}$
HMC029.96	$12.6^{+0.5}_{-0.5}$	$25.7^{+0.7}_{-0.7}$
HMC031.41	$22.0^{+2.3}_{-2.2}$	$38.6^{+5.0}_{-4.5}$
HMC034.26	$8.6^{+0.3}_{-0.3}$	$21.0^{+0.5}_{-0.4}$
HMC045.47	$19.1^{+1.1}_{-1.1}$	$18.0^{+1.2}_{-1.1}$
HMC075.78	$11.1^{+1.3}_{-1.2}$	$19.0^{+0.7}_{-0.6}$
W3H2O	$4.8^{+0.7}_{-0.7}$	$13.9^{+0.5}_{-0.5}$
W3IRS5	$8.0^{+1.6}_{-1.5}$	$8.8^{+0.3}_{-0.7}$
NGC7538B	$5.9^{+0.7}_{-0.7}$	$11.6^{+0.5}_{-0.5}$
ORION-KL	$3.1^{+0.4}_{-0.4}$	$14.2^{+2.8}_{-2.6}$
UCH005.89	$18.7^{+0.3}_{-0.3}$	$11.0^{+1.5}_{-1.4}$
UCH010.10		$12.8^{+0.4}_{-0.4}$
UCH010.30	$17.7^{+0.7}_{-0.7}$	$11.8^{+0.6}_{-0.6}$
UCH012.21	$10.5^{+0.9}_{-0.9}$	$25.0^{+0.5}_{-0.5}$
UCH013.87	$15.9^{+1.5}_{-1.4}$	
UCH030.54	$4.4^{+1.3}_{-1.3}$	$15.2^{+0.5}_{-0.5}$
UCH035.20	$8.8^{+1.0}_{-1.0}$	$11.4^{+1.1}_{-1.0}$
UCH045.12	$4.3^{+0.8}_{-0.8}$	$27.0^{+1.5}_{-1.4}$
UCH045.45	$8.9^{+1.9}_{-1.8}$	$8.8^{+1.0}_{-0.9}$

Notes. The optical depth was derived by comparing T_{mb} of the main isotopologue with T_{mb} of the minor isotopologue and under the assumption of the atomic ratio $^{12}C/^{13}C$=89 (see Section 3.5.3). The optical depth was only used in the cases where $\tau < 50$. All other cases were considered as unreliable.

Table 3.9 Parameters of the best-fit IRDC model.

Parameter	Symbol	Model *A*	Model *B*
Inner radius	r_0	12 700 AU	12 650 AU
Outer radius	r_1	0.5 pc[a]	0.5 pc[a]
Density at the inner radius	ρ_0	1.4×10^5 cm^{-3}	1.7×10^5 cm^{-3}
Average density with a beam of 26 000 AU	$\bar{\rho}$	8.9×10^4 cm^{-3}	1.0×10^5 cm^{-3}
Average density with a beam of 54 000 AU	$\bar{\rho}$	5.2×10^4 cm^{-3}	5.5×10^4 cm^{-3}
Density profile	p	1.5	1.8
Temperature at the inner radius	T_0	11.3 K	
Average temperature	$\bar{T}$	11.3 K	20.0 K
Temperature profile	q	0	0
Lifetime		5 300 years	19 000 years

Notes. Model *A* with an ortho-para H_2 ratio of 3:1 and model *B* with only para-H_2 present.
[a] This value is limited by the largest 29″ IRAM beam size used in our observations.

Table 3.10 Parameters of the best-fit HMPO model.

Parameter	Symbol	Model *A*	Model *B*
Inner radius	r_0	103 AU	310 AU
Outer radius	r_1	0.5 pc[a]	0.5 pc[a]
Density at the inner radius	ρ_0	1.5×10^9 cm^{-3}	4.6×10^8 cm^{-3}
Average density with a beam of 21 725 AU	$\bar{\rho}$	1.6×10^6 cm^{-3}	2.2×10^6 cm^{-3}
Average density with a beam of 57 275 AU	$\bar{\rho}$	3.7×10^5 cm^{-3}	3.6×10^5 cm^{-3}
Density profile	p	1.8	2.0
Temperature at the inner radius	T_0	72.2 K	40.2 K
Average temperature	$\bar{T}$	20.5 K	$20 - 21$ K
Temperature profile	q	0.4	0.4
Lifetime		38 400 years	6 400 years

Notes. Model *A* with an ortho-para H_2 ratio of 3:1 and model *B* with only para-H_2 present.
[a] This value is limited by the largest 29″ IRAM beam size used in our observations.

Table 3.11 Parameters of the best-fit HMC model.

Parameter	Symbol	Model *A*	Model *B*
Inner radius	r_0	310 AU	3 430 AU
Outer radius	r_1	0.5 pc[a]	0.5 pc[a]
Density at the inner radius	ρ_0	4.6×10^8 cm^{-3}	1.0×10^7 cm^{-3}
Average density with a beam of 45 400 AU	$\bar{\rho}$	1.2×10^6 cm^{-3}	8.1×10^5 cm^{-3}
Average density with a beam of 63 100 AU	$\bar{\rho}$	7.6×10^5 cm^{-3}	5.0×10^5 cm^{-3}
Density profile	p	1.7	1.8
Temperature at the inner radius	T_0	278.6 K	
Average temperature	$\bar{T}$	$47 - 51$ K	$56 - 61$ K
Temperature profile	q	0.4	0.4
Lifetime		32 400 years	85 700 years

Notes. Model *A* with an ortho-para H_2 ratio of 3:1 and model *B* with only para-H_2 present.
[a] This value is limited by the largest 29″ IRAM beam size used in our observations.

Table 3.12 Parameters of the best-fit UCHII model.

Parameter	Symbol	Model *A*	Model *B*
Inner radius	r_0	103 AU	1 143 AU
Outer radius	r_1	0.5 pc[a]	0.5 pc[a]
Density at the inner radius	ρ_0	8.2×10^9 cm^{-3}	2.2×10^7 cm^{-3}
Average density with a beam of 57 800 AU	$\bar{\rho}$	1.3×10^6 cm^{-3}	4.7×10^5 cm^{-3}
Average density with a beam of 85 400 AU	$\bar{\rho}$	6.7×10^5 cm^{-3}	2.5×10^5 cm^{-3}
Density profile	p	1.95	1.5
Temperature at the inner radius	T_0	411.6 K	155.1 K
Average temperature	$\bar{T}$	$47 - 52$ K	$38 - 42$ K
Temperature profile	q	0.4	0.4
Lifetime		8 000 years	2 300 years

Notes. Model *A* with an ortho-para H_2 ratio of 3:1 and model *B* with only para-H_2 present.
[a] This value is limited by the largest 29″ IRAM beam size used in our observations.

Table 3.13 Median column densities in $a(x) = a \times 10^x$ for observations (including detections and upper limits) and best-fit IRDC model with ortho-para H_2 ratio of 3:1 (model *A*) and with only para-H_2 (model *B*). Modeled best-fit values in italics do not agree with the observed values within one order of magnitude. If the molecule is detected in less than 50% of the sources we marked it as an upper limit.

Molecule	Obs. col. den. [cm^{-2}]	Model *A* col. den. [cm^{-2}]	Model *B* col. den. [cm^{-2}]
CO	1.9(18)	1.1(18)	2.1(18)
HNC	3.8(14)	3.9(14)	2.8(14)
HCN	6.9(13)	5.4(14)	3.3(14)
HCO^+	3.9(14)	3.9(13)	5.5(13)
HNCO	2.4(12)	3.2(12)	2.6(12)
H_2CO	1.7(13)	2.8(13)	3.4(13)
N_2H^+	2.2(13)	*3.9(11)*	2.2(12)
CS	$\leq$4.7(14)	8.0(14)	4.9(14)
SO	$\leq$6.6(12)	2.0(13)	5.7(13)
OCS	$\leq$4.2(15)	3.0(12)	1.5(12)
C_2H	4.8(14)	2.4(14)	1.7(14)
SiO	2.3(12)	3.7(12)	4.4(12)
CH_3CN	$\leq$3.7(12)	4.7(12)	5.0(12)
CH_3OH	$\leq$4.1(13)	2.0(12)	1.0(13)
DCO^+	$\leq$3.1(11)	1.9(11)	1.9(12)
DCN	6.1(11)	1.0(12)	4.1(12)
DNC	6.1(11)	6.0(11)	3.6(12)
N_2D^+	6.8(11)	4.0(8)	1.2(11)
Agreement		17/18 = 94%	18/18 = 100%

Table 3.14 Median column densities in $a(x) = a \times 10^x$ for observations (including detections and upper limits) and best-fit HMPO model with ortho-para H_2 ratio of 3:1 (model *A*) and with only para-H_2 (model *B*). Modeled best-fit values in italics do not agree with the observed values within one order of magnitude. If the molecule is detected in less than 50% of the sources we marked it as an upper limit.

Molecule	Obs. col. den. [cm^{-2}]	Model *A* col. den. [cm^{-2}]	Model *B* col. den. [cm^{-2}]
CO	5.0(18)	4.8(18)	4.5(18)
HNC	6.2(14)	5.0(14)	3.8(14)
HCN	1.3(14)	6.0(14)	5.0(14)
HCO^+	8.3(14)	3.5(14)	*4.4(13)*
HNCO	3.8(12)	3.7(13)	*8.5(13)*
H_2CO	4.1(13)	3.8(13)	5.0(13)
N_2H^+	4.6(13)	1.2(14)	4.6(12)
CS	1.1(15)	3.2(14)	9.2(14)
SO	8.2(13)	*2.4(15)*	1.4(14)
OCS	$\leq$2.0(14)	3.5(13)	6.7(12)
C_2H	1.9(15)	2.1(14)	*1.5(14)*
SiO	5.9(12)	1.4(13)	7.7(12)
CH_3CN	3.4(12)	8.0(12)	1.3(13)
CH_3OH	1.4(14)	*2.9(12)*	1.0(14)
DCO^+	6.7(11)	3.2(12)	1.8(12)
DCN	2.0(12)	2.4(12)	7.4(12)
DNC	1.0(12)	1.6(12)	6.4(12)
N_2D^+	$\leq$3.8(11)	8.7(11)	1.6(12)
Agreement		16/18 = 89%	15/18 = 83%

Table 3.15 Median column densities in $a(x) = a \times 10^x$ for observations (including detections and upper limits) and best-fit HMC model with ortho-para H_2 ratio of 3:1 (model *A*) and with only para-H_2 (model *B*). Modeled best-fit values in italics do not agree with the observed values within one order of magnitude. If the molecule is detected in less than 50% of the sources we marked it as an upper limit.

Molecule	Obs. col. den. [cm^{-2}]	Model *A* col. den. [cm^{-2}]	Model *B* col. den. [cm^{-2}]
CO	2.2(19)	5.3(19)	4.8(19)
HNC	1.5(15)	2.3(15)	2.1(15)
HCN	3.5(14)	2.7(15)	2.5(15)
HCO^+	2.2(15)	1.5(15)	1.4(15)
HNCO	1.7(13)	*7.1(16)*	*1.3(15)*
H_2CO	2.7(14)	1.8(14)	5.5(14)
N_2H^+	5.5(13)	7.1(13)	6.3(13)
CS	1.3(16)	5.0(15)	9.1(15)
SO	5.2(14)	*4.4(16)*	*5.9(16)*
OCS	1.7(15)	5.0(14)	1.6(15)
C_2H	4.3(15)	*2.0(14)*	4.4(14)
SiO	2.2(13)	5.6(13)	3.3(13)
CH_3CN	5.2(13)	7.0(13)	3.7(13)
CH_3OH	8.7(14)	*6.5(12)*	*4.5(13)*
DCO^+	2.0(12)	1.8(13)	*2.4(13)*
DCN	8.0(12)	9.0(12)	8.5(12)
DNC	8.7(11)	8.2(12)	8.3(12)
N_2D^+	≤2.2(11)	4.8(11)	7.1(11)
Agreement		14/18 = 78%	14/18 = 78%

Table 3.16 Median column densities in $a(x) = a \times 10^x$ for observations (including detections and upper limits) and best-fit UCHII model with ortho-para H_2 ratio of 3:1 (model *A*) and with only para-H_2 (model *B*). Modeled best-fit values in italics do not agree with the observed values within one order of magnitude. If the molecule is detected in less than 50% of the sources we marked it as an upper limit.

Molecule	Obs. col. den. [cm^{-2}]	Model *A* col. den. [cm^{-2}]	Model *B* col. den. [cm^{-2}]
CO	1.4(19)	3.8(19)	3.2(19)
HNC	5.0(14)	8.8(14)	5.8(14)
HCN	3.4(14)	8.8(14)	7.0(14)
HCO^+	1.6(15)	8.9(14)	8.6(14)
HNCO	2.7(11)	*2.2(16)*	*2.0(14)*
H_2CO	7.5(13)	7.1(13)	1.5(14)
N_2H^+	3.7(13)	5.9(13)	4.5(13)
CS	2.3(15)	2.4(15)	2.7(15)
SO	7.7(13)	*4.2(16)*	*4.9(16)*
OCS	≤5.1(13)	3.9(14)	2.9(14)
C_2H	3.0(15)	*7.8(13)*	*8.9(13)*
SiO	3.4(12)	*3.7(13)*	2.2(13)
CH_3CN	8.6(12)	8.6(13)	7.7(12)
CH_3OH	6.6(13)	5.6(13)	4.4(13)
DCO^+	4.6(11)	*9.9(12)*	*1.7(13)*
DCN	1.9(12)	2.2(12)	3.3(12)
DNC	≤3.0(11)	1.7(12)	3.0(12)
N_2D^+	≤3.3(11)	3.9(11)	6.1(11)
Agreement		13/18 = 72%	14/18 = 78%

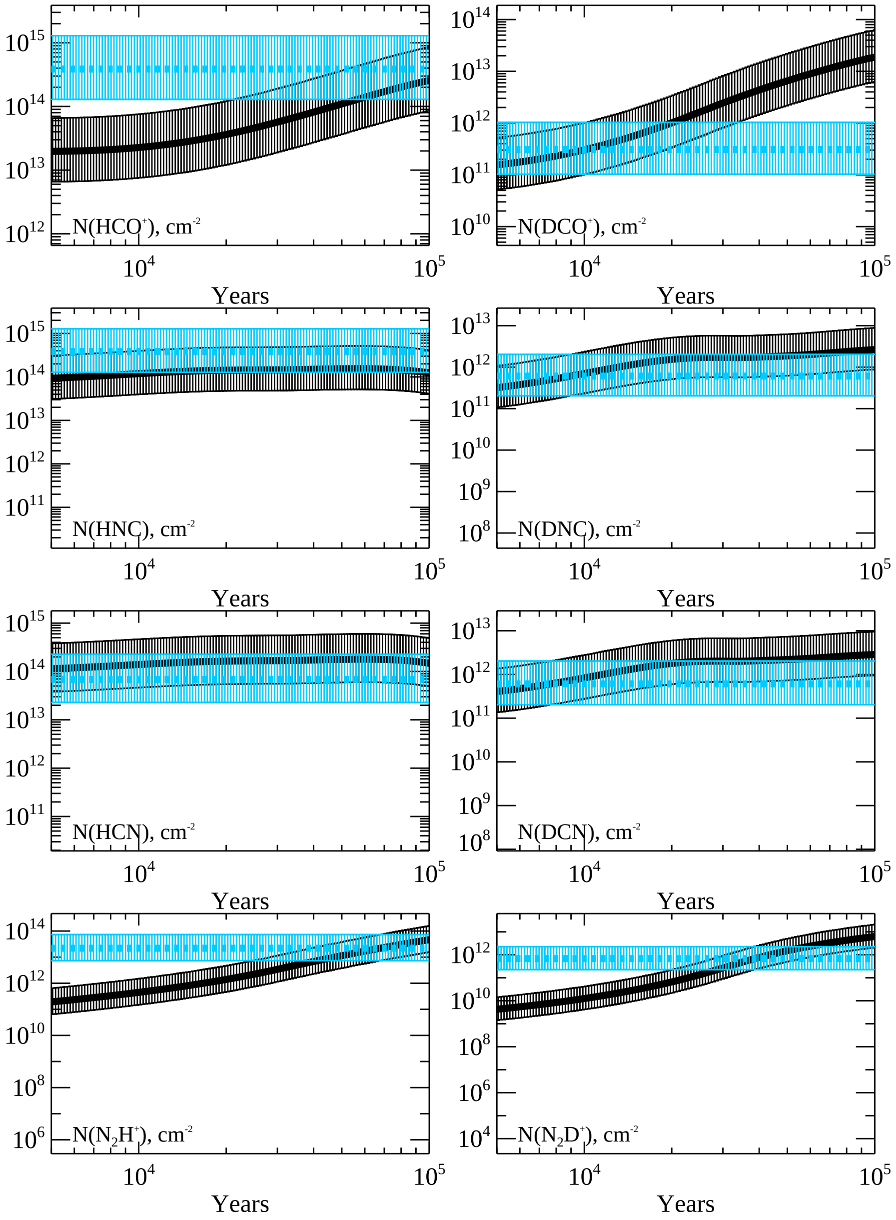

Figure 3.15 Observed and modeled column densities in cm^{-2} in the IRDC stage for the model with only para-H$_2$ present. The observed values are shown in blue, the modeled values in black. The error bars are indicated by the vertical marks. Molecules are labeled in the plots.

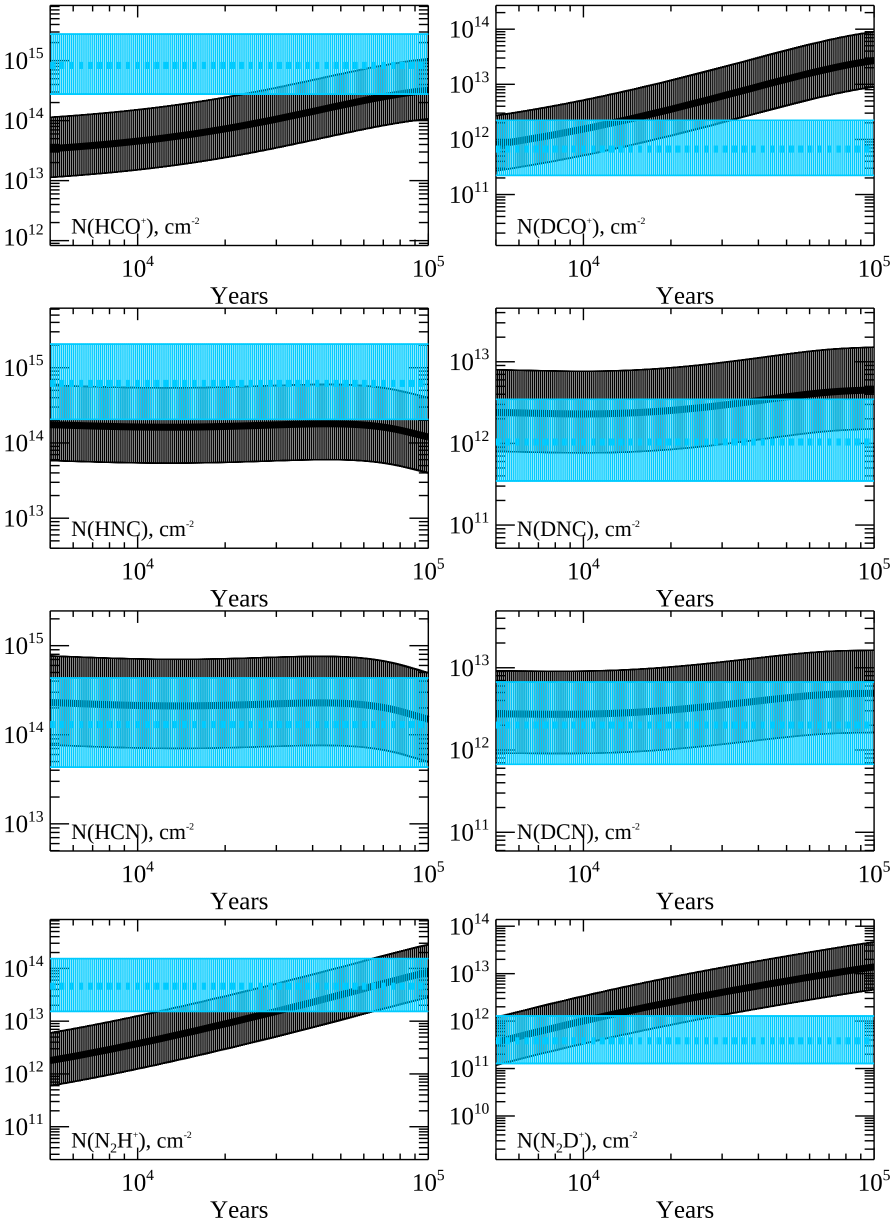

Figure 3.16 Observed and modeled column densities in cm^{-2} in the HMPO stage for the model with only para-H_2 present. The observed values are shown in blue, the modeled values in black. The error bars are indicated by the vertical marks. Molecules are labeled in the plots.

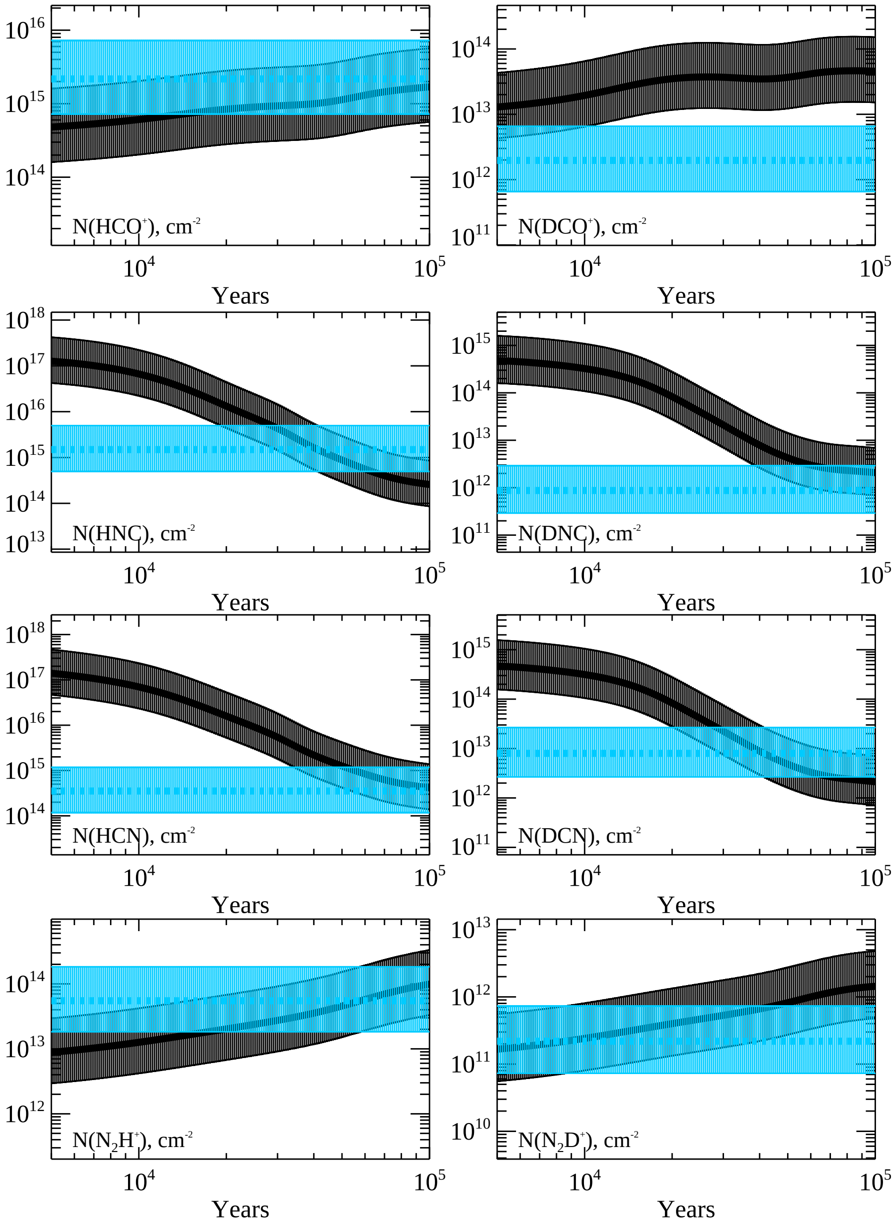

Figure 3.17 Observed and modeled column densities in cm^{-2} in the HMC stage for the model with only para-H_2 present. The observed values are shown in blue, the modeled values in black. The error bars are indicated by the vertical marks. Molecules are labeled in the plots.

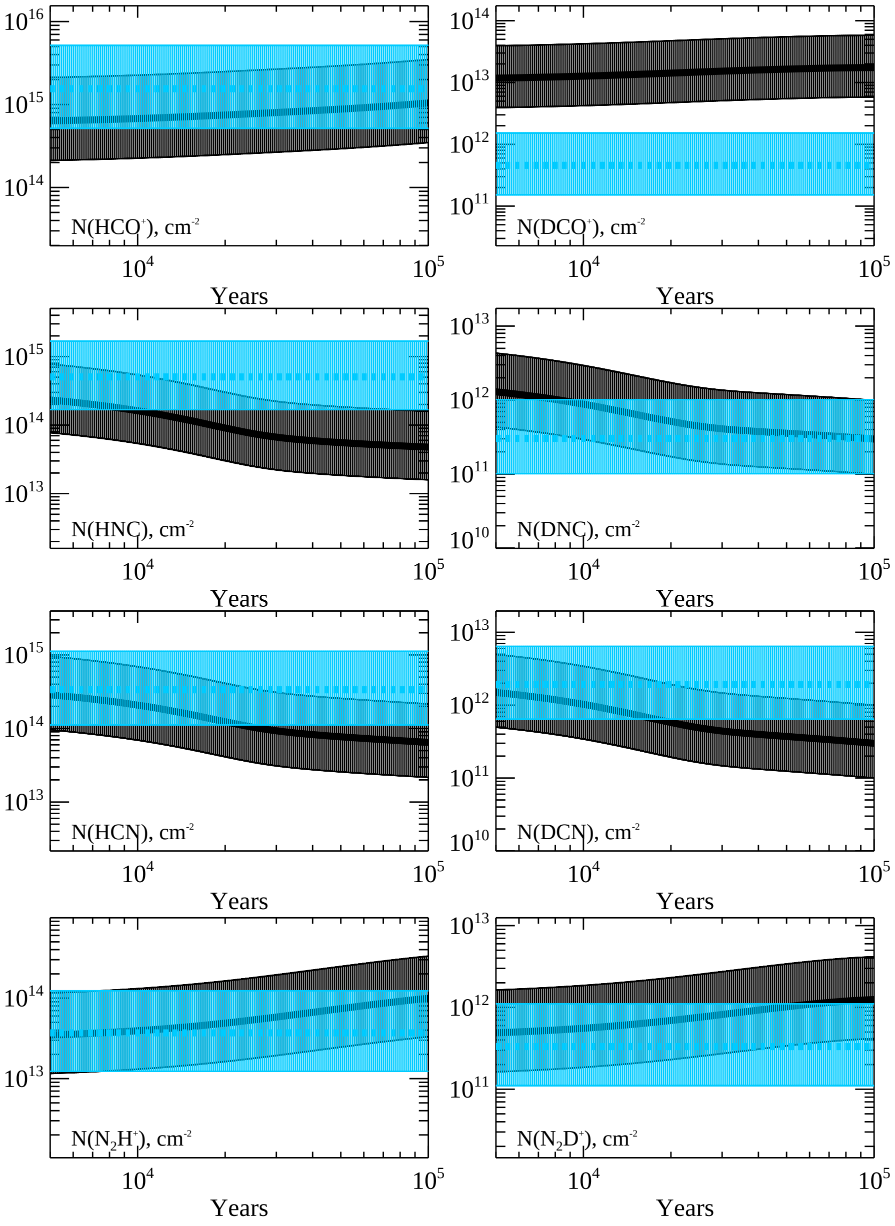

Figure 3.18 Observed and modeled column densities in cm^{-2} in the UCHII stage for the model with only para-H_2 present. The observed values are shown in blue, the modeled values in black. The error bars are indicated by the vertical marks. Molecules are labeled in the plots.

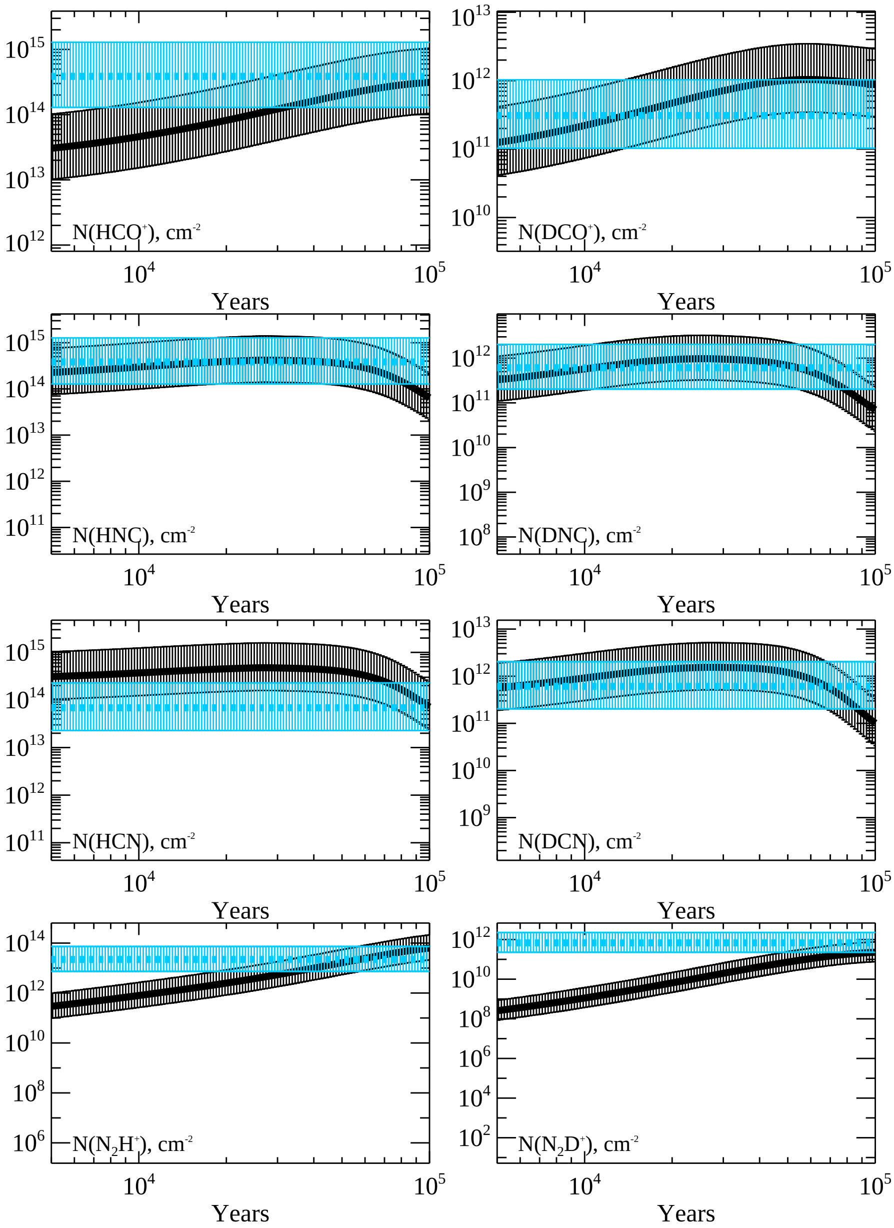

Figure 3.19 Observed and modeled column densities in cm^{-2} in the IRDC stage for the model with an ortho-para H_2 ratio of 3:1. The observed values are shown in blue, the modeled values in black. The error bars are indicated by the vertical marks. Molecules are labeled in the plots.

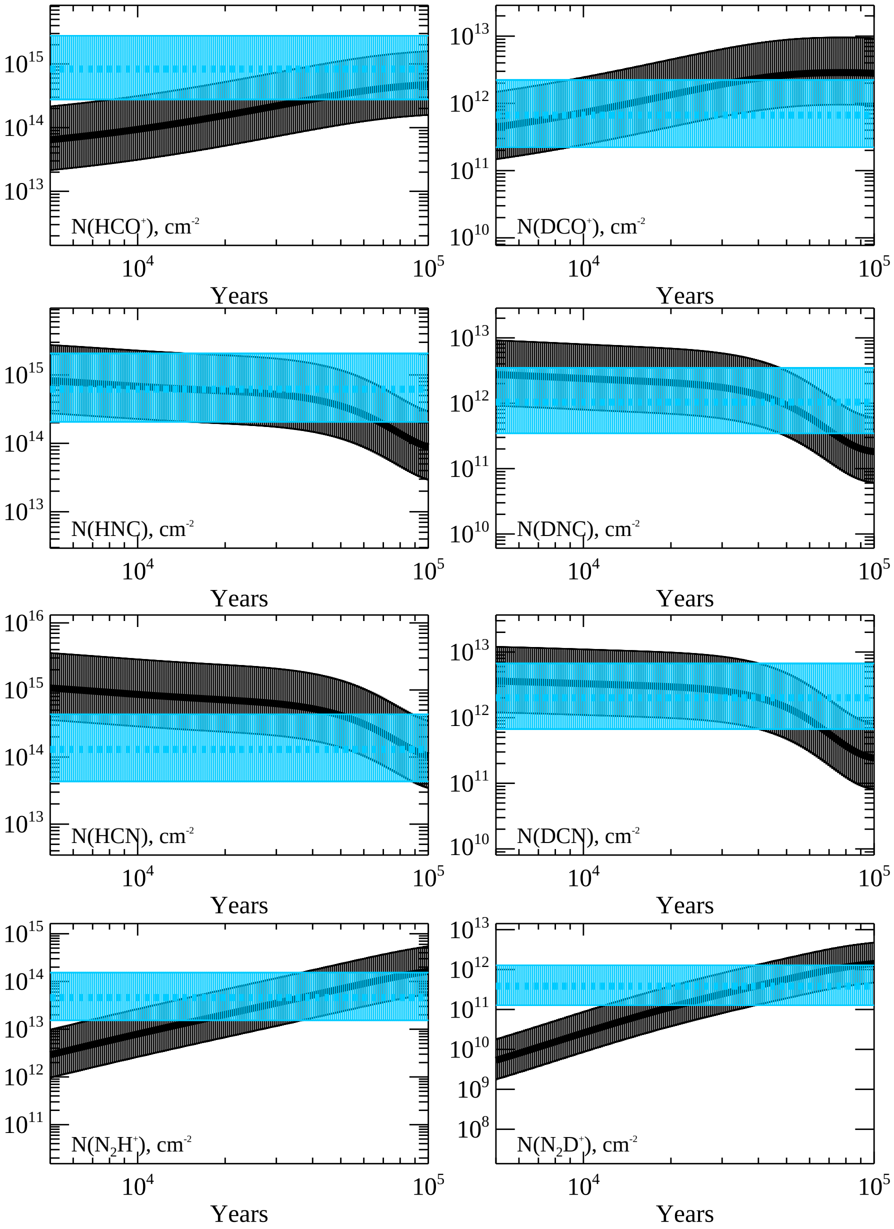

Figure 3.20 Observed and modeled column densities in cm^{-2} in the HMPO stage for the model with an ortho-para H_2 ratio of 3:1. The observed values are shown in blue, the modeled values in black. The error bars are indicated by the vertical marks. Molecules are labeled in the plots.

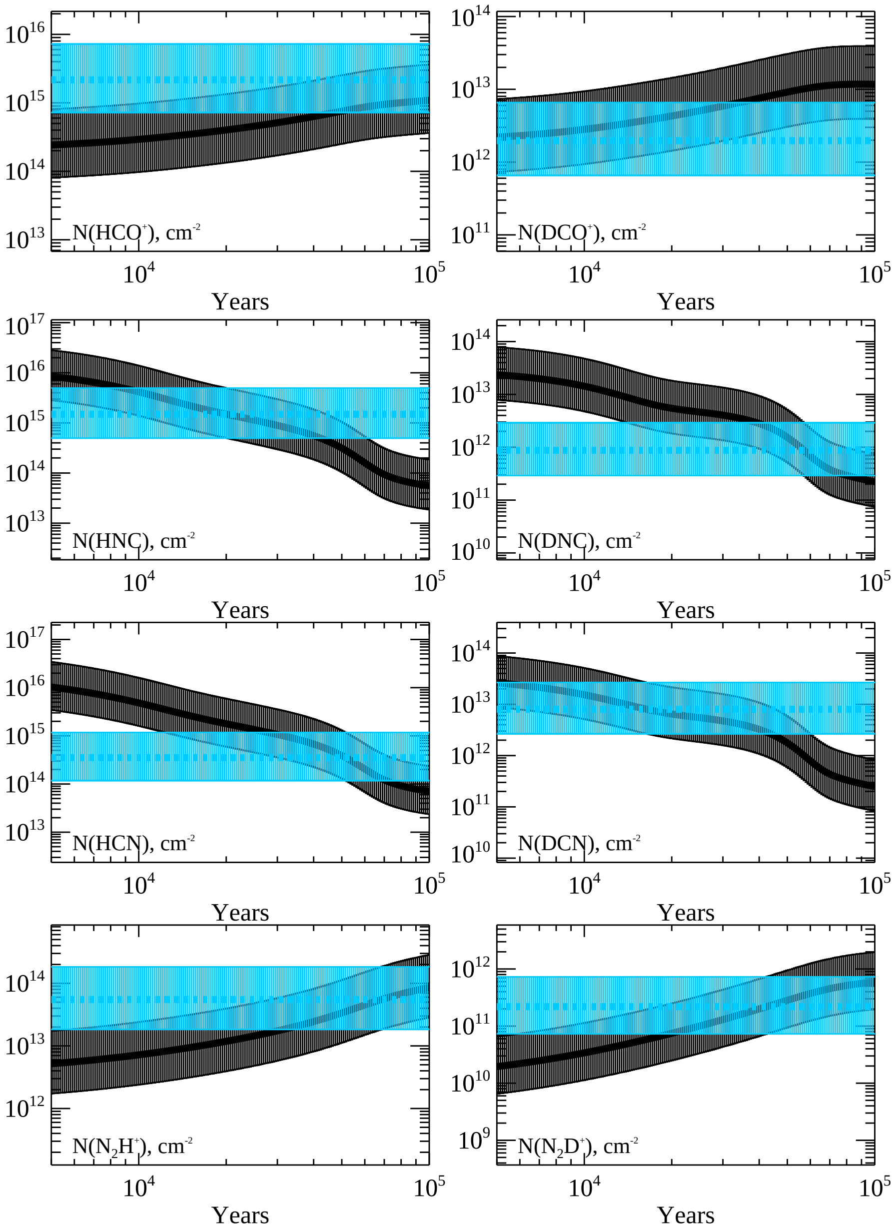

Figure 3.21 Observed and modeled column densities in cm^{-2} in the HMC stage for the model with an ortho-para H_2 ratio of 3:1. The observed values are shown in blue, the modeled values in black. The error bars are indicated by the vertical marks. Molecules are labeled in the plots.

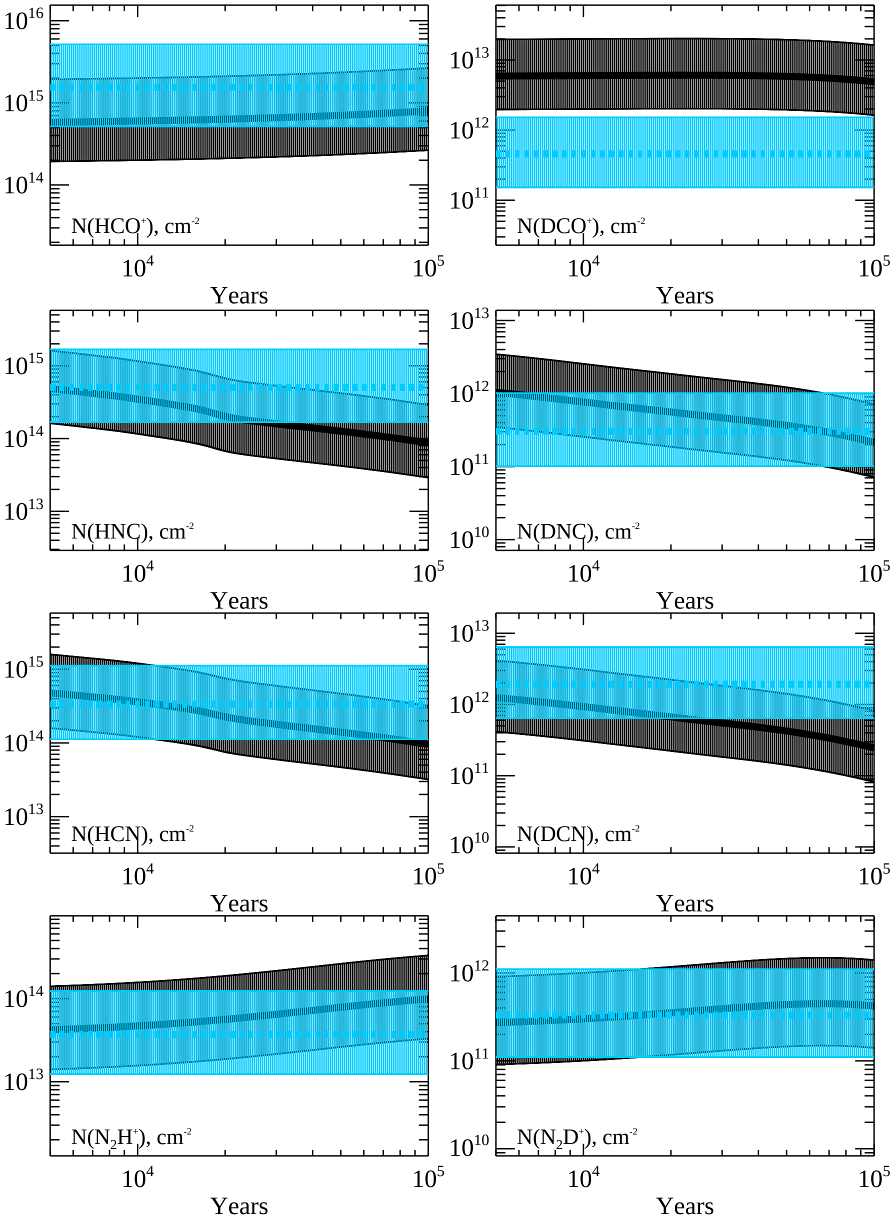

Figure 3.22 Observed and modeled column densities in cm^{-2} in the UCHII stage for the model with an ortho-para H_2 ratio of 3:1. The observed values are shown in blue, the modeled values in black. The error bars are indicated by the vertical marks. Molecules are labeled in the plots.

Chapter 4

Mapping the ionization fraction and the cosmic ray ionization rate

The models used to describe and fit the observed star-forming regions rely on the knowledge of various parameters. Many quantities such as chemical rate coefficients for many different types of reactions in different conditions such as chemistry in the gas phase and on grain surfaces, need to be known. Other important quantities are physical input parameters like the temperature and density in the observed regions. Possible ways are to calculate them based on theoretical models, to measure them in laboratory experiments or to determine them with observations. Depending on the quantity, not all of these ways are possible or yield results with differing uncertainties. One important and, although measured in a variety of objects, still uncertain parameter is the cosmic ray ionization rate (CRIR). The studies that exist so far commonly derive single values for an entire region. Since high-mass star-forming regions are more distant and thus the spatial resolution is worse, we studied the CRIR in the low-mass star- forming region NGC 1333 and mapped it in order to study environmental effects like protostars or the dependence on the density of the region.

An image of the region NGC 1333 is given in Fig. 4.1. We will use the nomenclature of the emission peaks shown in this map in the following. In the vicinity of NGC 1333 are several stars, e.g., the B5 star SVS3 in the north. Further in the north, the star BD +30°549 with the spectral type B6 illuminates NGC 1333 (van den Bergh 1966; Racine 1968). Currently NGC 1333 contains about 150 young stars with a median age of about 10^6 years (Walawender et al. 2008).

4.1 Introduction

The chemical evolution of the interstellar medium (ISM) can be roughly divided into two main parts. On the one hand, there are the chemical processes associated with the dense cores which start as starless cores with a cold core chemistry and may evolve, depending on the evolution and mass, into hot molecular cores for high-mass star-forming regions or so called hot corinos for the low-mass counterparts. These hot

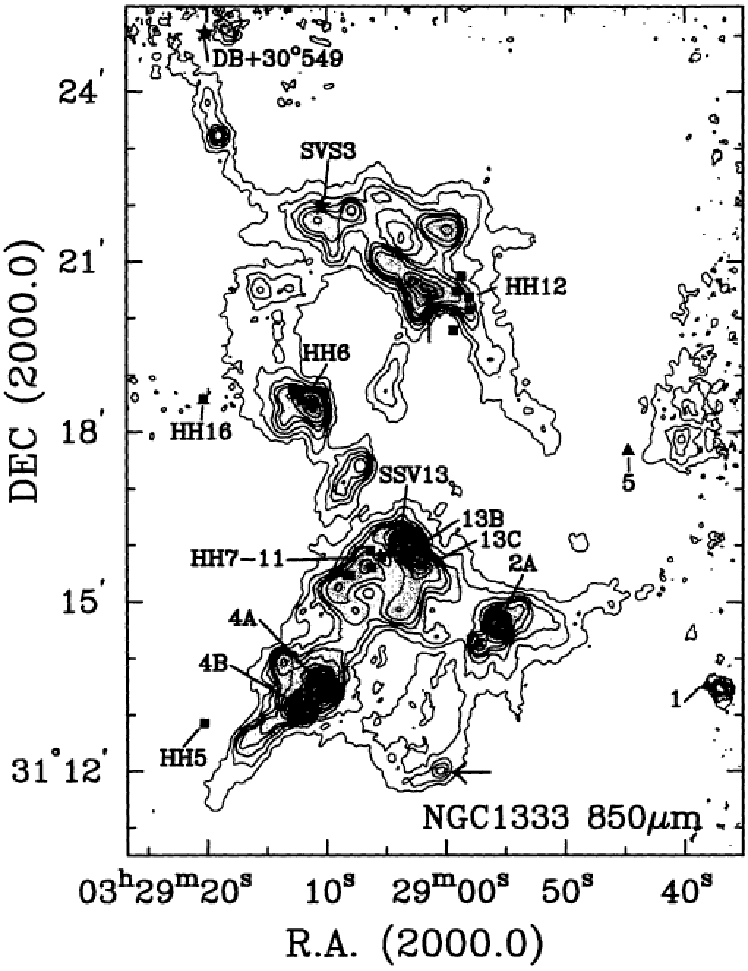

Figure 4.1 NGC 1333 shown in contours of 850μm continuum emission observed with SCUBA. Emission peaks identified by eye are marked with triangles and stars by star-symbols. The image is taken from Sandell & Knee (2001).

cores develop a complex chemical network where many of the approximately 150 interstellar detected molecules can be present.

On the other hand, during early cloud formation from the ionized and atomic phase to the molecular phase, no complex molecules have formed yet, but in addition to H_2, the molecular component consists of CO as well as molecular ions (e.g., Glover et al. 2010; Glover & Clark 2012). Over the last decade, tremendous progress in the theoretical work of cloud formation via turbulent flows took place (e.g., Bergin et al. 2004; Heitsch et al. 2008; Hennebelle et al. 2008; Banerjee et al. 2009; Glover et al. 2010), however, observational evidence for the proposed scenarios is still scarce (e.g., Nguyen Luong et al. 2011).

Furthermore, the existence of the ions is important as ion-neutral interactions make cloud matter coupled to the magnetic field. Hence, the degree of ionization (or the ionization fraction or the electron abundance $x(e) = N(\mathrm{e}^-)/N(\mathrm{H_2})$) of the ISM is directly related to the stabilization of clouds via magnetic fields as well as to the cloud contraction via ambipolar diffusion (e.g., Mouschovias et al. 2006). There is also an ongoing debate about the cosmic ray ionization rate between the diffuse ISM and dense cores. Observations of the diffuse ISM suggest that the cosmic ray ionization rate is relatively large, on the order of $10^{-16} - 10^{-15}$ s^{-1} (e.g., McCall et al. 2003; Indriolo et al. 2007; Indriolo & McCall 2012), while values within dense cores are much smaller, on the order of 10^{-17} s^{-1} (e.g., van der Tak & van Dishoeck 2000; Maret & Bergin 2007). With the existing data, one does not know whether the cosmic ray ionization rate is low everywhere where we have significant molecular gas, only becoming large in the diffuse ISM, or whether it is small only in dense cores, and large everywhere else in the cloud. In a recent study, Morales Ortiz et al. (2014) derived in the high-mass star-forming region NGC 6334I cosmic ray ionization rates of the outer and inner components of the envelope of $2 \cdot 10^{-16}$ s^{-1} and $8.5 \cdot 10^{-17}$ s^{-1} and found a tentative trend for the CRIR in the envelope to increase outward.

To address the spread in ionization rates within star-forming regions, we observed the low-mass star-forming region NGC 1333 in Perseus and mapped it at 2 and 3 mm with the IRAM 30m telescope in order to study the basic chemical properties of the targeted region as well as the ionization fraction and the cosmic ray ionization rate (CRIR) and their dependence on the environment. These information are crucial ingredients for a consistent understanding of molecular clouds and the ISM.

4.2 Observations and observed regions

We mapped two sub-regions of the Perseus molecular cloud. The two regions are shown in Figure 4.2 and the coordinates and the distance are given in Table 4.1.

The first region is NGC 1333 that already hosts embedded star formation activity. The other region is a cloud complex that barely shows any activity and should hence

---

[1] COMPLETE team, "FCRAO Perseus 13CO cubes and map", `http://hdl.handle.net/10904/10075` V2 [Version]

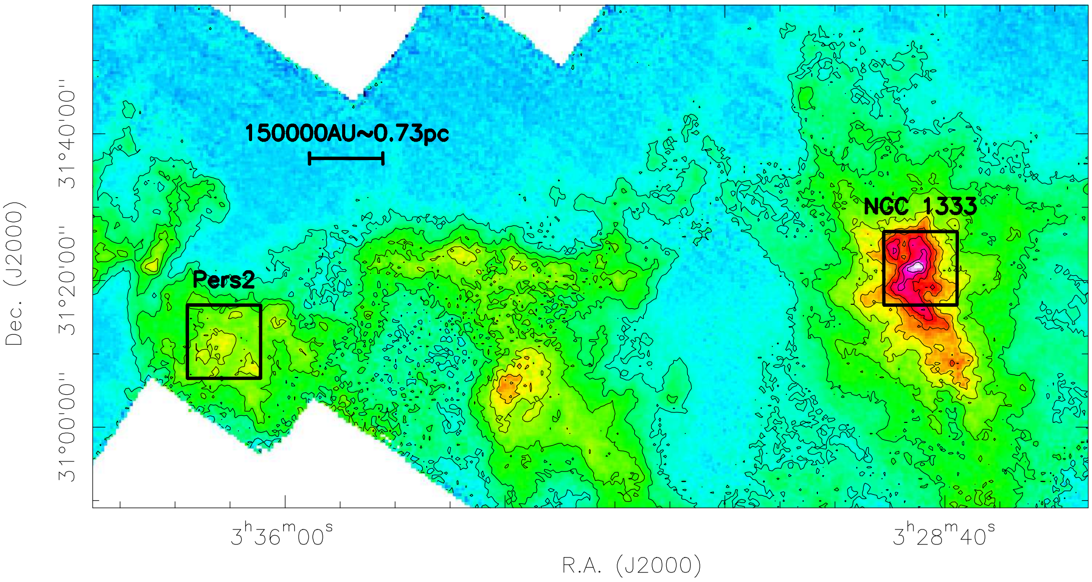

Figure 4.2 Integrated ^{13}CO(1-0) map from the Perseus molecular cloud taken from the COMPLETE survey[1] (Ridge et al. 2006). Contours show the 10% to 90% levels with respect to the peak value of 19.7 K km s^{-1}. The two boxes outline the two sub-regions mapped in this project.

be in a younger evolutionary phase (Kirk et al. 2007). In the following we will call the region that shows no star-forming activity Pers2.

In the literature values for the distance to NGC 1333 range between 220 − 350 pc (Walawender et al. 2008). In this work we assume a value used by other studies of $d = 250$ pc for both regions, following Enoch et al. (e.g., 2006); Ridge et al. (e.g., 2006); Curtis et al. (e.g., 2010). The maps are regions of $10' \times 10'$ and cover the dense cloud centers of as well as extend toward the cloud edges. Figure. 4.2 shows the entire region in ^{13}CO. The two sub-regions are marked with squares.

The observations of NGC 1333 and Pers2 were carried out in October and November 2011 with the IRAM 30 m telescope at 3 mm and 2 mm that cover the required molecules to estimate the ionization fraction simultaneously with the cosmic ray ionization rate following Hezareh et al. (2008)(hereafter H08) and are given in Table 4.2. The two areas were mapped in on-the-fly (OTF) mode using the FFTS backends. The spectral setups covered the frequency ranges from 86.6 − 94.3 GHz, 106.0 − 109.9 GHz and 146.5 − 150.5 GHz. The spectral resolution was 195 kHz, that corresponds to a resolution in velocity between 0.7 km s^{-1} at 86 GHz and 0.4 km s^{-1} at 150 GHz. Typical rms noise values of 0.55 K in the lower outer sideband at 3 mm (86.6 − 90.5 GHz), 0.45 K in the lower inner sideband at 3 mm (90.3 − 94.3 GHz), 0.9 K in the upper outer sideband at 3 mm (146.5 − 150.5 GHz) and 1.0 K at 2 mm per integration. The spectral setup at 3 mm is the same as used for the study described in Chapter 2.

Since the molecular transition of HCNH$^+$ at 148.2215 GHz, that is necessary to derive the ionization rate according to H08, was not detected in the maps, we observed two regions of higher density in NGC 1333 (see Table 4.1 for coordinates) with longer observations of 30 min. The resulting averaged spectrum is shown in Figure 4.3.

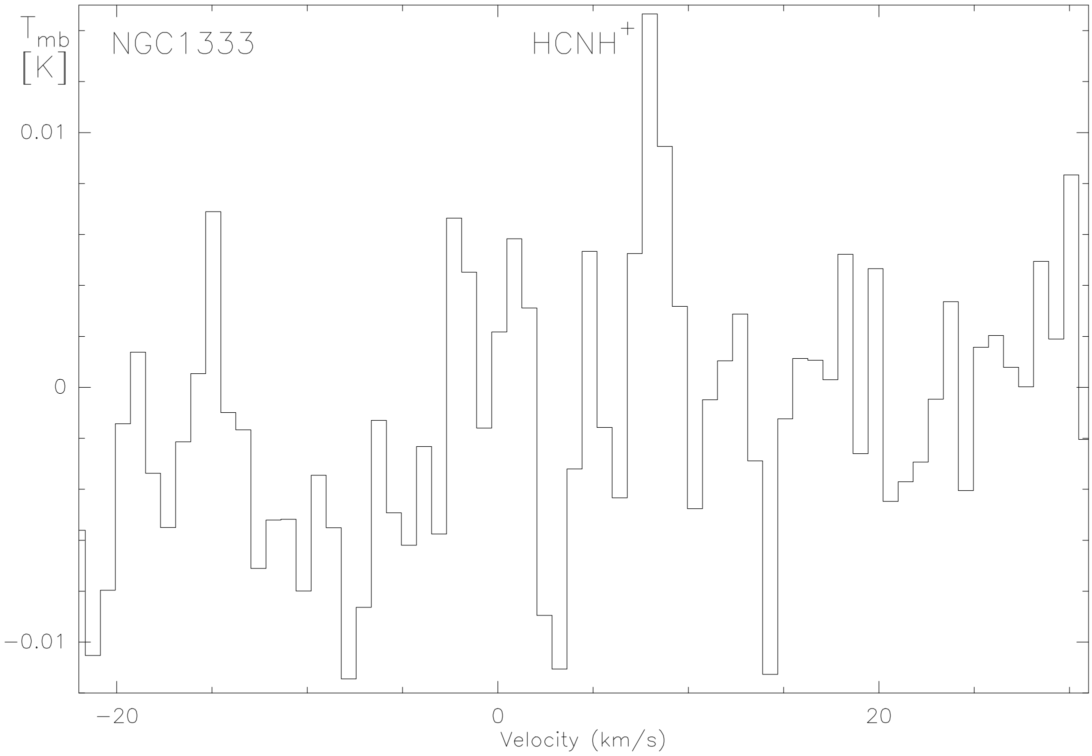

Figure 4.3 The detected $HCNH^+$(2-1)-transition at 148.2215 GHz. The spectrum is averaged of two long-time integrations on two positions in the dense parts of NGC 1333 (see Table 4.1 for coordinates). The spectrum was smoothed to a resolution of 0.8 km s^{-1}.

4.3 Results

The observed regions in the Perseus molecular cloud differ strongly in their star-formation activity. While NGC 1333 is showing a lot of ongoing star-formation with the presence of protostars of different evolutionary stages, Pers2 shows no significant activity. This is reflected in the difference in the spectra taken for this study and shown in Figure 4.4. This Figure shows spectra averaged over the mapped regions in 3 frequency ranges. Two of those are in common with the shown and analyzed frequency ranges discussed in Chapter 2.4. In the inactive region Pers2 only the simple and typical molecules HCN, HNC, HCO^+, N_2H^+ and $C^{18}O$ are detected, but their transitions are much weaker compared to NGC 1333.

4.3.1 Calculation of the H_2 column densities

The H_2 column densities were derived from dust continuum observations taken from the SCUBA Legacy Catalog (Di Francesco et al. 2008) in the same way described in

Table 4.1 Source list showing the positions of the map centers for NGC 1333 and Pers2, the coordinates for the two single pointings towards high density regions in NGC 1333, here called NGC 1333 A and NGC 1333 B, and the assumed distance to the Perseus molecular cloud region.

source	α (J2000.0)	δ (J2000.0)	galactic l [°]	galactic b [°]	distance [kpc]
NGC 1333	03:29:00.0	31:16:55.0	158.778	-20.016	250
Pers2	03:36:26.2	31:10:18.7	160.178	-19.121	250
NGC 1333 A	03:29:03.0	31:15:04.9	158.357	-20.571	250
NGC 1333 B	03:29:01.7	31:20:32.6	158.298	-20.507	250

Table 4.2 List of analyzed molecular transitions.

Molecule	Transition	Frequency [GHz]	E_u/k [K]
$H^{13}CO^+$	1-0	86.7543	4.2
$HN^{13}C$	1-0	87.0909	4.2
HCN	1-0	88.6316	4.3
HCO^+	1-0	89.1885	4.3
HNC	1-0	90.6636	4.4
N_2H^+	1-0	93.1737	4.5
$C^{18}O$	1-0	109.7822	5.3
$HCNH^+$	2-1	148.2215	10.7

Chapter 2. The bolometer maps were taken at 850μm and with a resolution of 22.9″. From these maps we derived H_2 following 4.1 from Schuller et al. (2009):

$$N_{H_2} = \frac{F_\nu \cdot R}{B_\nu \cdot \Omega \cdot \kappa_\nu \cdot \mu \cdot m_H}. \tag{4.1}$$

For the temperatures we used a temperature map of Perseus derived from Herschel measurements (private communications with the Herschel Gould Belt Survey (HGBS) team) (André et al. 2010; Pezzuto et al. 2012; Sadavoy et al. 2012, 2014). With 36.3″, it has a resolution lower than the resolution of the molecular data of 29″ observed for this study. The lower resolution of the temperature map leads to less pronounced extrema in the measured temperatures. The maxima and minima in that region get smeared out resulting in derived temperatures in the range between $10 - 25$ K across the map. We refrained from decreasing the resolution of the molecular data, since this would decrease the quality of the data artificially. Furthermore, we do not expect a dramatic difference in the measured temperatures on the two different scales.

4.3.2 Calculation of the molecular column densities

The molecular lines we used to derive molecular column densities are given in Table 4.2.

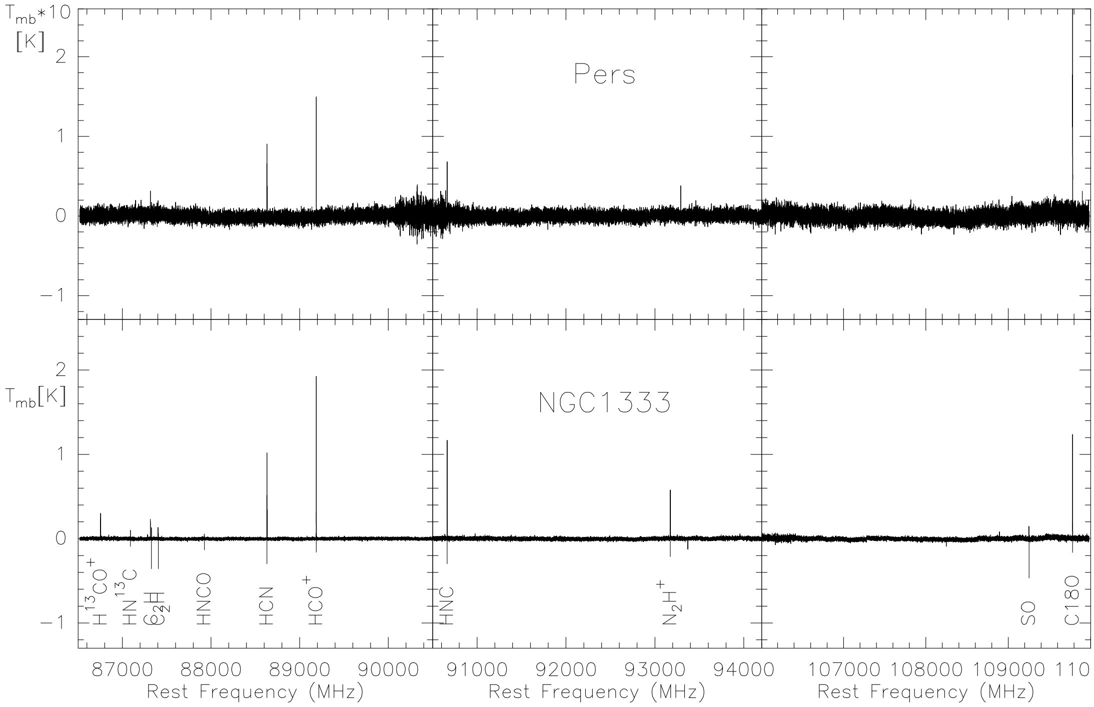

Figure 4.4 Spectra of the observed starless region in Perseus (top) and star-forming region NGC 1333 (bottom) at $86-94$ GHz and $106-110$ GHz.

We calculated the molecular column densities in a similar way described in Chapter 2, following the equations in Tielens (2005):

$$N_u = \frac{1.94 \cdot 10^3}{A_{ul}} \cdot \nu_{ul}^2 \cdot \int T_{mb} \delta v, \tag{4.2}$$

where the line frequency ν_{ul} is in GHz, the integrated intensity is in K km s^{-1}, and the Einstein coefficient A_{ul} is in s^{-1}. Then the total column density can be calculated,

$$N_{tot} = N_u \cdot \frac{Q}{g_u \cdot exp[-E_u/kT_{ex}]}, \tag{4.3}$$

where Q is the partition function, g_u the statistical weight of the upper level, E_u the upper state energy, and k the Boltzmann constant. T_{ex} is the excitation temperature and assumed to be equal to T_{kin} in the cases without reliable measurements. Only for N_2H^+ and HCN, we could measure the excitation temperature in the optical thick case, due to the hyper fine splitting of the observed transition. This also only worked for single spectra with high enough signal-to-noise ratio. In all other cases we used the temperature map derived from Herschel observations (see Section 4.3.1), assuming that the dust and the gas temperatures are in equilibrium.

The complete overview of the measured molecules of NGC 1333 is given in Figures 4.5–4.11 and discussed in Section 4.4.

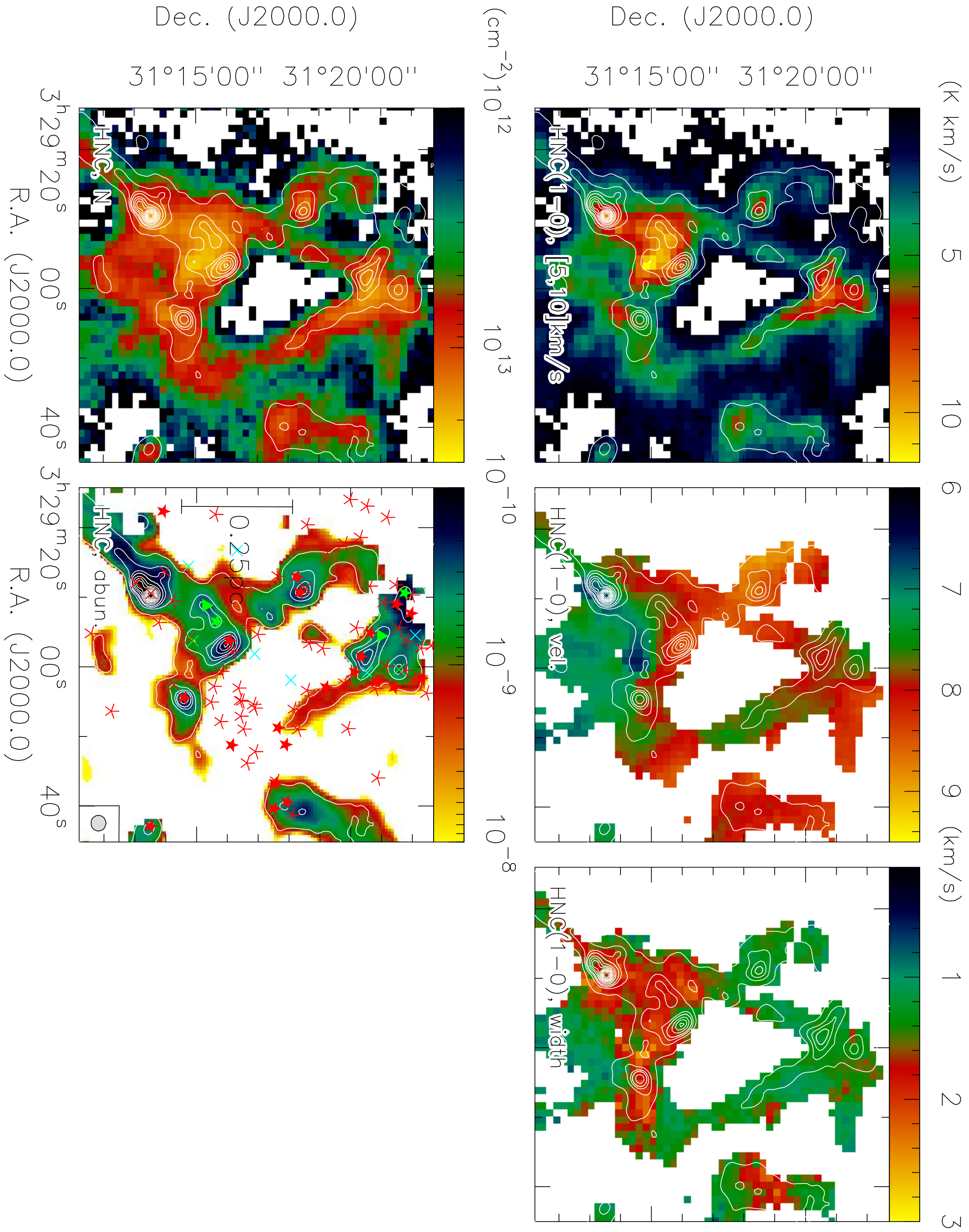

Figure 4.5 NGC 1333. Right: The maps show the integrated intensity (upper right), peak velocity (middle right) and FWHM (lower right) of HNC(1-0). Left: The maps show from bottom to top the column density (upper left) and the abundance with respect to H_2 (lower left). The contours in all maps show the SCUBA dust emission at 850μm. Class 0 objects from Hatchell et al. (2007) are shown with green triangles (starless cores), crosses (Class 0) and thick stars (Class 1), from Evans et al. (2009) with cyan crosses (Young stellar Object candidates), and from Gutermuth et al. (2008, 2009) with red crosses (deeply embedded source), thick stars (protostar with an infalling envelope), thin stars (pre-main sequence stars with an optically thick disc and transitional disc candidates). The beam size and the physical scale are shown in the abundance map and are for all panels the same.

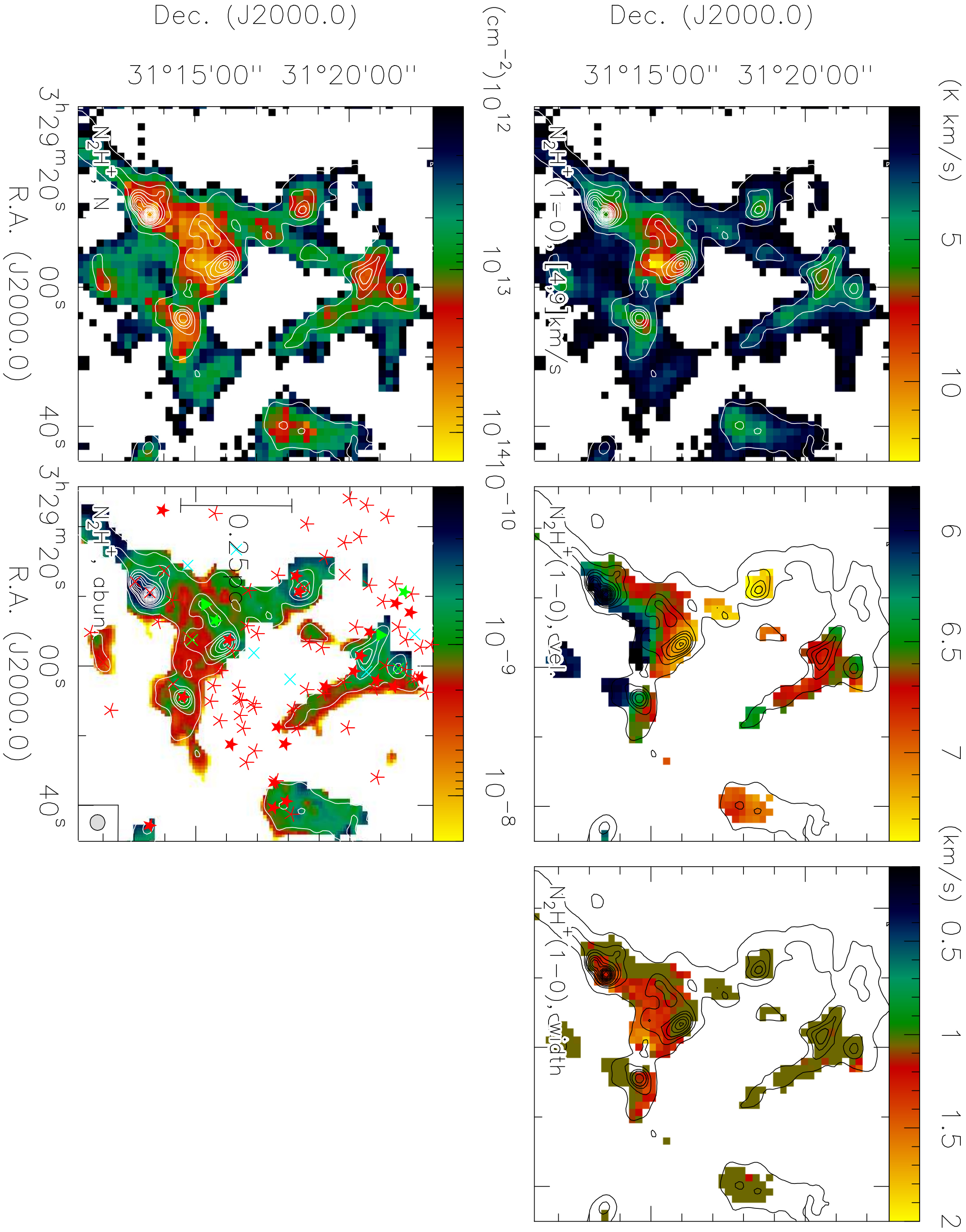

Figure 4.6 Same as Figure 4.5 for N_2H^+.

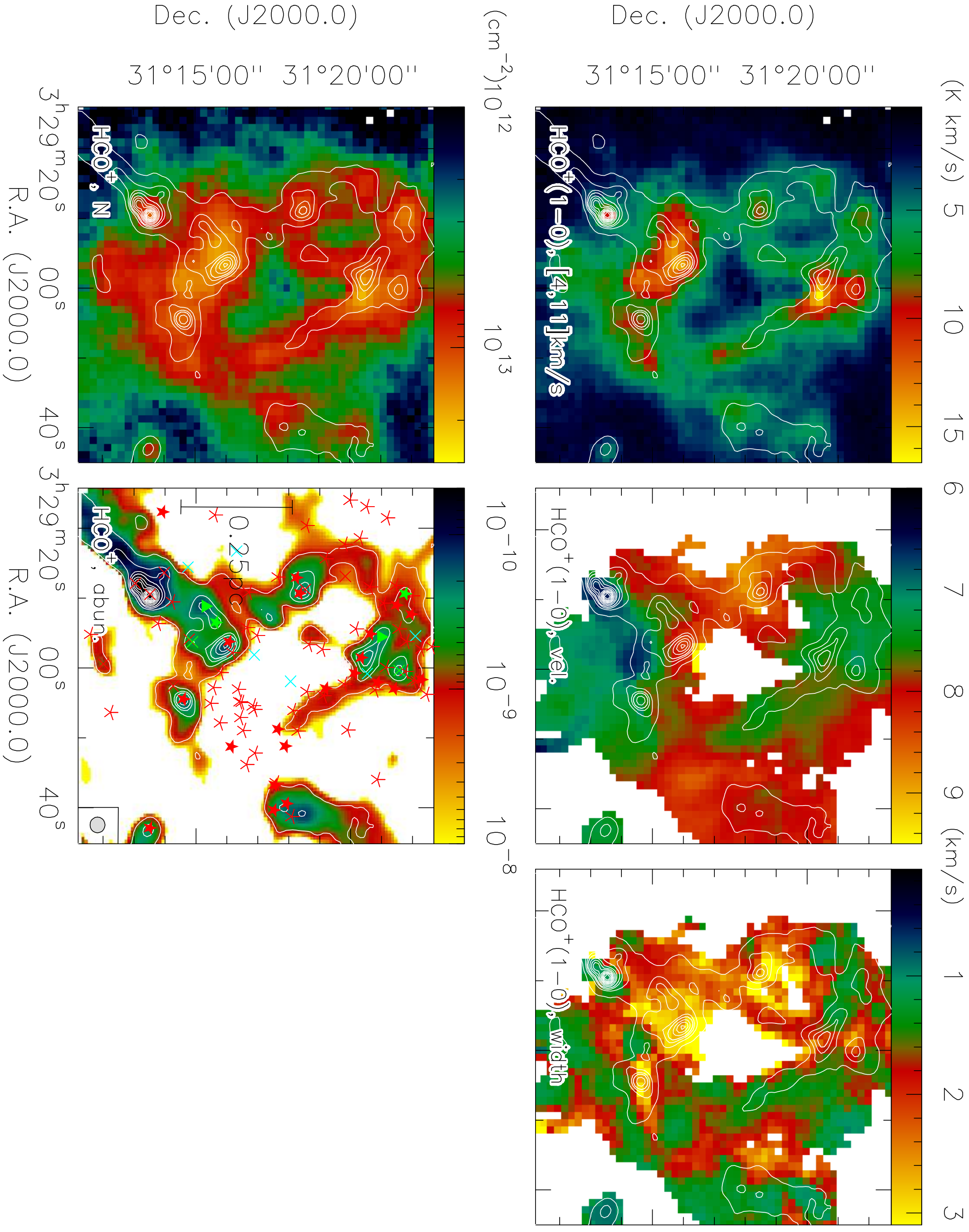

Figure 4.7 Same as Figure 4.5 for HCO$^+$.

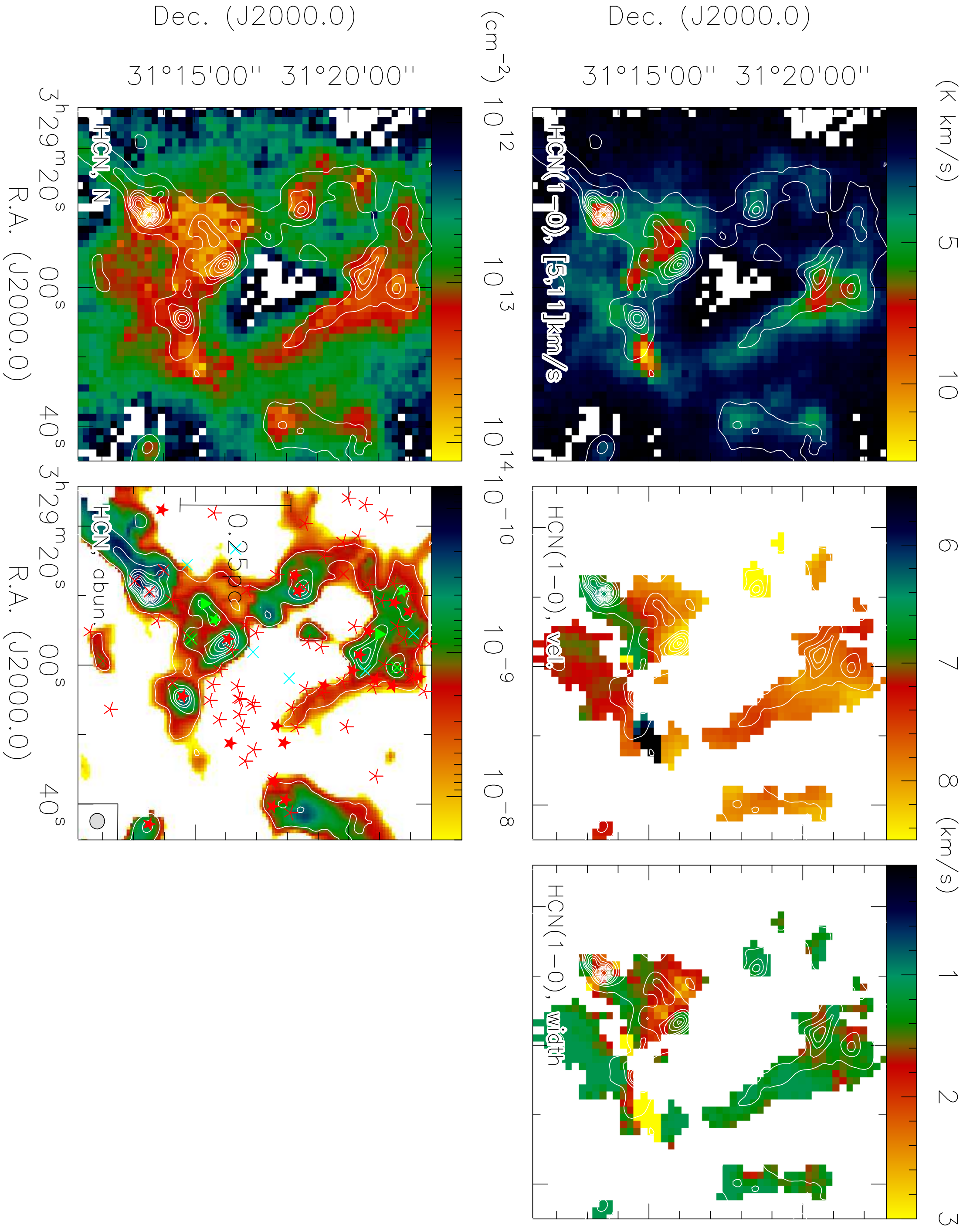

Figure 4.8 Same as Figure 4.5 for HCN.

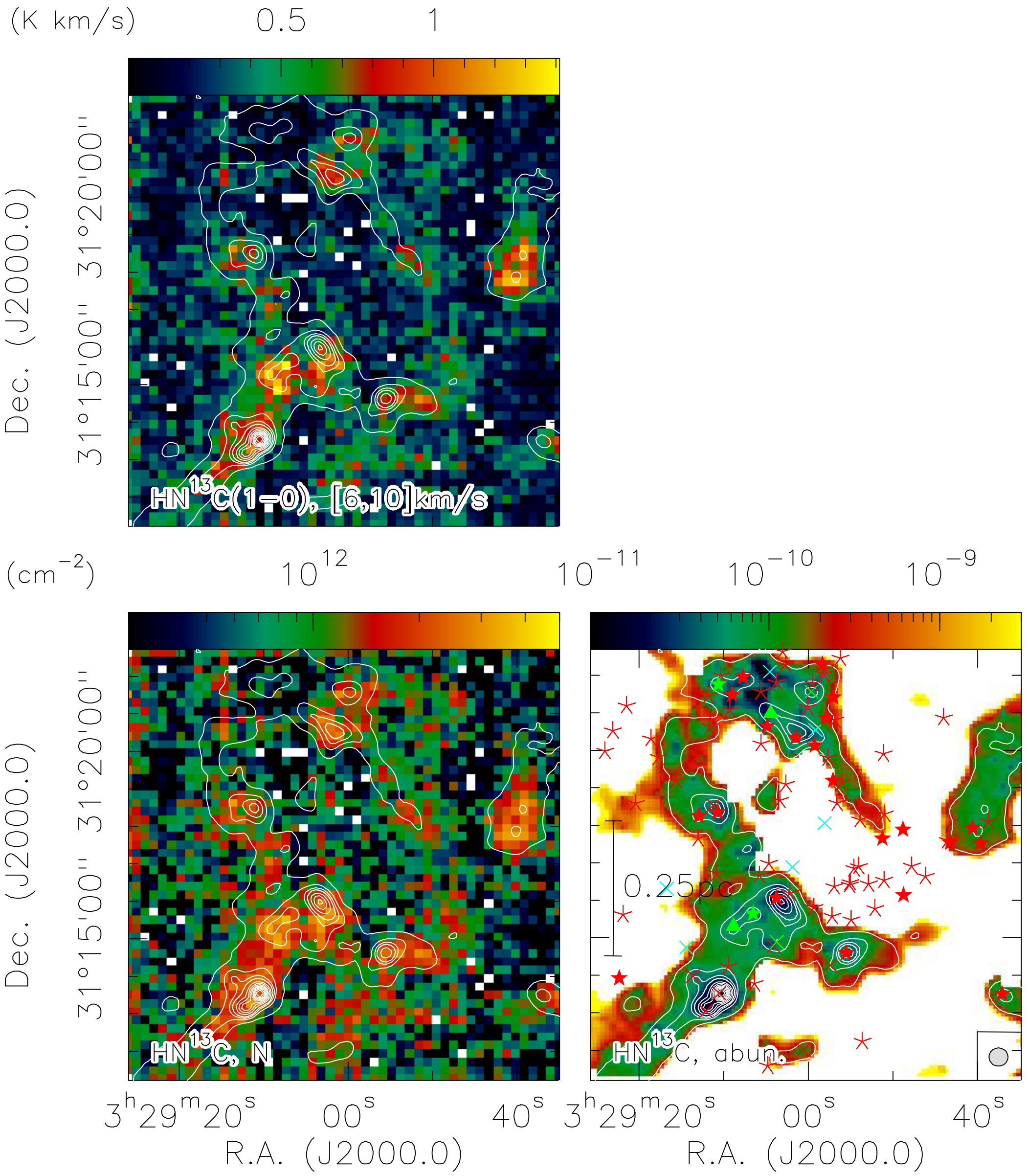

Figure 4.9 Same as Figure 4.5 for HN^{13}C. The first and second moment maps could of the HN^{13}C (1-0) transition could not reliably be determined due to their weak intensity and these maps are not shown.

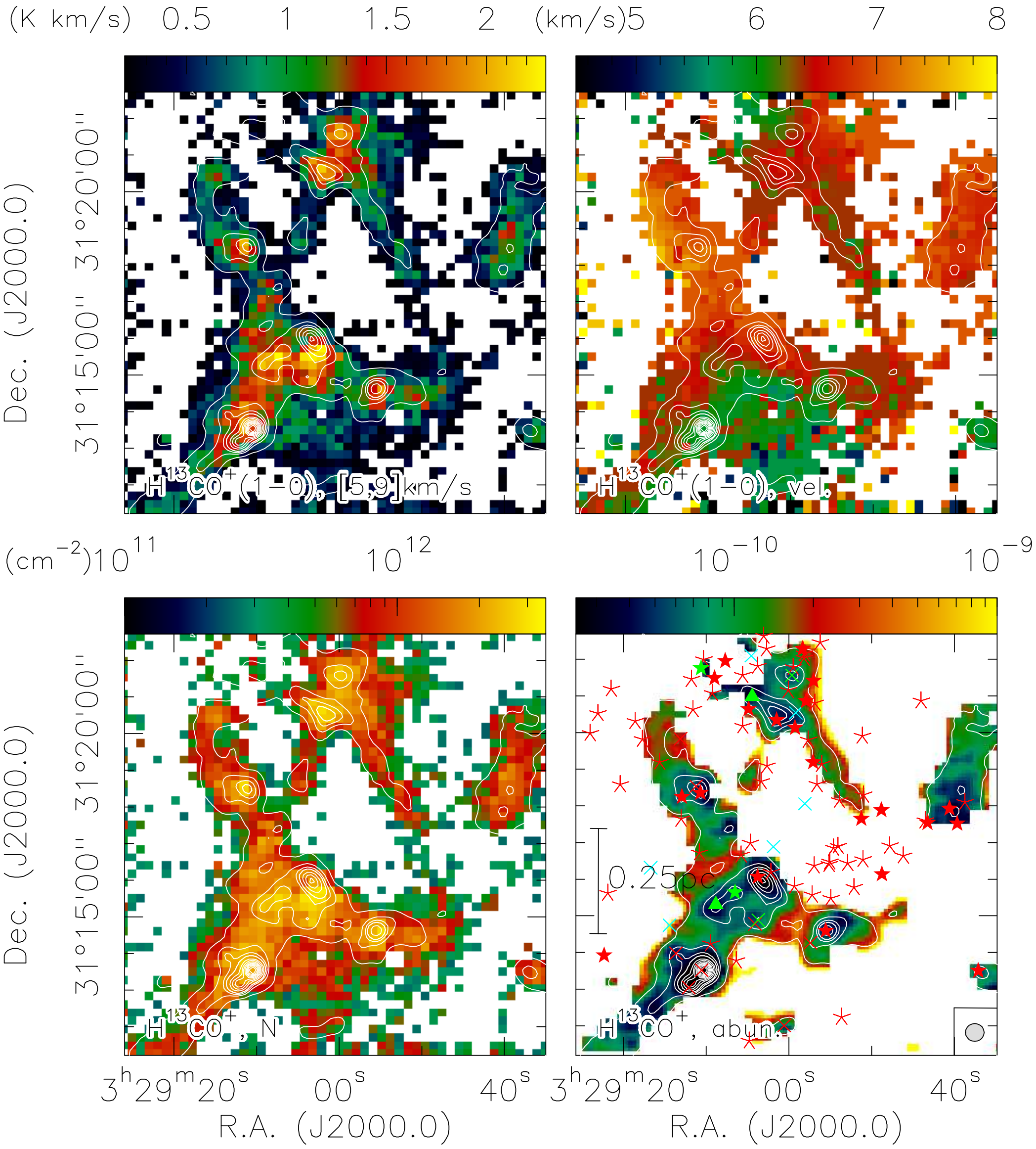

Figure 4.10 Same as Figure 4.5 for $H^{13}CO^+$. The second moment map of the $H^{13}CO^+$ (1-0) transition could not reliably be determined and the map is not shown.

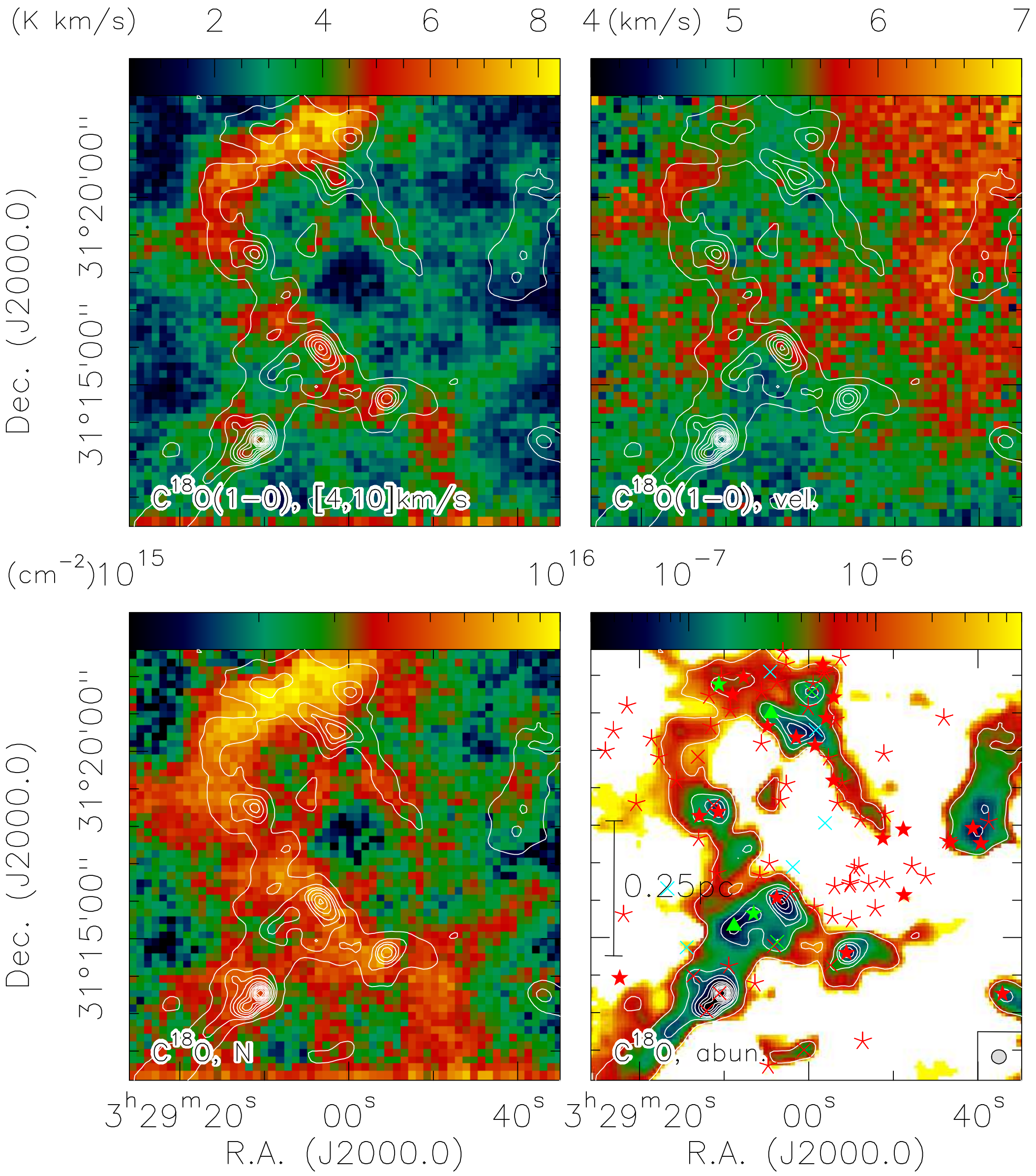

Figure 4.11 Same as Figure 4.5 for C^{18}O. The second moment map of the C^{18}O (1-0) line could not reliably be determined and the map is not shown.

Table 4.3 Integrated intensity, velocity for the (1-0) transition and derived column density for the detected molecules in Pers2 from the averaged spectra over the entire region. The $C^{18}O$ (1-0) line shows two peaks at different velocities.

Molecule	Integrated intensity $[\mathrm{K\,kms^{-1}}]$	Column density $[\mathrm{cm^{-2}}]$	Velocity $[\mathrm{km\,s^{-1}}]$
HCN	0.22	9.9(11)	6.3
HCO^+	0.32	4.6(11)	7.2
HNC	0.13	3.0(11)	7.5
$C^{18}O$	0.29	3.5(14)	6.0
$C^{18}O$	0.79	9.9(14)	8.4

$HCNH^+$ could only be detected in an averaged spectrum (Figure 4.3). The derived $HCNH^+$ column density from the integrated intensity is $3.6 \cdot 10^{12}$ $\mathrm{cm^{-2}}$ and gives also an upper limit for the entire map. The found value is ten times lower then the one found by H08 in the observed high-mass star-forming region.

In the case of the non-star-forming region Pers2, the OTF-maps were not sensitive enough and the molecular transitions too weak to allow making maps of this region in different molecules. However, the averaged spectra over the entire region shown in Figure 4.4 allowed to derive average values for the molecular column densities of HCN, HCO^+, HNC and $C^{18}O$ in this region. The (1-0) lines of N_2H^+ and the minor isotopologues of HCO^+ and HNC were not detected. The column densities for the detected molecules are shown in Table 4.3. For T_{ex} a typical value for this region of $T_{\mathrm{dust}} = 17.5$ K was used (Ridge et al. 2006), assuming that the gas and dust are in thermal equilibrium.

4.3.3 Ionization fraction and cosmic ray ionization rate

With the derived molecular column density maps we can infer the ionization fraction and the cosmic ray ionization rate spatially resolved for this region. According to H08, the ionization fraction e^- and the column density of H_3O^+ can be derived from the following equations, where we use column densities instead of volume densities as in H08:

$$N(\mathrm{e}^-) = [N(\mathrm{HCN}) + N(\mathrm{HNC})] \cdot \frac{N(\mathrm{H}_3^+) \cdot k1 + N(\mathrm{HCO}^+) \cdot k2 + N(\mathrm{H_3O}^+) \cdot k3}{N(\mathrm{HCNH}^+) \cdot k5} \tag{4.4}$$

and:

$$N(\mathrm{H}_3^+) = \frac{N(\mathrm{HCO}^+) \cdot N(\mathrm{e}^-) \cdot k3}{N(\mathrm{CO}) \cdot k5}. \tag{4.5}$$

The rate coefficients were taken from the UMIST database for astrochemistry 2012 (McElroy et al. 2013). The $^{16}O/^{18}O$ isotopic ratio of 540 used to convert $C^{18}O$ column densities into column densities of the main isotopologue CO was adopted from

Jørgensen et al. (2004b); Wilson & Rood (1994). In the literature different values have been measured between 250 at the galactic center (Wilson & Rood 1994) and up to 670 in a local diffuse cloud (Lucas & Liszt 1998). H_3O^+ was not observed in our study and for the column density we adopted the value of H08 of $1.3 \cdot 10^{16}$ cm^{-2}.

The CRIR is then given by:

$$\zeta_{H_2} = \frac{N(H_3^+) \cdot N(CO) \cdot k4 + N(H_3^+) \cdot N(e^-) \cdot k11}{N(H_2)}. \tag{4.6}$$

From that we can now derive a map of the cosmic ray ionization rate (CRIR). Since we deal with column densities, we need to assume a distance in order to derive the CRIR. Here we use $d = 250$ pc (see Section 4.2). The CRIR is inversely proportional to the assumed distance.

Another approach to derive $N(e^-)$ used by Caselli et al. (2002b)(hereafter C02) is based on adding up the column densities of the most abundant ion molecules, which are HCO^+ and N_2H^+. This gives a lower limit of the ionization fraction.

In Figure 4.12 we show the maps of the ionization fraction derived according to C02 and H08, the ratio of the results of these methods as well the map of the CRIR. Since the column density of $HCNH^+$ can be considered as an upper limit for the entire region, it is important to keep in mind that the derived map of the ionization fraction as well as the map of the cosmic ray ionization rate are subject to uncertainties of the assumptions. Lower values for $HCNH^+$ would lead to an increasing ionization fraction and CRIR. In contrast to that, lower values for the assumed column density of H_3O^+ would decrease the ionization fraction and the CRIR. The discussion of the found ionization fraction and the CRIR follows in Section 4.4.

4.4 Discussion

4.4.1 Molecule maps

In Figures 4.5–4.11 we show the integrated intensity maps, the first moment (line of sight velocities) and second (FWHM) moment maps of the (1-0) lines of the analyzed molecules $C^{18}O$, $H^{13}CO^+$, HCO^+, HCN, $HN^{13}C$, HNC and N_2H^+ as well as the derived column density and abundance maps. The contours show 850μm continuum emission revealing cold dust. Compared to the cold dust emission, HCO^+ shows an extended underlying, almost ringlike structure connecting the distributed dust peaks. The molecular emission does not exactly trace the dust, but the emission of HCO^+ peaks is close to peaks in the dust emission. The velocity distribution shows higher velocities of 8.5 km s^{-1} around HH6 (see Figure 4.1 for positions and names of emission peaks) and lower velocities of 7.0 km s^{-1} in the southern part, compared to 8 km s^{-1} velocity of the rest of the emission. The FWHM in the region with enhanced velocities around HH6 as well as the region around SSV13 is higher with almost 3.0 km s^{-1} compared to > 2.0 km s^{-1} in the more quiescent regions. That might be due to

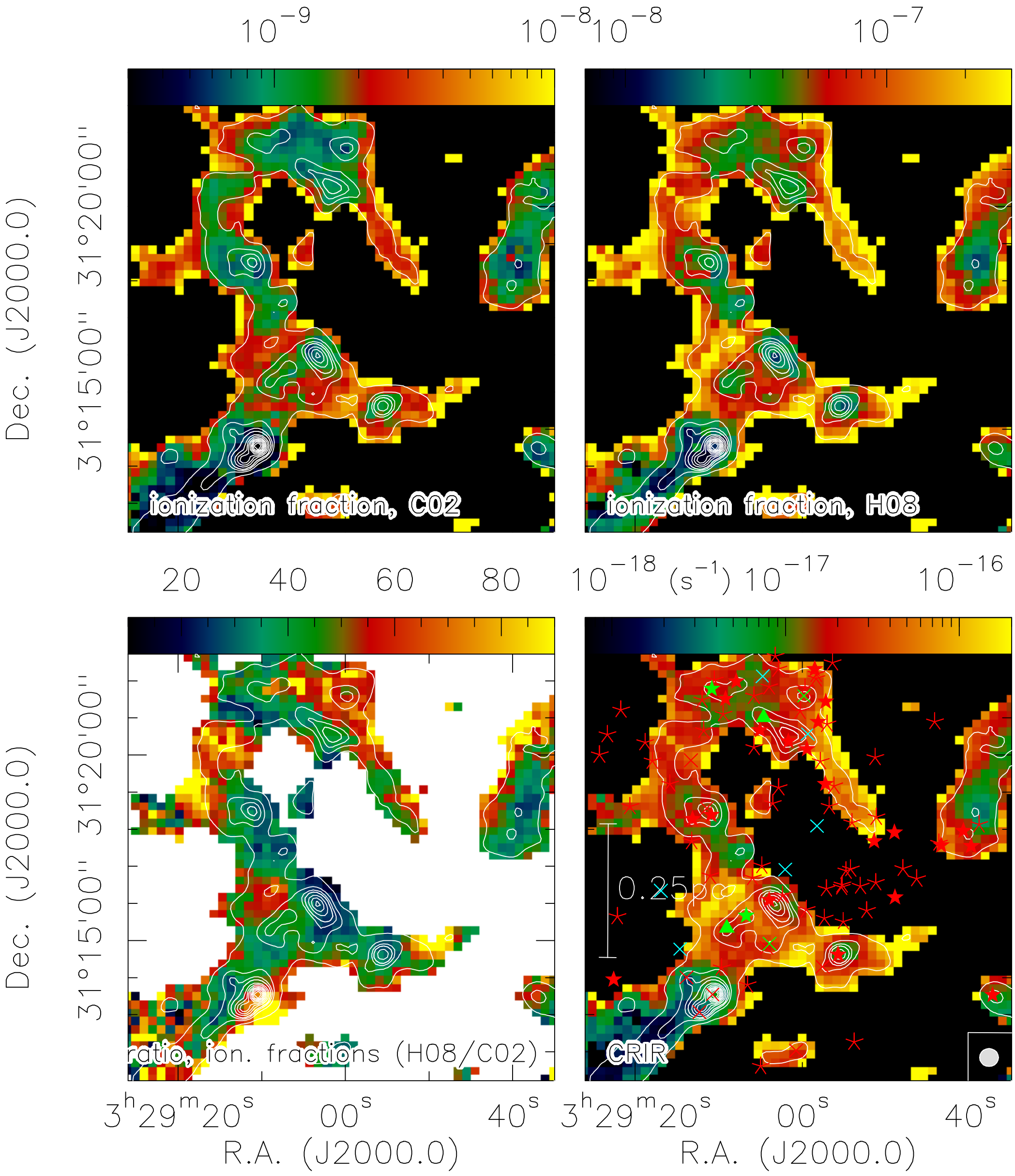

Figure 4.12 Top: From left to right the panels show the ionization fraction derived according to C02 and the ionization fraction derived according to H08 of NGC 1333. Bottom: From left to right the panels show the ratio of the ionization fraction derived with the method in H08 devided by the ratio derived with the method in C02 and CRIR. The contours in all maps show the SCUBA dust emission at 850μm. Class 0 objects from Hatchell et al. (2007) are shown with green triangles (starless cores), crosses (Class 0) and thick stars (Class 1), from Evans et al. (2009) with cyan crosses (Young stellar Object candidates), and from Gutermuth et al. (2008, 2009) with red crosses (deeply embedded source), thick stars (protostar with an infalling envelope), thin stars (pre-main sequence stars with an optically thick disc and transitional disc candidates). The beam size and the physical scale are shown in the CRIR map and are for all panels the same.

shocks caused by outflows that are found in the entire region (Knee & Sandell 2000; Walsh et al. 2007).

The distribution of the N_2H^+ emission shown in Figure 4.6 follows the dust emission and traces the high density regions very closely. However, the emission peaks deviate from the peaks of the dust emission and from the HCO^+ emission. In addition, there is no emission of N_2H^+ detected in the northeastern part where the continuum peak SVS3 is located. The intensity maps of HCO^+(1-0) and N_2H^+(1-0) are consistent with the maps from Walsh et al. (2007). The line of sight velocities are found to be between $6.0 - 7.5$ km s^{-1} and are 1.0 km s^{-1} lower than Walsh et al. (2007) found. The velocity structure is similar to their findings and shows an increase in velocity from south to north with the emission connected with HH6 having the highest velocities. The FWHM does not show strong variations and is between $1.0 - 1.5$ km s^{-1}. This might indicate that N_2H^+ is not effected as strongly by the outflows in this region than HCO^+. The derived column densities of N_2H^+ peak in the center of NGC 1333 connecting the dust peaks 4A, 4B and SSV13.

The emission of the HNC(1-0) transition is more extended compared to the dust emission, but not as much as HCO^+. The velocity structure is similar to the one of HCO^+, but the FWHM of the line peaks with 2.0 km s^{-1} around the central and southern dust peaks and, in contrast to HCO^+, do not show an increase in the northern part.

The emission of HCN(1-0) is mainly seen close to the dust peaks, but with a clear offset. The structure of the velocity and FWHM is only sparsely measured. The bilk velocity is around 8.0 km s^{-1} with small patch of lower velocities going from 4A to the northwest. This region of lower velocities is also visible in the HCO^+ map, but not as pronounced.

The emission maps of the minor isotopologues $H^{13}CO^+$ and $HN^{13}C$ show much weaker emission that is concentrated around the dust emission peaks. There is barely emission detected besides the dust peaks. The velocity structure of $H^{13}CO^+$ is similar to the one of HCO^+ and HNC. For $HN^{13}C$ we were not able to fit the velocity structure reliably as well as the FWHM for both minor isotopologues, due to their weak lines. The emission of $C^{18}O$ does not trace the dust peaks very well, but follows the structure of the dust emission in general with enhanced emission and higher column densities along the continuum emission. The velocity structure is divided into a generally slightly blueshifted eastern part and slightly redshifted western part. However, the total range in line of sight velocities is less than < 1.0 km s^{-1}, with velocities between $5.0 - 6.0$ km s^{-1}. These velocities are slightly lower than for the other molecules, that have similar absolute velocities. The second moment of $C^{18}O$(1-0) could not be reliably determined.

The abundances of $C^{18}O$ and $H^{13}CO^+$ decrease towards the dust peaks, especially the regions around 4A and 4B and SSV13. HCN, HCO^+, HNC and N_2H^+ do not decrease so strongly towards SSV13, but also decrease towards the region around 4A and 4B sources. The abundance of $HN^{13}C$ is generally lower along the dust structure and not only at the specific dust peaks. The differences in the distributions of the molecules indicate a difference in their chemistry and difference of the environmental conditions.

The variety of the chemical composition across the measured region is possibly also related to that the single sub-regions are in different evolutionary stages. The decrease of abundances at the dust peaks is surprising at first place, since in Gerner et al. (2014) we found that the more evolved cores tend to have higher molecular abundances. However, the optical depth towards these regions will also be higher, such that the molecular column densities will be underestimated. Environmental conditions like outflows and chemical effects such as freeze-out of CO might also effect the distribution of the molecular species.

4.4.2 Ionization fraction and cosmic ray ionization rate

The maps of the ionization fraction are shown in Figure 4.12. The two maps derived with the two different ways described in Section 4.3.3 have the basic structures in common. However, the method of C02 only gives a lower limit and the method given in H08 allows to derive the absolute value. The comparison of two methods can be seen in the middle panel at the bottom, showing the ratio of the ionization fraction H08/C02. The method of H08 is in general giving higher values for the ionization fraction of a factor of $30 - 80$ with absolute values of 10^{-8} in the denser parts to $> 10^{-7}$ towards the edge of the detectable background in the continuum emission. The values are in the range of values found in previous observational studies and models of dense cores (Bergin & Tafalla 2007). The lower ionization fractions at the dust-emission peaks is lowest around 4A and 4B, where the least evolved reside. However, also at the positions of Class 1 objects, the ionization fraction is not enhanced compared to the outer regions. The bulk of more evolved stars is located in a region west of SVS13 and to the north around HH12. That leads to the conclusion that the measured ionization is rather due to external sources outside of the dense, molecular region than due to internally forming protostars. The irradiation of the local forming stars seems to be too weak to have a visible effect on the resolved scales and the still abundant high density gas can shield the external ionizing radiation efficiently enough. Also a stronger dependence of recombination with the density compared to the ionization (Hobbs 1974; Welty & Hobbs 2001) might effect the ionization fraction such that it drops towards the denser parts.

In comparison to our work on a low-mass star-forming region, Zinchenko et al. (2009) observed high-mass star forming region and studied the spatial distribution of several simple molecules and determined from that the ionization fraction as well as they tried to find chemical indicators of massive protostars in the earliest phases. They concluded that strong emission of high-density tracers such as N_2H^+ seems to be a good indicator for very young protostars. However, the abundances of N_2H^+ and other high-density tracers like HCO^+ or HNC spatially vary and especially decrease towards the embedded protostars. They explain that in the case of N_2H^+ with dissociative recombination as the dominant destruction process rather than freeze out. In contrast to low-mass cores, where molecular freeze-out is sufficient. The reason is that the temperature in the high-mass cores is too high with typical values of $T \leq 30$ K. Furthermore, they found that the ionization fraction increases towards the areas of higher densities and strong embedded IR sources. The CRIR shown in the panel in the lower right confirms that picture. In the dense peaks with star-formation in a very early evolutionary stage or without star-formation activity, the CRIR tends to be the lowest with ζ_{H_2} 10^{-18} s^-1 and increases towards the outer parts of the dense, molecular cloud and reaches the highest values of up to $> 10^{-16}$ s^-1.

Feigelson & Montmerle (1999) point out that in low-mass star-formation the X-ray ionization of circumstellar material typically dominates the galactic ray ionization on scales smaller than 10 000 AU that is approximately the size of three pixels and comparable to the resolution at 3 mm. Extreme values of ζ_{H_2} in the central molecular zone within the inner 200pc around the Galactic center are found to be $\zeta_{\mathrm{H}_2} > 10^{-15}$ s^{-1} (Goto et al. 2014) in diffuse gas and a similar lower limit for a dense cloud. That is considerably higher than values found in clouds outside of the Galactic center. Albertsson et al. (2014a) modeled the para-fraction of H_2 and H_3^+ for diffuse ISM conditions and compared it with line-of-sight observations of diffuse clouds. They found that the comic ray ionization rate effects the goodness of fit stronger than other physical parameters, such as density and chemical age. The best-fit value was found to be 10^{-15} s^{-1}. Observations by Indriolo & McCall (2012) revealed values of ζ_{H_2} $10^{-16} - 10^{-15}$ s^-1 in the diffuse interstellar medium. (Caselli 2003) points out that the CRIR was found to vary substantially depending on the environment and density of the region.

In order to derive the averaged ionization fraction and CRIR in Pers2 we assumed the same column densities for $\mathrm{H}_3\mathrm{O}^+$ as for NGC 1333 and derived for HCNH^+ an upper limit of $2.9 \cdot 10^{12}$. The average H_2 column density of $5 \cdot 10^{21}\mathrm{cm}^{-2}$ for this region was taken from Sadavoy et al. (2014). The results are $x(e) = 1.1 \cdot 10{-}8$ and $\zeta_{\mathrm{H}_2} = 1.7 \cdot 10^{-19}$. These values are low compared to NGC 1333. Since HCNH^+ was not detected, a lower column density than the assumed value would lead to higher values of $x(e)$ and ζ_{H_2}. Thus, this results should be taken with care. However, this result might also indicate environmental effects. In order to study that in more detail, observations of this region with higher sensitivity are needed.

4.5 Conclusion

We observed the low-mass star-forming region NGC 1333 with the IRAM 30m telescope at 2 mm and 3 mm and mapped it in several simple molecules. With these maps we derived maps of this region showing the ionization fraction and cosmic ray ionization rate. In addition, we tried to map a starless region in Perseus next to NGC 1333 in the same setup. While the averaged spectra showed detections of several molecules, the reconstruction of the maps showed no clear structure in the emission of the molecules. Thus, we only derived an averaged value for the molecular column densities as well as the ionization fraction and the CRIR. However, these values should be taken with care due to the non-detection of HCNH^+.

The observed molecules show in general a decrease in abundance towards the dust emission peaks. But the exact spatial distribution of the different molecular species is not uniform and likely depends on the physical properties such as temperatures and total densities, but also environmental effects like outflows that are traced by certain molecules, e.g. HCO^+. These outflows are also likely responsible for increased velocities and FWHM of the observed lines. The different distributions also might be due to differences in the excitation conditions of the specific molecules. Similar to the molecular abundances, the derived maps of the ionization fraction also show a decrease towards the denser parts of the molecular cloud with values between 10^{-8} in the denser parts up to $> 10^{-7}$ in the outer parts.

The map of the CRIR seems to follow that picture and reaches the highest values at the edges of the cloud, while the lowest values are found at the most densest peaks with ζ_{H_2} between 10^{-18} s^-1 and $> 10^{-16}$ s^-1 at the density peaks and the diffuse outer parts, respectively. However, more sensitive observations with higher spatial resolution are needed to study the spatial differences in more detail and to be able to constrain is with higher precision. On the observed spatial scales, the ionization due to the radiation of internally forming stars seems to be of minor importance compared to external sources such as the ambient cosmic ray ionization field. The derived values for the ionization fraction and CRIR are in agreement with previous studies.

Chapter 5

Summary and outlook

5.1 Summary

[1] The theory of the formation of high-mass stars is still under debate and up to now no comprehensive scheme exists that covers the whole evolutionary sequence. At the moment different theories try to explain the processes how high-mass stars form, but no conclusive picture has been proven yet. On the observational side, the large distances and rare occurrence of high-mass star forming regions as well as the strong dust obscuration and short lifetimes make it difficult to study them in large numbers and great detail. Astrochemistry is a promising tool to study the chemical evolution of high-mass star forming regions in order to better constrain the particular evolutionary stage of an object as well as to make use of the chemistry to infer its physical conditions. The search for the molecule(s) that can be used as a chemical clock is topic of current research and different candidates, e.g. deuterated species, have been proposed. However, no study exists so far that covers a larger number of sources sampling different stages along the evolutionary sequence in a larger number of molecules in a homogeneous way.

In order to add one piece of the puzzle to solve this issue we characterized the chemistry in the first evolutionary stages of high-mass star-forming regions and analyzed in total 18 molecular deuterated and non-deuterated species. We observed a sample of 59 regions that was split into different evolutionary stages, according to their physical properties. Adopting a categorization proposed in the literature, we made the final classification from an observational point of view, based on their chemical appearance. This classification divides the sample into sources with different number and types of detected molecular species and also follows in general temperature and density properties of the sources. The adopted sequence in our approach ranges from infrared dark clouds (IRDCs), high-mass protostellar objects (HMPOs) to hot molecular cores (HMCs) and finally ultra-compact HII regions (UCHIIs).

The sample was observed with single-dish telescopes in different frequency ranges at 1 mm and 3 mm. We derived column densities and abundances for all sources

---

[1] The chemical model used in this thesis was provided by Dmitry Semenov who also did the fits to the data under close collaboration. All other parts were done by me.

under some basic assumptions like, e.g., local thermal equilibrium (LTE) and typical physical parameters. The final results were analyzed in a statistical approach in order to find characteristic properties of the different stages and compared them with a model. Since the observations were performed with single-dish telescopes, some important effects on the results need to be kept in mind. Depending on the observed frequency and distance to the source, the full width half maximum (FWHM) of the beam covered a region of 10 000 au up to 300 000 au in physical units. The derived molecular column densities only represent averaged values over this regions and multiple objects of different kind can be present within the observed beam. Although the task to find a chemical clock is still unsolved and will be part of future studies, the work shown in this thesis helped to make progress in the characterization of the chemical properties of high-mass star forming regions. Together with the employed physico-chemical model the observations can serve as a chemical template for other studies.

In Chapter 2 we performed a study of non-deuterated molecules. It covered simple and light molecules that were detected across the whole evolutionary sequence as well as longer, more complex molecules, predominantly present in the chemically rich phases of the hot molecular cores. Besides an increase of the number and complexity of detected species from IRDCs to HMPOs and HMCs, also the intensity of the observed transitions increases until it decreases again in the phase of an UCHII region. The measured abundances showed as well a similar trend with the peak reached in the HMC phase. The data also allowed us to derive lower limits for the typical ionization fraction in the different stages. It increases from the IRDCs to the UCHII regions, where the central object starts to ionize the ambient medium itself.

On top of that we fitted the observed molecular column densities along the evolutionary sequence with a 1D physical model coupled with a gas-grain state-of-the chemical model. The model of the first stage starts with typical initial conditions. The resulting best-fit model of each stage is then used as new initial conditions for the next stage. The physical model takes the different evolutionary stages into account. The properties of the physical model are kept constant within one model run of a single stage, but varied in each model realization of each stage in order to find the best chemical fit to each stage. The best-fit solutions were in good agreement with the observed values. The comparison of the observed and modeled values based on chemical properties resulted in constraints on the temperature that, confirming the expectations, showed an increase along the evolutionary sequence. It also allowed us to make an estimate of the typical chemical age of the high-mass star formation process covered in this study of 125 000 years. By comparing lower limits of the ionization fraction derived for the different stages with the best-fit models we found that N_2H^+ and HCO^+ are giving a good approximation for the more evolved stages, but in the first stages contributions from deuterated ions and C^+ are not negligible. This was the first time, that the chemical characteristics of a larger sample across the evolutionary sequence of high-mass star formation was systematically studied in a homogeneous way.

In Chapter 3 we extended the types of analyzed molecules towards deuterated species. Due to the properties of its chemical formation and destruction pathways, the deuterium chemistry is particularly sensitive to specific temperature conditions. Furthermore, the thermal history of the observed cloud is imprinted on the amount of deuterated molecules. Thus, they are good candidates of chemical tracers of the different evolutionary stages. We observed the (3-2) transitions of the four deuterated species N_2D^+, DCO^+, DNC and DCN for the whole sample that we already analyzed in Chapter 2. We found high detection fractions of more than 50% for almost every stage and molecule, except N_2D^+. N_2D^+ was only observed in 30% of the IRDCs and 35% of the HMPOs and neither in the HMCs nor in the UCHII regions. In many cases the N_2D^+ were contaminated by on overlying atmospheric ozone line that increased the rms and made it in a few cases impossible to make use of the data. The detection fractions of the other three deuterated molecules increase from IRDCs to HMPOs and reach almost 100% in the HMC stage, except for one non-detection for DNC, and decrease again in the UCHII regions. We studied the ratio of the column density of the deuterated molecule with non-deuterated molecule, the deuteration fraction, and found overall decreasing trends with evolutionary stage for N_2D^+, DCO^+ and DNC. Only the deuteration fraction of HCN was found to be slightly increasing from IRDCs to HMCs and dropping again in the UCHII stage.

The found median deuteration fractions for the whole sample were 0.02 for HCN, 0.002 for HNC, 0.0009 for HCO^+ and 0.02 for N_2H^+. However, the spread of the deuteration fractions within one stage was found to be a few up to more than one order of magnitude. Possible reasons for that are the continuous evolutionary sequence with possible overlaps between different stages and intrinsic inhomogeneities of single sources and stages. The general trends are an indication for a difference in the chemistry between DCN and the other three deuterated molecules, but needs to be tested further. The different behavior of the two molecular groups could be an interesting tool to probe the evolutionary stage of high-mass star formation regions. Overall, the observed deuteration fractions were in agreement with literature values. Furthermore, we studied correlations of the deuteration fraction with the FWHM of the non-deuterated lines, the luminosity and the H_2 column densities of the observed sample. We could not find strong correlations with the FWHM and the H_2 column densities. The luminosity showed anti-correlations with the deuteration fractions of N_2H^+, HNC and HCO^+. However, with only 12 out of 54 detections for N_2D^+, the correlation should be taken with care and needs to be confirmed in future studies. Using the luminosity of a source as a proxy for its temperature, the correlations found indicate that the state of deuteration of a region is more sensitive to the fraction of warm and cold gas than to the total amount of gas and is emphasizing the potential of the deuterium chemistry in order to study the evolution of high-mass star forming regions.

In a similar way as in Chapter 2 we performed a fit with a physico- chemical model to the derived mean column densities of 14 non-deuterated and 4 deuterated molecules for each stage. We found good agreements with at least 13 of 18 species matching within the typical uncertainties in the model and the observations of one order of magnitude. The comparison of two models using two different initial ratios of the spin state of molecular hydrogen indicating different formation histories showed a few differences in the resulting best-fit models. However, the differences were not strong enough to definitely constrain the best ortho/para ratio. This was the first time that such a large number of deuterated molecules was studied in a larger source sample representing the evolutionary sequence of high-mass star formation.

In order to improve the models used to fit the observations and describing the theoretical background it is necessary to study the physical and chemical parameters the models are based on. In Chapter 4 we observed the nearby low-mass star-forming region NGC 1333 in order to study the validity of current assumptions on the cosmic ray ionization rate (CRIR). For that we mapped the column densities of several molecules in this region in order to derive the ionization fraction and the cosmic ray ionization rate. The ionization fraction was found to decrease towards regions of higher densities and is not strongly affected by the forming protostars on the resolved scales. Furthermore, the analysis revealed that the derived values for that region are comparable with the value of the model used in this thesis and also agree with previous studies of other regions. Also the variability of the CRIR depending on the environment seen in this work is in agreement with previous findings. Taking the variability into account would improve the chemical models of star-forming regions and allow for more precise results.

5.2 Outlook

The question for a consistent and comprehensive theory of high-mass star formation from the atomic and molecular clouds to fully evolved main-sequence stars is a topic recent research and needs more input from observational, theoretical and laboratory studies, in order to combine chemical and physical properties to reveal the responsible and driving processes. On the observational side, new telescopes, such as ALMA, and improved existing telescopes, such as PdBI (and in the future NOEMA), will allow to study the chemistry with higher spatial resolution as well as larger frequency coverage and higher sensitivity of the observations. In addition, other facilities such as SOFIA, that operates in the infrared, will help to understand the chemistry and physics of the high-mass star-formation process in much more detail. Together with better constrains of quantities affecting the chemistry like the cosmic ray ionization rate and a better knowledge of the involved reaction rates from laboratory measurements will lead to an better understanding of the complex picture and help to reduce systematic errors present in the models as well as in the analysis of the data.

An immediate next step to follow up on the results of this thesis are interferometric observations of the chemically characterized sample, together with a detailed non-LTE analysis taking radiative transfer into account and the use of more precise and sophisticated models. Current chemical models depend on a number of assumptions and uncertain parameters such as, e.g., the CRIR, chemical rate coefficients or dust properties (Caselli 2003). There has been already work done in sensitivity analysis that study the effect of the sources of uncertainties and try to find those parameters, that introduce the largest uncertainties and need to be constrained better in order to efficiently improve the models (e.g., Vasyunin et al. 2004, 2008; Taquet et al. 2012a; Albertsson et al. 2013).

In the case of the model employed in this thesis, a more detailed assessment of the parameter space regarding, e.g., the total density, the temperature or the CRIR would be needed in order to learn more about caveats in the determination of the uniqueness of the best-fit parameters and explore how strong the dependency on the specific parameters is. Observations with ALMA and other interferometers will help to resolve the observed regions into their different sub-regions into their different components, that are not necessarily in the same evolutionary stage or that are dominated by different physical processes like e.g., shocks, but are still seen as single objects with the resolutions of observations so far. Although current observations with ALMA that study the star formation processes already exist (e.g., Sakai et al. 2013; Tan et al. 2013), larger statistical samples of the chemical and physical conditions in the high-mass star-forming regions are needed for a better understanding.

Another point of improvement will be more sensitive observations that allow a deeper search for molecules not yet detected in already observed sources and substitute upper limits with measured values. That helps to put better constraints on the comparison with models and to understand the star-formation process as a whole. A current topic that uses and will take advantage of the improvements in sensitivity and spectral coverage of modern telescopes is the search for pre-biotic molecules. A promising key to study pre-biotic chemistry is glycine, the simplest amino acid relevant to life, that was already found in samples of comets in the solar system, but not yet detected in star-forming regions (e.g., Belloche et al. 2013; Jiménez-Serra et al. 2014; Neill et al. 2014).

Bibliography

Aikawa, Y., Herbst, E., Roberts, H., & Caselli, P. 2005, ApJ, 620, 330

Albertsson, T., Indriolo, N., Kreckel, H., et al. 2014a, ArXiv e-prints

Albertsson, T., Semenov, D., & Henning, T. 2014b, ApJ, 784, 39

Albertsson, T., Semenov, D. A., Vasyunin, A. I., Henning, T., & Herbst, E. 2013, ApJS, 207, 27

André, P. 1995, Ap&SS, 224, 29

André, P., Men'shchikov, A., Bontemps, S., et al. 2010, A&A, 518, L102

André, P., Ward-Thompson, D., & Barsony, M. 2000, Protostars and Planets IV, 59

Banerjee, R., Vázquez-Semadeni, E., Hennebelle, P., & Klessen, R. S. 2009, MNRAS, 398, 1082

Barnes, P. J., Ryder, S. D., O'Dougherty, S. N., et al. 2013, MNRAS, 432, 2231

Barnes, P. J., Yonekura, Y., Fukui, Y., et al. 2011, ApJS, 196, 12

Bel, N. & Leroy, B. 1989, A&A, 224, 206

Belloche, A., Müller, H. S. P., Menten, K. M., Schilke, P., & Comito, C. 2013, A&A, 559, A47

Bergin, E. A., Alves, J., Huard, T., & Lada, C. J. 2002, ApJ, 570, L101

Bergin, E. A., Hartmann, L. W., Raymond, J. C., & Ballesteros-Paredes, J. 2004, ApJ, 612, 921

Bergin, E. A., Phillips, T. G., Comito, C., et al. 2010, A&A, 521, L20

Bergin, E. A. & Tafalla, M. 2007, ARA&A, 45, 339

Beuther, H., Churchwell, E. B., McKee, C. F., & Tan, J. C. 2007a, in Protostars and Planets V, ed. B. Reipurth, D. Jewitt, & K. Keil, 165–180

Beuther, H., Schilke, P., Gueth, F., et al. 2002a, A&A, 387, 931

Beuther, H., Schilke, P., Menten, K. M., et al. 2002b, ApJ, 566, 945

Beuther, H., Schilke, P., Sridharan, T. K., et al. 2002c, A&A, 383, 892

Beuther, H., Tackenberg, J., Linz, H., et al. 2012, A&A, 538, A11

Beuther, H., Zhang, Q., Bergin, E. A., & Sridharan, T. K. 2009, AJ, 137, 406

Beuther, H., Zhang, Q., Bergin, E. A., et al. 2007b, A&A, 468, 1045

Beuther, H., Zhang, Q., Greenhill, L. J., et al. 2004, ApJ, 616, L31

Bisschop, S. E., Jørgensen, J. K., van Dishoeck, E. F., & de Wachter, E. B. M. 2007, A&A, 465, 913

Blake, G. A., Mundy, L. G., Carlstrom, J. E., et al. 1996, ApJ, 472, L49

Blake, G. A., Sutton, E. C., Masson, C. R., & Phillips, T. G. 1987, ApJ, 315, 621

Bourke, T. L., Myers, P. C., Caselli, P., et al. 2012, ApJ, 745, 117

Campbell, M. F., Butner, H. M., Harvey, P. M., et al. 1995, ApJ, 454, 831

Carey, S. J., Feldman, P. A., Redman, R. O., et al. 2000, ApJ, 543, L157

Caselli, P. 2003, Ap&SS, 285, 619

Caselli, P. & Ceccarelli, C. 2012, A&A Rev., 20, 56

Caselli, P., Stantcheva, T., Shalabiea, O., Shematovich, V. I., & Herbst, E. 2002a, Planet. Space Sci., 50, 1257

Caselli, P., Walmsley, C. M., Terzieva, R., & Herbst, E. 1998, ApJ, 499, 234

Caselli, P., Walmsley, C. M., Zucconi, A., et al. 2002b, ApJ, 565, 331

Caselli, P., Walmsley, C. M., Zucconi, A., et al. 2002c, ApJ, 565, 344

Cernicharo, J., Castets, A., Duvert, G., & Guilloteau, S. 1984, A&A, 139, L13

Cesaroni, R., Churchwell, E., Hofner, P., Walmsley, C. M., & Kurtz, S. 1994, A&A, 288, 903

Cesaroni, R., Neri, R., Olmi, L., et al. 2005, A&A, 434, 1039

Chen, H.-R., Liu, S.-Y., Su, Y.-N., & Wang, M.-Y. 2011, ApJ, 743, 196

Chen, H.-R., Welch, W. J., Wilner, D. J., & Sutton, E. C. 2006, ApJ, 639, 975

Chira, R.-A., Beuther, H., Linz, H., et al. 2013, A&A, 552, A40

Churchwell, E., Walmsley, C. M., & Cesaroni, R. 1990, A&AS, 83, 119

Conover, W. J. 1971

Crapsi, A., Caselli, P., Walmsley, C. M., et al. 2005, ApJ, 619, 379

Crutcher, R. M., Troland, T. H., Lazareff, B., & Kazes, I. 1996, ApJ, 456, 217

Crutcher, R. M., Troland, T. H., Lazareff, B., Paubert, G., & Kazès, I. 1999, ApJ, 514, L121

Cummins, S. E., Linke, R. A., & Thaddeus, P. 1986, ApJS, 60, 819

Curtis, E. I., Richer, J. S., & Buckle, J. V. 2010, MNRAS, 401, 455

Dalgarno, A. & Lepp, S. 1984, ApJ, 287, L47

Daniel, F., Cernicharo, J., Roueff, E., Gerin, M., & Dubernet, M. L. 2007, ApJ, 667, 980

Di Francesco, J., Johnstone, D., Kirk, H., MacKenzie, T., & Ledwosinska, E. 2008, ApJS, 175, 277

Draine, B. T. 2011, Physics of the Interstellar and Intergalactic Medium

Druard, C. & Wakelam, V. 2012, MNRAS, 426, 354

Dutrey, A., Wakelam, V., Boehler, Y., et al. 2011, A&A, 535, A104

Egan, M. P., Shipman, R. F., Price, S. D., et al. 1998, ApJ, 494, L199

Emprechtinger, M., Caselli, P., Volgenau, N. H., Stutzki, J., & Wiedner, M. C. 2009, A&A, 493, 89

Enoch, M. L., Young, K. E., Glenn, J., et al. 2006, ApJ, 638, 293

Evans, N. J. 1999, ARA&A, 37, 311

Evans, N. J., Dunham, M. M., Jørgensen, J. K., et al. 2009, ApJS, 181, 321

Feigelson, E. D. & Montmerle, T. 1999, ARA&A, 37, 363

Flower, D. R., Pineau Des Forêts, G., & Walmsley, C. M. 2006, A&A, 449, 621

Fontani, F., Beltrán, M. T., Brand, J., et al. 2005, A&A, 432, 921

Fontani, F., Caselli, P., Crapsi, A., et al. 2006, A&A, 460, 709

Fontani, F., Palau, A., Caselli, P., et al. 2011, A&A, 529, L7

Fontani, F., Sakai, T., Furuya, K., et al. 2014, MNRAS, 440, 448

Foster, J. B., Jackson, J. M., Barnes, P. J., et al. 2011, ApJS, 197, 25

Friesen, R. K., Kirk, H. M., & Shirley, Y. L. 2013, ApJ, 765, 59

Garrod, R. T. & Herbst, E. 2006, A&A, 457, 927

Garrod, R. T., Wakelam, V., & Herbst, E. 2007, A&A, 467, 1103

Garrod, R. T., Weaver, S. L. W., & Herbst, E. 2008, ApJ, 682, 283

Gavilan, L., Vidali, G., Lemaire, J. L., et al. 2012, ApJ, 760, 35

Gerakines, P. A., Whittet, D. C. B., Ehrenfreund, P., et al. 1999, ApJ, 522, 357

Gerlich, D., Herbst, E., & Roueff, E. 2002, Planet. Space Sci., 50, 1275

Gerner, T., Beuther, H., Semenov, D., et al. 2014, A&A, 563, A97

Gibb, E. L., Whittet, D. C. B., Schutte, W. A., et al. 2000, ApJ, 536, 347

Glassgold, A. E., Huggins, P. J., & Langer, W. D. 1985, ApJ, 290, 615

Glover, S. C. O. & Clark, P. C. 2012, MNRAS, 421, 116

Glover, S. C. O., Federrath, C., Mac Low, M., & Klessen, R. S. 2010, MNRAS, 404, 2

Goldsmith, P. F., Irvine, W. M., Hjalmarson, A., & Ellder, J. 1986, ApJ, 310, 383

Goto, M., Geballe, T. R., Indriolo, N., et al. 2014, ApJ, 786, 96

Graedel, T. E., Langer, W. D., & Frerking, M. A. 1982, ApJS, 48, 321

Guertler, J., Henning, T., Kruegel, E., & Chini, R. 1991, A&A, 252, 801

Gutermuth, R. A., Megeath, S. T., Myers, P. C., et al. 2009, ApJS, 184, 18

Gutermuth, R. A., Myers, P. C., Megeath, S. T., et al. 2008, ApJ, 674, 336

Harada, N., Herbst, E., & Wakelam, V. 2010, ApJ, 721, 1570

Harada, N., Herbst, E., & Wakelam, V. 2012, ApJ, 756, 104

Hartquist, T. W., Dalgarno, A., & Oppenheimer, M. 1980, ApJ, 236, 182

Hatchell, J., Fuller, G. A., Richer, J. S., Harries, T. J., & Ladd, E. F. 2007, A&A, 468, 1009

Hatchell, J., Thompson, M. A., Millar, T. J., & MacDonald, G. H. 1998, A&AS, 133, 29

Hatchell, J. & van der Tak, F. F. S. 2003, A&A, 409, 589

Heitsch, F., Hartmann, L. W., Slyz, A. D., Devriendt, J. E. G., & Burkert, A. 2008, ApJ, 674, 316

Hennebelle, P., Banerjee, R., Vázquez-Semadeni, E., Klessen, R. S., & Audit, E. 2008, A&A, 486, L43

Herbst, E. & Klemperer, W. 1973, ApJ, 185, 505

Herbst, E. & van Dishoeck, E. F. 2009, ARA&A, 47, 427

Herpin, F., Marseille, M., Wakelam, V., Bontemps, S., & Lis, D. C. 2009, A&A, 504, 853

Hezareh, T., Houde, M., McCoey, C., Vastel, C., & Peng, R. 2008, ApJ, 684, 1221

Hincelin, U., Wakelam, V., Hersant, F., et al. 2011, A&A, 530, A61

Hiraoka, K., Ushiama, S., Enoura, T., et al. 2006, ApJ, 643, 917

Ho, P. T. P. & Townes, C. H. 1983, ARA&A, 21, 239

Hobbs, L. M. 1974, ApJ, 188, L107

Hoq, S., Jackson, J. M., Foster, J. B., et al. 2013, ApJ, 777, 157

Indriolo, N., Geballe, T. R., Oka, T., & McCall, B. J. 2007, ApJ, 671, 1736

Indriolo, N. & McCall, B. J. 2012, ApJ, 745, 91

Jackson, J. M., Rathborne, J. M., Foster, J. B., et al. 2013, ArXiv e-prints

Jenkins, E. B. 2009, ApJ, 700, 1299

Jiménez-Serra, I., testi, L., Caselli, P., & Viti, S. 2014, ApJ, 787, L33

Johansson, L. E. B., Andersson, C., Ellder, J., et al. 1984, A&A, 130, 227

Jørgensen, J. K., Hogerheijde, M. R., Blake, G. A., et al. 2004a, A&A, 415, 1021

Jørgensen, J. K., Schöier, F. L., & van Dishoeck, E. F. 2004b, A&A, 416, 603

Katz, N., Furman, I., Biham, O., Pirronello, V., & Vidali, G. 1999, ApJ, 522, 305

Kim, S.-J., Kim, H.-D., Lee, Y., et al. 2006, ApJS, 162, 161

Kirk, H., Johnstone, D., & Tafalla, M. 2007, ApJ, 668, 1042

Knee, L. B. G. & Sandell, G. 2000, A&A, 361, 671

Koda, J., Sawada, T., Wright, M. C. H., et al. 2011, ApJS, 193, 19

Kong, S., Caselli, P., Tan, J. C., & Wakelam, V. 2013, ArXiv e-prints

Krumholz, M. R. & Thompson, T. A. 2007, ApJ, 669, 289

Kuiper, R., Klahr, H., Beuther, H., & Henning, T. 2011, ApJ, 732, 20

Kurtz, S., Cesaroni, R., Churchwell, E., Hofner, P., & Walmsley, C. M. 2000, Protostars and Planets IV, Univ. of Arizona Press, Tuscon, eds. V. Mannings, A.P. Boss, S.S. Russel, 299

Lee, H.-H., Roueff, E., Pineau des Forets, G., et al. 1998, A&A, 334, 1047

Lee, T. J. 1972, Nature, 237, 99

Linsky, J. L. 2003, Space Sci. Rev., 106, 49

Linz, H., Stecklum, B., Henning, T., Hofner, P., & Brandl, B. 2005, A&A, 429, 903

Lodders, K. 2003, ApJ, 591, 1220

Loison, J.-C., Halvick, P., Bergeat, A., Hickson, K. M., & Wakelam, V. 2012, MNRAS, 421, 1476

Loughnane, R. M., Redman, M. P., Thompson, M. A., et al. 2012, MNRAS, 420, 1367

Lucas, R. & Liszt, H. 1998, A&A, 337, 246

Mangum, J. G. & Wootten, A. 1993, ApJS, 89, 123

Maret, S. & Bergin, E. A. 2007, ApJ, 664, 956

Martin-Pintado, J., Bachiller, R., & Fuente, A. 1992, A&A, 254, 315

McCall, B. J., Huneycutt, A. J., Saykally, R. J., et al. 2003, Nature, 422, 500

McElroy, D., Walsh, C., Markwick, A. J., et al. 2013, A&A, 550, A36

McKee, C. F. & Ostriker, E. C. 2007, ARA&A, 45, 565

McKee, C. F. & Tan, J. C. 2003, ApJ, 585, 850

Miettinen, O., Hennemann, M., & Linz, H. 2011, A&A, 534, A134

Millar, T. J., Bennett, A., & Herbst, E. 1989, ApJ, 340, 906

Morales Ortiz, J. L., Ceccarelli, C., Lis, D. C., et al. 2014, A&A, 563, A127

Motte, F. & André, P. 2001, A&A, 365, 440

Mouschovias, T. C., Tassis, K., & Kunz, M. W. 2006, ApJ, 646, 1043

Mueller, K. E., Shirley, Y. L., Evans, N. J., & Jacobson, H. R. 2002, ApJS, 143, 469

Narayanan, D., Cox, T. J., Shirley, Y., et al. 2008, ApJ, 684, 996

Neill, J. L., Bergin, E. A., Lis, D. C., et al. 2014, ApJ, 789, 8

Nguyen Luong, Q., Motte, F., Schuller, F., et al. 2011, A&A, 529, A41

Öberg, K. I., Linnartz, H., Visser, R., & van Dishoeck, E. F. 2009a, ApJ, 693, 1209

Öberg, K. I., van Dishoeck, E. F., & Linnartz, H. 2009b, A&A, 496, 281

Oliveira, C. M., Hébrard, G., Howk, J. C., et al. 2003, ApJ, 587, 235

Ossenkopf, V. & Henning, T. 1994, A&A, 291, 943

Pagani, L., Roueff, E., & Lesaffre, P. 2011, ApJ, 739, L35

Pagani, L., Salez, M., & Wannier, P. G. 1992, A&A, 258, 479

Pagani, L., Vastel, C., Hugo, E., et al. 2009, A&A, 494, 623

Parise, B., Leurini, S., Schilke, P., et al. 2009, A&A, 508, 737

Perault, M., Omont, A., Simon, G., et al. 1996, A&A, 315, L165

Pezzuto, S., Elia, D., Schisano, E., et al. 2012, A&A, 547, A54

Phillips, T. G., Huggins, P. J., Wannier, P. G., & Scoville, N. Z. 1979, ApJ, 231, 720

Pillai, T., Wyrowski, F., Carey, S. J., & Menten, K. M. 2006, A&A, 450, 569

Pillai, T., Wyrowski, F., Hatchell, J., Gibb, A. G., & Thompson, M. A. 2007, A&A, 467, 207

Pirogov, L., Zinchenko, I., Caselli, P., & Johansson, L. E. B. 2007, A&A, 461, 523

Qin, S.-L., Wu, Y., Huang, M., et al. 2010, ApJ, 711, 399

Racine, R. 1968, AJ, 73, 233

Ragan, S., Henning, T., Krause, O., et al. 2012, A&A, 547, A49

Reiter, M., Shirley, Y. L., Wu, J., et al. 2011, ApJS, 195, 1

Remijan, A. J., Leigh, D. P., Markwick-Kemper, A. J., & Turner, B. E. 2008, ArXiv e-prints

Ridge, N. A., Di Francesco, J., Kirk, H., et al. 2006, AJ, 131, 2921

Roberts, H. & Millar, T. J. 2000, A&A, 361, 388

Rolffs, R., Schilke, P., Zhang, Q., & Zapata, L. 2011, A&A, 536, A33

Röllig, M. & Ossenkopf, V. 2013, A&A, 550, A56

Roueff, E., Parise, B., & Herbst, E. 2007, A&A, 464, 245

Ruffle, D. P. & Herbst, E. 2001, MNRAS, 322, 770

Sadavoy, S. I., di Francesco, J., André, P., et al. 2012, A&A, 540, A10

Sadavoy, S. I., Di Francesco, J., André, P., et al. 2014, ApJ, 787, L18

Sakai, N., Sakai, T., Hirota, T., & Yamamoto, S. 2010, ApJ, 722, 1633

Sakai, T., Sakai, N., Foster, J. B., et al. 2013, ApJ, 775, L31

Sakai, T., Sakai, N., Furuya, K., et al. 2012, ApJ, 747, 140

Sakai, T., Sakai, N., Kamegai, K., et al. 2008, ApJ, 678, 1049

Sandell, G. & Knee, L. 2001, in Astronomical Society of the Pacific Conference Series, Vol. 235, Science with the Atacama Large Millimeter Array, ed. A. Wootten, 154

Sanhueza, P., Jackson, J. M., Foster, J. B., et al. 2012, ApJ, 756, 60

Sarrasin, E., Abdallah, D. B., Wernli, M., et al. 2010, MNRAS, 404, 518

Schilke, P., Benford, D. J., Hunter, T. R., Lis, D. C., & Phillips, T. G. 2001, ApJS, 132, 281

Schilke, P., Groesbeck, T. D., Blake, G. A., & Phillips, T. G. 1997a, ApJS, 108, 301

Schilke, P., Walmsley, C. M., Pineau des Forets, G., & Flower, D. R. 1997b, A&A, 321, 293

Schilke, P., Walmsley, C. M., Pineau Des Forets, G., et al. 1992, A&A, 256, 595

Schöier, F. L., van der Tak, F. F. S., van Dishoeck, E. F., & Black, J. H. 2005, A&A, 432, 369

Schuller, F., Menten, K. M., Contreras, Y., et al. 2009, A&A, 504, 415

Semenov, D., Hersant, F., Wakelam, V., et al. 2010, A&A, 522, A42

Semenov, D. & Wiebe, D. 2011, ApJS, 196, 25

Sridharan, T. K., Beuther, H., Saito, M., Wyrowski, F., & Schilke, P. 2005, ApJ, 634, L57

Sridharan, T. K., Beuther, H., Schilke, P., Menten, K. M., & Wyrowski, F. 2002, ApJ, 566, 931

Sutton, E. C., Blake, G. A., Masson, C. R., & Phillips, T. G. 1985, ApJS, 58, 341

Tan, J. C., Beltran, M. T., Caselli, P., et al. 2014, ArXiv e-prints

Tan, J. C., Kong, S., Butler, M. J., Caselli, P., & Fontani, F. 2013, ApJ, 779, 96

Taquet, V., Ceccarelli, C., & Kahane, C. 2012a, ApJ, 748, L3

Taquet, V., Ceccarelli, C., & Kahane, C. 2012b, A&A, 538, A42

Taquet, V., Peters, P. S., Kahane, C., et al. 2013, A&A, 550, A127

Testi, L., Hofner, P., Kurtz, S., & Rupen, M. 2000, A&A, 359, L5

Thompson, M. A. & MacDonald, G. H. 1999, A&AS, 135, 531

Tielens, A. G. G. M. 2005, The Physics and Chemistry of the Interstellar Medium (Cambridge University Press)

Turner, B. E. 2001, ApJS, 136, 579

van den Bergh, S. 1966, AJ, 71, 990

van der Tak, F. F. S. 2005, in IAU Symposium, ed. R. Cesaroni, M. Felli, E. Churchwell, & M. Walmsley, 70–79

van der Tak, F. F. S., Black, J. H., Schöier, F. L., Jansen, D. J., & van Dishoeck, E. F. 2007, A&A, 468, 627

van der Tak, F. F. S. & van Dishoeck, E. F. 2000, A&A, 358, L79

van der Tak, F. F. S., van Dishoeck, E. F., Evans, II, N. J., & Blake, G. A. 2000, ApJ, 537, 283

van Dishoeck, E. F. & Blake, G. A. 1998, ARA&A, 36, 317

van Dishoeck, E. F., Jonkheid, B., & van Hemert, M. C. 2006, in Faraday discussion, Vol. 133, Chemical evolution of the Universe, ed. I. R. Sims & D. A. Williams, 231–244

Vasyunin, A. I. & Herbst, E. 2013a, ApJ, 762, 86

Vasyunin, A. I. & Herbst, E. 2013b, ApJ, 769, 34

Vasyunin, A. I., Semenov, D., Henning, T., et al. 2008, ApJ, in press

Vasyunin, A. I., Sobolev, A. M., Wiebe, D. S., & Semenov, D. A. 2004, Astronomy Letters, 30, 566

Vasyunina, T., Linz, H., Henning, T., et al. 2011, A&A, 527, A88

Vasyunina, T., Vasyunin, A. I., Herbst, E., & Linz, H. 2012, ApJ, 751, 105

Vasyunina, T., Vasyunin, A. I., Herbst, E., et al. 2013, ArXiv e-prints

Wakelam, V. & Herbst, E. 2008, ApJ, 680, 371

Wakelam, V., Herbst, E., Le Bourlot, J., et al. 2010, A&A, 517, A21

Walawender, J., Bally, J., Francesco, J. D., Jørgensen, J., & Getman, K. . 2008, NGC 1333: A Nearby Burst of Star Formation, ed. B. Reipurth, 346

Walmsley, C. M. & Ungerechts, H. 1983, A&A, 122, 164

Walsh, A. J., Myers, P. C., Di Francesco, J., et al. 2007, ApJ, 655, 958

Walsh, A. J., Thorwirth, S., Beuther, H., & Burton, M. G. 2010, MNRAS, 404, 1396

Wang, Y., Beuther, H., Zhang, Q., et al. 2012, ApJ, 754, 87

Wannier, P. G., Encrenaz, P. J., Wilson, R. W., & Penzias, A. A. 1974, ApJ, 190, L77

Watson, W. D. 1974, ApJ, 188, 35

Welty, D. E. & Hobbs, L. M. 2001, ApJS, 133, 345

Wilson, T. L. & Rood, R. 1994, ARA&A, 32, 191

Wood, D. O. S. & Churchwell, E. 1989a, ApJ, 340, 265

Wood, D. O. S. & Churchwell, E. 1989b, ApJS, 69, 831

Zinchenko, I., Caselli, P., & Pirogov, L. 2009, MNRAS, 395, 2234

Zinnecker, H. & Yorke, H. W. 2007, ARA&A, 45, 481

Ziurys, L. M., Friberg, P., & Irvine, W. M. 1989, ApJ, 343, 201

Acknowledgements

I would like to thank all the people who contributed to this thesis and helped me with their advise and comments. First I want to thank my advisor Henrik Beuther for his great supported and his encouragement during the whole time of this thesis. I also want to thank Dima Semenov for his tremendous help in all chemistry related questions and for all his efforts and contributions. I want to thank Yancy Shirley for inviting me to Tucson, Arizona, USA, and becoming a second advisor for me during this time and also for all the nice non-scientific hours. I also want to thank Thomas Henning who had always good ideas and gave a lot of helpful comments about my work. And I thank all the co-authors for their contributions.

I want to thank Ralf Klessen for refereeing this thesis and Andreas Wolf for being part of my thesis committee as well as Kees Dullemond for being part of my IMPRS committee.

Thanks also to the IMPRS coordinator Christian Fendt and all the people from IMPRS, especially from the 7th generation for having good times during the retreats and in Heidelberg.

Also many thanks to all my office colleagues for the friendly company and enjoyable working atmosphere. I also enjoyed the regular student coffee meetings with fellow students and also thanks to all colleagues I spend many hours playing football with.

And I want to thank all members of the MPIA for the great scientific and non-scientific atmosphere.

Finally, I want to thank all other people who I forgot and who I spent good times with and who made that these last years will become a good memory. In particular, I want to thank my family and Anahí.

Thanks also for being supported by the Sonderforschungsbereich SFB 881 “The Milky Way System” (subproject B3) of the German Research Foundation (DFG).

This thesis is based on observations carried out with the IRAM 30m Telescope. IRAM is supported by INSU/CNRS (France), MPG (Germany) and IGN (Spain). Furthermore, I have made use of data from the Herschel Gould Belt survey (HGBS) project (http://gouldbelt-herschel.cea.fr). The HGBS is a Herschel Key Programme jointly carried out by SPIRE Specialist Astronomy Group 3 (SAG 3), scientists of several institutes in the PACS Consortium (CEA Saclay, INAF-IFSI Rome and INAF-Arcetri, KU Leuven, MPIA Heidelberg), and scientists of the Herschel Science Center (HSC).